

**RADIATION DOSIMETRY OF
CHARGED PARTICLES AND
NEUTRONS BY PASSIVE AND
ACTIVE DOSIMETERS AND ITS
APPLICATION TO RADIATION
PERSONNEL MONITORING**

By

SUJOY CHATTERJEE

Enrolment No: PHYS04201004010

Variable Energy Cyclotron Centre, Kolkata

*A thesis submitted to the
Board of Studies in Physical Sciences*

*In the partial fulfillment of the requirements
for the degrees of*

DOCTOR OF PHILOSOPHY

of

HOMI BHABHA NATIONAL INSTITUTE



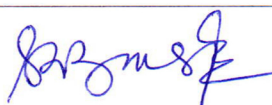
May, 2017

Homi Bhabha National Institute¹

Recommendations of the Viva Voce Committee

As members of the Viva Voce Committee, we certify that we have read the dissertation prepared by Shri Sujoy Chatterjee entitled "Radiation dosimetry of charged particles and neutrons by passive and active dosimeters and its application to radiation personnel monitoring" and recommend that it may be accepted as fulfilling the thesis requirement for the award of Degree of Doctor of Philosophy.

Chairman – Dr. S. R. Banerjee



Date:

24/5/2017

Guide / Convener – Dr. Tapas Bandyopadhyay



Date:

24/5/17

Co-guide - _____

Date:

Examiner – Dr. Dipankar Das



Date:

24/5/2017.

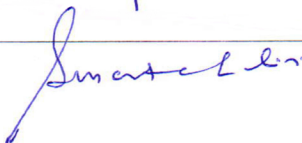
Member 1- Dr. Tapan Nayak



Date:

24/5/2017

Member 2- Dr. Susanta Lahiri



Date:

24/05/2017

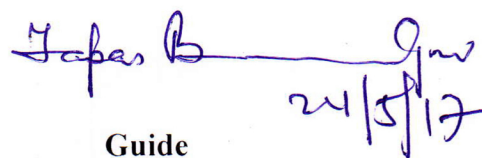
Final approval and acceptance of this thesis is contingent upon the candidate's submission of the final copies of the thesis to HBNI.

I/~~We~~ hereby certify that I/~~we~~ have read this thesis prepared under my/our direction and recommend that it may be accepted as fulfilling the thesis requirement.

Date: 24-05-2017

Place: Kolkata

Co-guide (if applicable)



24/5/17

Guide

¹ This page is to be included only for final submission after successful completion of viva voce.

STATEMENT BY AUTHOR

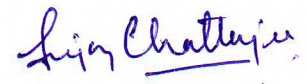
This dissertation has been submitted in partial fulfillment of requirements for an advanced degree at Homi Bhabha National Institute (HBNI) and is deposited in the Library to be made available to borrowers under rules of the HBNI.

Brief quotations from this dissertation are allowable without special permission, provided that accurate acknowledgement of source is made. Requests for permission for extended quotation from or reproduction of this manuscript in whole or in part may be granted by the Competent Authority of HBNI when in his or her judgment the proposed use of the material is in the interests of scholarship. In all other instances, however, permission must be obtained from the author.


(Sujoy Chatterjee)

DECLARATION

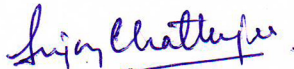
I, hereby declare that the investigation presented in the thesis has been carried out by me. The work is original and has not been submitted earlier as a whole or in part for a degree / diploma at this or any other Institution / University.


(Sujoy Chatterjee)

List of Publications arising from the thesis

Journal

1. "Calculation of Response Matrix of $\text{CaSO}_4:\text{Dy}$ based neutron dosimeter using Monte Carlo code FLUKA and Measurement of ^{241}Am -Be spectra" S. Chatterjee, A. K. Bakshi and S. P. Tripathy, Nuclear Instruments and Methods in Physics B, **2010** Vol. 268, 2825–2830.
2. "Estimation of induced activity in superconducting cyclotron at VECC:Monte Carlo Calculations" S. Chatterjee and T. Bandyopadhyay, Indian Journal of Pure & Applied Physics, Vol. 50, **2012**, 498-500.
3. "Salient features, response and operation of Lead-Free Gulmarg Neutron Monitor", S. Mufti, S. Chatterjee, P.M. Ishtiaq, M.A. Darzi, T.A. Mir, Nuclear Instruments and Methods in Physics A, **2016**, Vol. 813, 74 - 83.


(Sujoy Chatterjee)

Chapters in books and lectures notes

Conferences

1. “Monte Carlo simulated sensitivity and energy response of Lead-Free Gulmarg Neutron Monitor”, S. Mufti, and S. Chatterjee, Proceedings of 6th JK Science Congress, December 2 – 4 , **2010**, University of Kashmir, Srinagar.
2. Dose and residual activity estimations for 30 MeV DAE medical cyclotron, Kolkata”, S. Chatterjee, T.Bandyopadhyay, R.Ravisankar, Proceedings of International Symposium on Accelerator and Radiation Physics, **2011**, SINP, February 16-18,Kolkata.
3. “Estimation of Induced Activity in Super Conducting Cyclotron at VECC : Monte Carlo calculations” S. Chatterjee and T. Bandyopadhyay, Proceedings of International Conference on Accelerator Radiation Safety, **2011**, BARC, November 16-18,2011, Mumbai.
4. “Neutron and Photon shielding of beam dump for K130 Cyclotron at VECC: Monte Carlo Calculations” S. Chatterjee, K. Banerjee, P. Roy, S. Bhattacharyya, T. Bandyopadhyay, C. Bhattacharyya, DAE-BRNS Indian Particle Accelerator Conference, **2013**, VECC, November 19-22, Kolkata.

5. "Monte Carlo Calculations for beam dump design for K-130 Cyclotron at VECC" S. Chatterjee, K. Banerjee, P. Roy, S. Bhattacharyya, T. Bandyopadhyay, C. Bhattacharyya, International Symposium on Nuclear Physics, BARC, December 2-6, **2013**, Mumbai.

Others


(Sujoy Chatterjee)

DEDICATIONS

I dedicate this thesis to my mother *Late Smt. Krishna Chatterjee*, who always wanted to see me earn this degree, but could not live to see it happen.

ACKNOWLEDGEMENTS

I am privileged and honoured to have Dr. Tapas Bandyopadhyay as my guide for this work and guiding me throughout the completion of the thesis. His valuable directions, visionary suggestions, suitable appraisals and invaluable teachings have been responsible for this work. I am grateful to him for accepting me and guiding me all along.

I thank Dr. Y. S. Mayya (Ex-Head, RP&AD, BARC) for allowing me to carry out this work. I would also like to thank Dr. D. Datta (Head, RP&AD, BARC) for his encouragement during the writing of this thesis.

I thank Dr. Dinesh Kumar Srivastava (Ex-Director, VECC) for his mental support during the course work and also during the work carried out.

I thank Dr. A. K. Bakshi (Head, PMSS, BARC) for the motivation and experimental support on the study carried out for the generation of response matrix for $\text{CaSO}_4:\text{Dy}$ based neutron dosimeter.

I sincerely thank my colleagues of VECC, particularly, Dr. Kaushik Banerjee, Shri Pratap Roy, Dr.(Smt.) Chandana Bhattacharyya, Dr. S. R. Banerjee, Dr. Deepak Pandit, Dr. Surajit Pal and Dr. Sudipta Mukhopadhyay for their help and support during the experiment in the study of shielding calculations for beam dump.

I thank all my colleagues of Health Physics Unit, VECC, particularly, Dr. R. Ravishankar, Smt. Mausumi Sengupta Mitra, Shri K. Shrihari, Smt. Koushiki Ghosh Jana, Shri Ramesh C. Mohalla, Shri Lalit K. Mohanta and Shri Nirmal Kundu specially during my experimental work.

I specially thank Dr. Sailajananda Bhattacharyya (Raja Ramanna Fellow, DAE, VECC) and Dr. Amit Roy (Raja Ramanna Fellow, DAE, VECC) for their help and motivation during the writing of this thesis.

I thank Dr. Paramita Mukherjee and Dr. Gayanthri N. Banerjee of VECC for their motivation and support during my work.

I take this opportunity to thank all my colleagues of K-130 Cyclotron Operation for their help during the experimental work.

On personal note, I pay my gratitude to my parents, who have supported all through my academic career. I would like to thank my wife Smt. Pamela Chatterjee for her love, encouragement and support who silently suffered all through this sojourn. I would also like to thank my beloved son Shri Aritra Chatterjee for his innocent smile which has cherished me against all odds. I also thank my sister Smt. Soma Chatterjee for her support during this journey.

CONTENTS

	Page No.
SYNOPSIS	xiii
LIST OF FIGURES	xxv
LIST OF TABLES	xxx
1 Introduction	1
1.1 Natural sources of radiation	1
1.1.1 Cosmic radiation	2
1.1.2 Terrestrial radiation	4
1.1.3 Natural radioactivity in body	4
1.2 Man-made sources of radiation	4
1.2.1 Medical procedures	5
1.2.2 Consumer products	5
1.2.3 Radioactive fallout	5
1.2.4 Nuclear Power and fuel cycle	6
1.3 History of radiation protection	6
1.4 Biological effects of radiation	8
1.4.1 Stochastic effects	10
1.4.2 Deterministic effects	10
1.5 Radiation Protection Quantities	10
1.6 Institutional Framework	19
1.7 Radiation protection in India	20
1.7.1 External personnel monitoring with TLD badge	22
1.7.2 External personnel monitoring with CR-39	26
1.7.3 Personnel monitoring devices in other countries	29
1.8 Spectrometry in radiation protection and personnel monitoring	32
1.9 Fundamentals of Cyclotrons	36
1.9.1 History	36
1.9.2 Principle of Cyclotron	36
1.9.3 Relativistic considerations	39
1.9.4 Synchrocyclotron	39
1.9.5 Isochronous Cyclotron	40
1.10 Description of Accelerators and other facilities (Existing and upcoming)	40
1.10.1 High Altitude Research Laboratory (HARL)	41
1.10.2 K-130 Cyclotron	42

1.10.3	Super Conducting Cyclotron	43
1.10.4	Medical Cyclotron	44
1.11	Monte Carlo Simulation	46
1.11.1	History of Monte Carlo Method	47
1.11.2	Steps of Monte Carlo simulation	48
1.11.3	Probability Density Function	49
1.11.4	Cumulative Distribution Function	49
1.11.5	Random Numbers	49
1.11.6	Sampling	51
1.11.7	Scoring or Tallying	52
1.11.8	Error estimation	53
1.11.9	Variance Reduction Techniques	53
1.11.10	Parallelization or vectorization	55
1.12	Reverse Monte Carlo Method	56
1.13	Monte Carlo code used in thesis	56
1.13.1	Capabilities of FLUKA	57
1.13.2	FLUKA geometry and Input	58
1.13.3	Scoring in FLUKA	59
1.14	Motivation and Structure of the thesis	60
2	Response Matrix for CaSO₄:Dy based neutron detector	62
2.1	Introduction	62
2.2	Response Matrix Calculation	65
2.3	Determination of conversion factor	69
2.4	Experimental procedure	69
2.5	Parameterization of response function	72
2.6	Spectrum unfolding	73
3	Characterization of LFGNM	84
3.1	Introduction	84
3.2	Simulation with Monte Carlo code	87
3.2.1	Geometry of LFGNM simulation	88
3.3	Sensitivity to upper moderator thickness	89
3.3.1	Calculation with Monte Carlo code FLUKA	89
3.3.2	Experiment	90
3.4	Energy response of LFGNM	90
3.4.1	Simulation with FLUKA	92
3.5	Lead Test of LFGNM	93
3.6	Cadmium Test of LFGNM	94
3.7	Angular Response of LFGNM	96
4	Residual Nuclei Calculations	98
4.1	Introduction	98
4.2	Methodology for Medical Cyclotron	99
4.2.1	Residual Nuclei in Concrete	103
4.2.2	Residual Nuclei in soil after 50 cm layer of concrete	110
4.2.3	Residual Nuclei in soil after 100 cm of concrete	115

4.2.4	Residual Nuclei in Soil	117
4.3	Methodology for Super Conducting Cyclotron	123
4.3.1	Measurement of dose rates after different cooling times	124
4.3.2	Measurement of Residual Nuclei for SCC	127
5	Shielding of Beam Dump	141
5.1	Introduction	141
5.1.1	General description of K-130 Cyclotron	142
5.2	Shielding Calculations of Beam Dump	143
5.3	Experimental determination of Neutron and Photon spectra	156
5.3.1	Experimental determination of Neutron spectrum	156
5.3.2	Experimental determination of Photon spectrum	169
5.4	Residual nuclei estimation in the shield	176
5.4.1	Residual nuclei in Target	177
5.4.2	Residual nuclei in HDPE(Inside)	178
5.4.3	Residual nuclei in Pb	180
5.4.4	Residual nuclei calculation in HDPE(Outside)	182
5.4.5	Residual Nuclei in Fe	184
6	Summary and Conclusion	187
	BIBLIOGRAPHY	192



Homi Bhabha National Institute

SYNOPSIS OF Ph.D. THESIS

1. Name of the Student:	Sujoy Chatterjee
2. Name of the Constituent Institution:	Variable Energy Cyclotron Centre
3. Enrolment No.:	PHYS04201004010
4. Title of the Thesis:	Radiation dosimetry of charged particles and neutrons by passive and active dosimeters and its application to radiation personnel monitoring
5. Board of Studies:	Physical Sciences

SYNOPSIS

Scope of Work

Radiation dosimetry plays an important role to estimate the risk and assessment of detriment to personnel working in radiation environment. Evaluation of these dose has to be precise and in continuation of revision from time to time to reduce the risk factor. Scope of the present work is improvement of data for the personnel monitoring dosimetry at various radiation facilities. The radiation fields under study are photons, neutrons and charged particles. Considering the importance and challenges for neutron personnel monitoring dosimetry, workplace neutron

spectrometry using passive dosimeter is of importance and effort was given to emphasis the procedure. Response matrix of neutrons for the newly developed TL dosimeter based on $\text{CaSO}_4:\text{Dy}$, used for country wide personnel monitoring service in India was generated. For improvement in the dosimetric data for air-crew and space dosimetry, characterization of Neutron Monitor (NM) situated at high altitude was undertaken. Further, Monte Carlo simulations were carried out for the data on residual nuclei for the two upcoming accelerator facilities. In any radiation generating facilities, residual nuclei contribute significantly not only to occupational workers, but also to general public. In any accelerator, beam dump is a device in the beam line, which fully stops the accelerated primary projectiles after interaction with the target. Beam dump shielding optimization calculations were undertaken for the improved nuclear physics experiments and studies, and also for evaluating its contribution to dose, if any, for the workers involved in the maintenance of the accelerators.

Introduction

Personnel monitoring of occupational workers is one of the important pillars of radiation protection[1,2]. It is a systematic process for monitoring, recording, evaluating, and reporting the radiation doses received by occupationally exposed individuals. It comprises of external as well as internal radiation monitoring of the workers occupationally engaged in radiation related jobs. External radiation monitoring comprises of measurement of X-rays, beta particles and gamma rays using TLD badge and measurement of neutrons using CR-39 foils outside the human body. The aim of this research is to carry out the dosimetry of neutrons, photons and charged particles in various radiation facilities where personnel monitoring of occupational radiation workers are required.

Accelerators are becoming indispensable part of our daily life because of its huge societal benefits. They are widely used for the diagnosis and treatment in

medical domain, for research and development in science and technology, for food preservation, artificial jewellery and many more. These accelerators can be classified based on the energy of the projectile particles such as: 1) Low energy accelerators, 2) Medium energy accelerators and 3) High energy accelerators[3]. Considering their societal benefits, more and more low and medium energy accelerators are being installed in densely populated regions. These will create radiation hazard for occupational workers and for general public, if adequate radiation protection guidelines are not followed. Moreover, radiation fields generally encountered in any accelerator centres are very complex due to the contribution from both particles and photons. Hence the study of these radiation centres and its related dosimetry is of immense importance considering the *depth in defense*, especially at the conceptual stage of a program. Among the other radiation facilities, this work has emphasized accelerator centres.

Passive and active dosimeters are together important in mixed fields of radiations mainly encountered in the high and medium energy accelerator centres. For theoretical estimation, though semi-empirical formulation is preferred, but for practical constraints and increase of dimensionality of the problems, estimation of the same has been done using Monte Carlo simulation code FLUKA[4,5]. Similar Monte Carlo codes such as EGSnrc, PENELOPE, GEANT4, MCNP, etc are also available for performing similar jobs, but the choice of Monte Carlo code FLUKA was due to its versatility, free availability, improved graphical interfaces are few important points. With the development of computational technology, Monte Carlo methods are one of the indispensable tool for table top experiments, which otherwise would have taken more man hours and sophisticated detectors to arrive at the data. These have been possible with more accurate cross section libraries available in literature. The thesis is divided into following chapters:

1. Response matrix for CaSO₄:Dy based neutron detector:

Neutron energy spectrum measurement for personnel monitoring and work place monitoring is very important because neutron fluence to personnel dose equivalent (H_p [10]) and ambient dose equivalent (H^* [10]) changes with the energy of incident neutrons[6]. Among several passive techniques available, neutron spectrometry with Bonner sphere is of importance[7]. A thermal neutron detectors under different sizes of Bonner sphere (made up of High Density Polyethylene having density of 0.95 g/cm³) can be used for the neutron spectrometry upto 20 MeV. The thermal neutron detector used in this work is based on CaSO₄:Dy TL phosphor, which is also used for country wide personnel monitoring in India. It requires generation of response matrix[8] for the thermal neutron detector to be used. The response matrix has been generated in this work with Monte Carlo code FLUKA. Response matrix for the detector has been calculated in the energy range of 2.5×10^{-8} MeV to 20 MeV in steps of unequal energy binning. The detector has been considered to be kept inside different Bonner spheres having sizes varying from 3 to 12 inches including that in bare condition too.

This response matrix was used for the deconvolution of neutron energy spectrum from ²⁴¹Am-Be neutron source. De-convolution of the neutron energy spectrum was carried out using FRUIT parametric code[9]. The de-convoluted neutron spectrum was further compared with that available in the literature[10], which was found to be in order. So, the response matrix for this thermal neutron detector based on CaSO₄:Dy can be used very well for the neutron spectrometry in the fields of nuclear reactors and accelerators, where they contribute to dose to the occupational workers.

2. Characterization of LFGNM for aircrew and space dosimetry:

Lead Free Gulmarg Neutron Monitor (LFGNM) measures neutron fluence from the secondary neutrons due to the interaction of primary cosmic ray with earth's atmo-

sphere[11]. This neutron monitor can also be used for estimation of exposure from neutrons for air-crew dosimetry as it is located at 2743 m above sea level. International Commission on Radiation Protection [ICRP] in publication 60 (1991) recommended that exposure to cosmic radiation be part of occupational exposure in the operation of commercial jet air craft and space flight. It further clarified in its recommendation in publication 75(1997) that it is not necessary to treat the exposure of frequent-flyer passengers as occupationally exposed for the purpose of control. Only air crew should be considered as occupational workers.

LFGNM consists of 21 cylindrical BF_3 detectors placed over a paraffin reflector having a thickness of 28 cm. A Paraffin moderator is also kept above these 21 cylindrical detectors. In this work, the characterization of LFGNM has been carried out using Monte Carlo code FLUKA. Some theoretical data has been verified using experimental methods. Characterization of LFGNM includes: 1) Sensitivity of upper paraffin moderator thicknesses from bare to 48 cm, 2) Energy response of the detector in the range of 10^{-11} MeV to 10^4 MeV, 3) Lead test of the detector with bare, 2 inches and 4 inches lead inserts, 4) Cadmium test and 5) Angular response of the detector from 0° to 60° angle in the energy range of 10^{-11} MeV to 10^4 MeV. Sensitivity of the upper paraffin moderator test has been carried out experimentally using ^{239}Pu -Be neutron source.

3. Residual nuclei calculations for Medical cyclotron and Super conducting cyclotron:

With the construction of accelerators in densely populated public domains, with societal benefits, it possess radiation risk not only for the occupational workers, but also for general public, if sufficient radiation protection guidelines are not followed[3]. Residual nuclei calculations are important in this context as the energetic particles interact with the beam line components and radiation shield. If energy of the particle is sufficiently high, they may interact with the soil which is immediately after the

shield.

Residual nuclei calculations has been carried out for 30 MeV, 500 μ A beam current of Medical cyclotron(Department of Atomic Energy). FLUKA Monte Carlo code has been used for these calculations. In case of Medical Cyclotron, residual nuclei calculations has been carried out in concrete layers of different thicknesses, soil followed by concrete and in different layers of only soil considering worst possible scenario. Cyclotron run time for these calculations has been taken to be 1 week, 1 month and 1 year. Total activity in different layers of concrete and soil has been estimation with some of the major isotopes contributing to the total activity were also estimated.

Residual activity calculations for Super Conducting Cyclotron (SCC)[12] has been carried out in different beam line components such as Cu, Al and SS(316L) along with shielding material like concrete. These estimations has been carried out with 80 MeV proton with 0.1 μ A beam current. Along with the estimation of activity, ambient dose rates (H^* [10]) has been estimated for different cooling times of 1 h to 10^5 h. Variation of activity with cooling times has been plotted separately for different isotopes having half lives in minutes, hours, days and years. Reaction cross section for different isotopes have also been evaluated using TALYS code[13].

4. Optimization of beam dump shielding and experimental verification:

Nuclear physics experiments using ion beams from cyclotrons are carried out using very thin targets. As most of the beams passes through the target, it requires to be stopped in some material such as beam dump. So beam dump becomes the major source of neutrons and gammas due to interaction of the beam with dump, which is undesired. It interferes with the experimental detectors and requires proper shielding.

Shielding of beam dump in this work has been carried out for one of the beam line of Room Temperature Cyclotron[14] using 50 MeV alpha particles. Shielding

has been done with combination of materials such as Fe (density 7.874 g/cm³), Pb (density 11.35 g/cm³) and High Density Polyethylene (HDPE) (density 1 g/cm³). Theoretical calculations have been carried out with FLUKA. To validate the theoretical data, experiment has been carried out in which neutron and photon energy spectrum in different shielding configurations has been evaluated and compared.

The shielding materials of beam dump become major source of residual nuclei due to the interaction of neutrons, which in turn are generated by interaction of beam particles with dump materials. So, it may contribute exposure to the personnels, who are involved in the maintenance of cyclotron. Residual nuclei calculations were hence carried out in different shielding materials of the beam dump. In this calculation, Cyclotron “ON” period was considered for six months with 50 MeV α particles having beam current of 1 nA. Total activity and due to various radio-nuclides were estimated for different cooling periods of 0 h to six months.

5. Future work to continue:

The conclusion and overall summary of work has been presented along with future scope of work. The response matrix for present CaSO₄:Dy based dosimeter can be extended beyond 20 MeV, keeping pace with upcoming higher energy accelerators. De-convolution of neutron energy spectrum at work places will help in further improving radiation personnel monitoring dosimetry for neutrons. This requires the response matrix to be generated for improved Bonner spheres having metal inserts with higher atomic number. Personalized fluence to personnel dose equivalent factors depending on the neutron energy spectrum can be used based on the type of work in various accelerator centres with different projectile energies. Most of the data for characterization of LFGNM has been generated using FLUKA, which can be further validated experimentally, if dedicated neutron beam lines are available. Neutron dose rates available at such high altitude laboratory will be helpful for air-crew and space dosimetry, which has attracted world interest for quite some time.

Residual nuclei calculations, carried out for Medical cyclotron and Superconducting cyclotrons can be verified experimentally, once these becomes operational. This will help in validating the theoretical data generated using Monte Carlo code. This work will be useful for the design in radiation safety aspects of upcoming accelerators, to keep in stand with **As Low As Reasonably Achievable** (ALARA) and local regulatory authority.

Bibliography:

1. “Recommendations of the International Commission on Radiological Protection”, 1991, ICRP Publication 60 Ann. ICRP 21 (1-3).
2. “Hand book on the use of TLD badge based on $\text{CaSO}_4:\text{Dy}$ teflon discs for individual monitoring”, Pradhan A. S., Adtani M. M., Varadharajan G., Bakshi A. K., Srivastava K., Bihari R. R., 2002, BARC/2002/E/025.
3. “Safety Guidelines on Accelerators”, Atomic Energy Regulatory Board, 2005, Guideline No. AERB/SG/IS-5, AERB, Mumbai.
4. “The FLUKA Code: Developments and Challenges for High Energy and Medical Applications”, T. T. Bohlen, F. Cerutti, M. P. W. Chin. A. Fassò, A. Ferrari, A. Mairani, P.R. Sala, G. Smirnov, V. Vlachoudis, Nuclear Data Sheets, 120, 211-214 (2014).
5. “FLUKA: a multi-particle transport code”, A. Ferrari, P. R. Sala, A. Fassò, and J. Ranft, CERN-2005-10 (2005), INFN/TC_05/11, SLAC-R-773.
6. “The 2007 Recommendations of the International Commission on Radiological Protection”, Annals of the ICRP, Publication No 103, ICRP.
7. “Neutron spectrometry—historical review and present status”, F. D. Brooks, H. Klein, Nuclear Instruments and Methods in Physics Research Section A: Accelerators, Spectrometers, Detectors and Associated Equipment, Vol. 476(1), 2002.

8. "Response matrix for a multisphere spectrometer using a ^6LiF thermoluminescent dosimeter", H. R. Vega Carrillo, B. W. Wehring, K. G. Veinot and N. E. Hertel, *Radiation Protection Dosimetry*, 1999, Vol. 81(2).
9. "FRUIT: An operational tool for multisphere neutron spectrometry in workplaces", Roberto Bedogni, Carles Domingo, Adolfo Esposito and Francisco Fernandez, *Nuclear Instruments and Methods in Physics Research A*, 2007, Vol. 580.
10. "Compendium of Neutron Spectra and Detector Responses for Radiation Protection Purposes", Technical Report Series, IAEA, 2001, Supplement to Technical Reports Series No. 318.
11. "Lead-Free Gulmarg Neutron Monitor", G. N. Shah, S. Mufti, M. A. Darzi and P. M. Ishtiaq, *Astroparticle Physics*, Vol. 33(1), 2010.
12. "Super conducting Cyclotron Operation Manual", Variable Energy Cyclotron Centre, Kolkata, June 2008, http://project.vecc.gov.in:8080/Safety_web/Safety/Reportsandtrainingmanuals/SCC-Operation-Manual.pdf.
13. "TALYS-1.0", Arjan J Koning, Stephane Hilaire, Marieke C Duijvestijn, International Conference on Nuclear Data for Science and Technology, 2007, EDP Sciences.
14. "K-130 Cyclotron Operation Manual", Variable Energy Cyclotron Centre, Kolkata, June 2012, http://project.vecc.gov.in:8080/Safety_web/Safety/Reportsandtrainingmanuals/K-130-OM-2012.pdf.

Publications in Refereed Journal:

a. Published:

1. “Calculation of Response Matrix of CaSO₄:Dy based neutron dosimeter using Monte Carlo code FLUKA and Measurement of ²⁴¹Am-Be spectra” **S. Chatterjee**, A. K. Bakshi and S. P. Tripathy, Nuclear Instruments and Methods in Physics B, (2010) Vol. 268, pp 2825–2830.
2. “Estimation of induced activity in superconducting cyclotron at VECC:Monte Carlo Calculations” **S. Chatterjee** and T. Bandyopadhyay, Indian Journal of Pure & Applied Physics, Vol. 50, 2012, pp 498-500.
3. “Salient features, response and operation of Lead-Free Gulmarg Neutron Monitor”, S. Mufti, **S. Chatterjee**, P. M. Ishtiaq, M. A. Darzi, T. A. Mir, Nuclear Instruments and Methods in Physics A, Vol 813, pp 74 - 83, 2016.

b. Accepted:

c. Communicated:

d. Other Publications:

1. “Monte Carlo simulated sensitivity and energy response of Lead-Free Gulmarg Neutron Monitor”, S. Mufti, and **S. Chatterjee**, Proceedings of 6th JK Science Congress, December 2 – 4, 2010, University of Kashmir, Srinagar.
2. Dose and residual activity estimations for 30 MeV DAE medical cyclotron, Kolkata”, **S. Chatterjee**, T. Bandyopadhyay, R. Ravisankar, Proceedings of International Symposium on Accelerator and Radiation Physics 2011, SINP, February 16-18, Kolkata.
3. “Estimation of Induced Activity in Super Conducting Cyclotron at VECC : Monte Carlo calculations” **S. Chatterjee** and T. Bandyopadhyay, Proceedings of International Conference on Accelerator Radiation Safety 2011, BARC, November 16-18,2011, Mumbai.
4. “Neutron and Photon shielding of beam dump for K130 Cyclotron at VECC: Monte Carlo Calculations” **S. Chatterjee**, K. Banerjee, P. Roy, S. Bhattacharyya, T. Bandyopadhyay, C. Bhattacharyya, DAE-BRNS Indian Particle Accelerator Conference 2013, VECC, November 19-22, 2013, Kolkata.
5. “Monte Carlo Calculations for beam dump design for K-130 Cyclotron at VECC” **S. Chatterjee**, K. Banerjee, P. Roy, S. Bhattacharyya, T. Bandyopadhyay, C. Bhattacharyya, International Symposium on Nuclear Physics, BARC, December 2-6, 2013, Mumbai.

Sujay Chatterjee

Signature of the Student:

Date: 15/09/2016

The work has been completed. The candidate may now submit the synopsis and the thesis.

Doctoral Committee:

S. No.	Name	Designation	Signature	Date
1.	Dr. S. R. Banerjee	Chairman	<i>S.R. Banerjee</i>	15/09/2016
2.	Dr. Tapas Bandyopadhyay	Guide/ Convenor	<i>Tapas Bandyopadhyay</i>	15/9/16
3.	Dr. Tapan Nayak	Member	<i>T. Nayak</i>	15/9/2016
4.	Dr. Sushanta Lahiri	Member	<i>Sushanta Lahiri</i>	15/09/2016

List of Figures

1.1	Cosmic ray shower	2
1.2	Radiation sources contributing to human exposure	6
1.3	Single strand break and double strand break of DNA	9
1.4	Stochastic and deterministic effects of radiation	10
1.5	Radiation weighting factor for neutron as per ICRP 103	13
1.6	(a)Expanded radiation field (b)Aligned and expanded radiation field .	16
1.7	Relationship among different radiation protection quantities	18
1.8	International radiation protection bodies and agencies	21
1.9	Glow curve of CaSO ₄ :Dy TL phosphor	23
1.10	Energy response of CaSO ₄ :Dy TL disc under open filter and metal filters	24
1.11	Picture of TLD card with Front and slider part of cassette	27
1.12	CR-39 used for neutron personnel monitoring in India	27
1.13	Proton recoil tracks formed in CR-39 foils after exposure to neutrons	28
1.14	LiF based personnel monitoring dosimeter	29
1.15	OSL based personnel monitoring badge	30
1.16	Radio-photo Luminescence based personnel monitoring dosimeter . .	31
1.17	DIS based personnel monitoring dosimeter of CERN	31
1.18	Variation of dose conversion coefficients for H*(10), H _{p,slab} (10,0°) for neutrons	33
1.19	Variation of dose conversion coefficients for H*(10), H _p (10)and H _p (0.07) for photons	34
1.20	Cross sectional view of the cyclotron showing the Dees and the oscillator	37
1.21	Cyclotron with electro-magnets and path of the charged particle . . .	38
1.22	View of the building housing LFGNM	42
1.23	K-130 Cyclotron at VECC	43
1.24	Super Conducting Cyclotron machine at VECC	45
1.25	Medical Cyclotron machine at VECC	46
1.26	Layout of the building housing Medical Cyclotron at VECC	47
1.27	Probability density function	49
1.28	Cumulative distribution function	50
1.29	Input window of FLAIR	59
1.30	Geometry plot window of FLAIR	59
1.31	3D plot using FLAIR	60
2.1	Fluence to dose conversion factors for neutrons	63
2.2	Cross Section of ⁶ Li(n,α) ³ H reaction	65

2.3	Geometry used in FLUKA simulation for generation of response matrix	66
2.4	Response matrix of the CaSO ₄ :Dy based neutron dosimeter for Bonner sphere of different sizes generated using FLUKA.	68
2.5	Conversion factor based on response of TLDs generated using Monte Carlo simulation code FLUKA and by experimental methods with ²⁴¹ Am–Be neutron source under different Bonner spheres	70
2.6	Plot of net neutron response of TL dosimeter determined experimentally	71
2.7	Plot of fitted curve of the response of neutron dosimeter vs sphere mass with 3 rd order polynomial at energies A: 0.1 eV, B:10 eV, C:1 keV, D:144 keV, E:2.50 MeV and F:14.8 MeV	74
2.8	Flow Chart for the operation of FRUIT code (version 3.0)	82
2.9	Deconvoluted neutron spectrum along with standard spectrum from IAEA TRS 403.	83
3.1	Construction of LFGNM with BF ₃ detectors	85
3.2	Photograph of LFGNM with BF ₃ detectors	85
3.3	Variation of reaction cross section of B ¹⁰ with neutron energy	86
3.4	Input geometry of LFGNM showing all the 21 BF ₃ detectors array.	89
3.5	Variation of count rate of LFGNM with upper paraffin wax thickness as measured experimentally and by simulation	91
3.6	Energy response of LFGNM evaluated using Monte Carlo code FLUKA	92
3.7	Cross section of Pb ²⁰⁶	94
3.8	Response of LFGNM with different thickness of Pb insert	95
3.9	Angular response of LFGNM	97
4.1	Layout of Medical Cyclotron	99
4.2	Geometry used for Monte Carlo Simulation with layers of different materials	101
4.3	Variation of neutron fluence in radial direction	101
4.4	Variation of neutron fluence in transverse direction	102
4.5	Graphical representation of variation of activity in concrete (Bq/cm ³) in first five layers after 7 days run	105
4.6	Graphical representation of variation of activity in concrete (Bq/cm ³) in first five layers after 30 days run	106
4.7	Graphical representation of variation of activity in concrete (Bq/cm ³) in first five layers after 300 days run	108
4.8	Graphical representation of variation of activity in soil (Bq/cm ³) after 50 cm concrete after 7 days run	111
4.9	Graphical representation of variation of activity in soil (Bq/cm ³) after 50 cm concrete after 30 days run	112
4.10	Graphical representation of variation of activity in soil (Bq/cm ³) after 50 cm concrete after 300 days run	113
4.11	Graphical representation of variation of activity in soil (Bq/cm ³) after 7 days run	118
4.12	Graphical representation of variation of activity in soil (Bq/cm ³) after 30 days run	120

4.13	Graphical representation of variation of activity in soil (Bq/cm ³) after 300 days run	121
4.14	Layout of Super Conducting Cyclotron	123
4.15	3D geometry used for evaluation of residual nuclei of Super Conducting Cyclotron	124
4.16	Variation of dose rate with different cooling times for Al slab material	125
4.17	Variation of dose rate with different cooling times for Cu slab material	125
4.18	Variation of dose rate with different cooling times for SS slab material	126
4.19	Variation of dose rate with different cooling times for Concrete slab material	126
4.20	Variation of activity (T _{1/2} in minutes) with different cooling times for SS primary target	129
4.21	Variation of activity (T _{1/2} in hours) with different cooling times for SS primary target	129
4.22	Variation of activity (T _{1/2} in days) with different cooling times for SS primary target	130
4.23	Variation of activity (T _{1/2} in years) with different cooling times for SS primary target	130
4.24	Variation of activity (T _{1/2} in minutes) with different cooling times for Cu Slab1	133
4.25	Variation of activity (T _{1/2} in hours) with different cooling times for Cu Slab1	133
4.26	Variation of activity (T _{1/2} in days) with different cooling times for Cu Slab1	134
4.27	Variation of activity (T _{1/2} in years) with different cooling times for Cu Slab1	134
4.28	Variation of activity (T _{1/2} in minutes) with different cooling times for Concrete Slab1	137
4.29	Variation of activity (T _{1/2} in hours) with different cooling times for Concrete Slab1	137
4.30	Variation of activity (T _{1/2} in days) with different cooling times for Concrete Slab1	138
4.31	Variation of activity (T _{1/2} in years) with different cooling times for Concrete Slab1	138
4.32	Variation of activity with different cooling times for Aluminium Slab1	139
5.1	K-130 Cyclotron at VECC, Kolkata showing beam lines and main magnet	142
5.2	ECR ion source of K-130 Cyclotron at VECC, Kolkata	142
5.3	Layout of K-130 Cyclotron at VECC, Kolkata	143
5.4	The 3 rd beam line of K-130 Cyclotron with beam dump	144
5.5	Variation of mass attenuation coefficient for Pb	146
5.6	Different trial designs of Shielding of beam dump	148
5.7	The final design of the shielding of beam dump for 3 rd beam line of K-130 Cyclotron	149
5.8	The 3D design of the shielding of beam dump	150

5.9	Neutron fluence histogram plot for different figures which have different shielding of beam dump	151
5.10	Photon fluence histogram plot for different figures which have different shielding of beam dump	152
5.11	Spatial Distribution of neutron fluence without shield and with final design shield	153
5.12	Spatial Distribution of photon fluence without shield and with final design shield	153
5.13	The spectral energy distribution of neutrons, without and with beam dump shield	154
5.14	The spectral energy distribution of photons, without and with beam dump shield	155
5.15	Block diagram of neutron detector used for measurement of neutron spectra from beam dump	158
5.16	Experimental setup for the measurement of neutron spectrum. It shows the beam dump position, HDPE shield and the neutron detector	160
5.17	Experimental setup for the measurement of neutron spectrum from different viewing angle	161
5.18	Experimental spectra of neutrons from beam dump without shield, after 5 cm Pb and after 40 HDPE	162
5.19	Experimental spectra of neutrons from beam dump without shield and after two combination of composite shields of Pb and HDPE (i) 10 cm HDPE + 5 cm Pb + 30 cm HDPE (ii) 10 cm HDPE + 4 cm Pb + 10 cm HDPE	163
5.20	Experimental spectra of neutrons from beam dump without shield and after two combination of composite shields of Pb and HDPE (i) 5 cm Pb + 40 cm HDPE with Pb near beam dump (ii) 40 cm HDPE + 5 cm Pb with HDPE near beam dump	164
5.21	The experimental and FLUKA generated spectra of neutrons from beam dump without shield	165
5.22	The experimental and FLUKA generated spectra of neutrons after Pb shielding of 5.0 cm	166
5.23	The experimental and FLUKA generated spectra of neutrons after 40 cm thick HDPE	167
5.24	The experimental and FLUKA generated spectra of neutrons after composite shield of 10 cm HDPE and 5 cm Pb followed by 30 cm HDPE, where 10 cm HDPE is near the beam dump	168
5.25	Experimental setup for the measurement of photon spectrum. It shows the lead shield and the BaF ₂ detector along with the beam dump position	170
5.26	Experimental spectra of photons without shielding, after 5 cm Pb and 40 cm HDPE	171
5.27	Experimental spectra of photons after composite shield of Pb and HDPE (i) 5 cm Pb + 40 cm HDPE (ii) 4 cm Pb + 20 cm HDPE . . .	172
5.28	The experimental and FLUKA generated spectra of photons without shielding	173

5.29	The experimental and FLUKA generated spectra of photons after 5 cm Pb shielding	174
5.30	The experimental and FLUKA generated spectra of photons after 40 cm HDPE shielding	175
5.31	Variation of activity in ¹⁸¹ Ta target	177
5.32	Variation of activity in HDPE(Inside)	179
5.33	Variation of activity in Pb	181
5.34	Variation of activity in HDPE(outside)	183
5.35	Variation of activity in Fe	185

List of Tables

1.1	Radiation weighting factors	12
1.2	Tissue weighting factors as per ICRP 103	12
1.3	Summary of few physical and protection quantities	15
1.4	Characteristics of CaSO ₄ :Dy teflon TLD discs	25
1.5	Specifications of TLD cassette	26
1.6	Some of the common radio-isotopes to be produced by Medical Cyclotron	46
1.7	Relative error and the quality of Tally in Monte Carlo Simulation	53
1.8	Particle transport capabilities in FLUKA	58
2.1	Response matrix of CaSO ₄ :Dy based neutron dosimeters in the energy range of thermal to 20 MeV for different sizes of Bonner spheres.	67
2.2	Parameters A ₁ , A ₂ , A ₃ and A ₄ of the 3 rd order polynomial function representing the best fit of FLUKA calculated response of neutron dosimeter as a function of sphere mass.	73
3.1	Chemical compositions of materials used in FLUKA simulation	88
3.2	Response of LFGNM with Cd sheet placed over Upper paraffin moderator	95
3.3	Response of LFGNM with Cd sheet placed under Upper paraffin moderator	96
4.1	Elemental composition of concrete used in FLUKA	103
4.2	Instantaneous neutron dose rate in three detectors when beam on target	104
4.3	Activity in first five layers of concrete after 7 days run of Cyclotron .	104
4.4	Various Isotopes in different layers of Concrete after 7 days (Bq in whole volume)	105
4.5	Activity in first five layers of concrete after 30 days run of Cyclotron .	106
4.6	Various Isotopes in different layers of Concrete after 30 days (Bq in whole volume)	107
4.7	Activity in first five layers of concrete after 300 days run of Cyclotron	107
4.8	Various Isotopes in different layers of Concrete after 300 days (Bq in whole volume)	109
4.9	Elemental composition of soil used in FLUKA	110
4.10	Activity in five layers of soil placed after 50 cm concrete after 7 days run	111
4.11	Various Isotopes in different layers of soil after 50 cm concrete after 7 days (Bq in whole volume)	112

4.12	Activity in five layers of soil placed after 50 cm concrete after 30 days run	112
4.13	Various Isotopes in different layers of soil after 50 cm concrete after 30 days (Bq in whole volume)	113
4.14	Activity in five layers of soil placed after 50 cm concrete after 300 days run	113
4.15	Various Isotopes in different layers of soil after 50 cm concrete after 300 days (Bq in whole volume)	114
4.16	Activity in layers of soil after 100 cm concrete after 7 days operation	115
4.17	Isotopes produced in different layers of soil placed after 100 cm concrete after 7 days operation	115
4.18	Activity in layers of soil after 100 cm concrete after 30 days operation	116
4.19	Isotopes produced in different layers of soil placed after 100 cm concrete after 30 days operation	116
4.20	Activity in layers of soil after 100 cm concrete after 300 days operation	116
4.21	Isotopes produced in different layers of soil placed after 100 cm concrete after 300 days operation	116
4.22	Activity in first 5 layers of soil after 7 days Cyclotron operation . . .	117
4.23	Activity in last 5 layers of soil after 7 days Cyclotron operation . . .	118
4.24	Isotopes produced in first five layers of soil after 7 days of Cyclotron operation	119
4.25	Activity in first 5 layers of soil after 30 days Cyclotron operation . . .	119
4.26	Activity in last 5 layers of soil after 30 days Cyclotron operation . . .	119
4.27	Isotopes produced in first five layers of soil after 30 days of Cyclotron operation	120
4.28	Activity in first five layers of soil after 300 days of Cyclotron operation	121
4.29	Activity in last five layers of soil after 300 days of Cyclotron operation	121
4.30	Isotopes in first five layers of soil after 300 days of Cyclotron operation	122
4.31	Composition of SS 316L used in FLUKA simulation	127
5.1	Neutron and Photon fluence at two detector positions	145
5.2	Neutron fluence at two detector positions with different designs of beam dump shielding	149
5.3	Photon fluence at two detector positions with different designs of beam dump shielding	150
5.4	Properties of scintillator material BC501A	157
5.5	Variation of radio-isotopes with cooling time in Target	178
5.6	Variation of radio-isotopes with cooling time in HDPE(Inside)	180
5.7	Variation of radio-isotopes with cooling time in Pb	182
5.8	Variation of radio-isotopes with cooling time in HDPE(outside)	184
5.9	Variation of radio-isotopes with cooling time in Fe	186

Chapter 1

Introduction

The term *radiation* is the flow of energy either in the form of waves or in the form of particles. Radiation is always present around us in many forms. The term radiation in context of this thesis is ionizing radiation. It has ability to knock off electrons from the atoms. Thus ionizing radiations are capable of damaging our body cells. These include alpha, beta, gamma, neutrons and X-rays. The sources of these radiations can be broadly classified into two categories, namely 1) **Natural sources of radiation** and 2) **Man-made sources of radiation**.

1.1 Natural sources of radiation

Human beings are continuously exposed from the natural sources of radiation and is an inescapable feature of life on earth[1]. For most individuals, exposure to natural background radiation is the significant part of their total exposure to radiation. These natural sources are classified into three important categories namely:

- I. Cosmic radiation
- II. Terrestrial radiation and
- III. Natural radioactivity in human body

1.1.1 Cosmic radiation

Cosmic radiation can be divided in terms of its origin, energy and flux density (number of particles per unit area). When human exposure is taken into account, it is further classified according to their sources namely:

- (a) Galactic cosmic radiation
- (b) Solar cosmic radiation
- (c) Earth's radiation belts (Van Allen Belts)

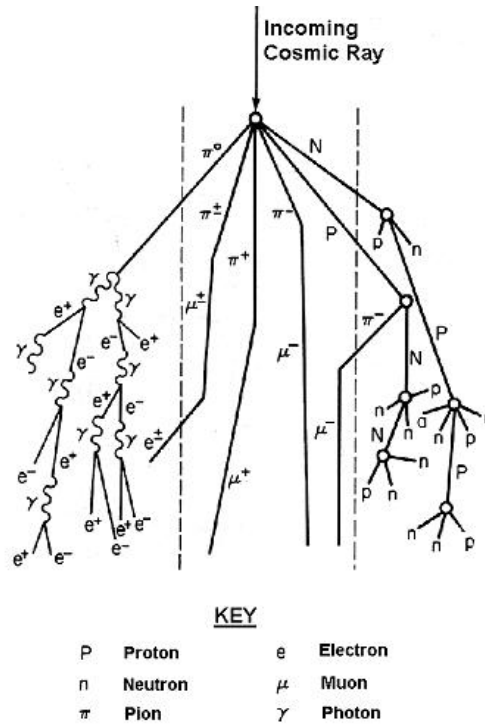


Figure 1.1: Cosmic ray shower

Shielding from these radiations are provided by the earth's magnetic field and also from the air layer of approximately $10,000 \text{ kg/m}^2$, which is comparable to 10 m thick layer of water. As a result, contribution of exposure due to cosmic radiation is maximum at higher altitudes and lowest at the sea level. At sea level, cosmic ray contributes to only 10% of total radiation exposure from the natural sources.

Cosmic ray interacts with nuclei of the earth's atmosphere and produces cascade of interactions and secondary reaction products which contributes to the exposure due to cosmic ray. The cosmic ray shower is shown in figure 1.1.

Galactic cosmic radiation

Galactic cosmic radiations (GCRs) originate outside our solar system. It consists of two components namely nucleonic component which contributes to 98% and electronic component which contributes only 2%. Out of the nucleonic component, 85.5% consists of protons, 12% alphas and the remaining 1% are heavier nuclei up to that of uranium. These particles have energy that extends from 10^8 eV to 10^{20} eV. GCR particle contribution depends on the solar activity and is lower when solar activity is higher. During solar activity, the energy spectrum of these particles also shifts towards higher energy.

Solar cosmic radiation

This component of cosmic ray originates from the surface of sun due to magnetic disturbance. Solar cosmic radiation (SCR) originates during the solar flares and the particles comprises of 99% protons, which are directed towards the surface of earth. Energy of these protons are only up to 100 MeV.

Van Allen radiation belts

Van Allen radiation belts are formed through the capture of protons and electrons by earth's magnetic field. There are two Van Allen radiation belts, an internal one centered around 3000 km and one at 22,000 km from the surface of earth. The internal Van Allen radiation belt contributes to significant exposure.

1.1.2 Terrestrial radiation

Naturally occurring radionuclides are present in various degrees in all environmental media. These are also known as primordial radionuclides. Only those radionuclides having half life comparable with the age of earth and their decay products which are present in sufficient quantities contributes to public exposure. Gamma emitting radionuclides present in soil are ^{40}K and ^{238}U and ^{232}Th families. These radionuclides are also present in building materials, which contributes to public exposure. Granite and marbles contains significant quantities of ^{226}Ra , ^{232}Th and ^{40}K . Uranium and Thorium present in earth's crust decays to their daughter products Radium which further decays to Radon(^{222}Rn). Radon being an alpha emitter gives high exposure to public. Concentration of Radon varies with the variation of Uranium and Thorium present in earth's surface.

1.1.3 Natural radioactivity in body

Small traces of many naturally occurring radioactive elements are present in trace levels inside human body. These come mainly from naturally occurring radioactive nuclides present in the food we eat and in the air we breathe. These isotopes include tritium (^3H), carbon-14 (^{14}C), and potassium-40 (^{40}K). About 11% of our radiation exposure comes from naturally occurring radioactive materials in the body, out of which ^{40}K contributes maximum. Radioactive potassium-40, as well as other radioactive materials (such as carbon-14) which occur naturally in air, water, and soil, are incorporated into the food we eat and then into our body tissues.

1.2 Man-made sources of radiation

We are also exposed to ionizing radiation from man-made sources, mostly through medical procedures. On the average, exposures from a diagnostic X-ray are much lower than natural background radiation. Radiation therapy, however, can reach

levels many times higher than natural background radiation but this is usually targeted only to the affected tissues. Besides medical applications, extremely small amounts of man-made background radiation are received from consumer products and facilities using radioactive material including research and teaching institutions, nuclear reactors and their supporting facilities such as uranium mills and fuel preparation plants. People who smoke receive additional radiation from radionuclides in tobacco smoke.

1.2.1 Medical procedures

Radiation used in medicine is the largest source of man-made radiation to which people are exposed. Most of our exposure is from diagnostic tools such as X-rays, CT Scan, PET/SPECT Scan and dental X-rays. Physicians use X-rays in more than half of all medical diagnoses to determine the extent of disease or physical injury. Radiation is also used in the treatment of malignant cells, where precisely targeted radiation destroys malignant cells without killing nearby healthy cells. Radio-pharmaceuticals, another tool in medical treatment, are used for diagnosis and therapy.

1.2.2 Consumer products

Small amounts of man-made background radiation is attributable to consumer products like televisions and monitors based on cathode-ray-tubes (CRTs), smoke detectors, gas lantern mantles, natural gas heating and cooking fuel, mining and agriculture products, such as coal, granite and potassium salt.

1.2.3 Radioactive fallout

Nuclear weapons derive their explosive power from the uncontrolled nuclear fission of plutonium and uranium. This yields a large number of radioactive daughter

products that are blown high into the atmosphere and are carried around the earth. These radioactive elements gradually fall back (fall-out) to earth over a period of many years. During 1950s and early 1960s, many test explosions were carried out in the atmosphere.

1.2.4 Nuclear Power and fuel cycle

A Nuclear reactor used for power generation, uranium mining and fuel enrichment contributes to very small amount of radiation exposure to general public.

Contribution of exposure from different radiation sources to general public is shown in figure 1.2.

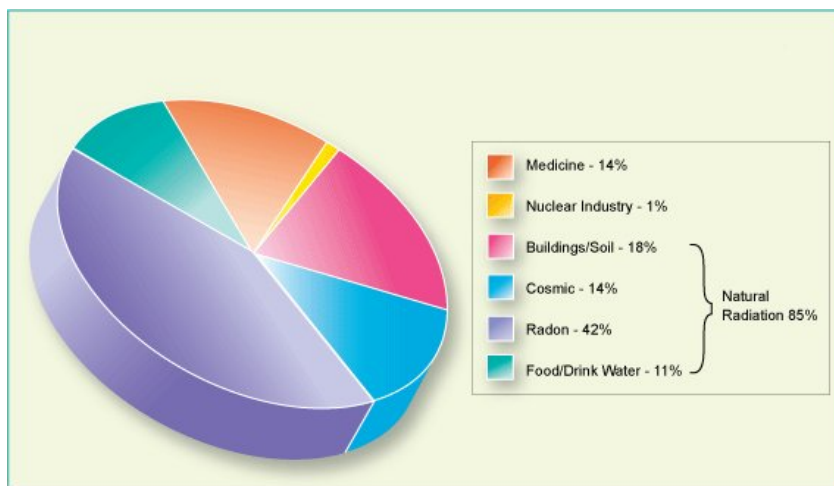


Figure 1.2: Radiation sources contributing to human exposure

1.3 History of radiation protection

Paradigm shift towards the use of radiation immediately after discovery of X-ray and radioactivity in 1895 and 1896 in the field of physics, chemistry and medicine prompted the safety and protection of flora and fauna. Ideally, if flora and fauna are safe, automatically human beings are saved. Early X-ray users were not aware of its harmful effects. No instruments were available to estimate ill effects of radiation.

Even calibration of X-ray tubes were based on the amount of skin reddening (erythema) produced when the operator placed a hand directly in the X-ray beam[2]. Ignorance of these led to severe ill effects in patients, technicians, scientists and physicians. Due to this, several researchers published related to radiation hazards, so that suitable steps can be taken to set limits for these exposures. In July, 1896, first dose limit of 10 rad per day was introduced. But this lowest limit was not based on biological effects of radiation, but rather on the limit of minimum amount of detection. Consequently more attention were paid to radiation safety and by 1903, animal studies had shown that X-rays could produce malignant cells and kill living tissue and that the organs most vulnerable to radiation damage were skin, blood-forming organs, and the reproductive organs. Arthur Mutscheller was the first person to recommend a “tolerance” dose rate for radiation workers, a dose rate that in his judgment could be tolerated indefinitely. He based his recommendation on observations of physicians and technicians who worked in shielded work areas. U.S. Advisory Committee on X-ray and Radium Protection, in the year 1934, came up with first formal standard for protecting personnel from radiation sources. As the quantitative standard during those times for radiation were in units of roentgen(R), the dose limit was recommended as 0.1 R per day.

With the recommendation of dose limits, radiation personnel monitoring became one of the important pillar of radiation protection. Radiation personnel monitoring and its related dosimetry enables individual control of radiation in order to make sure that the stipulated dose limits for occupational workers are not exceeded and supports the measures to be taken for further reduction of doses to as low as reasonably achievable (ALARA), taking socio-economic factors into account.

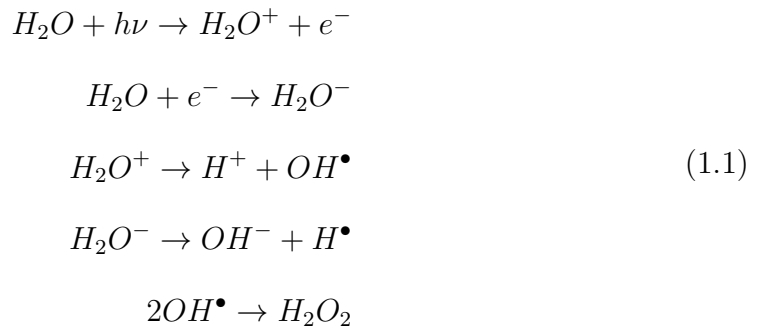
The philosophy of radiation protection has considerably changed during last century and so are the requirements and expectations. While radiation protection was initially concerned chiefly with limiting exposure to a level, where direct harmful effects (mainly non-stochastic) could be excluded, the assessment of radiation doses

became more important when the risk due to radiation doses to produce stochastic effects such as radiation induced carcinogenesis was observed to have no threshold value. At present, the recommended annual dose limit is mainly based on the results of radiobiological and epidemiological investigations of health risks due to exposure to ionizing radiation and opinions on additional health risk, which might be acceptable to workers and public. With increasing knowledge in the field, dose limits have been gradually reduced and since the last revision in 1990, International Commission on Radiological Protection [3] has reduced the limit from 50 mSv to 20 mSv per year averaged over 5 years for occupational exposure and from 5 mSv to 1 mSv for the public. Reduced dose limits have obviously increased the demands on the requirement of individual monitoring in terms of accuracy, performance and recording level. As per ICRP, recording level value for a monthly service has been reduced from 0.42 mSv of ICRP-26 (1977) to 0.17 mSv of ICRP-35 (1982) and now to 0.085 mSv of ICRP-75 (1999) for occupational exposure. Again, radiation dosimetry for the requirements of radiation personnel monitoring became important with future developments of nuclear reactors, high energy accelerators and even cosmic ray dosimetry.

1.4 Biological effects of radiation

The DNA (deoxyribonucleic acid) in cell nucleus is considered to be the most important target for radiobiological effects. DNA has a double helix structure with two polynucleotide strands held together by hydrogen bonds between the bases of nucleotides. The double-ringed nucleobases adenine (A) and guanine (G) pair with single-ringed thymine (T) and cytosine (C), respectively. Radiation may cause damage to the DNA, e.g. in the form of breaks on the strands, either directly by ionizing the DNA or indirectly by forming free radicals that damage the DNA. More than 50% of the DNA damage is caused by Hydroxyl radicals. The formation of Hydroxyl

radicals by the interaction of H_2O with radiation is shown below:



However, DNA damage is not always lethal to cell. Single strand breaks rarely cause cell death in normal cells since they are easily repaired by the repair system of cell using the opposite strand as a template. In case of double strand breaks, breaks close to each other on both of the strands, are more difficult to repair. Figure 1.3 shows the single strand break and double strand break of DNA. The effect of radiation can

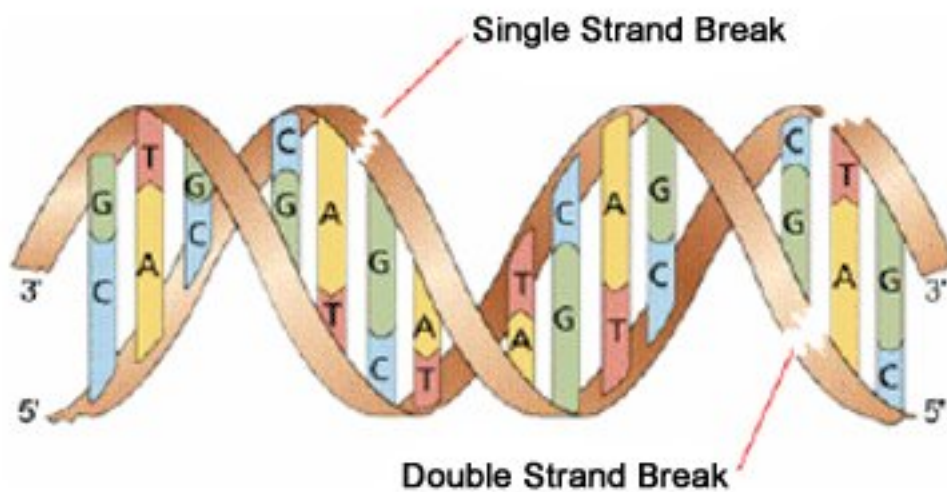


Figure 1.3: Single strand break and double strand break of DNA

be broadly classified into two categories: 1) Stochastic effects and 2) Deterministic effects.

1.4.1 Stochastic effects

These do not have any threshold value of exposure and hence cannot be avoided. The probability of stochastic effects increases with the increase in exposure. It is divided into *somatic effects* and *genetic effects*. Secondary cancer is an important somatic effect. It is caused by DNA mutation by radiation either directly or indirectly. Genetic effect is the predisposition of cancer in future generations.

1.4.2 Deterministic effects

These have threshold and does not happen if the exposure is lower than those threshold values. The severity of effect depends on the value of exposure. In the dose range of 0.25 to 2 Sv, it is sub-lethal. If the dose levels are more than 2 Sv it is lethal.

Figure 1.4 shows the stochastic and deterministic effects.

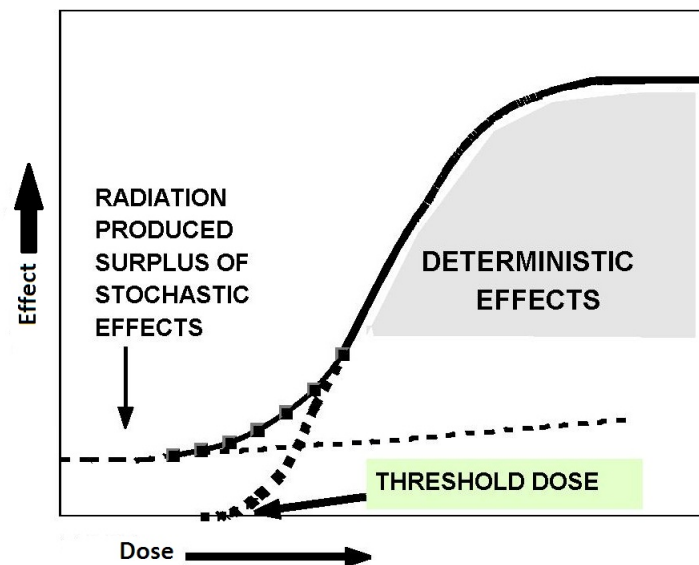


Figure 1.4: Stochastic and deterministic effects of radiation

1.5 Radiation Protection Quantities

International commissions such as International Commission on Radiation Protection (ICRP) and International Commission on Radiation Units (ICRU) have given

a hierarchy of quantities for radiation protection[4]. They can be divided into three categories:

- (i) Physical quantities
- (ii) Protection Quantities and
- (iii) Operational Quantities.

The first category includes those quantities, which are defined at any point of a radiation field, namely fluence, kerma and absorbed dose[5]. They being physical quantities, they can be directly measured with different radiation detectors. The reference value of a physical quantity is held by Primary Metrology Laboratories. Reference radiation fields, meeting the recommendations of International Organization for Standardization (ISO), are available at Secondary Metrological Laboratories for instrument calibration.

The basic concepts of the second category of quantities, i.e., protection quantities are to relate the risk of exposure to ionizing radiation by internal or external radiation sources. The protection quantities are namely equivalent dose and effective dose. These quantities take into account the man as receptor, the different radiation sensitivities of various organs and tissues and the different radiation qualities. These radiation protection quantities are the basis of dose limitations, but are not measurable quantities. Equivalent dose and effective dose were defined in ICRP 60 using radiation and tissue weighting factors w_R and w_T respectively. w_R takes into account the risk from various qualities of radiation in our body and w_T takes into account stochastic effects in different organs or tissues of the body. w_R are based on experimental data for radiobiological effectiveness (RBE). RBE is based on the ratio of the dose giving a certain effect in a cell irradiated by a reference radiation field to that giving the same effect in the radiation field under study. Radiation weighting factors as per ICRP 103 (2007) are summarized in table 1.1. w_T are based on epidemiological studies of cancer induction as well as on experimental ge-

netic data after radiation exposure and on judgment. These weighting factors are selected for application in radiological protection by judgment and include simplifications. Tissue weighting factors as per ICRP 103 (2007) are given in table 1.2.

To overcome the problem of the non-measurable quantities of radiation protec-

Table 1.1: Radiation weighting factors

Radiation Type	Radiation weighting factor (w_R)
Photons, all energies	1
Electrons, muons, all energies	1
Protons, charged pions	2
Alpha particles, fission fragments, heavy ions	20
Neutrons	A continuous function of energy (given below)

$$w_R = \begin{cases} 2.5 + 18.2e^{-[\ln(E_n)]^2/6}, & E_n < 1 \text{ MeV} \\ 5.0 + 17.0e^{-[\ln(2E_n)]^2/6}, & 1 \text{ MeV} \leq E_n \leq 50 \text{ MeV} \\ 2.5 + 3.25e^{-[\ln(0.04E_n)]^2/6}, & E_n > 50 \text{ MeV} \end{cases}$$

Table 1.2: Tissue weighting factors as per ICRP 103

Tissue or Organ	Tissue weighting factor (w_T)
Bone marrow (red), breast, lung, stomach, colon	0.12
Gonads	0.08
Thyroid, bladder, liver, oesophagus	0.04
Bone surface, skin, salivary glands, brain	0.01
Remainder	0.12

tion, the ICRU introduced the third set of quantities namely operational quantities. These quantities should provide an estimate of or an upper limit for the value of the limiting protection quantities due to an exposed, or potentially exposed, person and are often used in place of those quantities in practical regulations. Operational quantities are needed for monitoring external exposures because protection quantities generally are not measurable. The operational quantities defined by ICRU 51 are

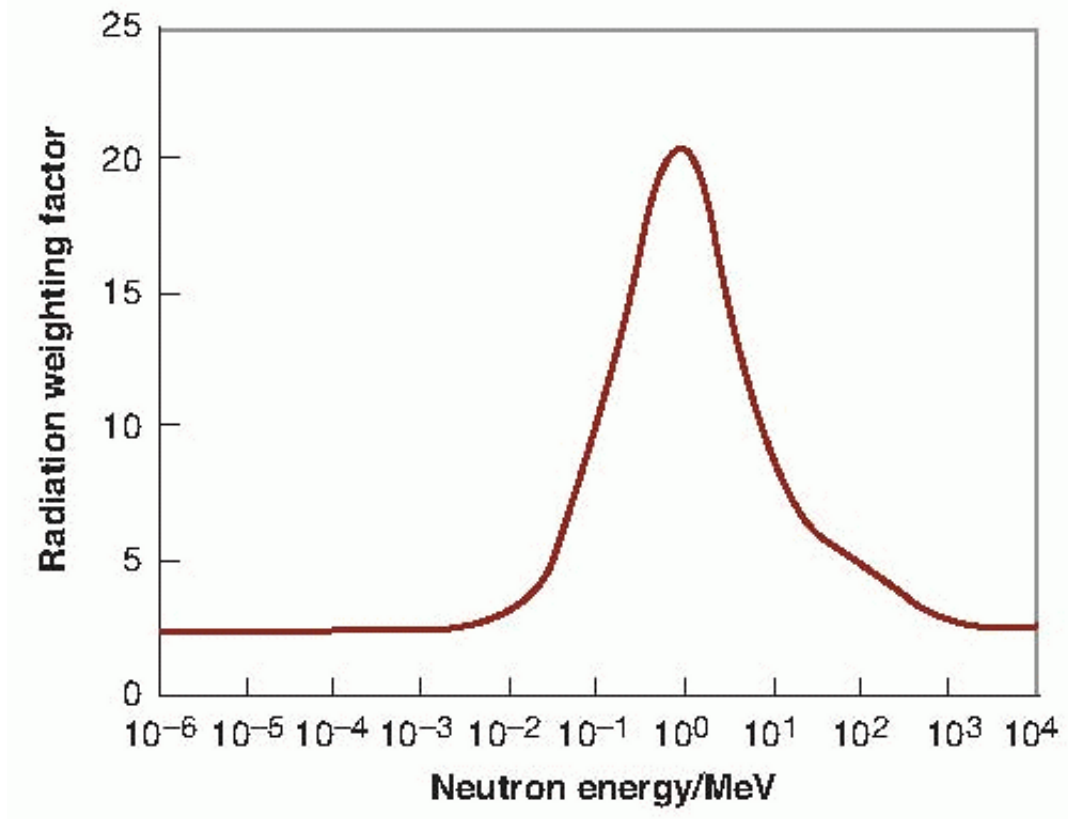


Figure 1.5: Radiation weighting factor for neutron as per ICRP 103

the ambient dose equivalent, $H^*(d)$, the directional dose equivalent, $H'(d, \Omega)$ and the personal dose equivalent, $H_p(d)$, and are expressed in terms of the dose equivalent H . The $Q(L)$ relationship is used for calculating the operational quantities.

$$H = \int_{L_{min}}^{L_{max}} Q(L) D(L) dL \quad (1.2)$$

ICRP 60 defined the quality factor Q as a function of the unrestricted linear energy transfer (LET), L_∞ , of charged particles in water. This $Q(L)$ function in equation 1.2 is the outcome of judgments taking account of results of radiobiological investigations on cellular and molecular systems as well as on the results of animal experiments. The connection between physical quantities and the operational quantities is given by the related conversion coefficients, which were calculated by ICRP-ICRU joint groups. These conversion coefficients are the tools that facilitate calibrating an instrument in reference radiation fields. The basic physical quantity such as fluence

for neutrons, the air-kerma for photons, and the absorbed dose in tissue for electrons are measured in the reference field and subsequently the operational quantity can be calculated through the conversion coefficients and taken as the true values.

The definition of Radiation Protection quantities and their units are given below:

Fluence

Fluence Φ is defined as the number of particles dN passing perpendicularly through the cross sectional area da .

$$\Phi = \frac{dN}{da} \quad (1.3)$$

The SI unit of fluence is m^{-2} .

KERMA

KERMA is Kinetic Energy Released in Matter. It is defined as

$$K = \frac{d\bar{E}_{tr}}{dm} \quad (1.4)$$

where $d\bar{E}_{tr}$ is the mean kinetic energy transferred to charged particles from uncharged particles in a mass dm of a given material. The unit of kerma is gray (Gy).

Absorbed Dose

It is defined as

$$D = \frac{d\bar{\varepsilon}}{dm} \quad (1.5)$$

where $d\bar{\varepsilon}$ is the mean energy imparted to matter of mass dm . The unit of absorbed dose is gray (Gy).

Equivalent Dose

Equivalent dose is defined as

$$H_T = \sum_R w_R \times D_{T,R} \quad (1.6)$$

where w_R is the radiation weighting factor and $D_{T,R}$ is the mean absorbed dose due to a particular radiation field R. Its unit is sievert (Sv).

Effective Dose

Effective dose is defined as

$$E = \sum_T w_T \times H_T \quad (1.7)$$

where w_T is the tissue weighting factor and H_T is the equivalent dose. Its unit is sievert (Sv). Table 1.3 summarizes the physical and protection quantities.

Table 1.3: Summary of few physical and protection quantities

Quantity	Definition	SI Unit
Fluence	$\frac{dN}{da}$	m^{-2}
Kerma	$\frac{d\bar{E}_{tr}}{dm}$	Gy
Absorbed Dose	$\frac{d\bar{\varepsilon}}{dm}$	Gy
Equivalent Dose	$\sum_R w_R \times D_{T,R}$	Sv
Effective Dose	$\sum_T w_T \times H_T$	Sv

Ambient Dose Equivalent

Ambient dose equivalent, $H^*(d)$, at a point in a radiation field is the dose equivalent that would be produced by the corresponding expanded and aligned field at a depth

“d” in the ICRU sphere, on the radius opposing the direction of the aligned field. The depth “d” is taken as 10 mm for strongly penetrating radiation. It is denoted as $H^*(10)$. For weakly penetrating radiation, depth of 0.07 mm and 3 mm is taken for skin and eye, with analogous notations. The unit is Jkg^{-1} and the special name is sievert (Sv).

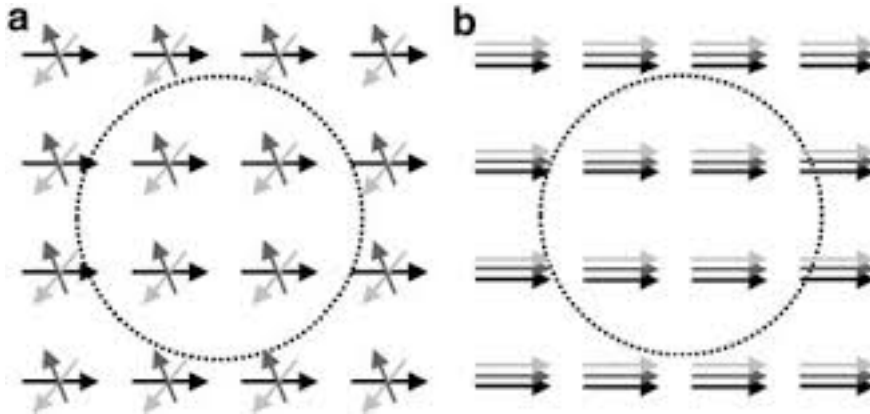


Figure 1.6: (a) Expanded radiation field (b) Aligned and expanded radiation field

ICRU sphere is a tissue equivalent 30 cm diameter sphere, made up of 76.2% Oxygen, 11.1% Carbon, 10.1% Hydrogen and 2.6% Nitrogen. It is having density of 1 g/cm^3 .

Directional Dose Equivalent

The directional dose equivalent, $H'(d, \Omega)$, at a point in a radiation field, is the dose equivalent that would be produced by the corresponding expanded field in the ICRU sphere at a depth “d”, on a radius in a specified direction Ω . For strongly penetrating radiation, “d” is taken as 10 mm, while for weakly penetrating radiation, the value is taken as 0.07 mm and 3 mm for skin and eye respectively. In the particular case of a unidirectional field, the direction can be specified in terms of the angle α between the radius opposing the incident field and the specified radius. The unit is Jkg^{-1} and the special name is sievert (Sv).

Personal Dose Equivalent

The Personal dose equivalent, $H_p(d)$, is the dose equivalent in ICRU tissue, at an appropriate depth “d” below a specified point on the body. For weakly penetrating radiation, a depth of 0.07 mm for the skin and 3 mm for the eye are used. The personal dose equivalent for these depths is then denoted by $H_p(0.07)$ and $H_p(3)$, respectively. For strongly penetrating radiation, a depth of 10 mm is used, with analogous notation. The unit is Jkg^{-1} and the special name is sievert (Sv).

The relationship between different quantities in radiation protection is shown in the figure [1.7](#).

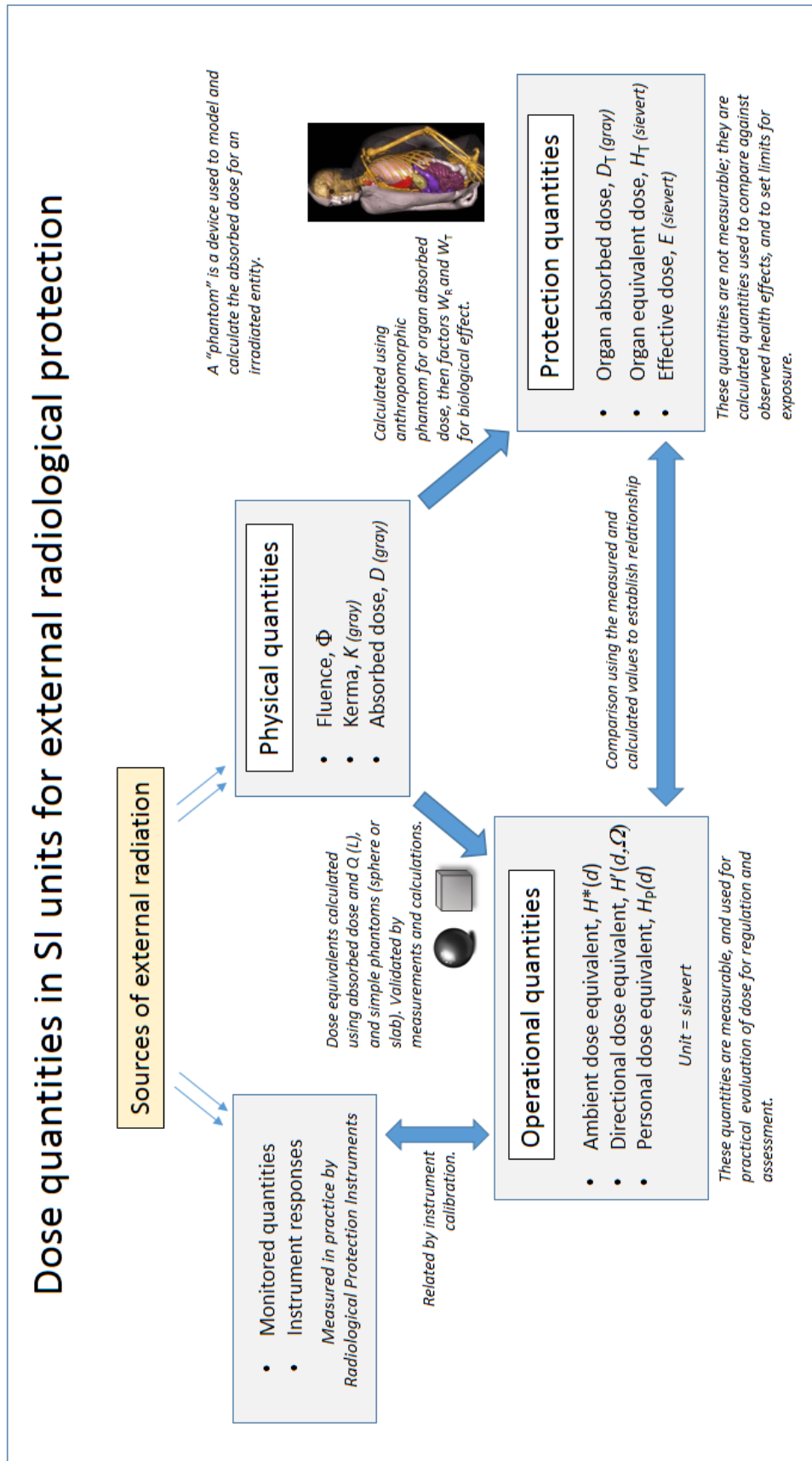


Figure 1.7: Relationship among different radiation protection quantities

1.6 Institutional Framework

There are several international organizations that contribute significantly towards establishment of scientific and legal framework in the field of radiation protection. The work carried out by various international organizations and agencies are given as follows:

1. **United Nations Scientific Committee on the Effects of Atomic Radiation (UNSCEAR):** In the year 1955, General Assembly of United Nations passed the resolution for the formation of UNSCEAR. The original Committee comprised of senior scientists from 15 designated UN member states. It collects and assesses scientific literature regarding exposure to ionising radiation, assessing world-wide exposure trends. The Committee has regularly evaluated the evidence for radiation-induced health effects from studies of the survivors of the atomic bombings in Japan and other exposed groups. It has also reviewed advances in scientific understanding of the mechanisms by which radiation-induced health effects can occur. These assessments have provided the scientific foundation used by the ICRP in developing its recommendations on radiological protection and by the relevant agencies in the UN system in formulating international protection standards.
2. **International Commission on Radiation Protection (ICRP):** The International Commission on Radiological Protection (ICRP) was created in 1928, as the International X-ray and Radium Protection Committee, and restructured in 1950 in order to address protection from emerging health effects of radiation, mostly in researchers and patients from X-rays and radium treatments. The ICRP works closely with the International Commission on Radiation Units and Measurements (ICRU), maintains important relations with various UN organizations (UNSCEAR, WHO, IAEA, ILO, UNEP) and works with the EC, OECD/NEA, the International Organization for Standardization

(ISO) and the International Electrotechnical Commission (IEC). It also has strong links with the International Radiation Protection Association (IRPA). The ICRP has, since its inception, issued recommendations regarding protection against the hazards of ionising radiation. The most fundamental of these, called the Commission's general recommendations, are issued approximately every 10 to 15 years to take into account new scientific evidence and managerial experience. Historically, national and international organizations and practitioners involved in activities that produce or use radiation and/or radioactive materials have taken the recommendations and principles issued by the ICRP as a key basis for their protective actions.

- 3. International Atomic Energy Agency (IAEA):** The IAEA was created in 1957 in response to the deep fears and expectations resulting from the discovery of nuclear energy. In the context of the international system of radiological protection, the IAEA plays a special role in establishing international standards. IAEA has issued many standards, the International Basic Safety Standards being among those having had the most impact. The standards supersede the previous basic international standards and reflect knowledge gained subsequently, developments in radiological protection, safety and related fields. The standards are based primarily on the recommendations of the ICRP.

1.7 Radiation protection in India

The Department of Atomic Energy (DAE), since its inception has accorded high priority to safety in activities dealing with radiation and various radiation sources [6]. This is evident from the emphasis given to health and safety aspects in the Atomic Energy Act, 1962 enacted by the Government to provide basic regulatory framework, promulgation of Radiation Protection Rule-1971 (RPR-71), and setting up an

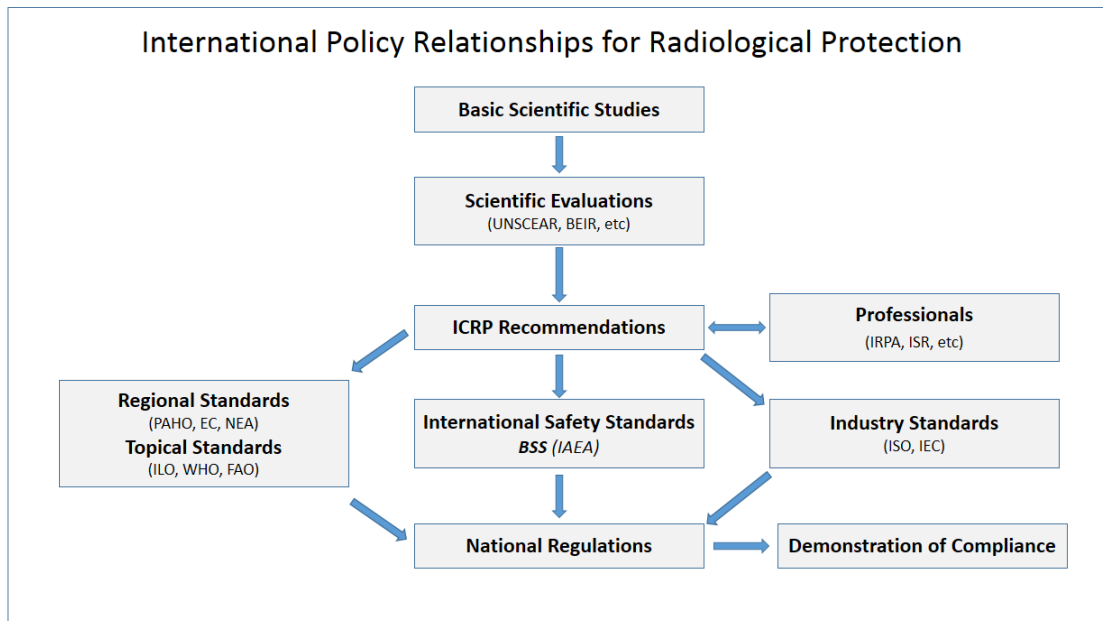


Figure 1.8: International radiation protection bodies and agencies

apex regulatory body - the Atomic Energy Regulatory Board (AERB). Under rule 15 of Atomic Energy (Radiation Protection) Rules 2004, the dose limits for exposures from ionizing radiation for workers and members of public are given below[7]:

1. The occupational exposure of any worker shall be so controlled that the following limits are not exceeded:
 - (a) an effective dose of 20 mSv/yr averaged over five consecutive years (calculated on a sliding scale of five years);
 - (b) an effective dose of 30 mSv in any year;
 - (c) an equivalent dose to the lens of the eye of 150 mSv in a year;
 - (d) an equivalent dose to the extremities (hands and feet) of 500 mSv in a year and
 - (e) an equivalent dose to the skin of 500 mSv in a year;
 - (f) limits given above apply to female workers also. However, once pregnancy is declared the equivalent dose limit to embryo/fetus shall be 1 mSv for the remainder of the pregnancy.

2. The occupational exposure of apprentices and trainees between 16 and 18 years of age shall be so controlled that the following limits are not exceeded:
 - (a) an effective dose of 6 mSv in a year;
 - (b) an equivalent dose to the lens of the eye of 50 mSv in a year;
 - (c) an equivalent dose to the extremities (hands and feet) of 150 mSv in a year and
 - (d) an equivalent dose to the skin of 150 mSv in a year.

3. The estimated average doses to the relevant members of the public shall not exceed the following limits:
 - (a) an effective dose of 1 mSv in a year;
 - (b) an equivalent dose to the lens of the eye of 15 mSv in a year; and
 - (c) an equivalent dose to the skin of 50 mSv in a year.

Individual monitoring constitutes an integral part of radiation protection programme and as per RPR-71, all radiation workers have to be covered by individual monitoring as specified by the competent authority. Bhabha Atomic Research Centre (BARC) started providing personnel monitoring services to radiation workers since 1952 using film badge system. With the indigenous development of a TLD badge system based on $\text{CaSO}_4:\text{Dy}$ Teflon TLD disc offering better dosimetric characteristics, process of replacing the prevalent film badge by the TLD system was initiated in 1975. TLD badge is used for the determination of the personnel dose due to X-rays, β and γ -rays. Fast neutron personnel monitoring in India is carried out with CR-39 films.

1.7.1 External personnel monitoring with TLD badge

TLD badge is based on $\text{CaSO}_4:\text{Dy}$ thermoluminescent phosphor as a radiation detector. It is used for external personnel monitoring for the measurement of exposure

due to X-rays, β and γ -rays only. The concentration of Dysprosium dopant to the extent of 0.05 mol% in CaSO_4 makes it highly sensitive thermoluminescent (TL) phosphor (about 40 times that of the most popular Lithium Fluoride based TLD-100). The response to neutrons remains negligible (only 3.8 mGy equivalent Co-60 gamma ray response per 10^{10} thermal neutron cm^{-2}). The phosphor exhibits a main TL glow peak at about 220 °C (TL peak of $\text{CaSO}_4:\text{Dy}$ Teflon Disc occurs at about 240 °C) with very small satellite glow peaks on higher and lower temperature sides of the main peak. Glow curve of $\text{CaSO}_4:\text{Dy}$ is shown in figure 1.9. Due to its high atomic number (Z), $\text{CaSO}_4:\text{Dy}$ exhibits energy response. The energy response shows a typical peak at 30 keV and the response becomes flat beyond 200 keV. Energy response of $\text{CaSO}_4:\text{Dy}$ TL discs under different filters are shown in figure 1.10.

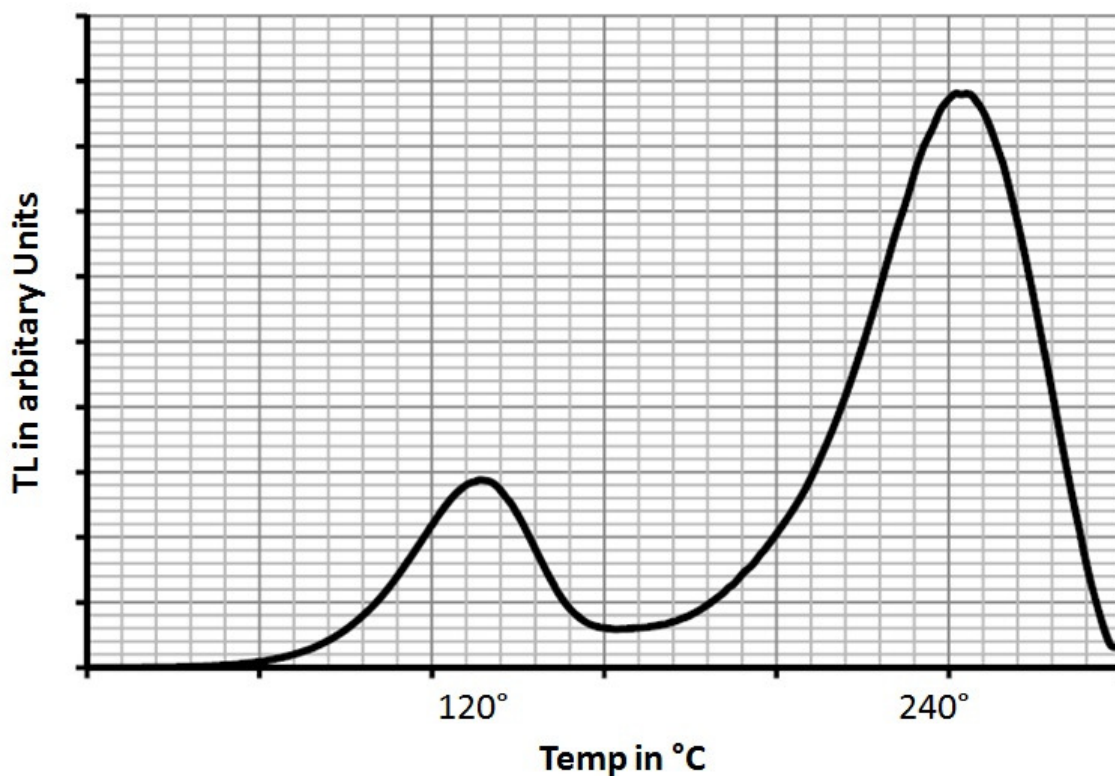


Figure 1.9: Glow curve of $\text{CaSO}_4:\text{Dy}$ TL phosphor

The TL response is linear and glow curve structure remains stable for both low and high LET radiation in the dose range of interest in radiation protection. The response and the chemical form are highly stable to the climatic variations. Though

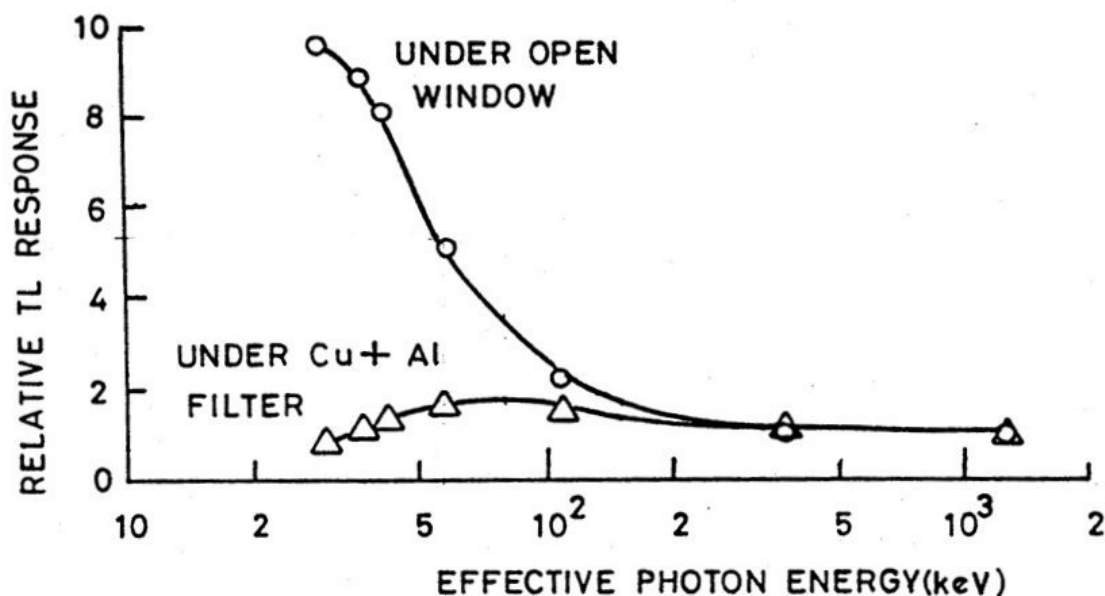


Figure 1.10: Energy response of CaSO₄:Dy TL disc under open filter and metal filters

the TL signal fades faster when exposed to bright sunlight, exposure to normal room light does not affect the response. However, the response of TLDs contained in paper wrapper and polythene pouches, is not affected by exposure to sunlight. In order to obtain large number of integrated dosimeters having the same TL sensitivity, CaSO₄:Dy phosphor was embedded in Teflon (Poly Tetra Fluoro Ethylene, PTFE) to make TLD discs. Teflon is a plastic which can withstand temperatures necessary for TL readout and annealing process for repeated use and thus provides rugged and handy dosimeter suitable for field use. Some of the characteristics of the CaSO₄:Dy Teflon embedded TLD discs are given in table 1.4.

The TLD badge comprises of a TLD card and plastic cassette / holder. TLD card has three Teflon TLD discs (13.3 mm dia. and 0.8 mm thick) that are mechanically clipped onto circular holes (12.0 mm diameter) punched in an aluminium plate of size 52.5 x 30 x 1 mm³. An asymmetric “V” cut is provided in the card to ensure its orientation. The card wrapped in a thin paper wrapper (thickness 10 mg/cm²) containing printed information regarding the user, service period and type of radiation etc. is put in a thin plastic pouch (thickness 3-4 mg/cm²) before loading

Table 1.4: Characteristics of CaSO₄:Dy teflon TLD discs

Ratio of CaSO₄:Dy and Teflon	1:3
Effective atomic number (Z)	15.1
Density of TL disc	2.52 g/cm ³
Softening point of Teflon	330 °C
Main glow peak temperature	240 °C
Sensitivity of TL disc	About 30-40 times that of LiF (TLD-100)
Fading	2-3% in six months
Climatic effect (Environmental)	Negligible
Effect of sunlight	Negligible when covered by paper wrapper and polythene pouch and loaded in cassette
Useful linear dose range	0.1 mSv to 20 Sv (linearity within $\pm 10\%$)
Reusability	20 Cycles
Beta response	60% of ⁶⁰ Co gammas for Nat.U (effective energy 0.8 MeV)
Thermal neutron response	⁶⁰ Co gamma ray equivalent to 2.4 mGy per 10 ¹⁰ n/cm ²
Fast Neutron response	Negligible

it in the plastic cassette. The paper wrapper protects the TLD discs from exposure to light whereas plastic pouch prevents contamination of the TLD card. Specifications of TLD cassette are given in table 1.5.

There are three well-defined regions in the plastic cassette / holder corresponding to three TLD discs of the TLD card. The asymmetric “V” cut of the card permits its loading in the plastic cassette in only one orientation and ensures proper positioning of three discs as follows: (i) Disc D1- sandwiched between a pair of filter combination of 1.0 mm thick Al and 0.6 mm thick Cu (Copper filter nearer to the disc), (ii) Disc D2- sandwiched between a pair of 1.6 mm thick (180 mg/cm²) plastic filters and (iii) Disc D3- under a circular open window. For identification purposes, photograph of the user could also be permanently fixed on the central transparent region of the badge. The metal filter combination not only corrects for the low energy response, but the response of the TL discs under different filters and their ratios helps for the identification of the type of exposure encountered by the badge and hence evaluated

Table 1.5: Specifications of TLD cassette

Main body of Cassette:	
Cu filter (rectangular)	32 mm x 16 mm x 1 mm
Al filter (circular)	13.6 mm & thickness- 0.6 mm
Plastic filter (rectangular)	30.5 mm x 21 mm x 1.6 mm
Open window	Dia- 14.5 mm
Slider part of Cassette:	
Cu filter (circular)	Dia - 15.6 mm, thickness- 1 mm
Al filter (circular)	Dia -12.6 mm, thickness – 0.6 mm
Plastic filter (circular)	Dia - 25 mm, thickness- 1.5 mm
Open window	Dia - 13.5 mm
Material:	
Eyelet	Silver eyelet 2030
Transparent window	General purpose polystyrene 666 clear
Copper Filter	Copper 99.9 % purity
Aluminium Filter	Aluminium (Emblem)
Slider	High impact polystyrene -975
Main Body	High impact polystyrene -975

the necessary dose contribution for each of them.

There are three types of TLD badges / cassettes in use namely, 1- Chest Badge, 2- Wrist Badge and 3- Head Badge. Though the dosimeter and design of all the three types of TLD badges are same, they have different attachment (clip/strap) for wearing purpose depending on their use.

1.7.2 External personnel monitoring with CR-39

Neutron radiation has wide applications worldwide ranging from nuclear reactors, accelerators, nucleonic gauge, radiography and others to name a few. Personnel working in such places require monitoring due to neutron fields. Personnel monitoring for neutron in India is carried out with CR-39 Solid State Nuclear Track Detector (SSNTD). CR stands for Columbia Resin. Its chemical name is Polyallyl Diglycol Carbonate (PADC) and its chemical formula is $C_{12}H_{18}O_7$. This detector in contact with 1 mm polythene radiator is used for personnel monitoring in the energy range of 100 keV to 10 MeV of neutrons. Figure 1.12 shows the bare CR-39 foils



Figure 1.11: Picture of TLD card with Front and slider part of cassette

and under the pouches used for neutron personnel monitoring in India. CR-39 is



Figure 1.12: CR-39 used for neutron personnel monitoring in India

a preferred neutron detector for personnel monitoring also because of the following reasons:

- Its (n,p) scattering cross section is large and smoothly varying.
- The efficiency of energy transfer from neutrons is greatest for protons.
- The ranges of recoil protons are much greater than for alpha particles and heavier ions.

- It is insensitive to X-rays, γ -rays and β particles, which normally accompanies neutrons.
- It is rugged, easy to handle for large scale personnel monitoring and reasonable inexpensive.
- It is having good signal stability with little/no fading due to ambient temperature.

Etching of CR-39 foils are carried out with Electro-Chemical process at 60°C with high alternating electric fields at 1250 V and with alkaline solution of 7 N KOH[8]. It is carried out in two steps. The first step of etching is carried out for 4 h at 100 Hz and in the next step at 3.5 kHz for 40 minutes. After etching, the readings of the foils are carried out in microfiche reader with magnification of x42. Figure 1.13 shows the proton recoils tracks formed in CR-39 foils after exposure to different neutron doses. These tracks are counted to evaluate the dose received by the radiation workers due to neutrons. The foil used for personnel monitoring is having dimension of

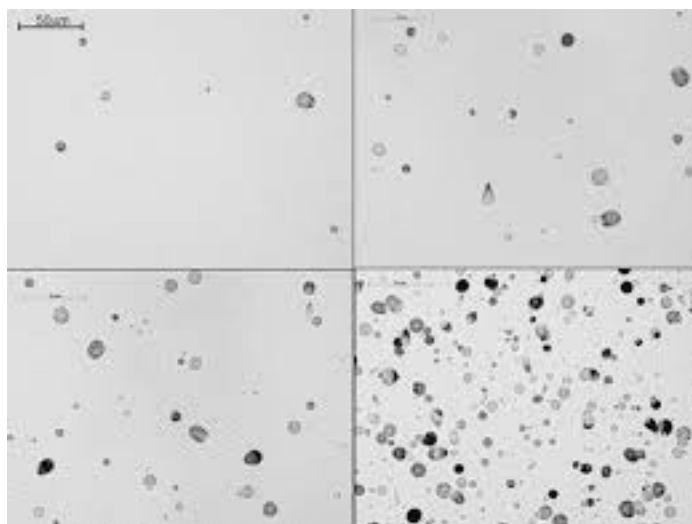


Figure 1.13: Proton recoil tracks formed in CR-39 foils after exposure to neutrons

3.0 cm x 3.0 cm which is sealed in triple laminated aluminized polyester pouches. Calibration of Cr-39 foils are carried out with $^{241}\text{AmBe}$ neutron source, where the foils are placed over water phantom to mimic the human torso. Minimum measurable

dose with these foils are 0.20 mSv. The measurable dose range is up to 10 mSv, as beyond this dose range, the track density becomes too dense to be counted. The disadvantages of CR-39 are its inherent background, sensitivity to etching conditions and its brittleness. Due to these disadvantages, large scale processing is also tedious.

1.7.3 Personnel monitoring devices in other countries

Personnel monitoring services in other countries are provided by several service providers[9], which uses other TL materials such as LiF:Mg, Ti, LiF:Mg, Cu, P, Li₂B₄O₇:Cu, Li₂B₄O₇:Mn, Si, Li₂B₄O₇:Cu, Ag, P. LiF based TL dosimeters have advantage over CaSO₄:Dy of being tissue equivalent ($Z_{eff} \sim 7.8$). But, it has several disadvantages of being low sensitivity, complicated glow curve and annealing procedure. LiF based dosimeters are mostly used in European countries, Brazil and United States. Figure 1.14 shows the LiF based personnel monitoring TLD badge used in other countries.

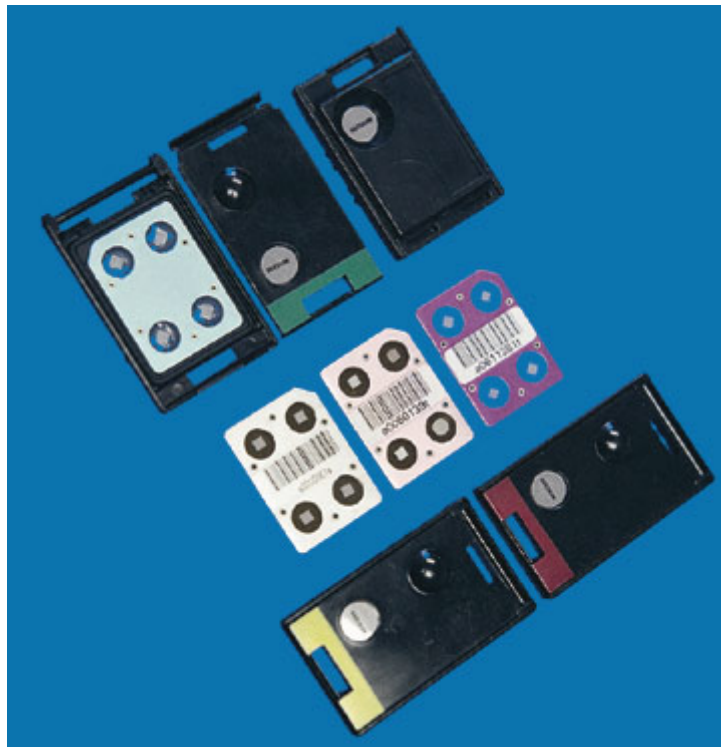


Figure 1.14: LiF based personnel monitoring dosimeter

With the growth of technology during 1990s, personnel monitoring badges based on Optically Stimulated Luminescence (OSL) were started[10]. In OSL based dosimeters, unlike TLDs, light is used for stimulating the light output, most of which are in different domains of wavelengths. Service providers such as Landauer Inc, USA and IBA OSL personnel dosimetry system uses $\text{Al}_2\text{O}_3:\text{C}$ and BeO as OSL materials in their personnel monitoring badges. OSL dosimeters based on $\text{Al}_2\text{O}_3:\text{C}$ by Landauer Inc., USA is responsible for providing personnel radiation monitoring to 1.7 million radiation workers, out of 5 million radiation workers worldwide. BeO based OSL dosimeters are used in some laboratories of Germany and Belgium. OSL based dosimeters have several advantages over TLD based dosimeters such as repeated readout of badges, fast and simple readout technique due to its all-optical process. Figure 1.15 shows the OSL based personnel monitoring badges being used in some countries.



Figure 1.15: OSL based personnel monitoring badge

Radio-photo Luminescence (RPL) glass dosimeters are mostly used in Japan[9]. RPL dosimeters are based on low atomic number silver-activated phosphate glass. These also have the advantage of repeated readout like OSL dosimeters. Figure 1.16 shows the RPL dosimeter being used in countries like Japan.

European Organization for Nuclear Research (CERN) uses personnel dosimeters based on Direct Ion Storage (DIS) memory cell[11]. It is a solid state memory cell, where electronic charges formed due to ionization of radiation exposure are trapped in the floating gate of MOSFET transistor. Although DIS based dosimeters are



Figure 1.16: Radio-photo Luminescence based personnel monitoring dosimeter

used as passive dosimeters, it has advantages of instant readout, whenever necessary.

Figure 1.17 shows DIS based personnel monitoring dosimeter.



Figure 1.17: DIS based personnel monitoring dosimeter of CERN

Personnel monitoring of neutrons in most of the countries are carried out mostly using CR-39 foils. Some uses pairs of $^6\text{Li}/^7\text{Li}$ based dosimeters for neutron monitoring using Albedo technique.

1.8 Spectrometry in radiation protection and personnel monitoring

The challenges in radiation monitoring of occupational workers are the presence of complex radiation fields in work place and energy dependence of most of the radiation monitors/detectors. The radiation fields outside the shielding wall of nuclear reactors and high energy accelerators comprises of neutrons, photons and electrons ranging from few keV to several MeV. So, single point energy calibration of radiation instruments used for radiation protection is not justified for different kinds of work place conditions. The reading of these dosimeters are used to evaluate the risk/hazard involved for the occupation workers and also to meet the compliance of the regulatory authority[12]. The instruments used for radiation monitoring should be able to provide good estimate of $H^*(10)$ or $H_p(10)$ and $H_p(0.07)$ in the energy domain encountered in the workplace. Passive dosimeters used for personnel monitoring needs to separate the dose due to each component of the radiation field. The conversion coefficients for $H_p(10)$ and $H_p(0.07)$ for different radiation fields are also energy dependent. The variation of the conversion coefficients for $H^*(10)$ and $H_{p,slab}(10,0^\circ)$ for neutron is shown in figure 1.18. The variation of conversion coefficients for $H^*(10)$, $H_p(10)$ and $H_p(0.07)$ for photons are shown in figure 1.19. It can be seen that the conversion factors for neutrons varies over the whole neutron energy except for very low energy of neutrons. Variation of conversion coefficients for photons is prominent only in the low energy domain. Thus the prior knowledge of the energy spectrum of the radiation fields is important for occupational radiation monitoring. This will help in understanding the response of the radiation monitoring instruments over the energy range of the neutrons, photons and electrons normally encountered in workplace. It will also help in the calibration of these instruments and arrive at the better and reliable estimate of dose equivalent (H) of the occupational workers. Moreover, Spectrometry of neutron and photon fields

have provided invaluable information in understanding their origin and in atomic physics and nuclear physics research.

Based on the principle of use, the neutron spectroscopy methods can be divided

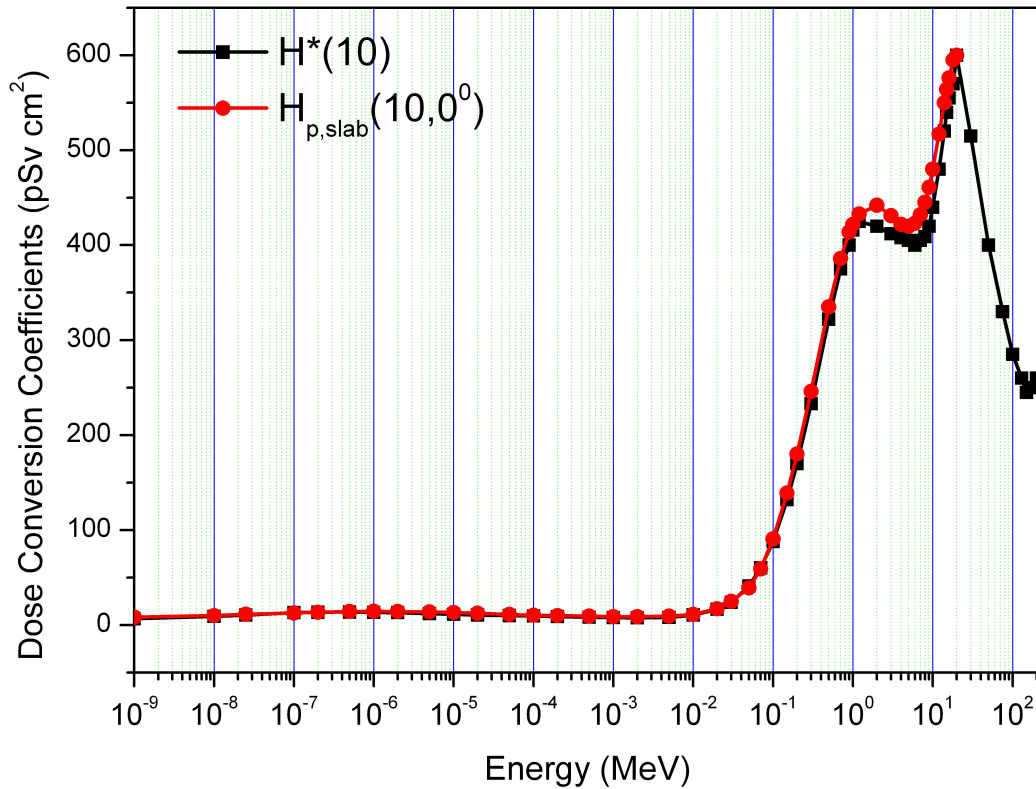


Figure 1.18: Variation of dose conversion coefficients for $H^*(10)$, $H_{p,slab}(10,0^\circ)$ for neutrons

into several groups given below[13]. Spectrometry of neutrons can be carried out with several detectors which may be both passive or active. Both the systems have its own limitations.

- Measurement of the recoil energy of the nucleus by scattered neutrons.
- Measurement of energies of the charged particles released in neutron-induced nuclear reactions.

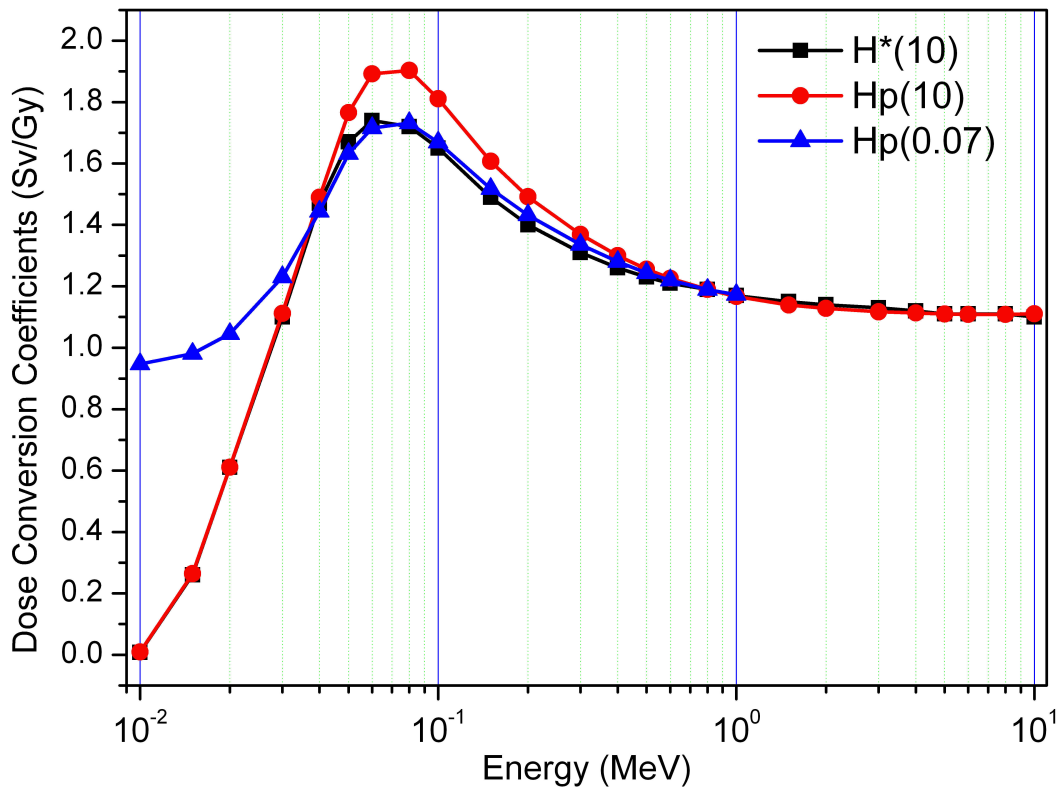


Figure 1.19: Variation of dose conversion coefficients for $H^*(10)$, $H_p(10)$ and $H_p(0.07)$ for photons

- Measurement of neutron velocity, which is proportional to the neutron energy.
- Threshold methods, in which minimum neutron energy is indicated by the appearance of a neutron induced effect such as radioactivity, a specific gamma-ray energy.
- Methods in which the neutron energy distribution is determined by unfolding a set of readings of detectors.
- Neutron diffraction measurements.
- Measurement of time-distribution of the slowing down of a short burst of high energy neutrons in a medium.

Out of these methods, two methods have been used in this work, namely (i) Neutron time-of-flight method and (ii) Bonner sphere system. In the first technique, neutron energy is determined by measuring the neutron flight time over known distances. Neutrons are detected using organic scintillators such as NE213 or BC501A. Organic scintillators are preferred because of their higher efficiency than other available neutron detectors. Detectors are required to register both the start and termination of the neutron flight. Two methods are used to do this. In the first method, the neutron is scattered in the first detector and the time of flight to a second detector at a known distance and angle is measured. In the second method, the start signal is provided by an associated particle that is emitted at the same time of that of neutron. This method of neutron spectroscopy is preferred, where the energy resolution is very important. The gamma discrimination is carried out with Pulse Shape Discrimination (PSD). But this technique is not appropriate for pulsed neutron beams from the accelerators.

Bonner sphere spectrometry employs a thermal neutron detector in the centre of different sizes of polythene spheres, commonly known as Bonner spheres. Although, this technique has poor energy resolution, it has many advantages. It can be used in the pulsed beam of the accelerators. It can be carried out using both passive and active detectors. The neutron spectrum is determined by measuring the output of the thermal neutron detector at the centre of different sized bonner spheres, and then unfolding these measurements using the response matrix of that particular detector system. Although basic Bonner spheres spectrometry is suitable only up to 20 MeV, the energy range can be enhanced by the use of lead inserts in the Bonner spheres.

Photon spectroscopy can be carried out using Scintillator based detector such as NaI(Tl) or CsI(Tl) or by using Semiconductor based detector such as Ge detector. But, if the photon is present along with the neutrons, the situation becomes complicated due to the neutron induced photons[14]. The responses of such photons

to the detectors are most of the time not known. Even if the neutron fluence has been obtained separately, the necessary corrections to the photon response cannot be carried out. In such cases, pulse shape analysis is the most preferred technique to separate out the neutron response. Although organic scintillators can be used for this, but in this work, BaF₂ based scintillator detector array has been used for the measurement of the photon spectrum.

1.9 Fundamentals of Cyclotrons

1.9.1 History

The concept of cyclotron was first conceived in Germany around 1920, but the first working cyclotron was developed and patented by Ernest Lawrence of the University of California, Berkley[15]. It was first operated in 1932. Lawrence was awarded the Nobel Prize for physics for this invention in 1939. M. Stanley Livingstone contributed significantly for the making of this device.

1.9.2 Principle of Cyclotron

Cyclotron accelerates a charged particle, such as proton, alpha or other heavy ions using high frequency voltage applied between a pair of Dees, placed opposite to each other. Figure 1.20 shows the Dees and the high frequency voltage applied using oscillator. These Dees are made up of metal, which are placed under high vacuum. Ion source puts the charged particle between the Dees, which are placed between the two poles of electro-magnet. Magnetic field confines the particle in the horizontal plane of the Dees. Figure 1.21 shows the cyclotron with electro-magnets. Each time the charged particles crosses the gap between the two Dees, it experiences electrostatic force due to the high voltage applied between the Dees, due to which it accelerates and gains energy. Since the particle is accelerated by the Dees many times, the final energy of the particle does not depend on the accelerating voltage,

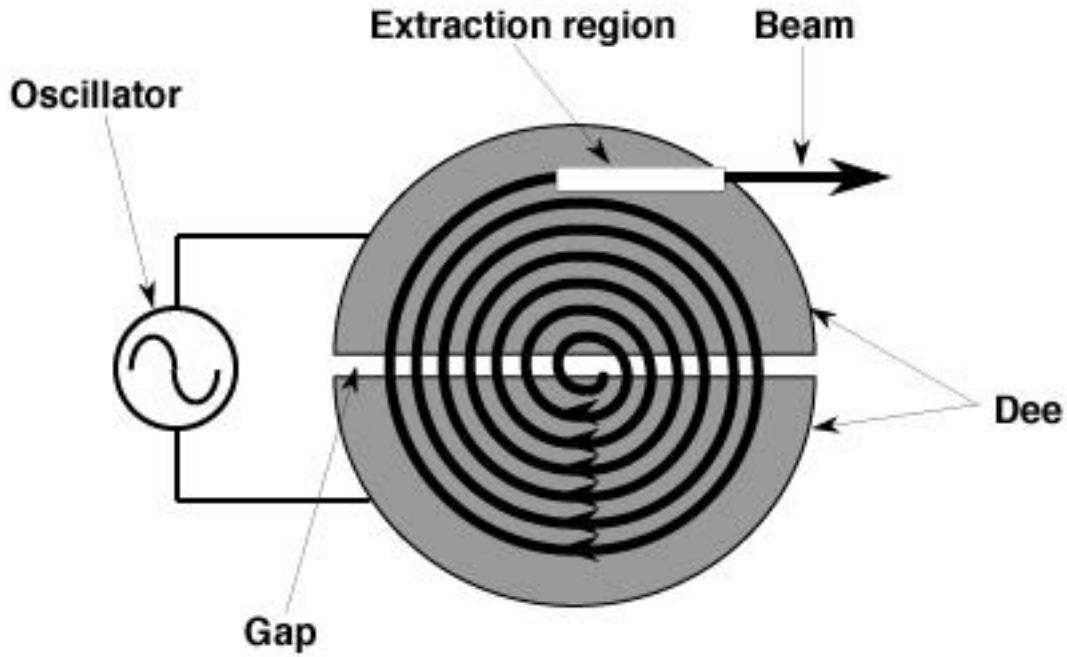


Figure 1.20: Cross sectional view of the cyclotron showing the Dees and the oscillator but on the size of the Dees. The high frequency applied between the Dees is such that the particle sees opposite field every time when it reaches the gap between the Dees. This is known as cyclotron frequency and is shown below.

$$f = \frac{QB}{2\pi m} \quad (1.8)$$

where Q is the charge of the particle and m is its mass. B is the applied magnetic field. For non-relativistic particles, the centripetal force is given by

$$F_c = \frac{mv^2}{r} \quad (1.9)$$

where v is the velocity and r is the radius of the path. The Lorentz force experienced by the charged particles placed in magnetic field B is given by

$$F_B = Q(v \times B) \quad (1.10)$$

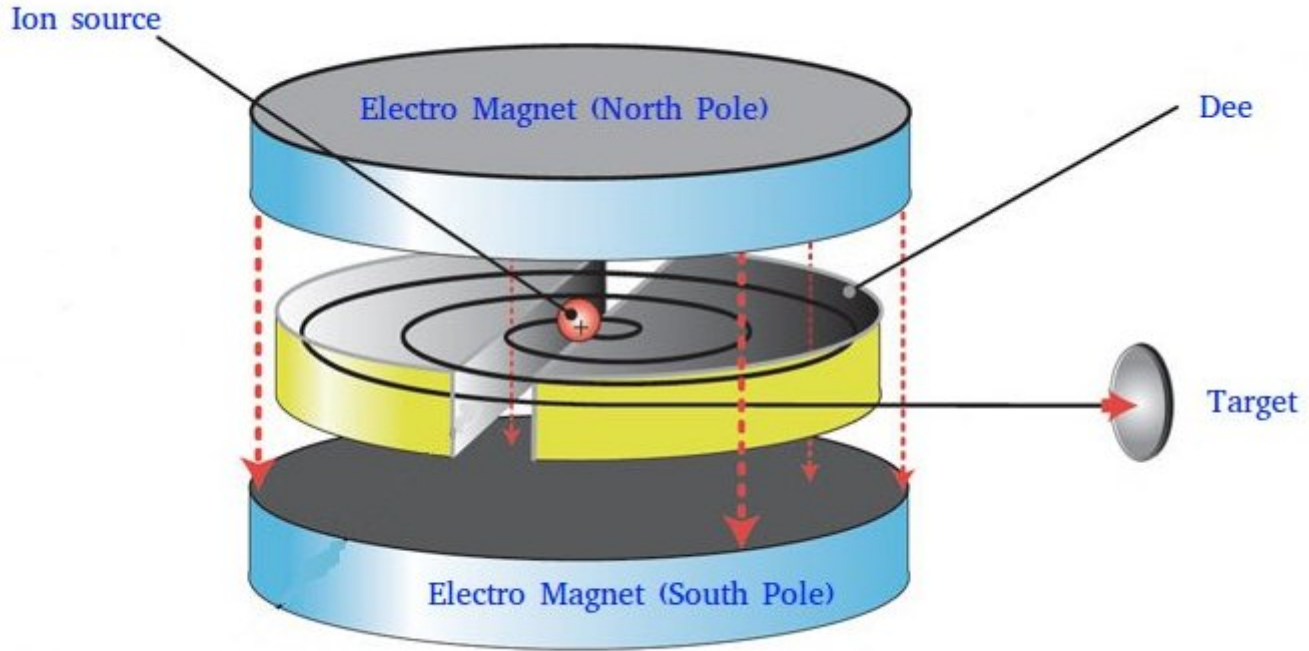


Figure 1.21: Cyclotron with electro-magnets and path of the charged particle

As the maximum energy of the particle is reached at the boundary of the path, putting $r=R$ and equating above equations, we get

$$\frac{mv^2}{r} = QvB \quad (1.11)$$

Here velocity v and the magnetic field B are always perpendicular to each other. So, the final kinetic energy of the particle is given by

$$E = \frac{1}{2}mv^2 = \frac{Q^2 B^2 R^2}{2m} \quad (1.12)$$

For a cyclotron, magnetic field B , extraction radius R is constant. So the equation can be written as

$$E = K \frac{Q^2}{A} \quad (1.13)$$

where A is the mass number of the particle. K is a constant for a particular cyclotron.

1.9.3 Relativistic considerations

In the non-relativistic regime, the frequency does not change, as the mass of the particle remains constant. Here, the period of the particle remains constant even after gain in their kinetic energy. But the situation is different, if the relativistic considerations are taken into account for the particle mass. Then the particle frequency and that of the high frequency oscillator becomes out of sync with each other and the further acceleration of the particle is not possible. This is taken care either with the modification of the frequency (synchrocyclotron) or with the modifications of the magnetic field (isochronous cyclotron). The relativistic mass of the particle can be written as

$$m = \frac{m_0}{\sqrt{1 - \left(\frac{v}{c}\right)^2}} = \frac{m_0}{\sqrt{1 - \beta^2}} = \gamma m_0 \quad (1.14)$$

where $\beta = \frac{v}{c}$ and $\gamma = \frac{1}{\sqrt{1 - \beta^2}}$. Here γ is also known as Lorentz factor.

The relativistic cyclotron frequency and the particle angular frequency is given by

$$f = \frac{QB}{2\pi\gamma m_0} = \frac{f_0}{\gamma} = f_0 \sqrt{1 - \beta^2} \quad (1.15)$$

$$\omega = 2\pi f = \frac{QB}{\gamma m_0} = \frac{\omega_0}{\gamma} = \omega_0 \sqrt{1 - \beta^2} \quad (1.16)$$

where f_0 and ω_0 are classical cyclotron frequency and angular frequency of the particle.

The radius of the particle moving in the static magnetic field is then given by

$$r = \frac{v}{\omega} = \frac{\beta c}{\omega} = \frac{\gamma \beta m_0 c}{QB} \quad (1.17)$$

1.9.4 Synchrocyclotron

In these types of cyclotron, the driving oscillator frequency is varied to compensate for the relativistic effect of the particle mass with its energy. In classical cy-

clotron the frequency of the oscillator is fixed. The frequency of the oscillator in synchrocyclotron is governed by equation 1.15. The frequency of oscillator in a synchrocyclotron is decreasing continuously instead of kept constant so as to maintain cyclotron resonance for relativistic velocities of the particle. The chief advantage of the synchrocyclotron is that there is no need to restrict the number of revolutions executed by the charged particle before its exit. One of the disadvantages of these machines is its low beam current. These machines are promising candidates for proton therapy because of its compact size.

1.9.5 Isochronous Cyclotron

In these machines, the oscillator frequency driving the cyclotron is kept constant, but the magnetic field increases azimuthally to take care of the relativistic effect of the particle mass. Recalling equation 1.17, if the magnetic field varies with the Lorentz factor, such that $B = \gamma B_0$, the relation $r = \frac{m_0 v}{QB_0}$ is again seen to be dependent only on the velocity of the particle, like non-relativistic case. The transverse de-focusing effect of this radial field gradient is compensated by ridges on the magnet faces which vary the field azimuthally as well. This allows particles to be accelerated continuously, on every period of the oscillator. This principle that alternating field gradients have a net focusing effect is called strong focusing. The biggest advantages of such machines are its high beam current.

1.10 Description of Accelerators and other facilities (Existing and upcoming)

The work carried out here has used detectors and radiation generating machines such as accelerators at various places. Some of these facilities are described briefly here.

1.10.1 High Altitude Research Laboratory (HARL)

HARL at Gulmarg in Jammu & Kashmir, India houses Neutron Monitors (NM), which carries out the measurement of neutron particle fluence from cosmic rays. Cosmic rays comprises of 89% proton, 10% alpha and rest 1% comprising of heavier nuclei all way up to uranium. When these particles enter the earth's atmosphere, they interact with nuclei of the atoms present in the atmosphere and produce secondary particles, such as neutrons, pions, mesons to name a few. From the early 1930s to the 1950s, cosmic rays played a critical role in the scientific study of the atomic nucleus and its components, for they were the only source of high-energy particles. Short-lived subatomic particles were discovered through cosmic-ray collisions. The field of particle physics was in fact established as a result of such discoveries, beginning with those of the positron and the muon. Even with the advent of powerful particle accelerators in the 1950s, investigators in the field have continued to study cosmic rays, albeit on a more limited scale, because they contain particles with energies far beyond those attainable under laboratory conditions.

Lead Free Gulmarg Neutron Monitor (LFGNM) records the transient solar modulation effects due to solar flares / coronal mass ejections and unique modulation in neutron bunches[16]. It has also been optimized for recording the neutron bunches from Atmospheric Lightning Discharge also, for measuring neutrons having energy 2.45 MeV[17]. The geometry has been changed considerably from the conventional Neutron Monitors such as IGY and NM64 types. Therefore, this monitor besides operating as a (24 x 7) cosmic ray neutron monitor in free running mode is also armed with an electrostatic field variation trigger mechanism to record 2.45 MeV neutrons conjectured to be produced in D-D fusion nuclear reactions in the atmospheric lightning discharges (ALD). It comprises of a bank of 21 cylindrical BF_3 counters made of thin walled brass tubes each 87 cm in active length and 3.8 cm in diameter. The counters are filled at a pressure of 450 torr. The ^{10}B enrichment in the BF_3 gas is $\sim 96\%$. The counters are laid in the form of an array (1 x 21)

spaced 15 cm from the centre of each other over 28 cm thick paraffin reflector blocks covering an area of $3 \times 10^4 \text{ cm}^2$. The counter array is also covered on top with 8 cm thick rectangular paraffin moderator blocks measuring 30 cm in breadth and 45 cm in length. Empty space between adjacent counters is occupied by air. The BF_3 counters are arranged to form three independent counting channels each comprising of seven tubes. The LFGNM rests on a low Z wooden floor eight meters above the ground level in order to minimize the contribution to the environmental effect due to neutron albedo splash produced in the ground below the monitor. A steep roof with an inclination of 70° is also provided above the LFGNM setup to avoid the snow absorption effect due to accumulation of snow overhead. The outside view of the building housing LFGNM is shown in figure 1.22.



Figure 1.22: View of the building housing LFGNM

1.10.2 K-130 Cyclotron

The K-130 Cyclotron at Variable Energy Cyclotron Centre (VECC), Kolkata is designed to accelerate protons from 6 to 65 MeV, deuterons from 12 to 60 MeV and alpha particles from 12 to 130 MeV using Penning Ion Gauge (PIG) ion source[18].

The cyclotron also accelerates heavy ions like Nitrogen, Oxygen, Neon and Argon etc. using ion sources based on Electron Cyclotron Resonance (ECR). The extracted current may fall within the range from a few pico-amperes to tens of micro-amperes, thus the beam power can rise up to 2kW. It is a sector focused isochronous magnetic field cyclotron with three spiral sectors. The water cooled main magnet of diameter 224 cm, produces a maximum magnetic field of 21.5 kG in the pole gap.

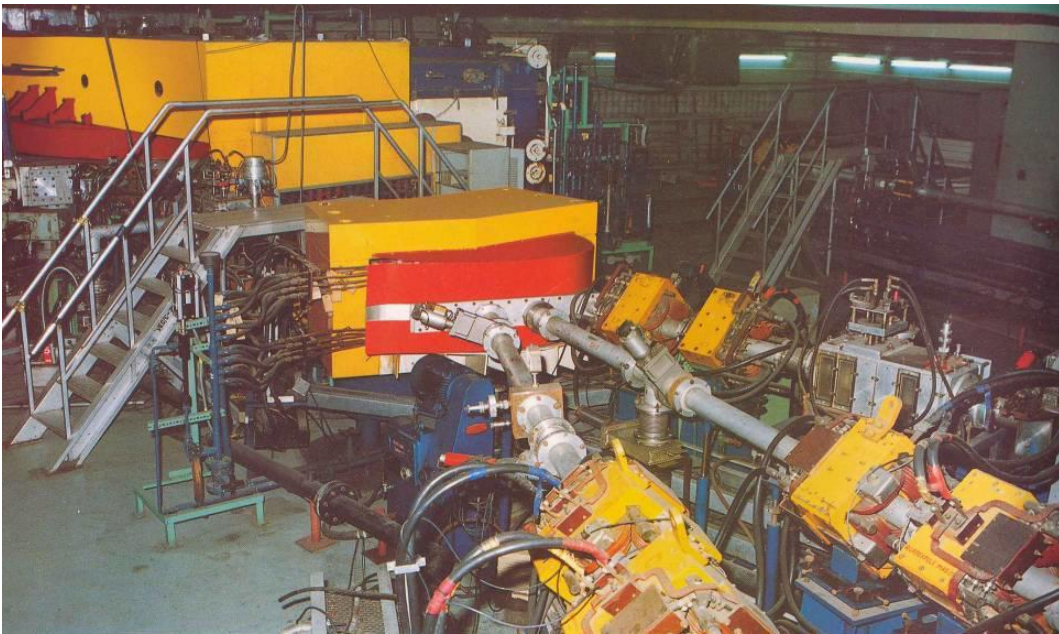


Figure 1.23: K-130 Cyclotron at VECC

This Cyclotron has been designed to carry out research and development in the fields of Nuclear Physics, Nuclear Chemistry, Radiation Biology, Material Science, Accelerator Physics to name a few. The Cyclotron produces proton rich isotopes, which are not produced by reactors, which have many applications in medical field for diagnosis and therapy. This cyclotron is also used as a primary source for Radioactive Ion Beam (RIB).

1.10.3 Super Conducting Cyclotron

Super conducting Cyclotron (SCC) has been developed at VECC, which can give very high energy of the beam particles as compared to K-130 Cyclotron[19]. The

machine of the Super Conducting Cyclotron is shown in figure 1.24. It can accelerate all elements of the periodic table in various charge states using ECR ion source. The beam injection is axial, from the top of the cyclotron. The energetic beams from SCC shall be powerful tools to explore new fields of research in Nuclear Physics, Nuclear Chemistry, Analytical Chemistry, Condensed Matter Physics and allied applied fields. The SCC is a sector-focused cyclotron like K-130 but having its main magnet coil superconducting. Super conducting coils of the magnet help to produce a maximum magnetic field (B) of 5.5 Tesla (T) in the pole gap. Super conducting coils are made up of NbTi, which is immersed in liquid Helium bath. As a result the kinetic energy of the output ions is significantly increased even at reasonably small value of pole radius $R = 71$ cm. To take care of relativistic mass increase effect there are 13 numbers of trim coils around each spiral sector. For atomic mass number (A) between 1 to 20, the energy per nucleon is given by equation 1.18. There are three Dees, at a angle of 53° . The Radio Frequency (RF) can operate at 9 - 27 MHz. Maximum Dee Voltage is 80 kV. Radiation shielding of the main vault is provided by 3.5 m thick RCC (Reinforced Cement Concrete) wall. Shielding of the caves is provided by 1.5 m RCC wall.

$$K.E. = 160 \frac{Q}{A} \quad (1.18)$$

For A greater than 20, the kinetic energy per nucleon is given by equation 1.19.

$$K.E. = 512 \frac{Q^2}{A^2} \quad (1.19)$$

where Q denotes the charge state of the element being accelerated and A is the mass number.

1.10.4 Medical Cyclotron

Medical Cyclotron at Chakgaria, Javadpur under VECC is at the advanced stage of commissioning. The machine has been supplied by M/s Ion Beam Application,

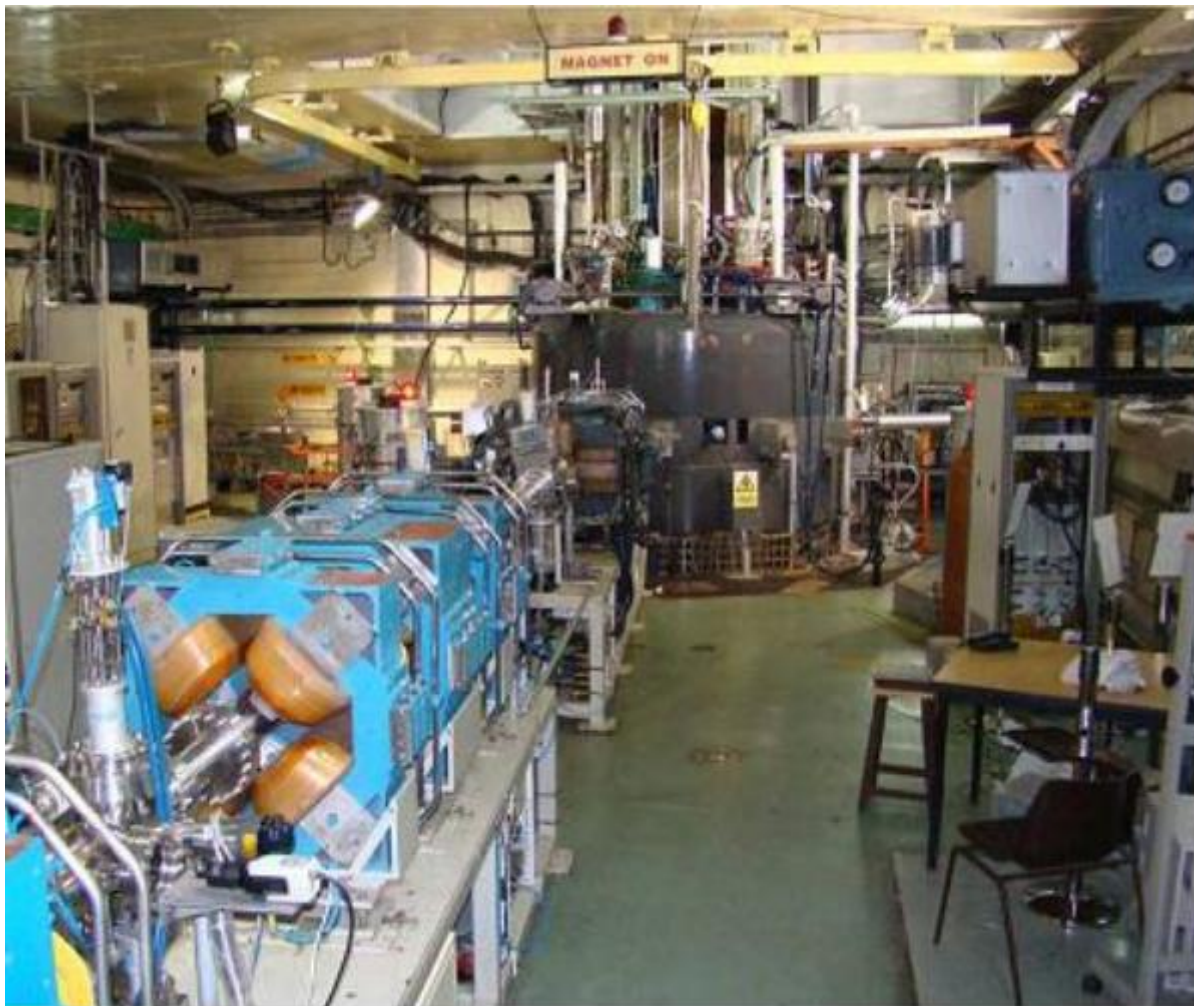


Figure 1.24: Super Conducting Cyclotron machine at VECC

Belgium. It is capable of delivering proton beam in the range of 15 to 30 MeV, with 350 μA beam current guaranteed. This is a negative hydrogen ion cyclotron, but positive proton beam will be extracted. Two RF cavities will accelerate the negative hydrogen ions. At the extraction radius carbon stripper foils will be used to extract two simultaneous proton beams from the machine. There will be five external beam lines—one for Positron Emission Tomography (PET) isotope production (mainly FDG), two for Single Photon Emission Computed Tomography (SPECT) isotope production (Ga-67, Tl-201 and many others) and the last two beam lines for research and development. Some of the radioisotopes to be produced by Medical Cyclotron for SPECT and PET are given in table 1.6. Research and development with

this machine will mainly comprise in the fields of material science, radiochemistry, liquid metal target development etc.

Table 1.6: Some of the common radio-isotopes to be produced by Medical Cyclotron

Isotope (half life)	Nuclear Reaction	Proton Energy (MeV)	Beam Current (μA)
^{67}Ga (78.3 h)	$^{68}\text{Zn}(p,2n)^{67}\text{Ga}$	28.5	200
^{201}Tl (73.5 h)	$^{203}\text{Tl}(p,3n)^{201}\text{Pb}$, (9.4 h) $^{201}\text{Pb}(\text{EC}/\beta^+)^{201}\text{Tl}$	28.5	200
^{111}In (67.9 h)	$^{112}\text{Cd}(p,2n)^{111}\text{In}$	28.5	200
^{18}F (1.8 h)	$^{18}\text{O}(p,n)^{18}\text{F}$	18	40



Figure 1.25: Medical Cyclotron machine at VECC

1.11 Monte Carlo Simulation

Monte Carlo methods for radiation transport calculations have become an indispensable tool in radiation dosimetry and radiation protection. Monte Carlo method is often the only means to link protection quantities with the operational quantities[20]. A number of Monte Carlo packages are available for radiation transport calculations.

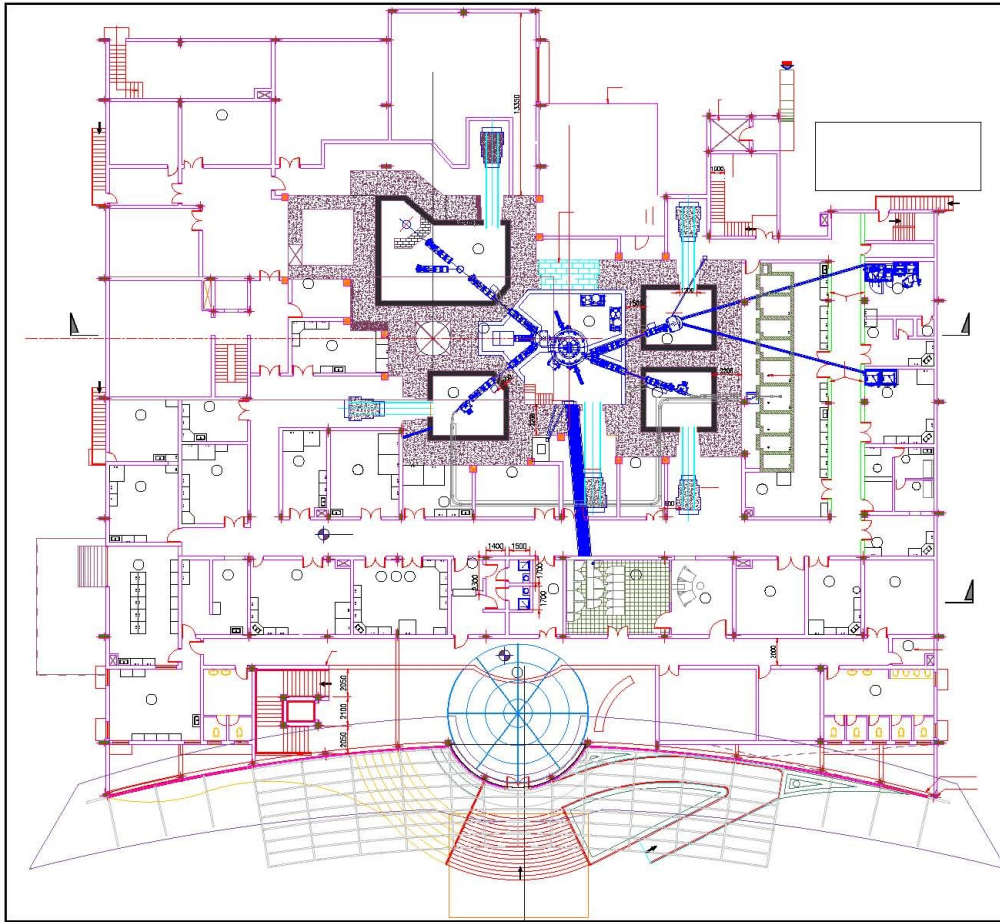


Figure 1.26: Layout of the building housing Medical Cyclotron at VECC

Some of the famous codes are EGSnrc[21], MCNP[22], MCNPX[23], FLUKA[24, 25], McBEND[26], ETRAN[27], PENELOPE[28], TRIPOLI[29], GEANT4[30] to name a few.

1.11.1 History of Monte Carlo Method

Monte Carlo method was first used for the calculation of π using Buffon's needle experiment in which needles were dropped on parallel lines of known distance between them. Enrico Fermi, in 1930s also used Monte Carlo method for neutron diffusion problem, but never published anything. The modern Monte Carlo method is credited to be invented by Stanislaw Ulam, John von Neumann and Nicholas Metropolis.

Ulam was a polish born mathematician, who worked for John von Neumann in the Manhattan Project. He was also known for designing the Hydrogen bomb with Edward Teller in 1951. In a thought experiment, he conceived the idea of Monte Carlo method to win a game of solitaire.

Ulam, von Neumann and Metropolis developed algorithms for computer implementations, as well as explored means to transform non-random problems to random forms that would facilitate their solution through statistical sampling. This work transformed statistical sampling from a mathematical curiosity to a formal methodology applicable to a wide variety of problems. It was Metropolis who coined the name “Monte Carlo method” after the casinos of a place named Monte Carlo. Ulam and Metropolis also published a paper called “The Monte Carlo method” in 1949[31].

1.11.2 Steps of Monte Carlo simulation

In general Monte Carlo simulation is composed of following important steps.

- Set up Probability Density Function (PDF).
- Build Cumulative Distribution Function (CDF).
- Generate random numbers: accept those which satisfies the given condition.
- Sampling.
- Scoring or tallying.
- Error estimation.
- Variance reduction techniques.
- Parallelization or vectorization.

1.11.3 Probability Density Function

Let us consider a true random event, where x is one of the possible outcome. If x can take any value from a continuous range, we can write $f(x)dx$ as the probability that the outcome of the random event lies between x and $x + dx$. The function $f(x)dx$ is known as *Probability Density Function*, which may depend on several other parameters.

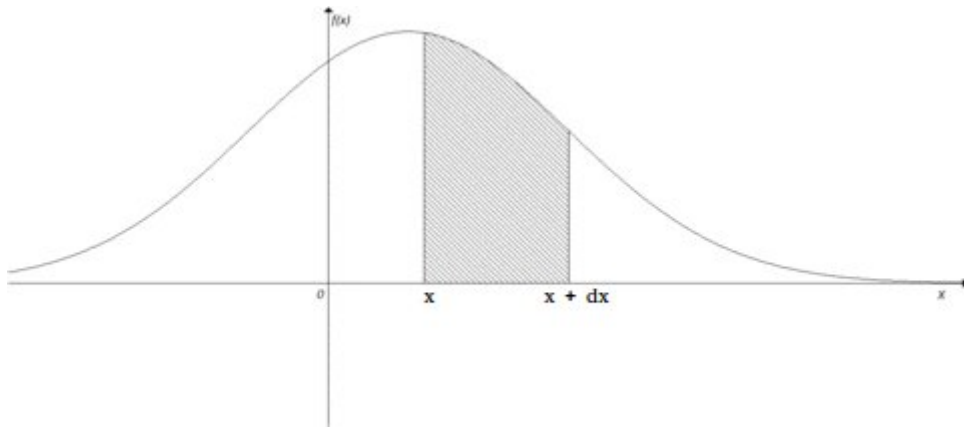


Figure 1.27: Probability density function

1.11.4 Cumulative Distribution Function

The *Cumulative Distribution Function* $F(x)$ is the probability that $\xi \leq x$:

$$F(x) = \int_a^x f(\xi) d\xi \quad (1.20)$$

The value of $F(x)$ is such that $0 \leq F(x) \leq 1$. $F(x)$ is non decreasing, and $P(c < \xi < d) = F(d) - F(c)$. $F(x)$ is a uniform distribution in the interval $(0,1)$.

1.11.5 Random Numbers

Random Number Generators (RNG) are integral part of any Monte Carlo simulation. Some of the properties of Ideal RNG are as follows:

- Uniformly distributed

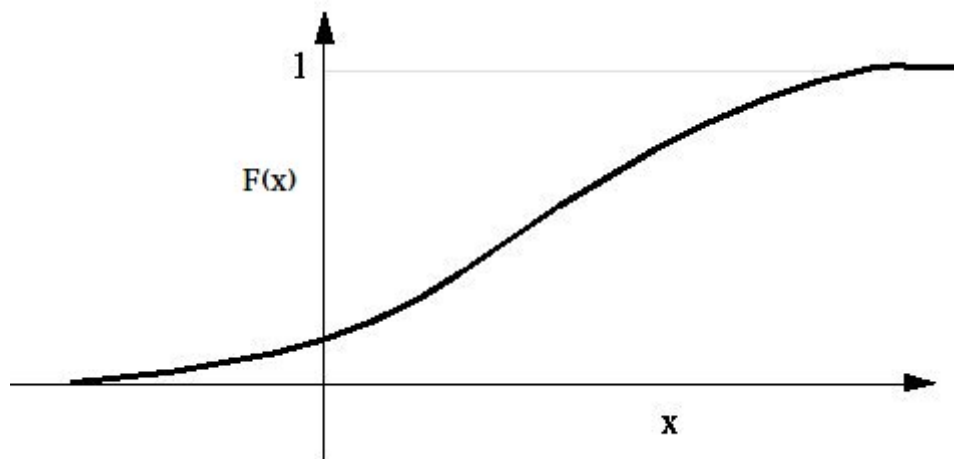


Figure 1.28: Cumulative distribution function

- Uncorrelated
- Never Cycles
- Satisfies any statistical test for randomness
- Machine independent
- Changing “seed” should change the sequence
- Easily split into independent subsequences
- Fast
- Limited memory requirement

No RNG satisfies all the conditions for an ideal RNG. Finite arithmetic precision gives rise to finite number of states. Hence they tend to “cycle” after some period. The requirement of reproducibility gives rise to correlations. So, the solution is to go for Pseudo RNGs. If the period of Pseudo RNG is more than the number of random number required for a particular simulation, then it tends to be practically acyclic. All modern day compilers have their own set of RNGs generated using different types of mathematical algorithms. One of the most used RNG, which has

been workhorse for many years is *Linear Congruential Random Number Generator*.

$$X_i = (a \times X_{i-1} + c) \text{Mod} M \quad (1.21)$$

In equation 1.21, “a” is the multiplicative constant, “c” is a additive constant, X_{i-1} is the initial seed and M is the modulus. M is also the period of RNG. In a 32-bit computer, M is generally taken as 2^{31} . Different compilers uses different sets of values for “a” and “c”.

1.11.6 Sampling

Common sampling techniques used by Monte Carlo techniques are as follows:

Inversion Method

If the probability density function is $f(x)$ in the range $a < x < b$, its cumulative distribution function is given as:

$$F(x') = \int_a^{x'} f(x) dx \quad (1.22)$$

$F(x')$ in equation 1.22 is itself a random variable distributed between [0,1]. If ξ is the random number, then $F(x') = \xi$ which leads to $x' = F^{-1}(\xi)$. This is the most simple sampling technique often used by Monte Carlo techniques.

Rejection Technique

There are some functions which cannot be inverted. In such cases, we use the *Rejection Technique*. Let $f'(x)$ is one such normalized distribution that requires sampling[32]. Let $g'(x)$ be another distribution, normalized, that can be sampled such that $Cg'(x) \geq f'(x)$ for all $x \in [x_{min}, x_{max}]$. Generate a random number ξ_1 to sample X from $g'(x)$. Generate a second random number ξ_2 . Accept X as a sample of $f'(x)$ if $\xi_2 < f'(X)/Cg'(X)$, otherwise resample with new values of ξ_1 and ξ_2 .

The disadvantage of this technique is the loss of random numbers generated.

To overcome the disadvantages of the above mentioned sampling techniques, a third technique is also used in Monte Carlo techniques.

Mixed Technique

This sampling technique takes the advantages of both *Inversion Technique* and *Rejection Technique*. If the distribution function is difficult to integrate and invert, it rules out the *Inversion Technique*. Moreover, if the distribution is “spiky” too, the *Rejection Technique* is also inefficient. In such a case, the distribution function $p(x) = f(x)g(x)$ can be factored and *Inversion Technique* and *Rejection Technique* can be suitably used for the separate distributions $f(x)$ and $g(x)$.

1.11.7 Scoring or Tallying

Scoring or Tallying in Monte Carlo Simulation is carried out with the help of various estimators or detectors[32]. For the estimation of fluence or current at the boundary of two physical regions, boundary crossing estimators are used. Possible outcomes are fluence spectra as a function of energy, angle, particle type, etc.

Track-length estimators are used for the calculations of fluence of particles in a region of real space. The results are fluence spectra as a function of energy, angle and particle type based on their path length within the region volume.

Pulse height estimators are used to simulate the response of a spectrometer. The quantity estimated is the energy deposited in the region of phase space, and the result is the spectrum of energy deposited within the region volumes.

Scalar integral estimators are used for the calculations of energy deposited, number of inelastic interactions and induced activity in the region of real space.

1.11.8 Error estimation

In a real experiment, a score is obtained by sampling from a statistical distribution. It is the average value of the number of measurement data, taken in a similar condition, along with a statistical error and systematic error. Similarly, a Monte Carlo score is an average of scores, a statistical error and may be even a systematic error. The standard deviation of a Monte Carlo estimator, calculated from several batches or single histories of run, is an estimate of the standard deviation of the actual distribution. The precision of such an estimate depends on the type of estimator, and on the particular problem, but the sample average converges to the actual distribution average as $N \rightarrow \infty$. The table from MCNP manual[22] shows the actual meaning of a calculated statistical error in Monte Carlo simulation than in an experiment. Table 1.7 is empirically based on experience and is not on a mathematical proof. It

Table 1.7: Relative error and the quality of Tally in Monte Carlo Simulation

Relative Error (%)	Quality of Tally
50-100	Garbage
20-50	Factor of a few
10-20	Questionable
<10	Generally reliable

has been generally confirmed in other codes as well.

1.11.9 Variance Reduction Techniques

Variance Reduction Techniques (VRTs) are generally used in Monte Carlo simulation for the faster statistical convergence of the score. To evaluate the effectiveness of the technique, it defines a Figure of Merit of the estimator:

$$F = \sigma^2 \times t \quad (1.23)$$

where σ^2 is the variance of the score and “t” is the computation time taken for the estimate per unit primary particle. Some techniques are aimed at reducing σ^2 ,

while others at reducing “t”, but all are referred to as VRTs. The variance σ^2 is proportional to $1/N$ and “t” is directly proportional to N , so reducing $\sigma^2 t$ means reducing σ^2 at a faster rate than “t”. Most of the choice of VRTs depends on the type of problem. Some of the commonly used techniques are given as follows:

Importance Biasing

Importance biasing plays an important role for deep shielding problems, where otherwise the contribution of particle fluence to the detector is very less. By employing this VRT, significant particle fluence is achieved in the region of detector. It is used to keep a constant particle population compensating for the attenuation due to absorption or distance. This also reduces the sampling in the regions, which otherwise may not contribute to the particle fluence to the detector of interest. The common form of importance biasing combines two techniques, namely Surface splitting and Russian Roulette. Surface splitting reduces σ^2 , but increases “t”, and Russian roulette does the opposite. This technique is the most simple and easy to use among the VRTs.

Energy Cutoff

Energy Cutoff in Monte Carlo simulation is a user supplied value, which may be independent of the geometry, valid for the whole problem geometry, or it may be region dependent. Particles having energy below the specified values are terminated on the spot and their energy is deposited locally. It is important for those high energy particle based problems, where the low energy particles do not contribute to the region of interest. It is similar to Russian Roulette of the particles based on their energy with zero survival probability. It reduces the computational time of the problem.

Weight Window

Weight window is space-energy-dependent splitting and Russian Roulette technique[22]. For each space-energy phase space cell, the user supplies a lower weight bound. The upper weight bound is the user supplied multiple of lower energy bound. These weight bounds define a window of acceptable weights. If the particle falls below the lower weight bound, Russian roulette is played and the weight of the particle is increased to a value of acceptable weights. If the weight of the particle goes below the upper bound weight, the particle is split and the reduced weight assigned to the particle is kept within the acceptable window of weights. No action is taken for the particles having weight within the window.

Exponential Transformation

Here the mean free path of the particle for inelastic interactions can be increased in the preferred direction[32]. This is very useful for thick shielding calculations. The exponential transformation accelerates convergence at large shielding depths, but slows it at smaller depths. This is generally accompanied with *Weight Window* so as to avoid large fluctuations in the phase space.

1.11.10 Parallelization or vectorization

Although with *Variance Reduction Techniques* the computational time of the Monte Carlo simulation can be reduced with acceptable variance of the score, still it has been found that for efficient sampling over the whole space of the geometry, large histories are required, which further increases the computational time. In such cases, advancement of the modern day computer comes to the rescue with the help of parallelization. With the computer processors becoming cheaper and plentiful, there is a great potential for having them compute together in a coordinated way. Some of the well known Monte Carlo codes give the user the choice to run them in parallel mode, which reduces the computational time to a great extent.

1.12 Reverse Monte Carlo Method

The Reverse Monte Carlo (RMC) modeling method, which is also known as Inverse Monte Carlo method is a variation of the standard Metropolis-Hastings algorithm to solve an inverse problem whereby a model is adjusted until its parameters have the greatest consistency with experimental data within the acceptable limits[33]. Following the acceptance/rejection test, the procedure is repeated many number of times. Inverse problems are found in many branches of science and mathematics, but this approach is probably best known for its applications in condensed matter physics and solid state chemistry. This method is often used in condensed matter sciences to produce atom-based structural models that are consistent with experimental data and subject to a set of constraints. The RMC method suffers from a number of potential problems. The most notable problem is that often more than one qualitatively different model will give similar agreement with experimental data. A second problem comes from the fact that without constraints the RMC method will typically have more variables than observables.

1.13 Monte Carlo code used in thesis

Monte Carlo code has been used extensively in this work. It has been used for the generation of the response matrix of neutron detector, for characterization of neutron detector based on BF_3 , for the evaluation of residual nuclei for Medical Cyclotron and Superconducting Cyclotron and also for the design of the shield for the beam dump of K-130 Cyclotron at VECC. The code which has been used is FLUKA[24, 25]. FLUKA is a general purpose tool for calculations of particle transport and interactions with matter, covering an extended range of applications spanning from proton and electron accelerator shielding to target design, calorimetry, activation, dosimetry, detector design, Accelerator Driven Systems, cosmic rays, neutrino physics, radiotherapy etc. Some of the important reasons for the choice of

this code and its capabilities are given as follows[25]:

1.13.1 Capabilities of FLUKA

FLUKA can simulate with high accuracy the interaction and propagation in matter of about 60 different particles, including photons and electrons from 100 eV-1 keV to thousands of TeV, neutrinos, muons of any energy, hadrons of energies up to 20 TeV (up to 10 PeV by linking FLUKA with the DPMJET code) and all the corresponding antiparticles, neutrons down to thermal energies and heavy ions. The program can also transport polarized photons (e.g., synchrotron radiation) and optical photons. Time evolution and tracking of emitted radiation from unstable residual nuclei can be performed online.

The FLUKA hadron-nucleon interaction models are based on resonance production and decay below a few GeV, and on the Dual Parton model above. Two models are used also in hadron-nucleus interactions. At momenta below 3–5 GeV/c the PEANUT package includes a very detailed Generalised Intra-Nuclear Cascade (GINC) and a pre-equilibrium stage, while at high energies the Gribov-Glauber multiple collision mechanism is included in a less refined GINC. Both modules are followed by equilibrium processes: evaporation, fission, Fermi break-up, gamma de-excitation. FLUKA can also simulate photonuclear interactions (described by Vector Meson Dominance, Delta Resonance, Quasi-Deuteron and Giant Dipole Resonance).

For neutrons with energy lower than 20 MeV, FLUKA uses its own neutron cross section library (P5 Legendre angular expansion, 260 neutron energy groups), containing more than 250 different materials, selected for their interest in physics, dosimetry and accelerator engineering and derived from the most recently evaluated data.

FLUKA uses an original transport algorithm for charged particles, including complete multiple Coulomb scattering treatment giving the correct lateral displacement even near a boundary. The variations with energy of the discrete event cross

sections and of the continuous energy loss in each transport step are taken into account exactly. Differences between positrons and electrons are taken into account concerning both stopping power and bremsstrahlung. Some of the transport capabilities for various particles in FLUKA code are given in table 1.8.

Table 1.8: Particle transport capabilities in FLUKA

Particle Types	Secondary Particles	Primary Particles
Charged hadrons	1 keV-20 TeV	100 keV-20 TeV
Neutrons	thermal-20 TeV	thermal-20 TeV
Anti neutrons	1 keV-20 TeV	10 MeV-20 TeV
Muons	1 keV-1000 TeV	100 keV-1000 TeV
Electrons	1 keV-1000 TeV	70 keV-1000 TeV (low-Z materials) 150 keV-1000 TeV (hi-Z materials)
Photons	100 eV-10000 TeV	1 keV-10000 TeV
Heavy ions	<10000 TeV/n	<10000 TeV/n

1.13.2 FLUKA geometry and Input

FLUKA uses the Combinatorial Geometry (CG) package for its geometry. Two concepts are fundamental in CG: bodies and regions. Geometrical bodies include Rectangular Parallelepiped, Right Circular Cylinder, Sphere, Planes, Wedges, Cones, etc. Regions are defined as combinations of bodies obtained by boolean operations: Union, Subtraction and Intersection. These regions are filled with different materials or vacuum or “BLACK HOLE”, which is a fictitious materials which stops the further transport of all particles. The input and geometry of FLUKA is also handled by a powerful GUI called FLAIR[34]. It contains a fully featured editor for editing the input files in a human readable way with syntax highlighting, without hiding the inner functionality of FLUKA from the users. It provides also means for building the executable, debugging the geometry, running the code, monitoring the status of one or many runs, inspection of the output files, post processing of the binary files (data merging) and interface to plotting utilities like gnuplot and PovRay for high quality plots or photo-realistic images. The program includes also a database of selected properties of all known nuclides and their known isotopic composition as well

a reference database of ~ 300 predefined materials together with their Sternheimer parameters.

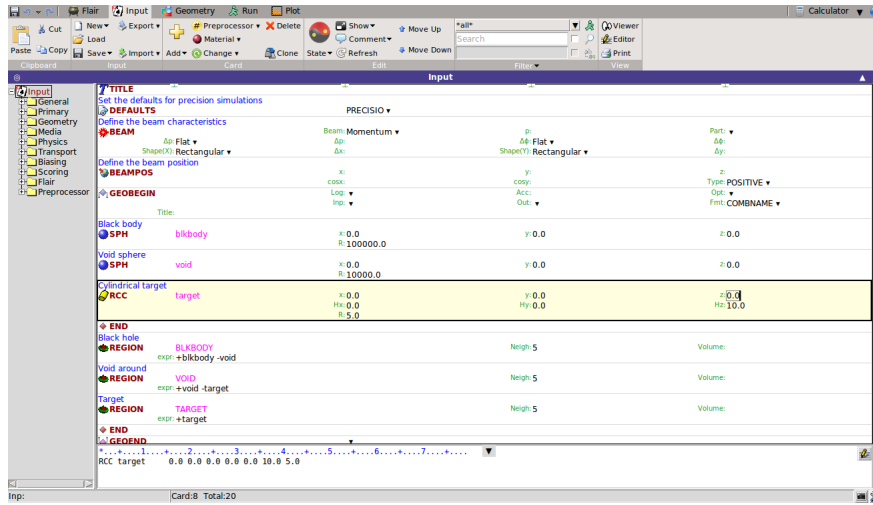


Figure 1.29: Input window of FLAIR

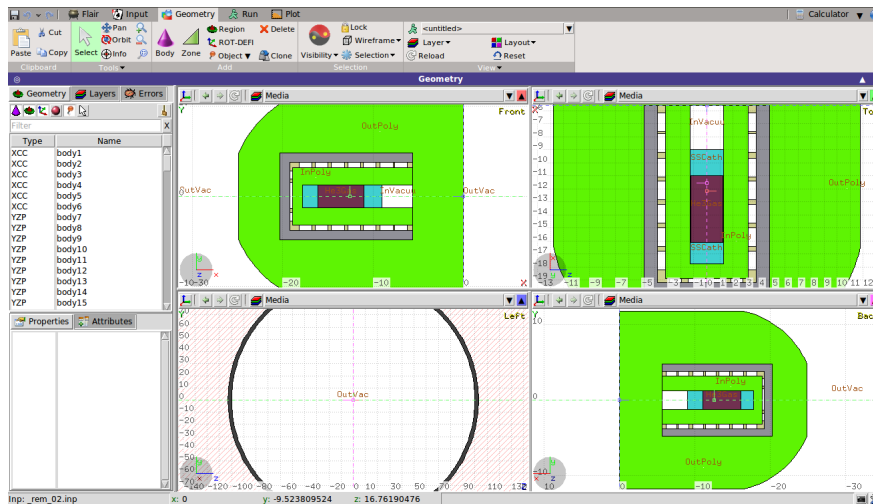


Figure 1.30: Geometry plot window of FLAIR

1.13.3 Scoring in FLUKA

FLUKA Monte Carlo code is capable of scoring fluence, current, energy deposition, dose, dose-equivalent, residual nuclides, activity, Displacement per Atom DPA, Non Ionizing Energy Loss (NIEL) and many more. Scoring in FLUKA is carried out with track-length detectors, boundary crossing detectors or point integral detectors.

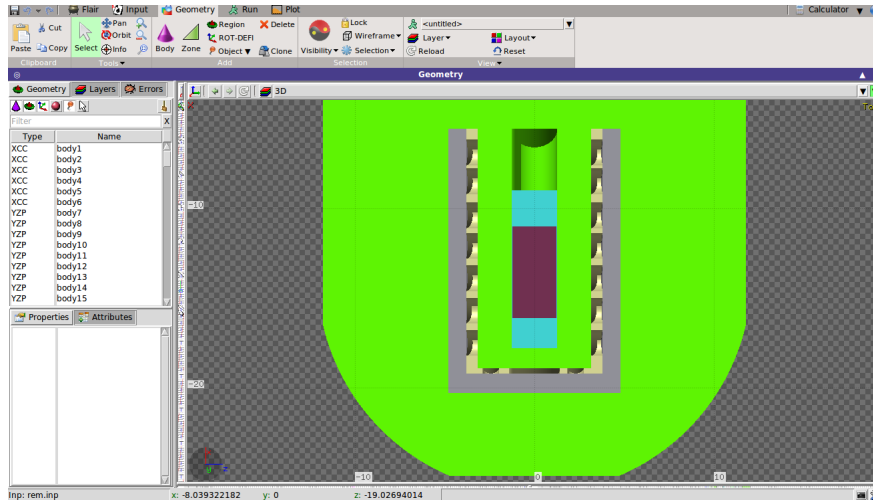


Figure 1.31: 3D plot using FLAIR

Some detectors are used for scoring these values based on regions in the geometry, and even some are independent of the regions in the geometry. From the input file the users can request scoring the respective quantities they are interested in. For additional requirements, FLUKA provides a set of user routines, which the users can modify as per their requirements. All types of detectors write their results into logical output units assigned by the user. The score is presented with the relative error, if the input file has been run many times, so that user can have the idea about the statistical convergence of the data. The data are also presented in user friendly ASCII files for plotting them either in FLAIR, or in any other software suited to the user.

1.14 Motivation and Structure of the thesis

The motivation of this thesis is to address some of the challenges in neutron and charged particle dosimetry, with the continuous evolution of the field of radiation protection and its implication in radiation personnel monitoring. Radiation dosimetry and radiation protection is becoming more and more complex with the development of high energy accelerators, modern nuclear reactors and space explorations. The structure of the thesis can be categorized as follows:

1. In the introduction of this thesis (Chapter 1) a brief description of the evolution of the radiation protection with the discovery of X-rays and radioactivity, radiation protection quantities, inception of radiation protection in India and the devices used for external personnel monitoring, importance of spectrometry of photons and neutrons in radiation protection and the Monte Carlo method capable of handling radiation transport and radiation dosimetry are given.
2. Chapter 2 describes the Bonner sphere spectroscopy with thermal neutron detector based on TLDs, generation of the response matrix for the same and its use to generate the spectrum of ^{241}Am -Be neutron source. The spectrum generated has been compared with the same spectrum available in the literature.
3. Chapter 3 characterizes the Lead Free Gulmarg Neutron Monitor. The optimization of the upper paraffin block has been carried out for ^{239}Pu -Be neutron source and energy response of LFGNM has been evaluated for mono-energetic neutrons in the range of 10^{-11} MeV to 10^4 MeV. The Lead test, Cadmium test and the angular response for the same has also been carried out.
4. Chapter 4 evaluates the residual nuclei in different layers of materials like concrete and soils for 30 MeV proton beam from Medical Cyclotron. Calculations have also been carried out for different beam line components like Al, SS(316L), Cu and in structural materials like concrete for Superconducting Cyclotron of VECC. The activity produced due to operation of these Cyclotron poses risk not only for the radiation workers in these facilities, but also for general public.
5. Chapter 5 describes the shielding calculations carried out for the beam dump of K-130 Cyclotron of VECC. The calculations have been carried out with Monte Carlo code FLUKA. An effort has also been made to validate the photon and neutron energy spectra produced from the interaction of ^4He particles with the beam dump, evaluated with the Monte Carlo code with the experimental evaluated spectra in different shielding configurations.

Chapter 2

Response Matrix for $\text{CaSO}_4:\text{Dy}$ based neutron detector

2.1 Introduction

Nuclear reactors, intermediate and high energy accelerators are in demand for their different societal activities. Many of them are situated in public domain considering their utilities for medical purposes. These facilities are capable of generating neutron and gamma rays. It is essential to estimate the dose obtained by the radiation workers and general public. It is also essential to estimate the dose due to the individual components of neutrons and gamma rays. Hence the individual monitoring in the mixed fields of neutron and gamma rays which exists in these radiation installations requires the prior knowledge of neutron spectra for accurate dosimetry as conversion coefficient from fluence to Personal dose equivalent $[H_p(d,\alpha)]$ depends on the energy of the neutrons. $H_p(d,\alpha)$ is the dose deposited at a depth d mm in International Commission on Radiation Units & Measurements (ICRU) slab phantom due to neutron at an angle α with respect to normal incidence. ICRU slab phantom is made up of tissue equivalent material having density of 1 g/cm^3 . It is having a dimension of $30 \text{ cm} \times 30 \text{ cm} \times 15 \text{ cm}$. It is made up of 76.2 % Oxygen, 11.1 %

Carbon, 10.1 % Hydrogen and 2.6 % Nitrogen. Figure 2.1 shows the variation of

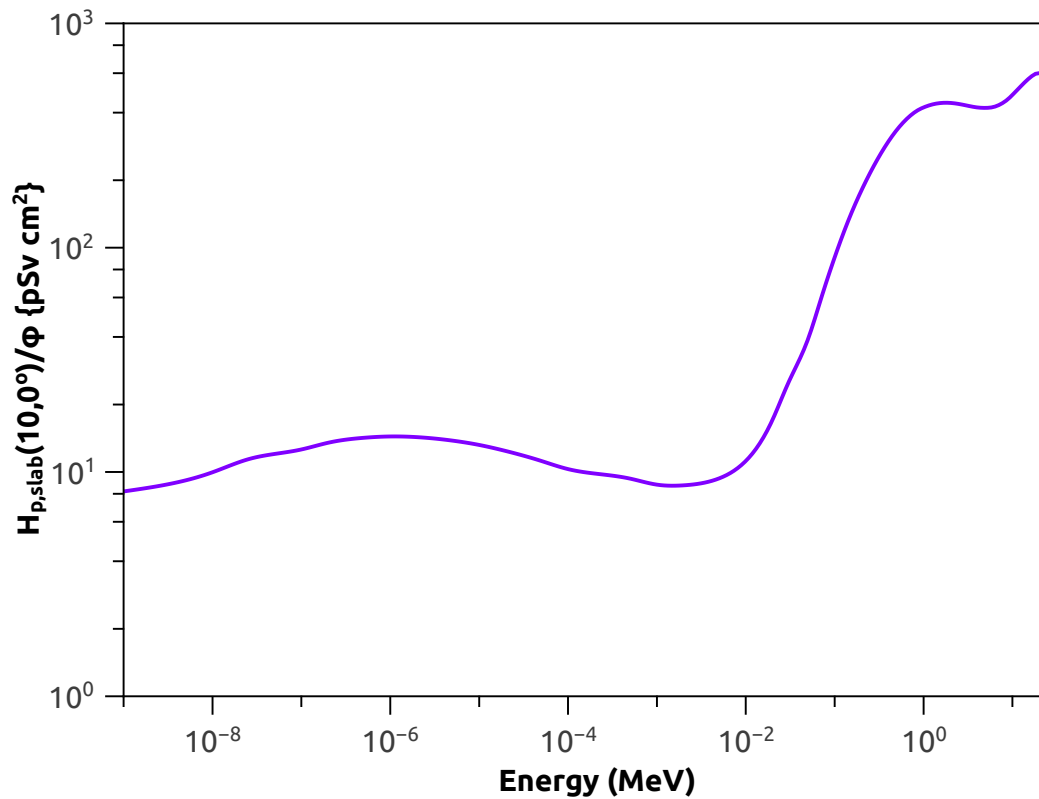


Figure 2.1: Fluence to dose conversion factors for neutrons

$H_{p,slab}(10,0^\circ)$ for neutrons with energy. $H_{p,slab}(10,0^\circ)$ is the dose deposited due to neutrons in ICRU slab phantom at a depth of 10 mm from the surface with normal incidence of neutrons.

Neutron spectrum can be measured by various techniques such as time-of-flight (TOF) technique, foil activation, pulse shape discrimination and Bonner sphere spectrometry (BSS). TOF technique of neutron spectrometry consists of measuring the neutron flight time over a known distance. The detectors are placed to record both start and termination of neutron flight. Foil activation technique is based on the observation of a radioactive product in the foil, when the neutron energy has exceeded the threshold for the nuclear reaction. The neutron spectrum is determined by comparing the measurements of several different neutron induced activities (with

different threshold energies), made by irradiating an appropriate set of target foils in the field[13].

Neutron spectrometry using Bonner sphere has several advantages and disadvantages [35]. BSS is the only spectrometer which covers a range from thermal energy to GeV, but has poor resolution. It has better gamma discrimination. BSS initially developed using active dosimeter has the additional drawback of pulse pileup and dead time effect, which is generally encountered in the high intensity and pulsed fields of radiation. To overcome these drawbacks of active dosimeters, passive dosimeters have become an obvious choice in this field. Thermoluminescent dosimeter (TLD) is usually preferred over the other passive detectors due to its high TL sensitivity, re-usability, small size and simple to process after irradiation. BSS using TLD-600 and TLD-700 pairs is well known and also well established[35]. Here, TLD-600 and TLD-700 are the trade names of $^6\text{LiF:Mg,Ti}$ and $^7\text{LiF:Mg,Ti}$. However, although $\text{CaSO}_4\text{:Dy}$ based neutron dosimeter had been developed[36], so far it has not been used for the purpose of neutron spectrometry. Polytetrafluoroethylene (PTFE) embedded $\text{CaSO}_4\text{:Dy} + ^6\text{LiF}$ based neutron dosimeter had been developed in our laboratory in the recent past for using it in the large scale routine personnel monitoring program. The enriched ^6LiF powder, which is locally available, of grain size in the range of 10 - 20 μm was mixed uniformly with $\text{CaSO}_4\text{:Dy}$ phosphor of average grain size about 40 μm along with Teflon powder (which is a binding material). In the mixture, $\text{CaSO}_4\text{:Dy}$ phosphor, ^6LiF powder and Teflon were added in weight ratio of 1:1:2(70:70:140 mg). The mixing was carried out in the presence of liquid nitrogen. After evaporation of liquid nitrogen, small pouches of required quantity of the mixture were taken and neutron discs were pressed using a hydraulic press. Subsequently, the discs were cleaned with acetone, dried and annealed at 400°C for 1 h in an air oven to make it strong and flexible. In the dosimeter, alphas produced through (n, α) reaction with ^6Li deposit their energy to $\text{CaSO}_4\text{:Dy}$ phosphor, which in turn produce TL during readout. The response of this dosimeter was found to be

about one-third of the response of TLD-600 in the fields thermal to fast neutrons. It may be noted that response of this dosimeter is energy dependent due to energy dependence of capture cross section (as shown in fig.2.2) of ⁶LiF powder (a constituent of neutron dosimeter). In this study, (1) the response matrix for CaSO₄:Dy

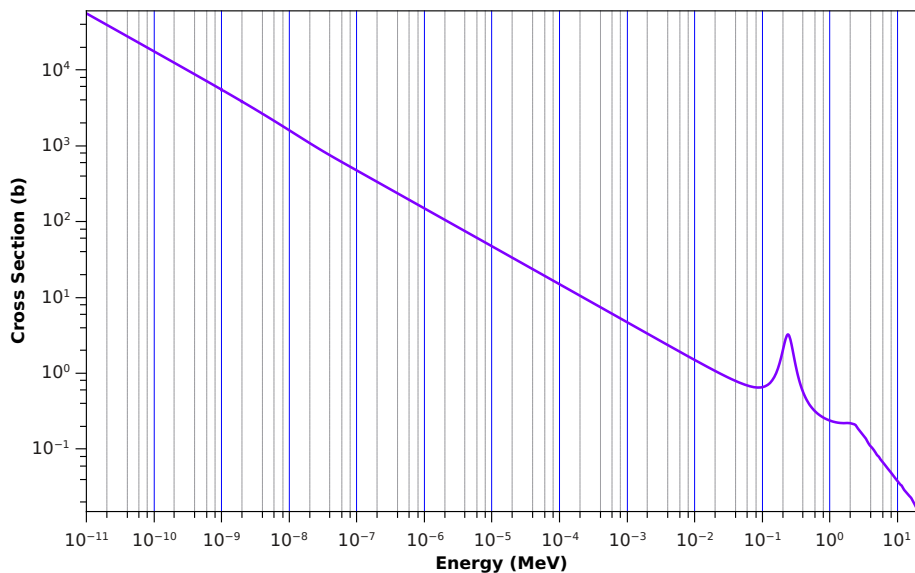


Figure 2.2: Cross Section of ⁶Li(n,α)³H reaction

+ ⁶LiF based neutron dosimeter was generated using Monte Carlo code FLUKA[24, 25] in the energy range thermal to 20 MeV for a set of eight Bonner spheres, (2) experimental response of the neutron dosimeter was measured for the above set of spheres for ²⁴¹Am-Be neutron source and (3) using FRUIT unfolding code [37], the neutron spectrum was de-convoluted and compared with well established spectrum reported in literature.

2.2 Response Matrix Calculation

Response matrix calculation in this study was carried out using Monte Carlo code FLUKA version 2008.3b. FLUKA can simulate the transport of neutron, photon, electron, positron, muons, neutrinos, protons as well as many heavy ions. For neutrons with energy lower than 20 MeV, FLUKA uses its own neutron cross section

libraries (P5 Legendre angular expansion, 260 neutron energy groups), containing more than 200 different materials. But for few isotopes like ⁶Li, neutron transport is carried out by continuous cross section in FLUKA. The geometry of simulation for the generation of response matrix consisted of Bonner spheres of varying sizes and TL dosimeter. The Bonner spheres used were modeled with high density polyethy-

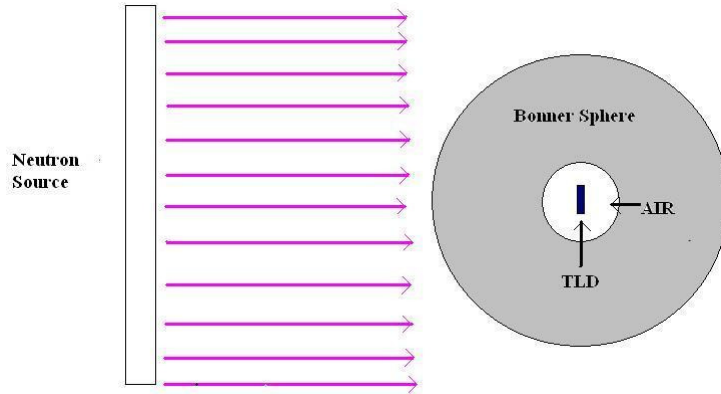


Figure 2.3: Geometry used in FLUKA simulation for generation of response matrix

lene having a density of 0.95 g/cm^3 . TL material, which is the detector part, was considered inside these spheres of varying sizes from 3 inches to 12 inches and also for bare detector (with no sphere around the detector). The size of the TLD considered was of 7.0 mm in diameter and thickness of 0.8 mm. Further, TLD inside the Bonner spheres was surrounded with an air cavity of 1.0 cm diameter. Sternheimer density correction [38] was applied for Bonner spheres of all sizes. In the simulation, neutron beam was considered to be a broad parallel beam of radius 15.5 cm placed at a distance from the Bonner spheres in vacuum. TLD was positioned in such a way inside the Bonner spheres that the circular face was perpendicular to beam direction. The geometry of the simulation is shown in fig.2.3. Response of the TLD was evaluated by finding the energy deposited by alpha particles which are generated by (n,α) reaction from ⁶Li. This was carried out using the USRBIN card in FLUKA, which evaluates the total energy deposited per unit volume normalized to per unit starting particle (here neutrons). Energy deposition contribution due to alpha particles was separated from other particle contributions by using AUXS-

CORE card of FLUKA. With increase in the size of Bonner sphere, thermal neutron fluence contributing to the TL dosimeter decreases and hence for better statistical convergence of data, variance reduction technique of importance biasing was used for Bonner spheres having diameter greater than 4 inches. Spheres were divided into annular regions and each region were assigned an importance value increasing as the neutron is moving towards the TL dosimeter. Each data point was generated by running 5 cycles of FLUKA code, where each cycle consisted of 10^7 particles. Energy deposited due to alpha particles was having an error value less than 5%. Table 2.1 shows response matrix of the neutron dosimeter based on $\text{CaSO}_4\text{:Dy}$ in

Energy (MeV)	Response (cm^2)							
	Bare	3"	4"	5"	6"	8"	10"	12"
2.5E-08	1.649E-05	7.318E-06	5.564E-06	4.513E-06	3.412E-06	1.835E-06	9.204E-07	4.856E-07
6.00E-08	1.175E-05	8.900E-06	7.114E-06	5.449E-06	4.112E-06	2.237E-06	1.135E-06	5.582E-07
1.00E-07	9.442E-06	9.759E-06	7.815E-06	6.018E-06	4.552E-06	2.457E-06	1.255E-06	6.252E-07
3.16E-07	5.643E-06	1.103E-05	9.233E-06	7.177E-06	5.418E-06	2.901E-06	1.442E-06	7.039E-07
1.00E-06	3.316E-06	1.204E-05	1.034E-05	8.056E-06	6.110E-06	3.242E-06	1.638E-06	7.873E-07
1.00E-05	1.054E-06	1.236E-05	1.175E-05	9.446E-06	7.194E-06	3.918E-06	1.985E-06	9.708E-07
1.00E-04	3.478E-07	1.142E-05	1.183E-05	1.030E-05	8.044E-06	4.367E-06	2.271E-06	1.061E-06
1.00E-03	1.102E-07	1.031E-05	1.157E-05	1.058E-05	8.689E-06	4.782E-06	2.446E-06	1.217E-06
8.15E-03	3.505E-08	8.748E-06	1.077E-05	1.077E-05	9.101E-06	5.294E-06	2.727E-06	1.396E-06
2.74E-02	2.015E-08	7.816E-06	1.056E-05	1.112E-05	9.631E-06	5.867E-06	3.046E-06	1.466E-06
7.10E-02	1.454E-08	7.472E-06	1.051E-05	1.153E-05	1.043E-05	6.634E-06	3.567E-06	1.703E-06
1.44E-01	1.664E-08	6.533E-06	1.031E-05	1.205E-05	1.144E-05	7.566E-06	4.105E-06	2.060E-06
2.50E-01	7.751E-08	5.776E-06	9.994E-06	1.242E-05	1.247E-05	8.904E-06	5.010E-06	2.552E-06
5.65E-01	9.545E-09	4.099E-06	8.832E-06	1.219E-05	1.368E-05	1.161E-05	7.438E-06	4.154E-06
1.20E+00	6.332E-09	2.747E-06	6.756E-06	1.042E-05	1.303E-05	1.369E-05	1.049E-05	7.181E-06
2.50E+00	7.410E-09	1.542E-06	4.258E-06	7.540E-06	1.032E-05	1.337E-05	1.269E-05	1.044E-05
5.00E+00	3.247E-09	8.197E-07	2.383E-06	4.641E-06	6.977E-06	1.079E-05	1.210E-05	1.169E-05
8.00E+00	2.523E-09	4.310E-07	1.411E-06	2.916E-06	4.794E-06	7.984E-06	9.578E-06	1.019E-05
1.48E+01	2.219E-09	2.135E-07	7.693E-07	1.653E-06	2.745E-06	4.986E-06	6.669E-06	7.539E-06
2.00E+01	1.246E-09	1.848E-07	5.903E-07	1.241E-06	2.106E-06	3.923E-06	5.639E-06	6.227E-06

Table 2.1: Response matrix of $\text{CaSO}_4\text{:Dy}$ based neutron dosimeters in the energy range of thermal to 20 MeV for different sizes of Bonner spheres.

the energy range of thermal to 20 MeV generated using Monte Carlo code FLUKA. Data generated by code, which is the energy deposited by alpha particles per unit fluence of neutron beam (GeV cm^2) has been converted to output of the TL dosimeter (light output) by using the conversion factor, which is described in the section below. It may be noted that response matrix plot as seen from figure 2.4 generated in this work is similar to the plot of response matrix generated for $^6\text{LiF:Mg,Ti}$ by

Carrillo et al [35]. Similarity can be attributed to the fact that the neutron detection in both the cases has been carried out by ${}^6\text{Li}$ by (n,α) reaction. Difference in absolute response can be attributed to the fact that the response of neutron detector used in present work has less sensitivity as compared to sensitivity of ${}^6\text{LiF}:\text{Mg},\text{Ti}$ for all energies of neutron. In figure 2.4, it can be seen that response of the bare TL

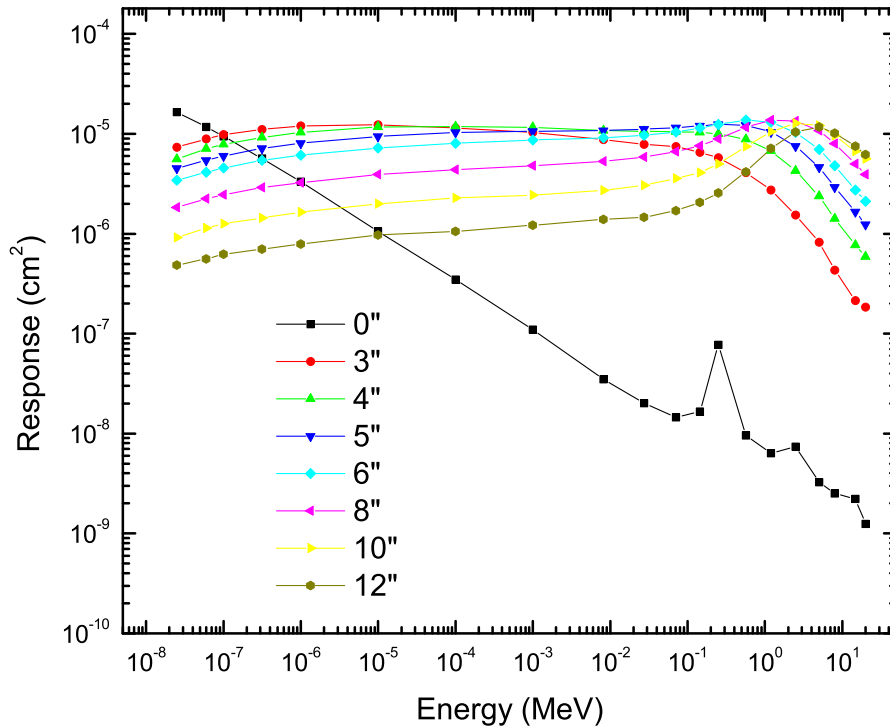


Figure 2.4: Response matrix of the $\text{CaSO}_4:\text{Dy}$ based neutron dosimeter for Bonner sphere of different sizes generated using FLUKA.

dosimeter is similar to plot of the variation of cross section with neutron energy for ${}^6\text{Li}$ (fig. 2.2). As the Bonner sphere is inserted, the response peaks at higher energy side due to generation of thermal neutrons, which contributes to TL output. With further increase in the thickness of Bonner sphere, the response shows a gradual decrease at higher energy side, as thermal neutrons generated are not able to reach the detector and contribute to TL output. It can also be seen from figure 2.4, that the response of TL detector, inside all sizes of Bonner sphere, peaks at around 1 to

10 MeV and then the response starts decreasing. One of the drawback with Bonner sphere technique, which is based on high density polythene (density 0.95 g/cm^3), is that such system is not suitable for neutron energies beyond 20 MeV.

2.3 Determination of conversion factor

The ultimate goal of response matrix is to generate output of the thermal neutron detector, which is Thermoluminescence (TL) in this case. But TL output cannot be generated with any Monte Carlo code. Hence a conversion factor was found based on the simulated response and experimental response of the TL dosimeter. Actual TL dosimeter response was generated experimentally by keeping it under different Bonner spheres, with TL dosimeter at a distance of 43.5 cm from ^{241}Am -Be neutron source. Similar response was generated through simulation and neutron energy spectrum of ^{241}Am -Be source was used from ISO report[39]. The conversion factor as described in fig 2.5 was found to be $0.528 \pm 3.0\%$. This conversion factor was multiplied with the simulated response generated using Monte Carlo code to arrive at real value of the response of the TLDs under different Bonner spheres and at different energies.

2.4 Experimental procedure

For experimental determination of net response of TL dosimeter due to neutron spectrum from ^{241}Am -Be source, TL dosimeter based on $^6\text{Li} + \text{CaSO}_4\text{:Dy}$ (neutron sensitive) having diameter 7.0 mm and thickness 0.8 mm were used. TL dosimeter based on only $\text{CaSO}_4\text{:Dy}$ (gamma sensitive) having same dimension were used for gamma response. This TL dosimeter was having $\text{CaSO}_4\text{:Dy}$ powder mixed with Teflon (Polytetrafluoro ethylene) in the ratio of 1:3 (70:210 mg). Both the TL dosimeters were having similar response to photons. Five pairs of neutron and gamma sensitive TLDs were sealed in plastic pouches having thickness less than $0.5 \mu\text{m}$ to avoid

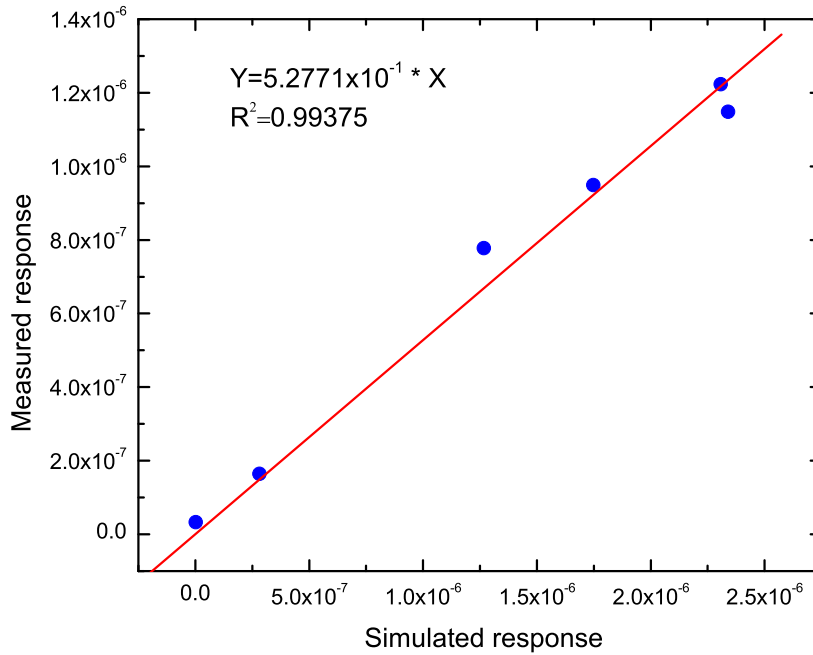


Figure 2.5: Conversion factor based on response of TLDs generated using Monte Carlo simulation code FLUKA and by experimental methods with ²⁴¹Am–Be neutron source under different Bonner spheres

overlapping during exposure. TL dosimeter pairs kept inside different high density polythene spheres (Bonner spheres) having density 0.95 g/cm³ with different diameter were exposed by keeping them along the axis of the source at a distance of 43.5 cm for 40.67 hours. Spheres having diameter 3 inches, 5 inches, 6 inches, 8 inches and 10 inches were used along with the bare TL dosimeter. Calibration of both the types of TL dosimeters to photons were carried out by exposing TL dosimeters to a well collimated beam of ¹³⁷Cs gamma rays under charge particle equilibrium to an air-kerma value of 30.0 ± 0.6 mGy. Charge particle equilibrium was achieved by exposing the dosimeters under 4.0 mm thick perspex plates. Neutron source was always kept under 2.0 mm thick Pb container to cutoff 60 keV gamma rays and have better signal to noise ratio. The neutron multiplications due to inelastic reactions with Pb are assumed to be negligible as neutron energy is not sufficient to initiate any (n,xn') reactions. TL dosimeters were read after a gap of 7-8 days,

on a TLD reader having PMT (Photo Multiplier Tube) of S-11 response. A gap of 7-8 days were taken, so that satellite TL peak at 120°C fades away and the output is only due to contribution from the dosimetric peak at 240°C. TL reader was set at a heating rate of 5°C/s and the maximum temperature was set at 290°C. Photon contribution was subtracted from the neutron sensitive TL dosimeter by using the following formulae.

$$R_1^n = R_1^{n+\gamma} - k \times R_2^\gamma \quad (2.1)$$

where R_1^n is net response of the neutron sensitive TLD, $R_1^{n+\gamma}$ is total response of the neutron sensitive TLD to both photons and neutrons and R_2^γ is photon response of the gamma sensitive TLD. The factor 'k' in equation 2.1 was generated by exposing both types of TLDs to ¹³⁷Cs under charged particle equilibrium.

$$k = \frac{R_1^\gamma}{R_2^\gamma} \quad (2.2)$$

Here R_1^γ is gamma response of the neutron sensitive TLD and R_2^γ is gamma response of the gamma sensitive TLD. The value of 'k' here was 0.82 for this system. The

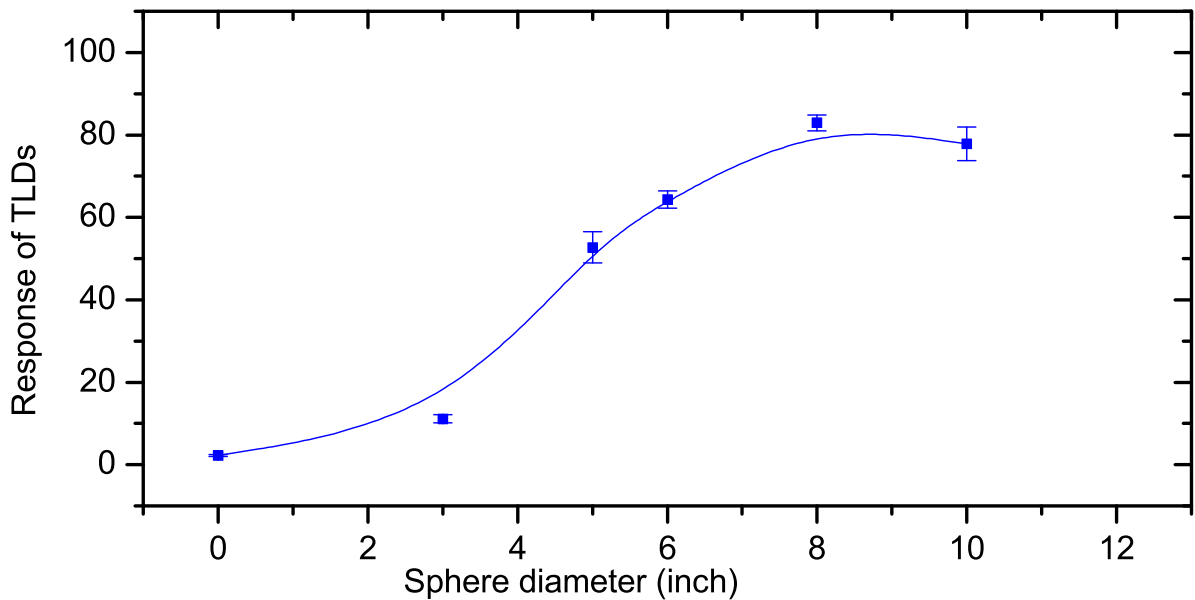


Figure 2.6: Plot of net neutron response of TL dosimeter determined experimentally

figure 2.6 shows the experimentally determined net neutron response of neutron sensitive TL dosimeters to ²⁴¹Am-Be source when exposed under Bonner spheres of different sizes. It can again be seen from the figure that there is a decreasing trend in response of the TL dosimeter beyond 8 inches Bonner sphere. The thermal neutrons generated by multiple scattering in HDPE are not able to reach the detector. Further increase in thickness of Bonner sphere will lead to decrease in the output of TL dosimeter.

2.5 Parameterization of response function

Efforts have been made by several authors [40, 35] to arrive at analytical expression for the Bonner sphere response function. In this work, a similar effort has been carried out to arrive at the analytical expression for response function of the Bonner sphere with the present neutron detector. Response function generated for different neutron energies (Table 2.1) were plotted as a function of mass of Bonner sphere for a particular neutron energy and fitted with a 3rd order polynomial function given in equation 2.3.

$$R(m_i, E) = A_1(E) + A_2(E)m_i + A_3(E)m_i^2 + A_4(E)m_i^3 \quad (2.3)$$

where $R(m_i, E)$ is the response function, m_i is mass of i^{th} sphere in kg, E is neutron energy in MeV and A_1 , A_2 , A_3 and A_4 are fitting parameters determined by fitting method adopted. Table 2.2 will be useful to arrive at the response function at a particular neutron energy for sizes other than those used in the present work for this neutron dosimeter. Figure 2.7 shows fitted response of the neutron dosimeter for energies such as 0.1 eV, 10 eV, 1.0 keV, 144.0 keV, 2.50 keV and 14.8 MeV. The response shows an increase at higher masses of the sphere with increase in the neutron energy.

Energy (MeV)	A ₁	A ₂	A ₃	A ₄	Regression coefficient
2.50E-08	4.4433E-06	-4.4760E-06	1.6111E-07	6.1829E-07	0.9999
6.00E-08	5.5099E-06	-5.6688E-06	-4.9794E-08	1.0781E-06	0.9999
1.00E-07	6.0772E-06	-6.2348E-06	-7.1168E-08	1.1961E-06	0.9999
3.16E-07	7.2610E-06	-7.2065E-06	-9.6215E-07	1.9887E-06	0.9999
1.00E-06	8.1582E-06	-7.9300E-06	-1.4914E-06	2.4713E-06	0.9999
1.00E-05	9.5901E-06	-8.4568E-06	-3.6290E-06	3.9370E-06	0.9992
1.00E-04	1.0254E-05	-7.5868E-06	-5.7704E-06	4.7424E-06	0.9996
1.00E-03	1.0574E-05	-6.5885E-06	-7.3289E-06	5.1975E-06	0.9995
8.15E-03	1.0585E-05	-4.9193E-06	-8.6121E-06	5.1135E-06	0.9968
2.74E-02	1.0856E-05	-3.7250E-06	-9.6907E-06	4.9964E-06	0.9965
7.10E-02	1.1231E-05	-2.5307E-06	-1.0094E-05	4.3117E-06	0.9924
1.44E-01	1.1765E-05	-9.5762E-06	-1.1405E-05	4.0852E-06	0.9858
2.50E-01	1.2148E-05	1.2516E-06	-1.1687E-05	2.6658E-06	0.9796
5.65E-01	1.2081E-05	6.1205E-06	-1.0427E-05	-1.0584E-06	0.9787
1.20E+00	1.0401E-05	1.0496E-05	-5.6149E-06	-5.4074E-06	0.9887
2.50E+00	7.4914E-06	1.2018E-05	-1.6603E-06	-70977E-06	0.9990
5.00E+00	4.6324E-06	9.9760E-06	2.9365E-06	-5.4209E-06	0.9990
8.00E+00	2.9710E-06	7.2876E-06	3.0751E-06	-3.4155E-06	0.9992
1.48E+01	1.6508E-06	4.4387E-06	2.4821E-06	-1.5959E-06	0.9989
2.00E+01	1.2334E-06	3.5732E-06	2.2733E-06	-1.3123E-06	0.9963

Table 2.2: Parameters A₁, A₂, A₃ and A₄ of the 3rd order polynomial function representing the best fit of FLUKA calculated response of neutron dosimeter as a function of sphere mass.

2.6 Spectrum unfolding

Spectrum unfolding has been carried out using FRUIT code[37] version 3.0. The response of a thermal neutron dosimeter inside a Bonner Sphere to a given neutron spectrum is given by the first order Fredholm integral equation of first kind as shown in equation 2.4.

$$R_i^n = \int_{E_{min}}^{E_{max}} S_i(E)\phi(E) dx \quad (2.4)$$

where R_i^n is net neutron response obtained from the TLDs when exposed under i^{th} Bonner sphere, $S_i(E)$ is the response function of i^{th} sphere (cm²) and $\phi(E)$ is the neutron spectral fluence(cm²). Equation 2.4 reduces to matrix equation for solution

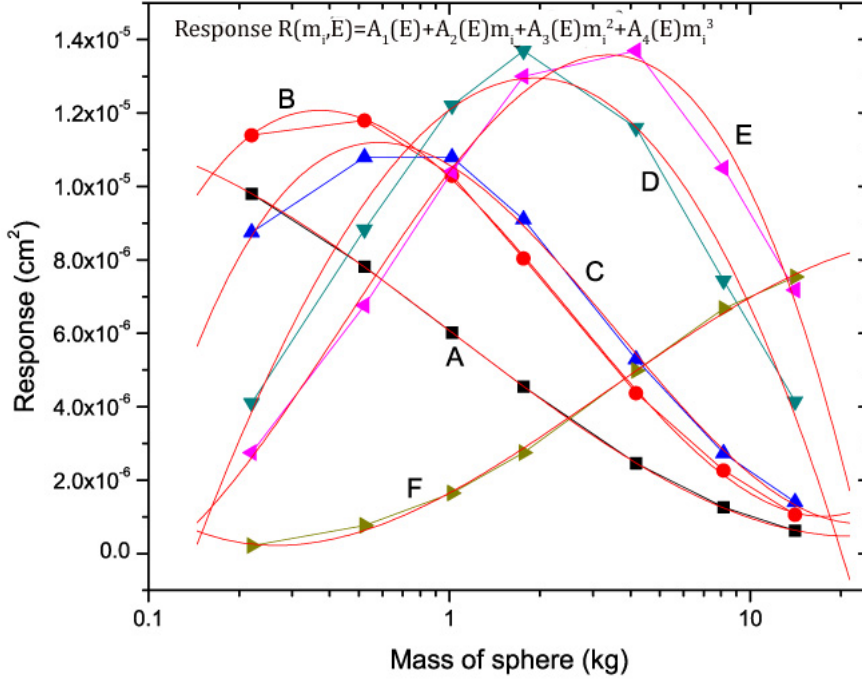


Figure 2.7: Plot of fitted curve of the response of neutron dosimeter vs sphere mass with 3rd order polynomial at energies A: 0.1 eV, B:10 eV, C:1 keV, D:144 keV, E:2.50 MeV and F:14.8 MeV

given in equation 2.5.

$$R_i^n = \sum_{g=1}^G S_{i,g} \phi_g \quad (2.5)$$

where ϕ_g is measure of the total neutron fluence between upper bound energy E_{g+1} and lower bound energy E_g , $S_{i,g}$ is the multi group form of i^{th} detector response. It is desirable to produce an output spectrum with many energy groups. However, the system of equations, namely the number of unknown energy groups and number of equations (number of spheres) are such that the matrix equation is under-determined and there is no unique solution to this equation because total number of energy groups is typically larger than the number of Bonner spheres used. Since the system is under-determined, an iterative solution process is sought starting from an initial hypothesis. There are a number of computer codes available for solving this system of equations. Some of the well established computational codes such

as BUNKI [41], MAXED [42], GRAVEL [43], GA [44, 45], Frascati Unfolding Interactive Tool (FRUIT) [37], MITOM [46], etc., are used frequently to unfold the spectral information from these detector responses. Some of these methods require guess spectrum or a priori information to start the iteration procedure, while others model/calculate the starting spectrum which is very useful when a priori information is not sufficient.

Fruit is a parametric code written using Lab-View software. Here, user do not have to feed the initial guess spectrum for unfolding, which is one of the advantage of this code. The type of “radiation environment” is selected in the code by using a check-box window, among the following options:

- fission-like fields, such as those found in vicinity of nuclear reactors or fuel elements;
- radionuclide neutron sources;
- evaporation-based field, such as those found in medical LINACs or PET cyclotrons;
- high-energy electron fields;
- high-energy hadron accelerators;
- Gaussian peak;
- user-defined (in this case a parameter file is required)

A neutron spectrum in the code is described by linear superposition of the four components given in equation 2.6.

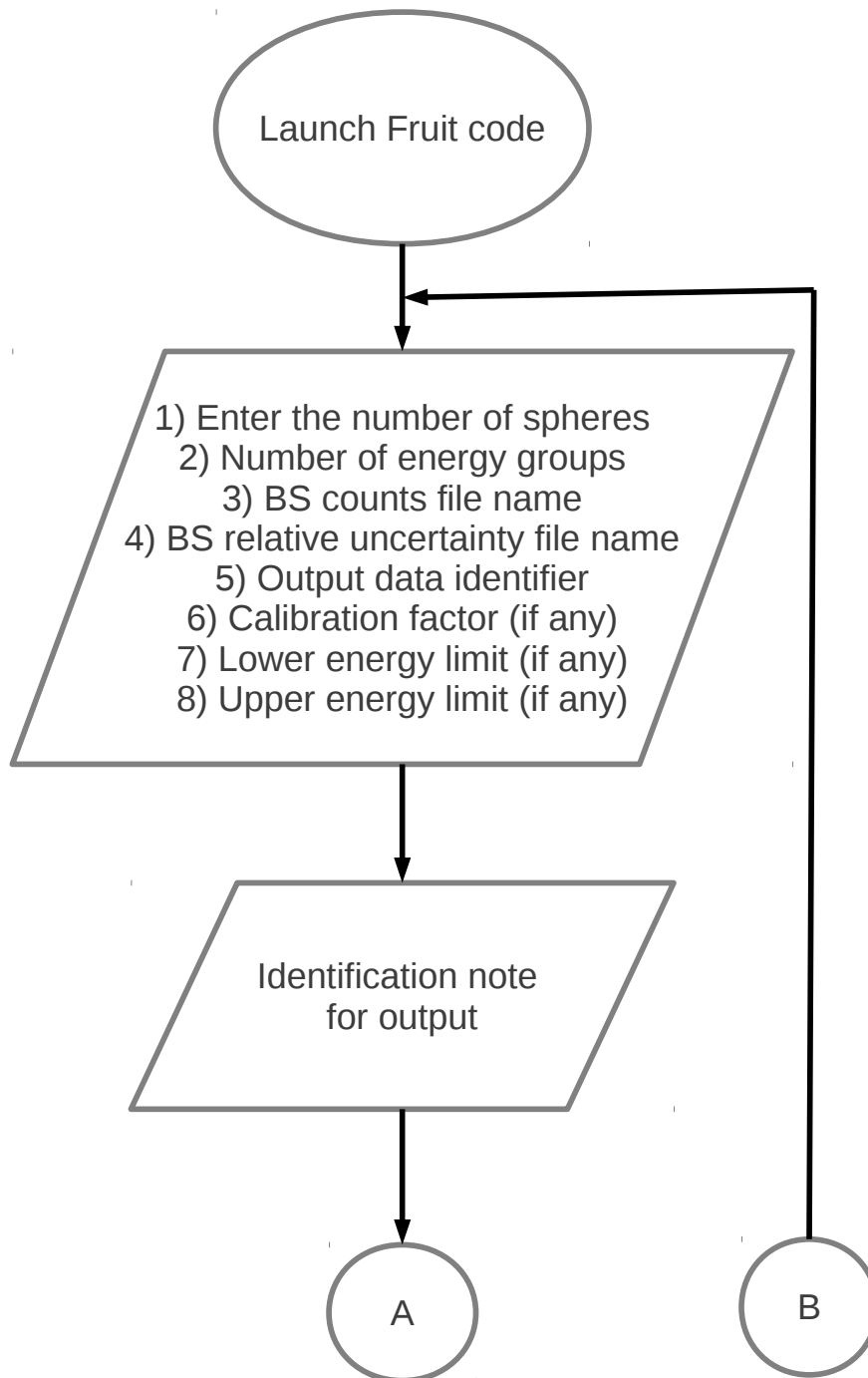
$$\phi(E) = P_{th}\phi_{th}(E) + P_e\phi_e(E) + P_f\phi_f(E) + P_{hi}\phi_{hi}(E) \quad (2.6)$$

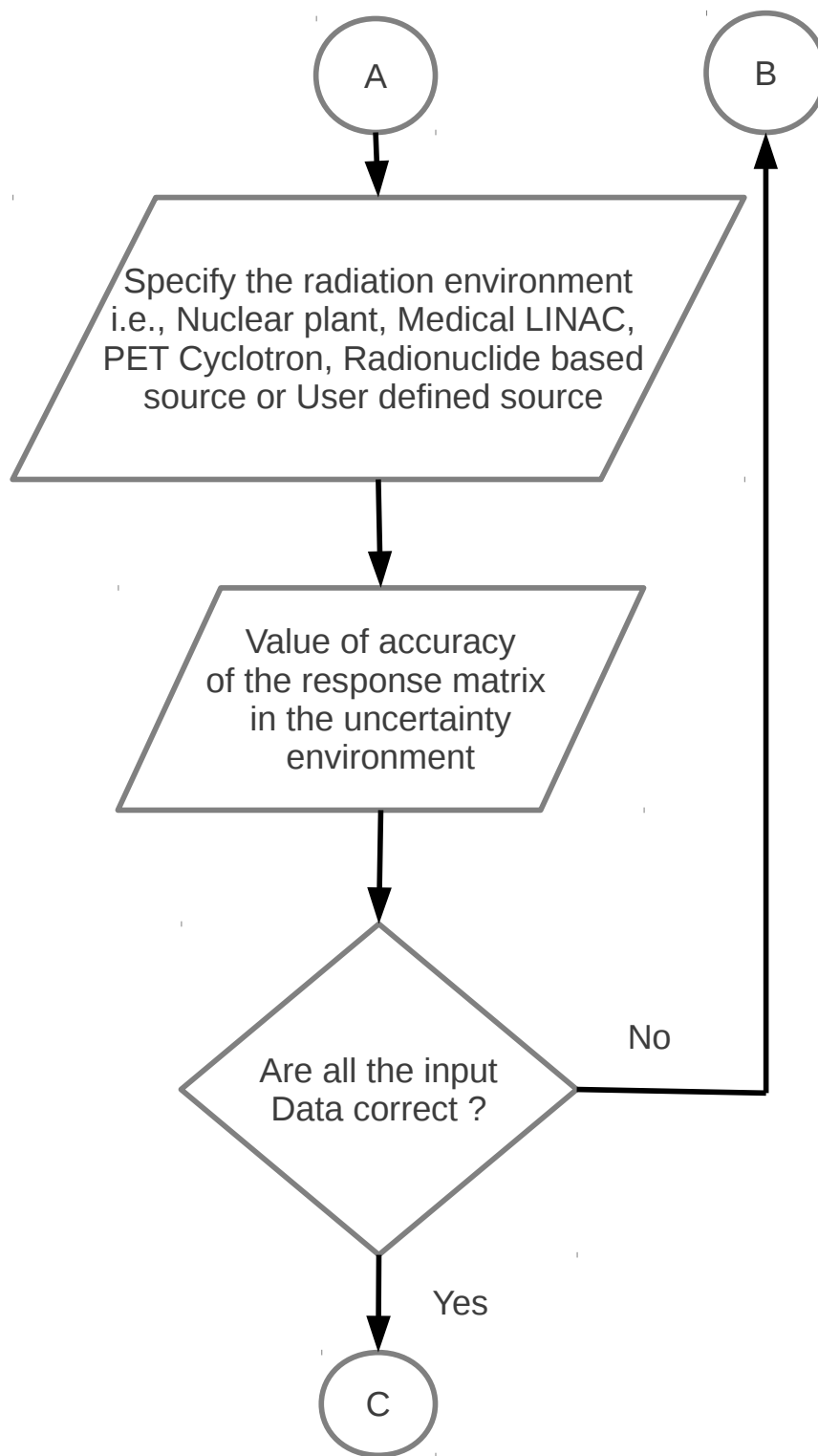
where $\phi_{th}(E)$ is thermal Maxwellian component, $\phi_e(E)$ the epithermal one, $\phi_f(E)$ is fast component and $\phi_{hi}(E)$ is high energy component. P_{th} , P_e , P_f and P_{hi} rep-

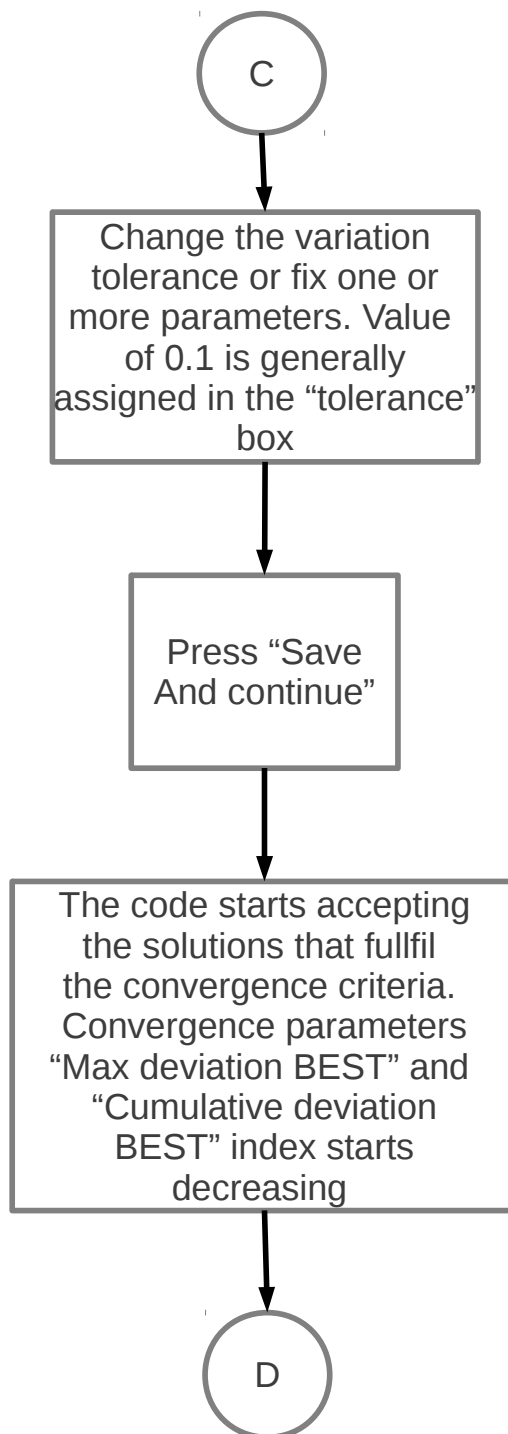
resents the fraction of thermal, epithermal, fast and high energy neutrons, respectively. Only three of them are independent as the sum should be equal to unity as a normalization constraint. All unfolding codes are based on iterative convergence techniques. In MAXED and GRAVEL unfolding codes, final spectrum is derived by perturbing the “initial guess” spectrum, which is required from the user. In parametric codes like FRUIT, there is a unique correspondence between an array of parameters and related neutron spectrum. These types of codes uses Monte Carlo technique to generate a large number of parameter arrays, and for each of them, a neutron spectrum is generated. The measured readings obtained from experimental technique is compared with calculated readings and a likelihood indicator is derived. If the indicator is small enough, then those parameter values are selected and their average, or the limit of their convergent succession, is regarded as best estimation of the parameter array. The solution spectrum is generated from this final array. The “robust convergence theory” [47] was modified and adapted in the FRUIT code to reduce the influence of initial hypothesis on the result and speed up convergence. The steps involved in running the FRUIT code[48] is shown in figure 2.8. For running FRUIT code, the user needs to make some ascii files such as “Ecentrale.txt” which have energy binning in units of MeV in a single column format, “deltaE.txt” should have the width of each energy bin in units of MeV. The response function needs to be specified in single column format for each sphere, in energy binning defined by “Ecentrale.txt”. The sphere counts and related uncertainties have to be provided in separate text files with the usual format. The response function of each sphere in units of cm^2 , in the energy binning provided in the “Ecentrale.txt”, should have the name in the format of “Sphere-*nn*.txt”, where “*nn*” specifies the number of the spheres (such as 01, 02, etc). Experimental readings of the Bonner sphere, with any arbitrary name and ascii text file format should have the number of lines equal to the number of experimental readings of Bonner spheres. Another file with arbitrary name can have the uncertainty values of experimental

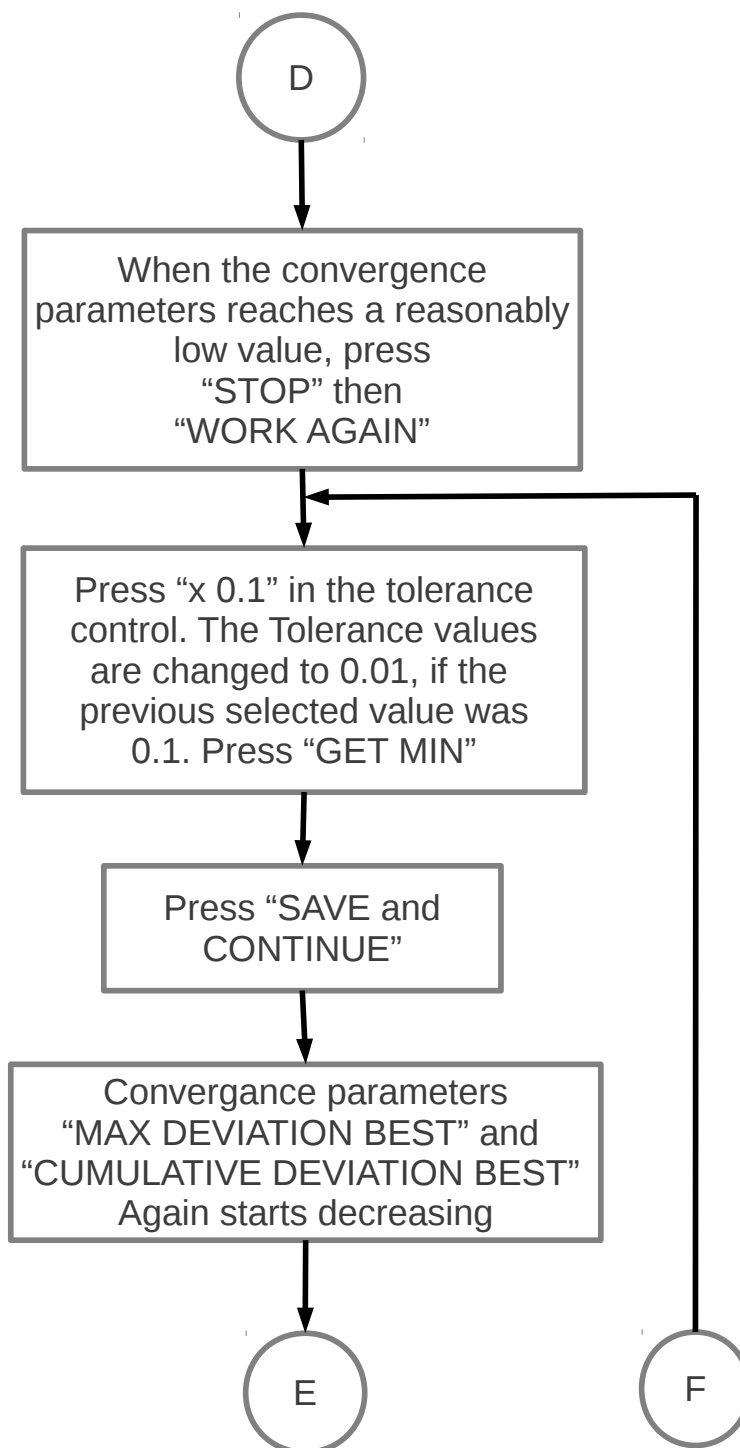
readings. Text used in the “Output data identifier” window will be used as the name of the output file of the FRUIT code. It generates three types of output files. The first one is the summary file, which contains the details of all input filenames, lower and upper energy cutoff values (if any), calibration factor (if any) used, experimental values of the sphere counts used for unfolding, relative uncertainty in the experimental values, total fluence in the units of cm² along with the uncertainty value, unfolded spectrum and the ambient dose equivalent H*[10] values in units of μSv if used during unfolding. The spectrum file contains only the de-convoluted spectrum of neutrons. The parameter file contains the input values of the experimental data of BSS sphere counts used for unfolding.

Figure 2.9 shows the deconvoluted neutron spectrum from ²⁴¹Am-Be source, which has been compared with standard spectrum obtained from IAEA Technical Report Series No. 403[49]. Figure shows a good agreement between the two neutron spectrums. The difference in the spreading of peak and peak heights with respect to IAEA spectrum could be attributed to the inherent error associated with response matrix calculations and the unfolding method.









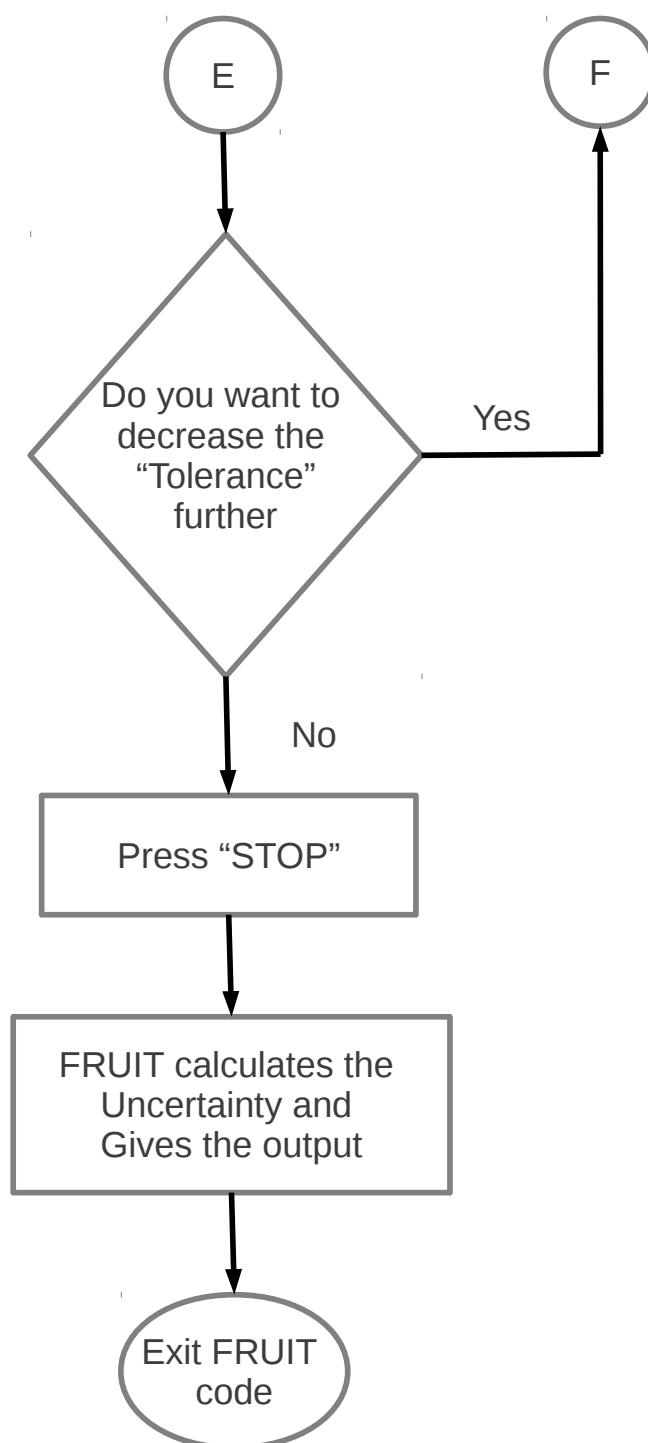


Figure 2.8: Flow Chart for the operation of FRUIT code (version 3.0)

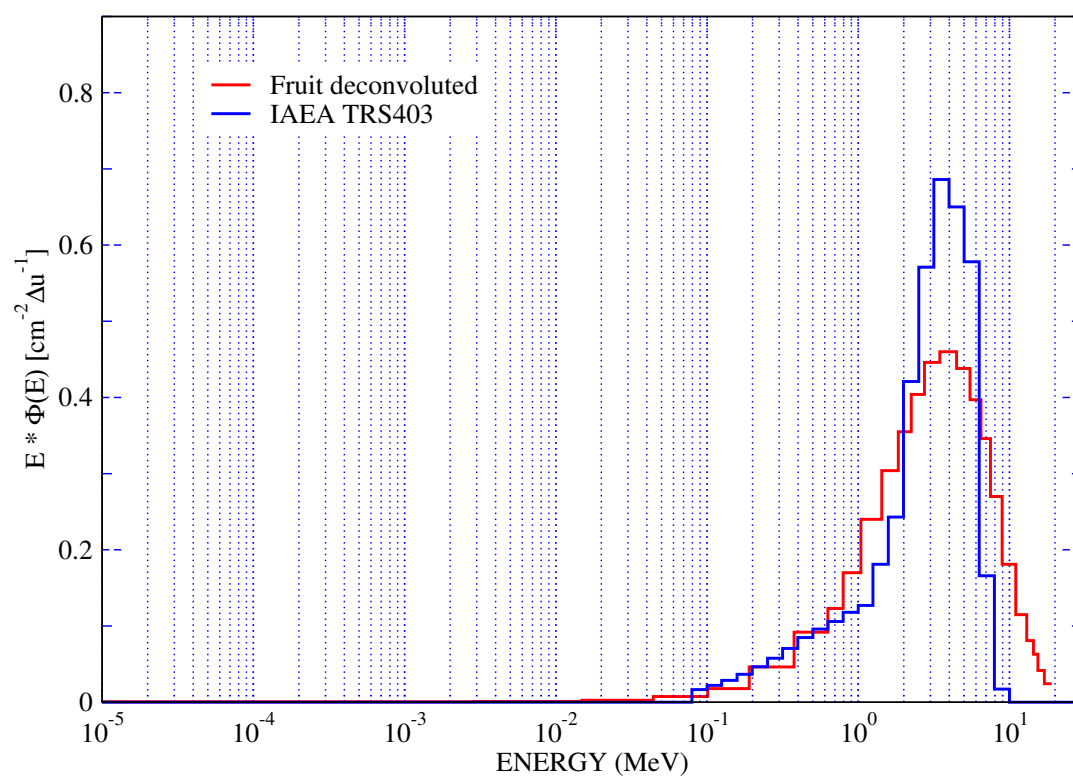


Figure 2.9: Deconvoluted neutron spectrum along with standard spectrum from IAEA TRS 403.

Chapter 3

Characterization of LFGNM

3.1 Introduction

Lead Free Gulmarg Neutron Monitor (LFGNM) is an instrument situated at Gulmarg, India, which is responsible for the intensity measurement of atmospheric secondary neutrons produced due to the interaction of primary cosmic rays with Earth's atmosphere. This detector is operated continuously 24 × 7. The Lead-Free Gulmarg Neutron Monitor[16] comprises of an assembly of BF₃ proportional counter tubes sandwiched in between rectangular paraffin wax moderator-reflector blocks. It comprises of an array of 21 cylindrical BF₃ counters made of thin walled 0.05 cm thick brass tubes each measuring 87 cm in active length and 3.8 cm in diameter. The central anode wire is 25 μm thick. The counters are filled at a pressure of 450 torr. These counters are laid in the form of an array (1 x 21) spaced 15 cm from each other over 28 cm thick paraffin wax reflector blocks covering a total area of 3 x 10⁴ cm². The counter array is also covered on top with 8 cm thick rectangular paraffin wax moderator block array (11 x 2) measuring 30 cm in breadth and 45 cm in length. Empty space between adjacent counters is occupied by air. Figure 3.1 shows the construction of LFGNM with moderator, reflector and the detector assembly. The LFGNM rests on a low Z wooden floor 8.0 meters above the ground

level to avoid snow moderating effects, a steep roof with an inclination of 70° is also provided above the LFGNM setup to avoid accumulation of snow overhead. Figure 3.2 shows photograph of the setup of LFGNM. The BF_3 counters are arranged to

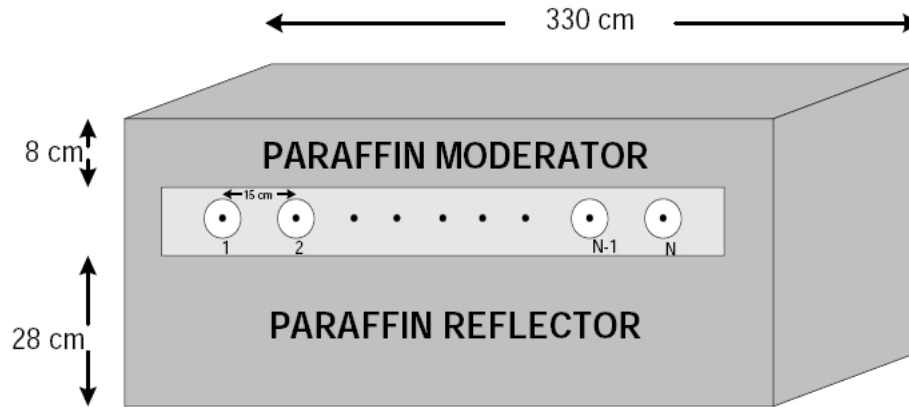


Figure 3.1: Construction of LFGNM with BF_3 detectors



Figure 3.2: Photograph of LFGNM with BF_3 detectors

form three independent counting channels each comprising of seven tubes in the

actual setup. The B^{10} enrichment in BF_3 gas is $\sim 96\%$ thereby enhancing thermal neutron capture probability on B^{10} . Neutron absorption by B^{10} nucleus is generally followed by the emission of charged particles (helium and lithium) which are detected by depositing (part of) their energy in the gas and creating a charge cloud in the stopping gas. The reaction cross section of B^{10} nuclei with neutron is shown in figure 3.3. The equations 3.1 below describe the reaction of a neutron with B^{10} .

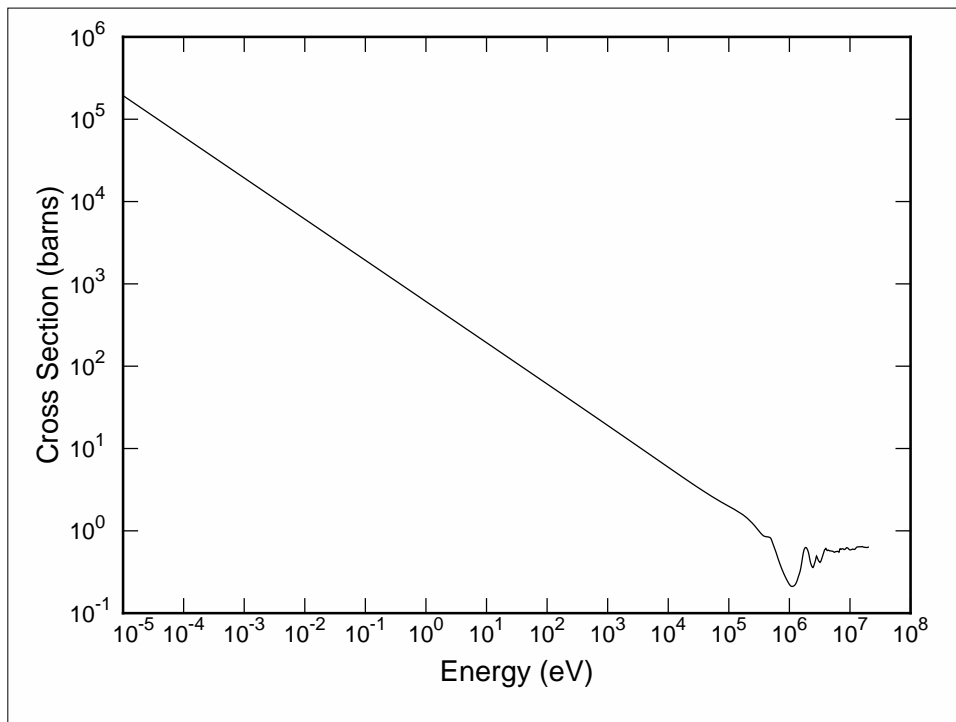
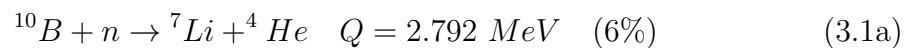


Figure 3.3: Variation of reaction cross section of B^{10} with neutron energy

The reaction can proceed in two ways. In the first reaction Li nucleus is produced in ground state, and in the second reaction Li is in an excited state and then falls into the ground state, emitting a gamma ray of 0.482 MeV.



The energy of the alpha particle can be found using the definition of Q-value of the reaction and neglecting the neutron energy (usually thermal).

From the conservation of Kinetic Energy:

$$\frac{1}{2}m_{\gamma Li^*}v_{\gamma Li^*}^2 + \frac{1}{2}m_{\alpha}v_{\alpha}^2 = Q \quad (2.310 \text{ MeV}) \quad (3.2a)$$

From the conservation of momentum:

$$m_{\gamma Li^*}v_{\gamma Li^*} = m_{\alpha}v_{\alpha} \quad (3.2b)$$

$$v_{\alpha} = \frac{m_{\gamma Li^*}v_{\gamma Li^*}}{m_{\alpha}} \quad (3.2c)$$

Substituting the value of v_{α} in equation 3.2(a), we get the energy of α as:

$$E_{\gamma Li^*} = \frac{Qm_{\alpha}}{m_{\gamma Li^*} + m_{\alpha}} = 0.84 \text{ MeV} \quad (3.2d)$$

$$E_{\alpha} = Q - E_{\gamma Li^*} = 1.47 \text{ MeV} \quad (3.2e)$$

3.2 Simulation with Monte Carlo code

Monte Carlo simulation of LFGNM was carried out with FLUKA[24, 25]. The use of FLUKA Monte Carlo code has been done earlier for the simulation of these kinds of detectors[50, 51]. The following characterization of LFGNM has been carried out using the Monte Carlo code:

1. Sensitivity to upper moderator thickness
2. Energy response of LFGNM
3. Lead Test of LFGNM
4. Cadmium Test of LFGNM

5. Angular response of LFGNM

3.2.1 Geometry of LFGNM simulation

An accurate geometrical modeling of the detector setup as far as possible is an important step for successful simulation. Geometrical representation for the paraffin wax $(C_2H_4)_n$ moderator / reflector and for the BF_3 counters was realized by using Rectangular Parallelepiped (RPP) and Right Circular Cylinder (RCC) geometry card options respectively available in FLUKA code. Chemical compositions of materials with their mass density and stoichiometry used for the simulation are listed in table 3.1. Natural isotopic abundances were used for all the elements, except Boron. BF_3 gas density required as input data for the simulation is calculated as follows: Each detector tube with effective volume of 986.7 cm^3 is filled to a pressure of 450 torr. From the gas composition ratios of 24% ^{10}B , 1% ^{11}B and 75% of F, the BF_3 gas molecular weight inside the tube was found to be equal to 67.82. Then, using ideal gas law the density of BF_3 gas is calculated at ambient room temperature of $\sim 296 \text{ K}$ [52]. It is found to be equal to $\sim 0.001643 \text{ gcm}^{-3}$.

Material name	Density (g/cm^3)	Composition, mass fraction
Paraffin Wax	0.93	$(C_2H_4)_n$
Air	0.0012048	N:75.53 O:23.18 Ar:1.28
Brass	8.52	Cu:70 Zu:30
Boron-triflouride	0.001643	BF_3 , ^{10}B :96, ^{11}B :4

Table 3.1: Chemical compositions of materials used in FLUKA simulation

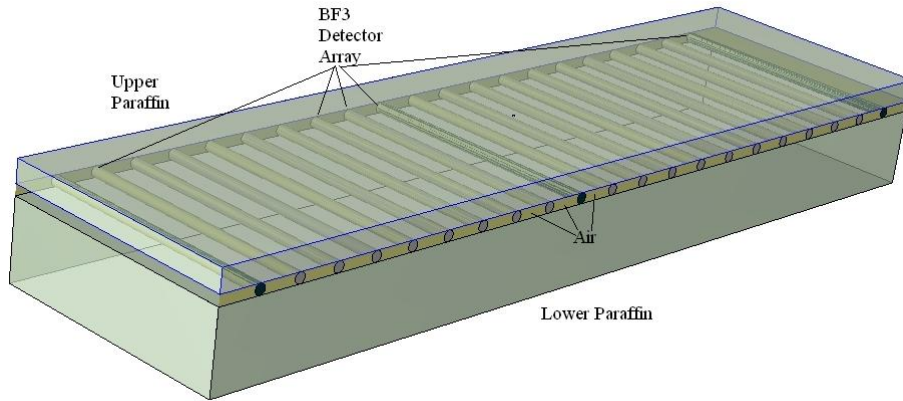


Figure 3.4: Input geometry of LFGNM showing all the 21 BF_3 detectors array.

3.3 Sensitivity to upper moderator thickness

3.3.1 Calculation with Monte Carlo code FLUKA

The simulation for the study of sensitivity of LFGNM to upper paraffin wax moderator thickness was carried out using a isotropic neutron source from a Pu- α -Be neutron source. Pu- α -Be neutron source is having an average energy of 4.5 MeV. Pu- α -Be neutron source spectrum was taken from IAEA technical report series no: TRS-403 [49]. In the simulation, neutrons emitted from a Pu- α -Be source were followed on entering paraffin wax moderator covering an ensemble of seven BF_3 tubes (i.e. one channel) placed on a fixed 28 cm paraffin wax reflector. The point isotropic source was placed at a distance of 50 cm from the front face of base plane of the paraffin wax moderator for all simulation runs. The upper paraffin wax moderator thickness was varied from zero (bare) to 48 cm in steps of 2 cm for each run respectively. The estimate of the number of (n,α) type nuclear reactions inside BF_3 tube volume being the goal of Simulation. The relationship between the upper paraffin wax moderator thickness and count rate was then obtained by tallying the number of neutron interactions of (n,α) type with BF_3 per unit neutron fluence from the residual nuclei yield using the RESNUCLEi FLUKA Card option available in the code. Each data was generated by running five cycles with 10^7 neutron histories in

each cycle. The overall statistics is nearly $\pm 1\%$.

3.3.2 Experiment

The experiment for the sensitivity of LFGNM to upper paraffin wax moderator thickness was carried out by observing the number of neutrons detected in each seven counter channel of LFGNM in response to the number of neutrons emitted from a 42 mCi Pu- α -Be neutron source having neutron fluence of nearly 7.5×10^4 n/s. Paraffin wax slabs of 0 to 48 cm thicknesses were used to cover the bare BF₃ counters. The source to upper surface of the paraffin wax slab distance was maintained at 50 cm for all the measurements. The count rate was recorded for each corresponding slab thickness. Finally the relation between net count rate of each seven counter channel and moderator thickness was obtained and recorded.

Figure 3.5 shows the variation of count rate of LFGNM with the thickness of upper paraffin wax as measured experimentally and by simulation. It shows a initial increase in the count rate with the slab thickness, and a maxima at 6.0 cm thickness of the slab. With the increase of the slab thickness, more number of neutrons lose their kinetic energy, as paraffin wax is having high Hydrogen content and the net contribution of thermal neutron increases. As ¹⁰B is having larger cross section for thermal neutrons, the output of LFGNM increases. After 6.0 cm thickness, the output decreases due to the attenuation of thermal neutrons in the upper paraffin wax. The output of LFGNM has been found to saturate after 24 cm of upper paraffin thickness for the experimental data, and after 32 cm in simulation data.

3.4 Energy response of LFGNM

Energy response of any detector is very important for having meaningful and understanding the output generated by it. Although, ideally any radiation detector should be energy independent, but all detectors used for radiation detection are

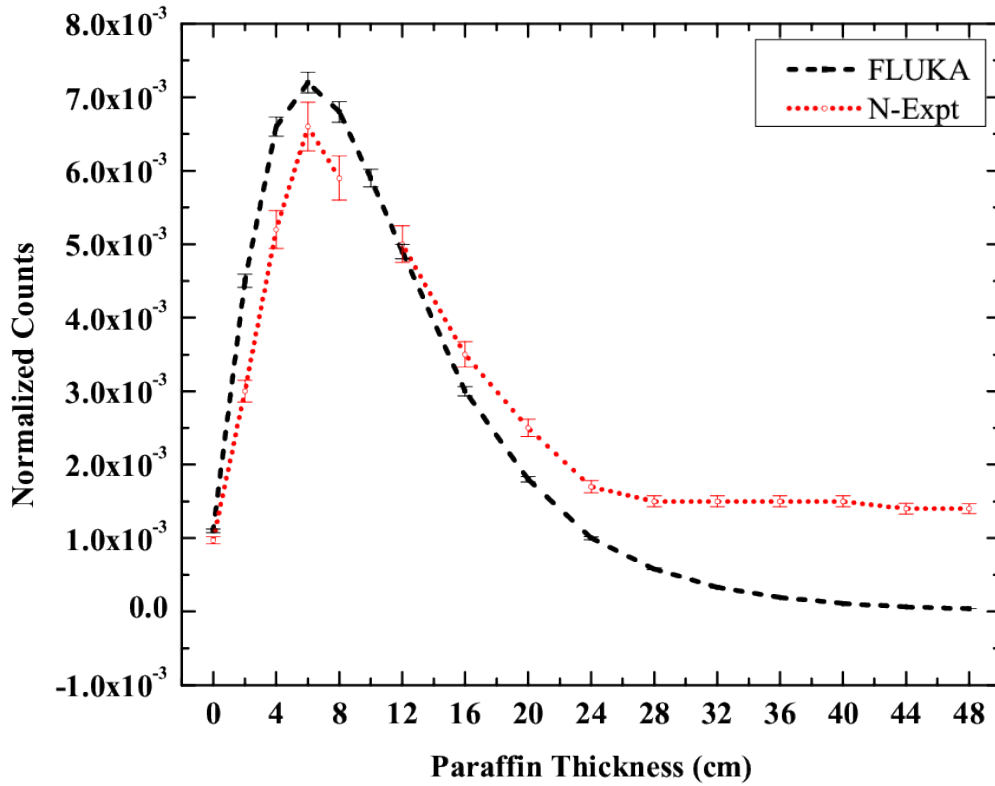


Figure 3.5: Variation of count rate of LFGNM with upper paraffin wax thickness as measured experimentally and by simulation

energy dependent. Energy dependence of LFGNM arises due to inherent nature of ^{10}B , whose cross section varies with the energy of the neutrons. This study can be very well carried out with Monte Carlo simulations as we can vary the initial energy of the neutron beams in small steps over a wide domain, which is seldom available experimentally. Moreover, but for the few energies, most of the neutron beams available experimentally are not fully monoenergetic, but quasi-monoenergetic. These quasi-monoenergetic beams are available by bombarding low- Z targets (D , T , ^7Li) with light ions (p , d) accelerated with Van-de-Graaff (VdG) accelerators or cyclotrons[53]. Due to the effects of finite target thickness, neutron scattering in the target surroundings and the finite detector size as well as breakup reactions at higher projectile energies the neutron fields obtained are only quasi-monoenergetic with a

high-energy peak of finite width and a low-energy continuum.

3.4.1 Simulation with FLUKA

Energy response calculation for LFGNM has been carried out with Monte Carlo code FLUKA. LFGNM has been considered with 8 cm thick Paraffin moderator above the BF_3 detector, which itself has been kept above 28 cm Paraffin reflector. A neutron source, in the energy range of 10^{-11} MeV to 10^4 MeV, at a distance of 50 cm above the upper Paraffin moderator has been taken. It is a planar neutron source, having area same as that of the upper Paraffin. RESNUCLE card of FLUKA has been used to score the total number of alpha particles generated in the active region of BF_3 detector, per unit incident neutron particle. Statistical error has been calculated for five cycles of run, each with 10^7 histories. In the energy range of this study, the statistical error obtained were better than $\pm 2\%$. It can be seen from the figure 3.6,

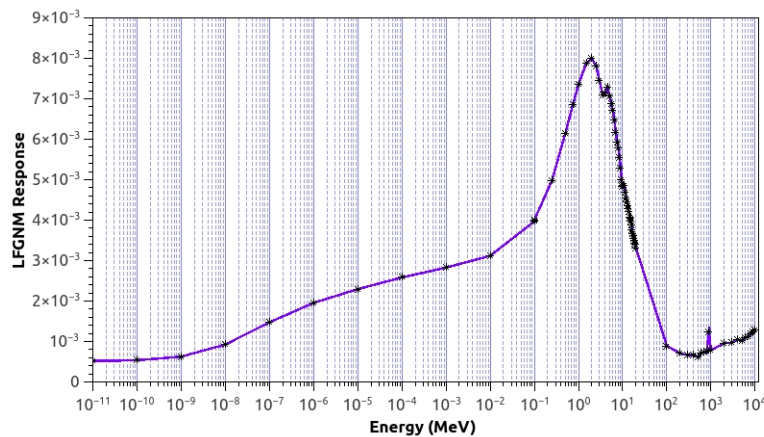


Figure 3.6: Energy response of LFGNM evaluated using Monte Carlo code FLUKA

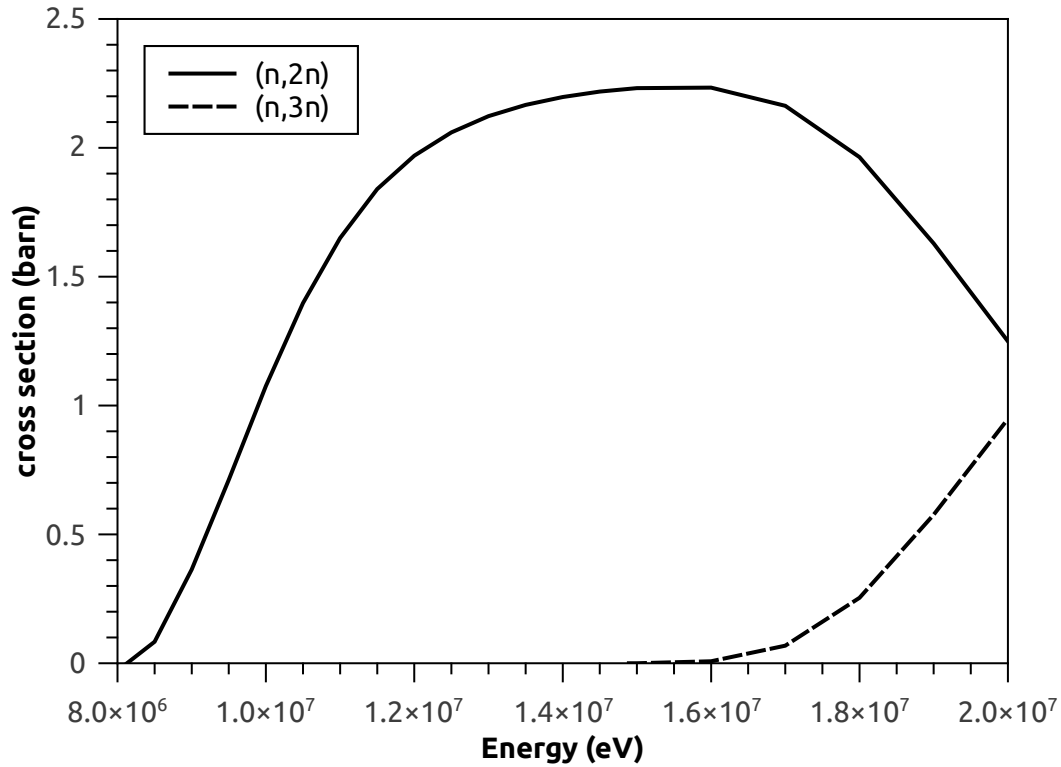
the output of the detector increases, in the energy range of 10^{-11} MeV to 2.0 MeV. The maximum energy response is at 2.0 MeV, after which the response decreases. The increases of detector output with increase of neutron energy can be attributed to more number of the neutrons reaching the active detector volume and undergoing nuclear reaction with ^{10}B which contributes to the increase in output. The output of the detector goes down till 300.0 MeV after which it again increases. The decrease

in output up to 300 MeV can be attributed to very higher energy of neutrons, which due to its increase in the energy have reduced reaction cross section with ^{10}B nuclei. The cross section of $^{10}\text{B}(\text{n},\alpha)^7\text{Li}^*$ has $1/v$ dependence. With increase of kinetic energy of neutrons, this reaction cross section decreases. Further increase in the energy response beyond 300 MeV may be due to increase in the number of reaction channels at these high energies. The kinks in the output response shows resonance structure of $^{10}\text{B}(\text{n},\alpha)^7\text{Li}^*$ reaction.

3.5 Lead Test of LFGNM

LFGNM is a neutron monitor, which is free from any lead components. Similar neutron monitors elsewhere have lead inserts because, due to the presence of lead, there is an increase of output response at higher energies of neutrons. Presence of lead increases the probability of (n,xn') reaction, which is dominant at higher energies of neutrons. To check similar response of LFGNM, lead inserts with different thickness of lead has been used, and the output response has been evaluated by scoring the number of alphas in the active volume of BF_3 detector using Monte Carlo code FLUKA. It can be seen from figure 3.7, the cross section of Pb^{206} increases in the higher energy domain of neutron energies. These cross sections has been taken from the ENDFB-VII.1 library[54].

This response study of LFGNM has been carried out in higher energy range of 100 MeV to 500 MeV, where in the absence of any lead insert, the response of LFGNM goes down. It can be seen from figure 3.8, that the output response of LFGNM increases with increase in the thickness of Pb. With enhanced thickness of Pb, the cross section of (n,xn') reaction increases. Moreover, it can also be seen that response increases with the increase in the energy of neutrons.

Figure 3.7: Cross section of Pb^{206}

3.6 Cadmium Test of LFGNM

Cadmium test of LFGNM has been carried out using Cd sheet placed at different positions near the upper paraffin moderator having thickness of 8 cm. This study has been carried out using Cd sheet having the thickness of 0.05 cm, covering the entire array of BF_3 detectors of LFGNM. Cd stops the neutrons having energy less than 0.4 eV. Pu- α -Be source having isotropic response was kept at a distance of 50 cm from the top edge of the upper paraffin moderator. The response of the detector was evaluated by calculating the number of α particles generated inside BF_3 detectors using RESNUCLEi card of FLUKA. Response has been calculated for the middle most seven detectors of the Neutron Monitor. In the first step, the Cd sheet was kept over the upper paraffin moderator of LFGNM and the response of the detectors have been shown in table 3.2.

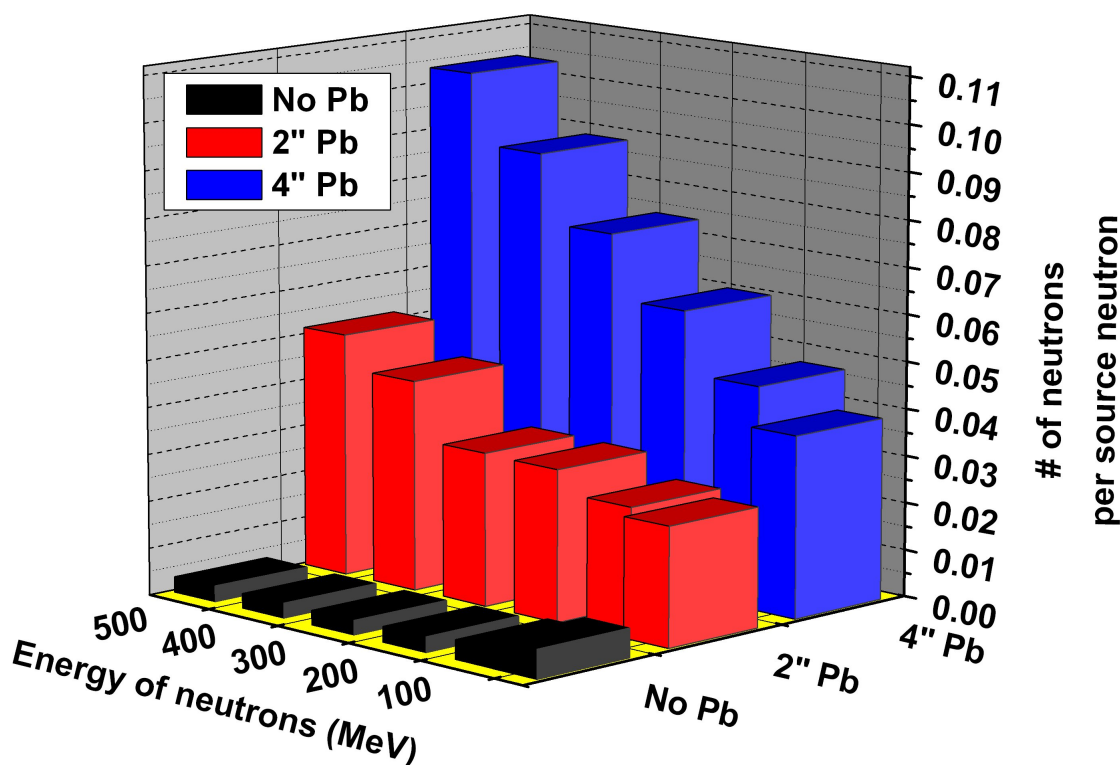


Figure 3.8: Response of LFGNM with different thickness of Pb insert

Table 3.2: Response of LFGNM with Cd sheet placed over Upper paraffin moderator

Sl. No.	Position of the detector with respect to the central detector	Output (arb. units)
1	+45.0 cm	7.112E-04 +/- 0.297 %
2	+30.0 cm	9.530E-04 +/- 0.599 %
3	+15.0 cm	1.153E-03 +/- 0.232%
4	0.0 cm	1.247E-03 +/- 0.477 %
5	-15.0 cm	1.163E-03 +/- 0.535 %
6	-30.0 cm	9.471E-04 +/- 0.772 %
7	-45.0 cm	7.037E-04 +/- 0.540 %

In second step, the Cd sheet has been kept under the Upper paraffin moderator. The output of the middle most seven detectors are given in table 3.3. It can be seen comparing table 3.2 and table 3.3, response of the detectors of the Neutron Monitor goes down as the Cd sheet placed just after the upper paraffin moderator is able to

Table 3.3: Response of LFGNM with Cd sheet placed under Upper paraffin moderator

Sl. No.	Position of the detector with respect to the central detector	Output (arb. units)
1	+45.0 cm	9.854E-05 +/- 1.965 %
2	+30.0 cm	1.315E-04 +/- 1.282 %
3	+15.0 cm	1.632E-04 +/- 1.437%
4	0.0 cm	1.765E-04 +/- 1.449 %
5	-15.0 cm	1.645E-04 +/- 1.396 %
6	-30.0 cm	1.331E-04 +/- 1.701 %
7	-45.0 cm	9.671E-05 +/- 1.269 %

cut-off the thermal neutrons below 0.4 eV.

3.7 Angular Response of LFGNM

The primary function of LFGNM is to measure the cosmic ray neutrons, but the scattering contribution from ground and surroundings of neutron also contributes to the output response. Hence the angular response study of any neutron monitor is very important. Angular response study of LFGNM has been carried out with Monte Carlo code FLUKA. The thickness of Paraffin moderator over the BF_3 detectors was kept at 8.0 cm. Planar source, having dimension of 330 cm x 90 cm, with various monoenergetic neutrons from energy 10^{-11} MeV to 10^4 MeV were chosen for the simulation at various angles of 0° to 60° at a distance of 200 cm from the top surface of upper paraffin moderator. The source angle in the simulation was varied using BEAMAXES card, where the cosine angles were fed. The angle of 0° corresponds to the normal position of the source, with respect to LFGNM geometry. The response of LFGNM were taken to be the total number of alphas produced in all the 21 BF_3 detectors, through $\text{B}^{10}(\text{n},\alpha)\text{Li}^{7*}$ reaction.

In figure 3.9, the output from LFGNM has been normalized with respect to the response at 0° angle. It can be inferred from figure 3.9, the maximum response is at 0° angle, and it goes down with increase in the angle of the source with respect to the normal of LFGNM geometry. The decrease in the response with the increase in

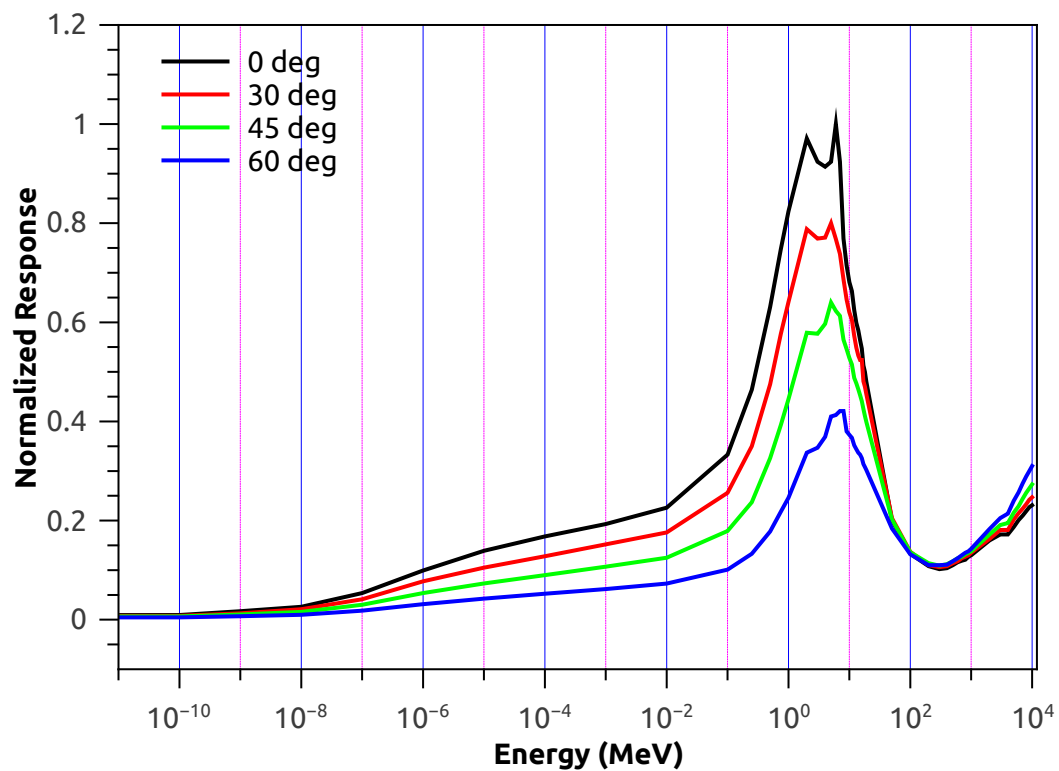


Figure 3.9: Angular response of LFGNM

the source angle can be attributed to the low contribution of the incident neutrons to the far off detectors.

Chapter 4

Residual Nuclei Calculations

4.1 Introduction

Accelerators are having diverse applications in several fields. Due to this, more and more accelerators are being commissioned in the densely populated regions. These facilities possess radiation risk mainly due to its “Prompt radiation” and “Induced activity”. Radiological risk due to prompt radiation is taken care by appropriate shielding, proper ventilation and by suitable administrative and engineering control of various areas of the accelerator facility. Induced activity in the various components and other materials around the accelerators are generated by the interaction of many particles generated in the target and other beam loss points. Induced activity produced inside the cyclotron vault possess low radiological risk due to shielding, administrative and engineering control of various areas of an accelerator. But, induced activity generated in concrete and soil by high energy neutrons possesses radiological risk not only to the personnel, but also for general public. These possess radiological risk even during the decommissioning of an accelerator facility. Radioactive waste is also required to be addressed for the removal of the concrete during decommissioning.

by different thicknesses of concrete and only soil. Estimation of various activation products in the different layers of parallelepiped each having size $30 \times 30 \times 10 \text{ cm}^3$ were carried using Monte Carlo code FLUKA. Cyclotron operation times for this study were 7 days, 30 days and 300 days. This study chooses these typical times for Cyclotron operation to estimate the production of residual nuclei having half life ranging from few hours to many years. Short half life isotopes will be produced even after 7 days of operation of cyclotron, but isotopes having long half life will be produced in scant quantities. With the increase in the run time of the cyclotron, more and more isotopes will be produced having considerable half life. Isotopes mainly with the moderate half life ($T_{1/2}$) play an important role in terms of generation and migration. Three detectors were placed very near to the target before the concrete or soil layers. Sufficient number histories were considered for each cycle and recommended numbers of cycles were run for better statistical convergence of the results. FLUKA cards, namely USRBIN and RESNUCLEi were triggered for this calculation. USRBIN card in FLUKA calculates the total activity (in Bq) in the regular spatial structure, irrespective of the geometry. RESNUCLEi card calculates the residual nuclei in the regions of geometry after inelastic interactions. The preparation of the geometry for FLUKA simulation was carried out using Flair[34].

Figure 4.2 shows the geometry of the simulation. It shows the Ta target, three spherical detectors and different layers of materials, where the residual nuclei calculations were carried out. Figure 4.3 and 4.4 shows the spatial distribution of the neutron fluence along the radial and transverse direction in different material layers.

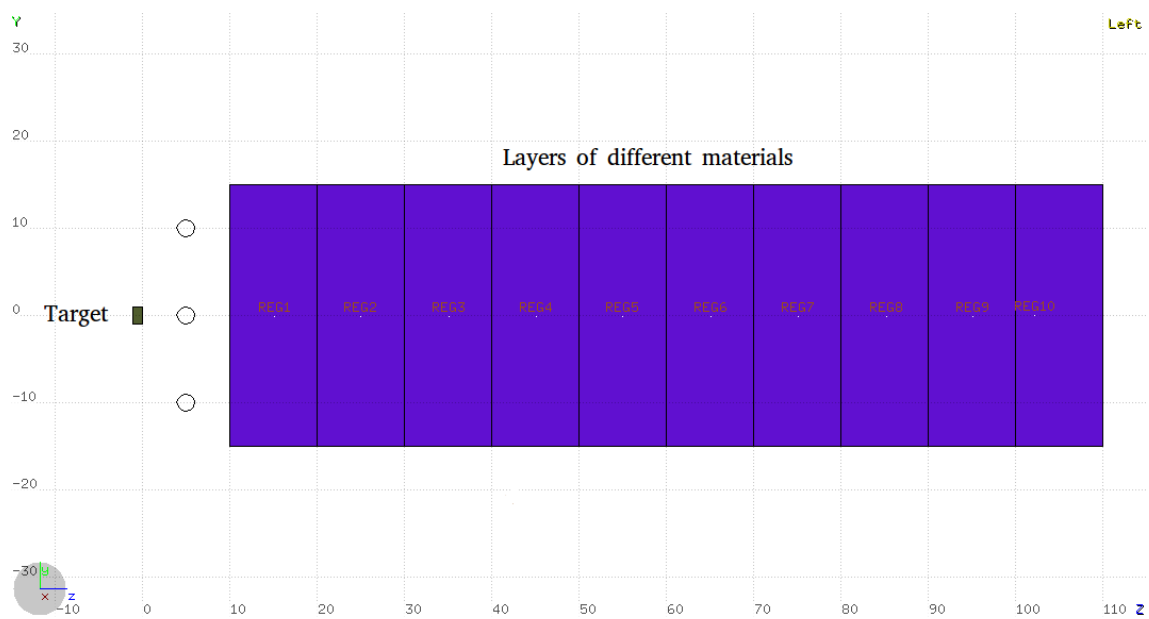


Figure 4.2: Geometry used for Monte Carlo Simulation with layers of different materials

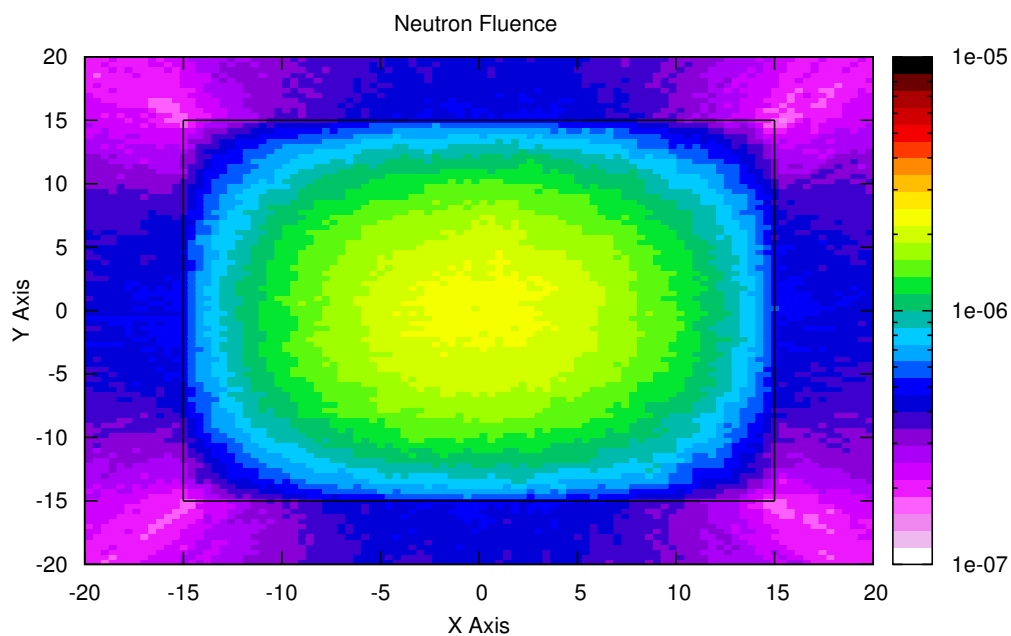


Figure 4.3: Variation of neutron fluence in radial direction

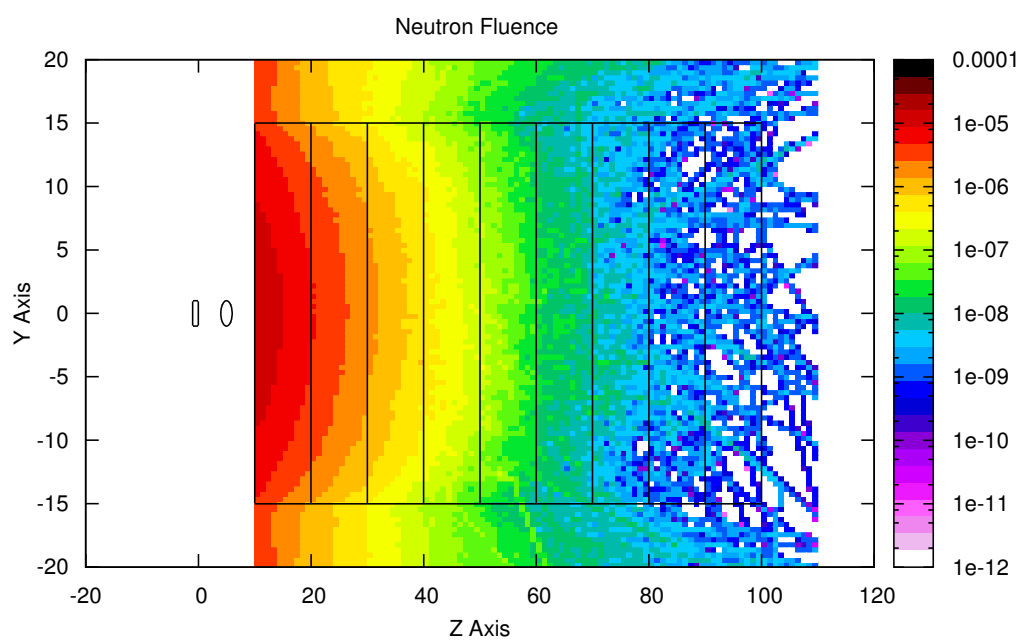


Figure 4.4: Variation of neutron fluence in transverse direction

4.2.1 Residual Nuclei in Concrete

In this simulation, 10 layers of concrete were taken each of size 30 cm x 30 cm x 10 cm. The density of concrete was 2.34 g/cm³. The elemental composition of the concrete used in the simulation is given in table 4.1. This composition of concrete is for poured structural concrete with 10% moisture content. Concrete block will have a density of about 2.05 g/cm³. Ranges of concrete composition are : C (8-25%), O (38-60%), Si (8-18%). Other concrete used for shielding are serpentine concrete, hematite concrete and ilmenite concrete. This study was carried out with ordinary concrete as the composition of the concrete used for shielding this medical cyclotron was very close to it.

Table 4.1: Elemental composition of concrete used in FLUKA

Element	Mass fraction (%)
C	23.0
O	40.0
Si	12.0
Ca	12.0
H	10.0
Mg	2.0

The proton beam after interacting with Ta target produces neutrons and photons. Table 4.2 shows the instantaneous dose rate of due to neutrons for beam current of unit particle/s and converted with suitable multiplication factor for 500 μ A for three different detector positions. Table 4.3 shows the activity for all the residual nuclei produced in the first five layers of concrete. Activity is shown in the units of Bq/cm³ for unit particle/s and in-terms of MBq/cm³ for 500 μ A beam current. Figure 4.5 shows the graphical representation of the activity with error for the first five layers after 7 days of Cyclotron run. Table 4.4 shows the major isotopes produced in these five layers of concrete after 7 days of Cyclotron operation in units of Bq. Table 4.5 shows the total activity in the first five layers in units of Bq/cm³ for unit particle/s and in units of MBq/cm³ for 500 μ A beam current for 30 days of Cyclotron operation. Figure 4.6 shows the graphical representation of the activity in the first five layers

with errors for 30 days of Cyclotron operation. Table 4.6 shows the major isotopes produced in these five layers of concrete in units of Bq after 30 days of Cyclotron run. Table 4.7 shows the total activity in the first five layers in units of Bq/cm³ for unit particle/s and in units of MBq/cm³ for 500 μ A beam current of proton for 300 days of Cyclotron operation. Figure 4.7 shows the graphical representation of the activity in the first five layers with errors for 300 days of Cyclotron operation in units of Bq/cm³. Table 4.8 shows the major isotopes produced in these five layers of concrete in units of Bq after 300 days of Cyclotron run.

Table 4.2: Instantaneous neutron dose rate in three detectors when beam on target

Detector position	Ambient dose rate (pSv/s)	Ambient dose rate for 500 μ A current (Sv/h)
1	8.7019E-02	9.790E+05
2	2.0113E-02	2.263E+05
3	1.9081E-02	2.147E+05

Table 4.3: Activity in first five layers of concrete after 7 days run of Cyclotron

Region	Layer 1	Layer 2	Layer 3	Layer 4	Layer 5
Activity for 1 p/s (Bq/cc)	1.1709E-09	3.7465E-10	1.2064E-10	3.6603E-11	1.4109E-11
Activity for 500 μ A (MBq/cc)	3.66	1.17	0.38	0.11	0.04

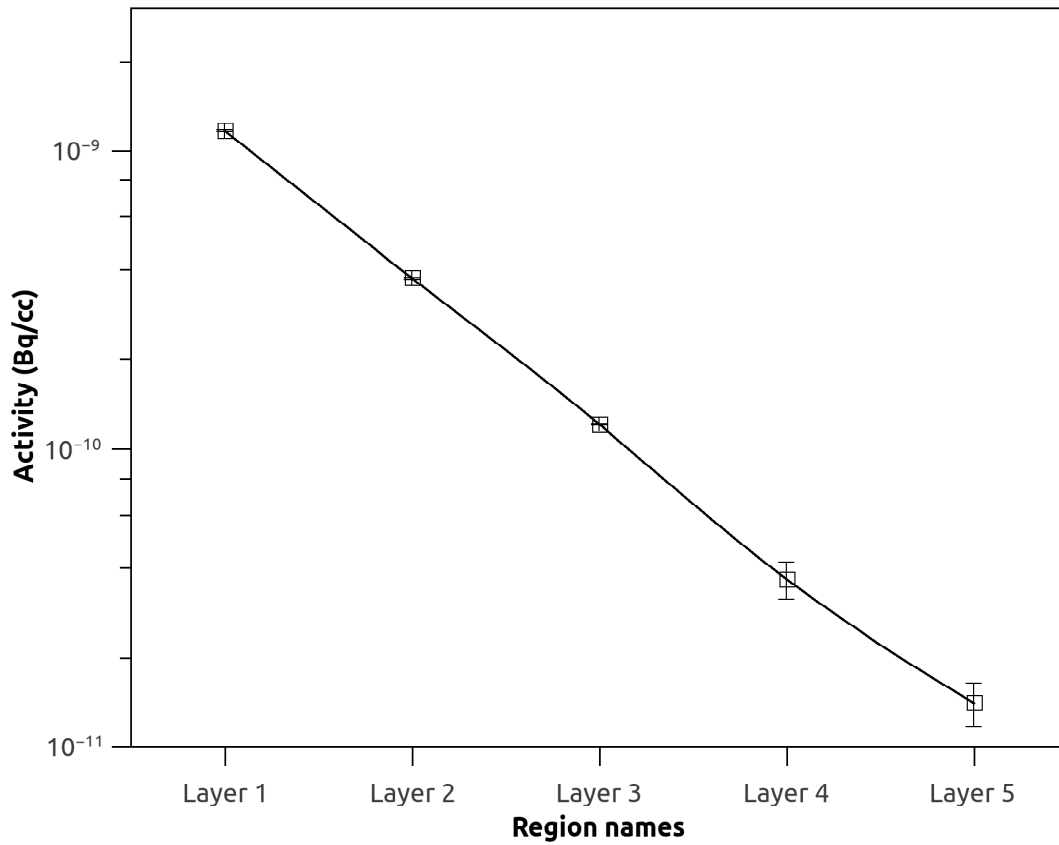


Figure 4.5: Graphical representation of variation of activity in concrete (Bq/cm^3) in first five layers after 7 days run

Table 4.4: Various Isotopes in different layers of Concrete after 7 days (Bq in whole volume)

Isotope	Layer 1	Layer 2	Layer 3	Layer 4	Layer 5
⁴⁷ Sc	6.90E-009	—	—	—	—
⁴⁵ Ca	1.03E-008	1.27E-008	1.06E-008	1.85E-009	2.24E-009
⁴³ K	1.05E-008	—	—	—	—
⁴² K	3.39E-008	3.20E-009	2.94E-009	—	—
⁴¹ Ca	1.07E-012	1.34E-012	9.07E-013	3.48E-013	1.43E-013
⁴⁰ K	2.72E-016	7.16E-017	2.09E-017	6.70E-018	2.20E-018
³⁹ Ar	2.91E-011	1.04E-011	3.59E-012	1.33E-012	3.29E-013
³⁷ Ar	1.29E-006	3.37E-007	1.04E-007	3.43E-008	1.13E-008
³⁶ Cl	2.36E-014	8.02E-015	2.96E-015	9.28E-016	4.64E-016
³¹ Si	3.07E-007	2.49E-007	9.42E-008	5.59E-008	1.0076E-08
²⁴ Na	4.09E-007	1.56E-007	5.10E-008	3.76E-008	4.32E-009
¹⁶ N	1.61E-006	4.12E-007	1.26E-007	5.49E-008	9.37E-009
¹⁵ O	1.38E-007	4.47E-008	1.33E-008	—	—
¹² B	2.23E-007	5.50E-008	3.24E-008	1.10E-008	—
¹¹ C	4.00E-008	2.00E-008	—	—	—
³ H	6.98E-011	4.57E-011	—	—	—

Table 4.5: Activity in first five layers of concrete after 30 days run of Cyclotron

Region	Layer 1	Layer 2	Layer 3	Layer 4	Layer 5
Activity for 1 p/s (Bq/cc)	1.5300E-09	4.7112E-10	1.5274E-10	4.6687E-11	1.7977E-11
Activity for 500 μ A (MBq/cc)	4.78	1.47	0.48	0.14	0.056

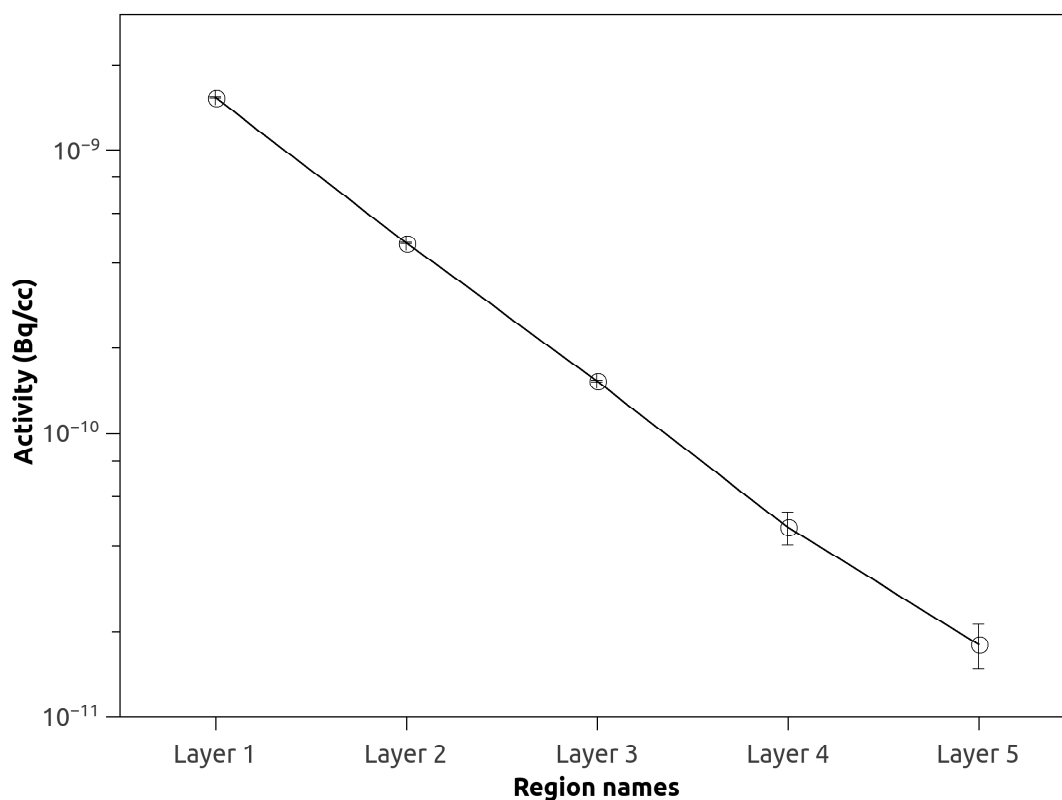
Figure 4.6: Graphical representation of variation of activity in concrete (Bq/cm^3) in first five layers after 30 days run

Table 4.6: Various Isotopes in different layers of Concrete after 30 days (Bq in whole volume)

Isotope	Layer 1	Layer 2	Layer 3	Layer 4	Layer 5
⁴⁷ Sc	1.90E-008	—	—	—	—
⁴⁵ Ca	4.23E-008	5.21E-008	4.32E-008	7.55E-009	9.15E-009
⁴³ K	1.05E-008	—	—	—	—
⁴² K	3.39E-008	3.20E-009	2.94E-009	—	—
⁴¹ Ca	4.60E-012	5.76E-012	3.89E-012	1.49E-012	6.13E-013
⁴⁰ K	1.17E-015	3.07E-016	8.98E-017	2.87E-017	9.45E-018
³⁹ Ar	1.25E-010	4.45E-011	1.54E-011	5.68E-012	1.41E-012
³⁷ Ar	4.47E-006	1.17E-006	3.60E-007	1.19E-007	3.9200E-08
³⁶ Cl	1.01E-013	3.44E-014	1.27E-014	3.98E-015	1.99E-015
³¹ Si	3.07E-007	2.49E-007	9.42E-008	5.59E-008	1.01E-008
²⁴ Na	4.10E-007	1.56E-007	5.11E-008	3.76E-008	4.32E-009
¹⁶ N	1.61E-006	4.12E-007	1.26E-007	5.49E-008	9.37E-009
¹⁵ O	1.38E-007	4.47E-008	1.33E-008	—	—
¹² B	2.23E-007	5.50E-008	3.24E-008	—	—
¹¹ C	4.00E-008	2.00E-008	—	—	—
³ H	2.99E-010	1.95E-010	—	—	—

Table 4.7: Activity in first five layers of concrete after 300 days run of Cyclotron

Region	Layer 1	Layer 2	Layer 3	Layer 4	Layer 5
Activity for 1 p/s (Bq/cc)	2.1651E-09	6.5952E-10	2.2610E-10	6.7109E-11	2.8472E-11
Activity for 500 μ A (MBq/cc)	6.76	2.06	0.71	0.21	0.09

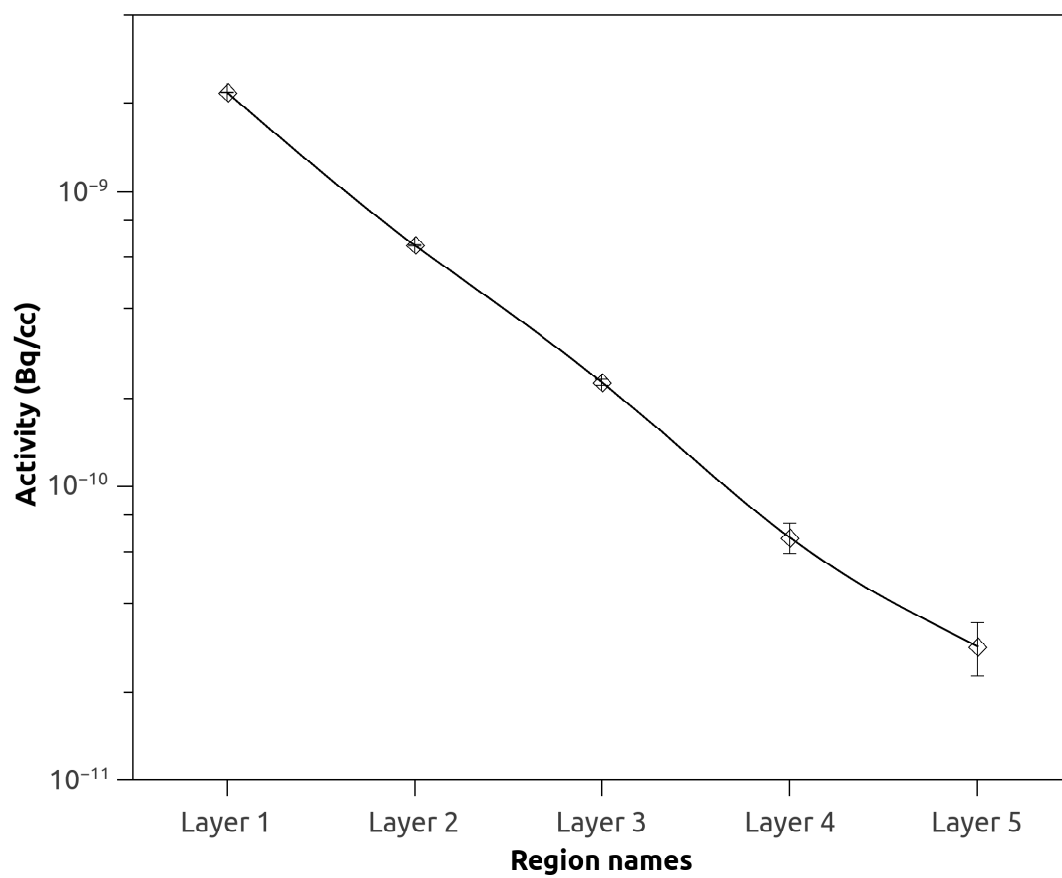


Figure 4.7: Graphical representation of variation of activity in concrete (Bq/cm^3) in first five layers after 300 days run

Table 4.8: Various Isotopes in different layers of Concrete after 300 days (Bq in whole volume)

Isotope	Layer 1	Layer 2	Layer 3	Layer 4	Layer 5
^{47}Sc	1.96E-008	—	—	—	—
^{45}Ca	2.55E-007	3.14E-007	2.61E-007	4.55E-008	5.52E-008
^{43}K	1.05E-008	—	—	—	—
^{42}K	3.39E-008	3.20E-009	2.94E-009	—	—
^{41}Ca	4.60E-011	5.76E-011	3.89E-011	1.49E-011	6.13E-012
^{40}K	1.17E-014	3.07E-015	8.98E-016	2.87E-016	9.45E-017
^{39}Ar	1.25E-009	4.45E-010	1.54E-010	5.67E-011	1.41E-011
^{37}Ar	9.97E-006	2.60E-006	8.03E-007	2.64E-007	8.74E-008
^{36}Cl	1.01E-012	3.44E-013	1.27E-013	3.98E-014	1.99E-014
^{31}Si	3.07E-007	2.49E-007	9.42E-008	5.59E-008	1.01E-008
^{24}Na	4.10E-007	1.56E-007	5.11E-008	3.76E-008	4.32E-009
^{16}N	1.61E-006	4.12E-007	1.26E-007	5.49E-008	9.37E-009
^{15}O	1.38E-007	4.47E-008	1.33E-008	—	—
^{12}B	2.23E-007	5.50E-008	3.24E-008	1.10E-008	—
^{11}C	4.00E-008	2.00E-008	—	—	—
^3H	2.92E-009	1.91E-009	—	—	—

4.2.2 Residual Nuclei in soil after 50 cm layer of concrete

Here the residual nuclei calculation has been carried out for soil, which has been placed 50 cm (5 layers) of concrete. Each concrete layer and soil layer was having a size of 30 cm x 30 cm x 10 cm. The density and composition of soil varies from place to place. In this study, the soil taken is having a density of 1.35 g/cm³. Elemental composition of soil, used in this study is shown in table 4.9. Neutrons generated by interaction with Ta target, gets attenuated while moving inside concrete layers.

Table 4.9: Elemental composition of soil used in FLUKA

Element	Mass fraction (%)
Fe	38.9
Na	2.5
K	2.5
Mn	0.0851
Ni	0.0124
Zn	8.51E-03
Co	4.77E-03
Cu	3.32E-03
Ca	0.311
Mg	1.9
Si	34.3
O	19.5

Table 4.10 shows the activity in different layers soil placed after 50 cm of concrete, after 7 days of Cyclotron operation. Figure 4.8 shows the graphical representation of the total activity in different layers of soil placed after 50 cm concrete. Due to statistical fluctuation in the data, there is little variation in the total activity for the layer 8 to 10. Table 4.12 shows the activity in different layers of soil after 30 days of Cyclotron operation. Figure 4.9 shows the graphical representation of the total activity in different layers of soil with errors placed after 50 cm concrete in units of Bq/cm³. Table 4.13 shows various isotopes produced in different layers of soil after 30 days of Cyclotron operation. Table 4.14 shows the activity in different layers of soil after 300 days of operation in units of Bq/cm³ for 1 p/s and in units of MBq/cm³ for 500 μ A beam current. Figure 4.10 shows the activity in different layers of the

soil with errors after 300 days of operation. Various isotopes in different layers after 300 days of Cyclotron run is shown in table 4.15.

Table 4.10: Activity in five layers of soil placed after 50 cm concrete after 7 days run

Region	Layer 6	Layer 7	Layer 8	Layer 9	Layer 10
Activity for 1 p/s (Bq/cc)	8.3271E-12	2.2016E-12	8.1960E-13	8.4854E-13	8.3622E-13
Activity for 500 μ A (MBq/cc)	0.026	0.007	0.002	0.002	0.002

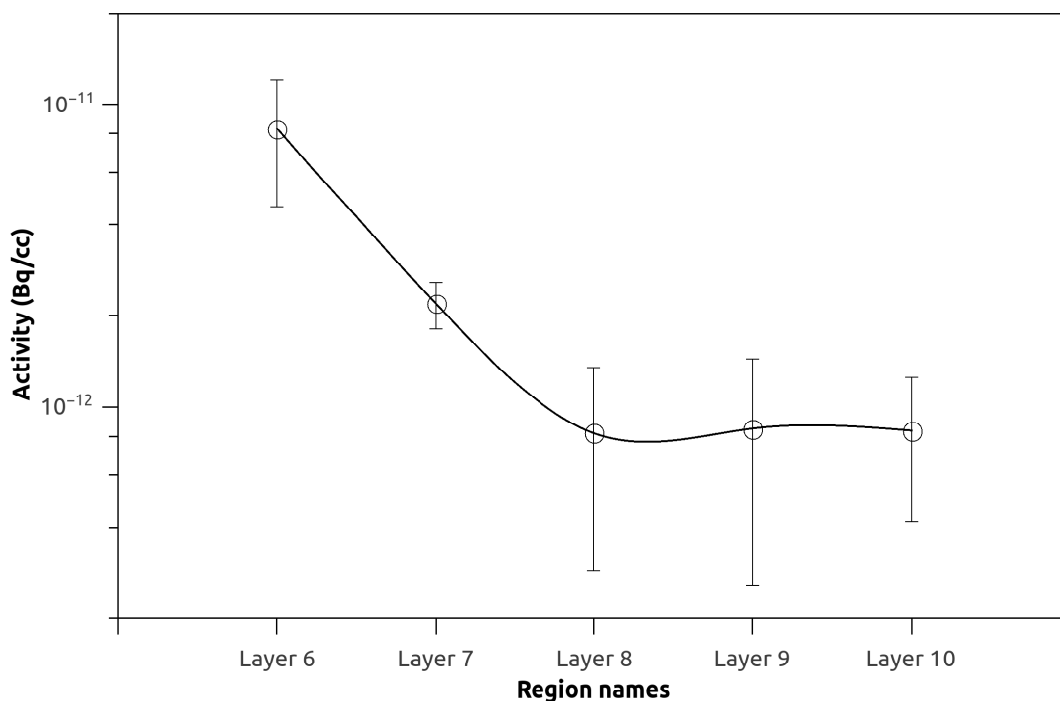


Figure 4.8: Graphical representation of variation of activity in soil (Bq/cm^3) after 50 cm concrete after 7 days run

Table 4.11: Various Isotopes in different layers of soil after 50 cm concrete after 7 days (Bq in whole volume)

Isotope	Layer 6	Layer 7	Layer 8	Layer 9	Layer 10
^{59}Fe	6.89E-011	—	—	—	—
^{55}Fe	1.46E-010	3.92E-011	2.14E-011	1.72E-011	—
^{54}Mn	3.76E-011	5.28E-011	—	—	—
^{40}K	2.58E-019	2.72E-019	2.36E-020	—	—
^{39}Ar	6.65E-014	1.42E-013	8.38E-014	—	—
^{36}Cl	8.44E-017	7.88E-017	—	—	—
^{31}Si	1.44E-009	1.98E-009	6.67E-010	—	—
^{24}Na	2.73E-008	6.99E-009	—	—	—

Table 4.12: Activity in five layers of soil placed after 50 cm concrete after 30 days run

Region	Layer 6	Layer 7	Layer 8	Layer 9	Layer 10
Activity for 1 p/s (Bq/cc)	8.4151E-12	2.3180E-12	8.3312E-13	8.5478E-13	8.3622E-13
Activity for 500 μA (MBq/cc)	0.026	0.007	0.0026	0.002	0.002

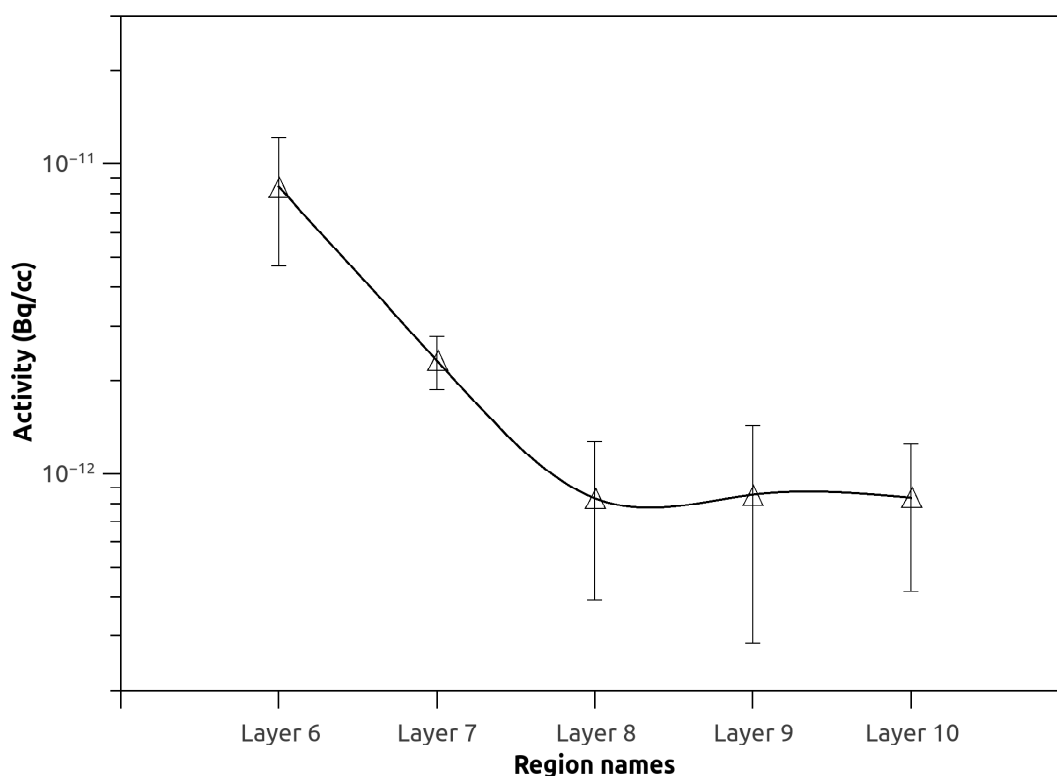
Figure 4.9: Graphical representation of variation of activity in soil (Bq/cm^3) after 50 cm concrete after 30 days run

Table 4.13: Various Isotopes in different layers of soil after 50 cm concrete after 30 days (Bq in whole volume)

Isotope	Layer 6	Layer 7	Layer 8	Layer 9	Layer 10
^{59}Fe	2.49E-010	—	—	—	—
^{55}Fe	6.22E-010	1.67E-010	9.09E-011	7.30E-011	—
^{54}Mn	1.57E-010	2.21E-010	—	—	—
^{40}K	1.10E-018	1.16E-018	1.01E-019	—	—
^{39}Ar	2.85E-013	6.07E-013	3.59E-013	—	—
^{36}Cl	3.62E-016	3.38E-016	—	—	—
^{31}Si	1.44E-009	1.98E-009	6.67E-010	—	—
^{24}Na	2.73E-008	6.99E-009	—	—	—

Table 4.14: Activity in five layers of soil placed after 50 cm concrete after 300 days run

Region	Layer 6	Layer 7	Layer 8	Layer 9	Layer 10
Activity for 1 p/s (Bq/cc)	9.1435E-12	2.7729E-12	9.7641E-13	9.2107E-13	8.3622E-13
Activity for 500 μA (MBq/cc)	0.028	0.0086	0.003	0.0028	0.002

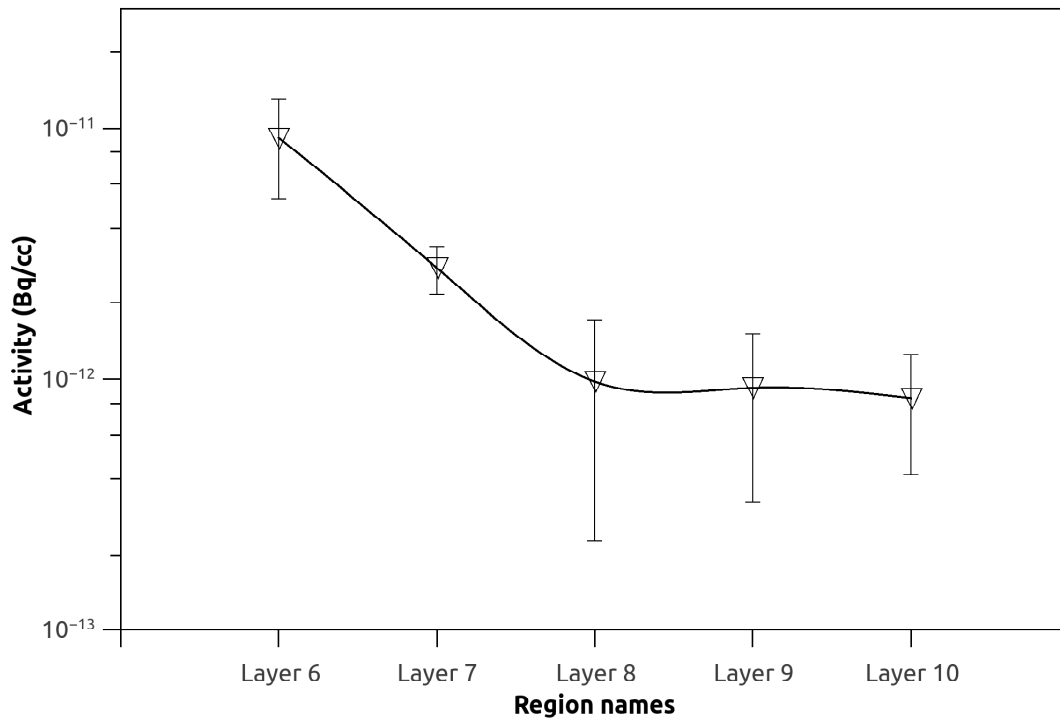
Figure 4.10: Graphical representation of variation of activity in soil (Bq/cm^3) after 50 cm concrete after 300 days run

Table 4.15: Various Isotopes in different layers of soil after 50 cm concrete after 300 days (Bq in whole volume)

Isotope	Layer 1	Layer 2	Layer 3	Layer 4	Layer 5
59 Fe	6.60E-010	—	—	—	—
55 Fe	5.67E-009	1.52E-009	8.29E-010	6.66E-010	—
54 Mn	1.19E-009	1.6639E-09	—	—	—
40 K	1.10E-017	1.16E-017	1.01E-018	—	—
39 Ar	2.85E-012	6.07E-012	3.59E-012	—	—
36 Cl	3.62E-015	3.38E-015	—	—	—
31 Si	1.44E-009	1.98E-009	6.67E-010	—	—
24Na	2.73E-008	6.99E-009	—	—	—

4.2.3 Residual Nuclei in soil after 100 cm of concrete

As done in the previous section, the residual activities in the five layers of soil were further evaluated, when placed after 100 cm of concrete. The density and composition of the soil and concrete remains the same for the simulation, as described earlier. Activity in different layers of soil after 7 days of Cyclotron operation is shown in table 4.16. Isotopes produced in these layers are shown in table 4.17. Activity in different layers of the soil after 30 days operation is shown in table 4.18 and the isotopes produced in them are shown in table 4.19. Activity produced in the soil layers after 300 days of operation are shown in table 4.20 and various isotopes produced are shown in table 4.21. As the numbers of neutrons reaching the soil layers are highly attenuated due to the presence of 100 cm of concrete, the activity is mainly produced in the first layer of the soil. Only major isotope produced is ^{39}Ar in the first layer of the soil. This shows that the burden of radioactive waste produced, with 300 days of cyclotron operation is very less, due to the attenuation produced by the concrete layer of 100 cm.

Table 4.16: Activity in layers of soil after 100 cm concrete after 7 days operation

Region	Layer 11	Layer 12	Layer 13	Layer 14	Layer 15
Activity for 1 p/s (Bq/cc)	1.7325E-18	—	—	—	—
Activity for 500 μA (MBq/cc)	5.413E-09	—	—	—	—

Table 4.17: Isotopes produced in different layers of soil placed after 100 cm concrete after 7 days operation

Isotopes	Layer 11	Layer 12	Layer 13	Layer 14	Layer 15
^{39}Ar	1.5593E-14	—	—	—	—

Table 4.18: Activity in layers of soil after 100 cm concrete after 30 days operation

Region	Layer 11	Layer 12	Layer 13	Layer 14	Layer 15
Activity for 1 p/s (Bq/cc)	7.4246E-17	—	—	—	—
Activity for 500 μ A (MBq/cc)	0.232E-06	—	—	—	—

Table 4.19: Isotopes produced in different layers of soil placed after 100 cm concrete after 30 days operation

Isotope	Layer 11	Layer 12	Layer 13	Layer 14	Layer 15
³⁹ Ar	6.6821E-14	—	—	—	—

Table 4.20: Activity in layers of soil after 100 cm concrete after 300 days operation

Region	Layer 11	Layer 12	Layer 13	Layer 14	Layer 15
Activity for 1 p/s (Bq/cc)	7.4175E-17	—	—	—	—
Activity for 500 μ A (MBq/cc)	0.232E-06	—	—	—	—

Table 4.21: Isotopes produced in different layers of soil placed after 100 cm concrete after 300 days operation

Isotopes	Layer 11	Layer 12	Layer 13	Layer 14	Layer 15
³⁹ Ar	6.6757E-13	—	—	—	—

4.2.4 Residual Nuclei in Soil

In this simulation, only soils were taken for the generation of residual nuclei. Although, the chances of soil getting exposed to the direct neutron fluence is very less, which are generated by the interaction of the protons are various beam loss points, this study will give us the estimation of the residual activity produced and various isotopes generated in them for the worst case scenario. The density and the composition of the soil remains the same for this simulation, as taken previously. Soils layers were having a dimension of 30 cm x 30 cm x 10 cm. Proton beam interacts with the Ta target, which has been placed at a distance of 5 cm from the front layer of soil. Table 4.22 and 4.23 shows the activity produced in different layers of soil after 7 days of Cyclotron operation in units of Bq/cm³ for 1 p/s beam current and in units of MBq/cm³ for 500 μ A of beam current. Figure 4.11 shows the graphical representation of activity in various soil layers with errors. Table 4.24 shows the important isotopes produced in different layers of the soil after 7 days of run. The activity in units of Bq/cm³ in different layers of soil after 30 days of Cyclotron operation is shown in table 4.25 and 4.26. Table 4.27 shows the important isotopes produced in the first five layers of soil, when exposed to the direct secondary neutrons after Cyclotron operation for 30 days. Table 4.28 and 4.29 shows the activity in units of Bq/cm³ for 1 p/s beam current and in units of MBq/cm³ for 500 μ A beam current for 300 days of Cyclotron operation. Figure 4.13 shows the activity in different layers of soil with errors after 300 days of Cyclotron operation. Table 4.30 shows the important isotopes produced in first five layers of soil after 300 days of operation.

Table 4.22: Activity in first 5 layers of soil after 7 days Cyclotron operation

Region	Layer 1	Layer 2	Layer 3	Layer 4	Layer 5
Activity for 1 p/s (Bq/cc)	1.1176E-09	4.5494E-10	2.1380E-10	9.1176E-11	5.0269E-11
Activity for 500 μ A (MBq/cc)	3.49	1.42	0.668	0.285	0.157

Table 4.23: Activity in last 5 layers of soil after 7 days Cyclotron operation

Region	Layer 6	Layer 7	Layer 8	Layer 9	Layer 10
Activity for 1 p/s (Bq/cc)	2.8020E-11	1.0116E-11	6.3676E-12	3.2718E-12	1.5714E-12
Activity for 500 μ A (MBq/cc)	0.087	0.031	0.02	0.010	0.0048

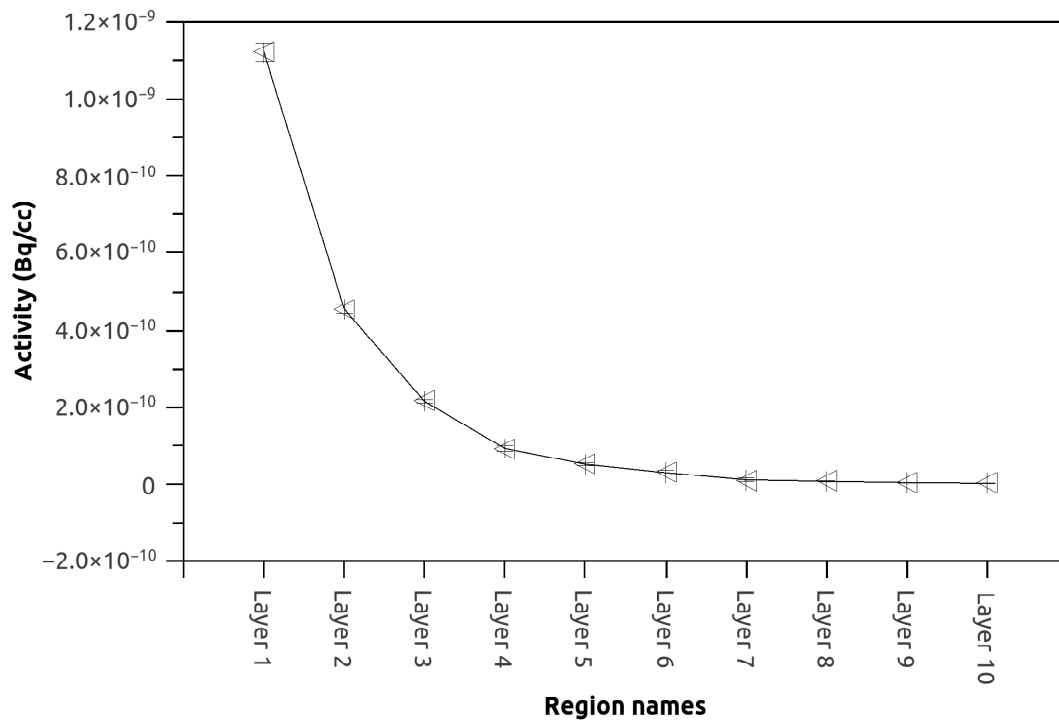
Figure 4.11: Graphical representation of variation of activity in soil (Bq/cm^3) after 7 days run

Table 4.24: Isotopes produced in first five layers of soil after 7 days of Cyclotron operation

Isotope	Layer 1	Layer 2	Layer 3	Layer 4	Layer 5
⁵⁹ Fe	4.36E-009	3.14E-009	—	—	—
⁵⁶ Mn	1.1740E-06	4.79E-007	2.42E-007	7.81E-008	8.03E-008
⁵⁵ Fe	7.83E-007	3.87E-007	1.81E-007	9.98E-008	3.76E-008
⁵⁴ Mn	4.38E-007	1.82E-007	6.87E-008	4.3158E-08	2.05E-008
⁵³ Mn	5.50E-014	2.85E-014	1.42E-014	5.32E-015	3.69E-015
⁵¹ Cr	7.86E-008	3.40E-008	6.43E-009	—	
⁴² K	2.03E-008	5.33E-009	1.33E-009	—	
⁴¹ Ca	6.27E-014	7.37E-015	3.69E-015	7.37E-015	3.69E-015
⁴⁰ K	1.05E-016	4.56E-017	2.18E-017	5.68E-018	1.32E-018
³⁹ Ar	3.52E-009	1.54E-009	5.99E-010	2.61E-010	1.32E-010
³⁷ Ar	8.43E-008	3.27E-008	2.0257E-08	6.68E-009	1.79E-009
³⁶ Cl	1.24E-012	5.47E-013	1.87E-013	9.45E-014	2.35E-014
³¹ Si	9.3333E-09	4.08E-009	—	—	
²⁴ Na	2.33E-007	1.07E-007	4.11E-008	2.76E-008	1.36E-008
²² Na	2.00E-008	1.41E-008	1.20E-009	3.10E-009	6.39E-010
³ H	8.27E-010	6.02E-010	6.02E-010	—	

Table 4.25: Activity in first 5 layers of soil after 30 days Cyclotron operation

Region	Layer 1	Layer 2	Layer 3	Layer 4	Layer 5
Activity for 1 p/s (Bq/cc)	1.1365E-09	4.6360E-10	2.1732E-10	9.2859E-11	5.0919E-11
Activity for 500 μ A (MBq/cc)	3.55	1.45	0.68	0.29	0.16

Table 4.26: Activity in last 5 layers of soil after 30 days Cyclotron operation

Region	Layer 6	Layer 7	Layer 8	Layer 9	Layer 10
Activity for 1 p/s (Bq/cc)	2.8366E-11	1.0440E-11	6.4441E-12	3.3075E-12	1.5896E-12
Activity for 500 μ A (MBq/cc)	0.089	0.032	0.020	0.010	0.005

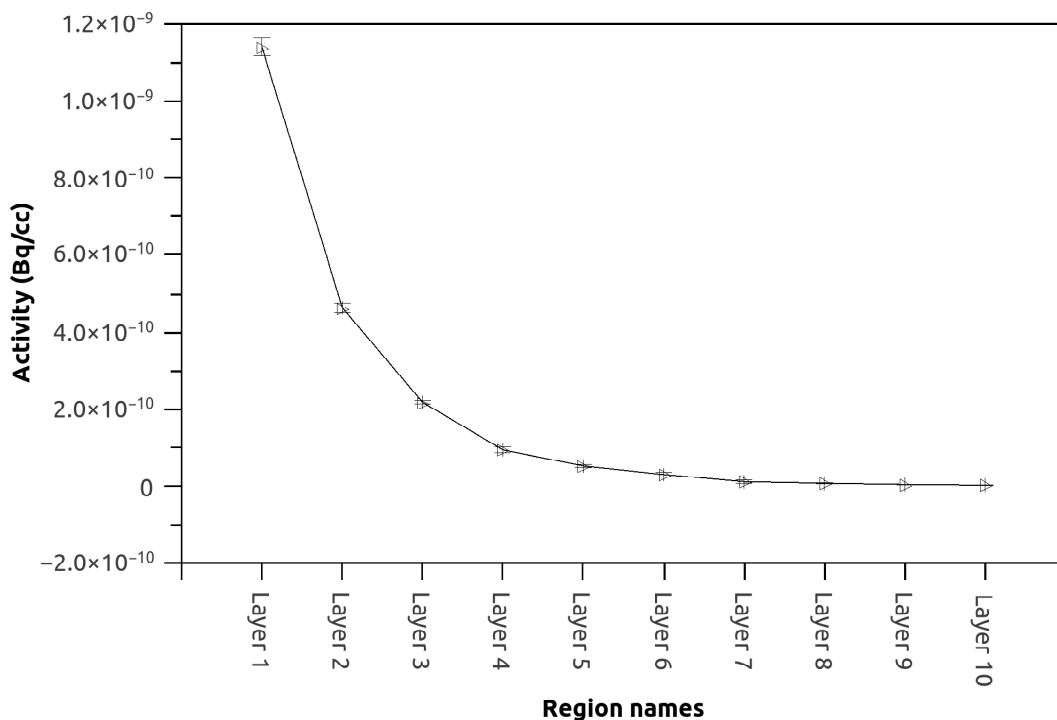


Figure 4.12: Graphical representation of variation of activity in soil (Bq/cm^3) after 30 days run

Table 4.27: Isotopes produced in first five layers of soil after 30 days of Cyclotron operation

Isotope	Layer 1	Layer 2	Layer 3	Layer 4	Layer 5
^{59}Fe	1.64E-009	1.18E-009	—	—	
^{56}Mn	1.17E-006	4.79E-007	2.42E-007	7.81E-008	8.03E-008
^{55}Fe	8.59E-008	4.24E-008	1.99E-008	1.09E-008	4.12E-009
^{54}Mn	5.80E-008	2.41E-008	9.11E-009	5.72E-009	2.7120E-09
^{53}Mn	5.50E-015	2.85E-015	1.42E-015	5.32E-016	3.69E-016
^{51}Cr	4.15E-008	1.80E-008	3.40E-009	—	—
^{42}K	2.03E-008	5.33E-009	1.33E-009	—	1.33E-009
^{41}Ca	6.27E-015	7.37E-016	3.69E-016	7.37E-016	3.69E-016
^{40}K	1.05E-017	4.56E-018	2.18E-018	5.68E-019	1.32E-019
^{39}Ar	3.52E-010	1.54E-010	5.99E-011	2.61E-011	1.32E-011
^{37}Ar	3.78E-008	1.47E-008	9.09E-009	3.00E-009	8.03E-010
^{36}Cl	1.24E-013	5.47E-014	1.87E-014	9.45E-015	2.35E-015
^{31}Si	9.33E-009	4.08E-009	—	—	—
^{24}Na	2.33E-007	1.07E-007	4.11E-008	2.76E-008	1.36E-008
^{22}Na	2.20E-009	1.55E-009	1.32E-010	3.42E-010	7.04E-011
^3H	8.45E-011	6.15E-011	6.15E-011	—	—

Table 4.28: Activity in first five layers of soil after 300 days of Cyclotron operation

Region	Layer 1	Layer 2	Layer 3	Layer 4	Layer 5
Activity for 1 p/s (Bq/cc)	1.2687E-09	5.2605E-10	2.4390E-10	1.0764E-10	5.6797E-11
Activity for 500 μ A (MBq/cc)	3.96	1.64	0.76	0.336	0.18

Table 4.29: Activity in last five layers of soil after 300 days of Cyclotron operation

Region	Layer 6	Layer 7	Layer 8	Layer 9	Layer 10
Activity for 1 p/s (Bq/cc)	3.1824E-11	1.2769E-11	7.2572E-12	3.6641E-12	1.7828E-12
Activity for 500 μ A (MBq/cc)	0.099	0.040	0.022	0.011	0.005

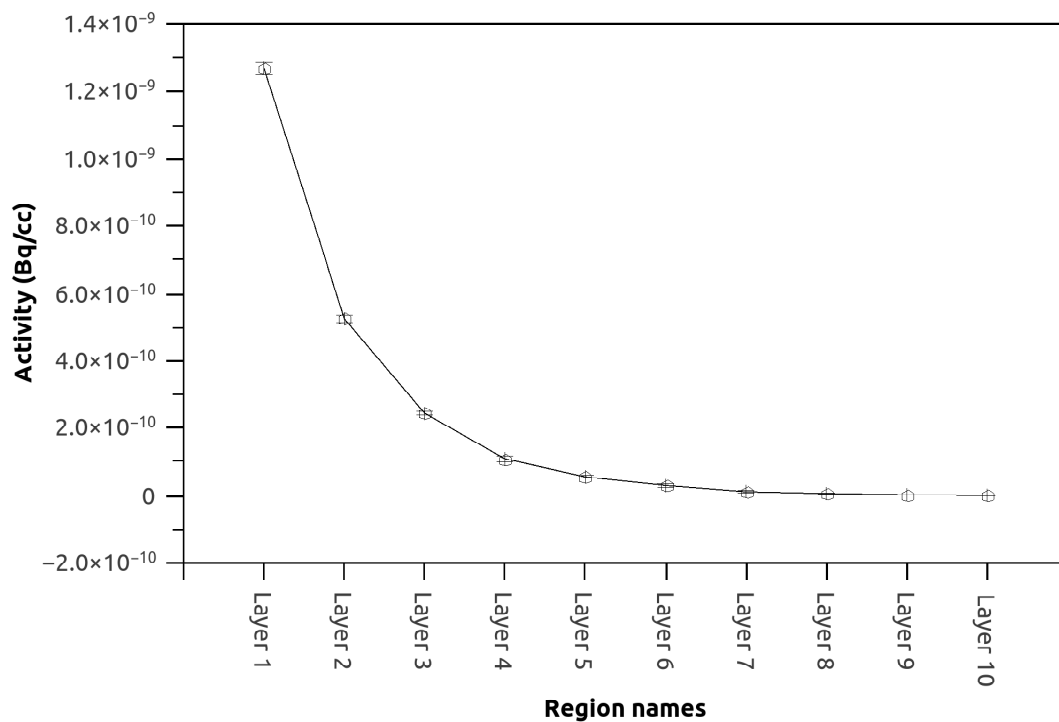
Figure 4.13: Graphical representation of variation of activity in soil (Bq/cm^3) after 300 days run

Table 4.30: Isotopes in first five layers of soil after 300 days of Cyclotron operation

Isotope	Layer 1	Layer 2	Layer 3	Layer 4	Layer 5
^{59}Fe	4.36E-009	3.14E-009	—	—	—
^{56}Mn	1.17E-006	4.79E-007	2.42E-007	7.81E-008	8.03E-008
^{55}Fe	7.83E-007	3.8712E-07	1.81E-007	9.98E-008	3.76E-008
^{54}Mn	4.38E-007	1.82E-007	6.87E-008	4.32E-008	2.05E-008
^{53}Mn	5.50E-014	2.85E-014	1.42E-014	5.32E-015	3.69E-015
^{51}Cr	7.86E-008	3.40E-008	6.43E-009	—	—
^{42}K	2.03E-008	5.33E-009	1.33E-009	—	—
^{41}Ca	6.27E-014	7.37E-015	3.69E-015	7.37E-015	3.69E-015
^{40}K	1.05E-016	4.56E-017	2.18E-017	5.68E-018	1.32E-018
^{39}Ar	3.52E-009	1.54E-009	5.99E-010	2.61E-010	1.32E-010
^{37}Ar	8.43E-008	3.27E-008	2.03E-008	6.68E-009	1.79E-009
^{36}Cl	1.24E-012	5.47E-013	1.87E-013	9.45E-014	2.35E-014
^{31}Si	9.33E-009	4.08E-009	—	—	—
^{24}Na	2.33E-007	1.07E-007	4.11E-008	2.76E-008	1.36E-008
^{22}Na	2.00E-008	1.41E-008	1.20E-009	3.10E-009	6.39E-010
^3H	8.27E-010	6.02E-010	6.02E-010	—	—

4.3 Methodology for Super Conducting Cyclotron

Super Conducting Cyclotron (SCC) has been designed, fabricated and commissioned at VECC, Kolkata which is capable to deliver a range of light ions to heavy ions. This machine consists of a magnet made of superconductor (NbTi alloy) operated at 4 K. The magnetic fields are 5.5 T and 4.3 T maximum at the Hill, Valley respectively. Radio frequency range is 9-27 MHz. The layout of Super Conducting Cyclotron is shown in figure 4.14. Residual nuclei calculations were carried out for different

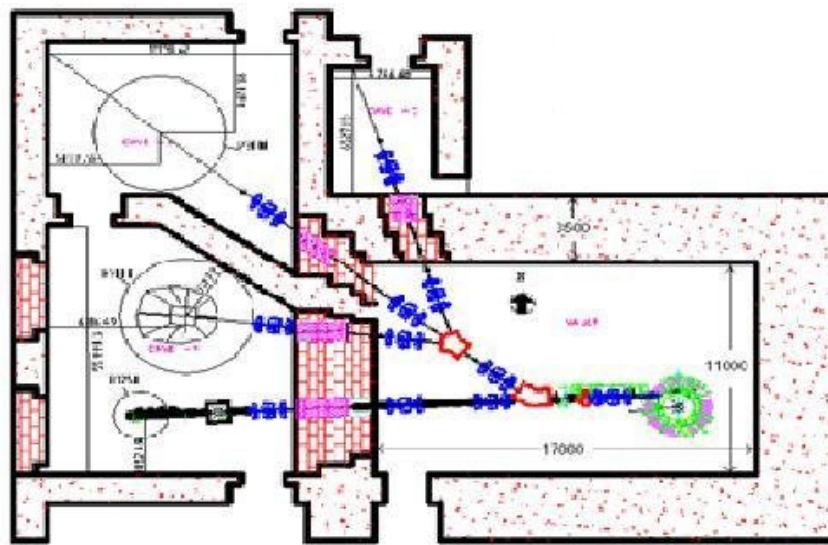


Figure 4.14: Layout of Super Conducting Cyclotron

materials, which are typically used for the fabrication of various components of any Cyclotron, such as Al, SS (316L), Cu and Concrete. Out of these materials, concrete is mainly used for the shielding of the Cyclotron. SS-316L is having density of 8.0 g/cm^3 with Fe (67%), Cr (18%), Ni (13%) and Mn (2%). Residual nuclei calculations have been carried out with Monte Carlo code FLUKA [37],[25]. Source term estimation has been carried out with 80 MeV proton beam falling on SS target, enough to stop completely the primary beam. Beam current used in this study was $0.1 \mu\text{A}$. Proton interacting with the target will generate neutrons, photons and other charged particles. These particles were made to fall on different materials mentioned earlier for the generation of the residual nuclei. The ambient dose rates (Hp[10])

from these isotopes were found after different cooling period of 1 hour to 10^5 hours. Figure 4.15 shows the geometry used for the simulation. The geometry consists of



Figure 4.15: 3D geometry used for evaluation of residual nuclei of Super Conducting Cyclotron

two cylinders. Slab 1 is the first cylinder having radius of 5.0 cm and thickness of 5.0 cm. Slab 2 is the second cylinder having radius 4.5 cm and thickness of 20.0 cm.

4.3.1 Measurement of dose rates after different cooling times

Ambient dose rates after different cooling times was measured by a cylindrical detector of radius 1.0 cm and thickness 1.0 cm placed immediately before the first cylinder of various materials. This detector is hence capable of measuring the dose rates due to the isotopes produced in the Cylindrical slabs as well as from the primary target, where the proton beam is dumped. Ambient dose rates have been calculated using fluence to Hp[10] conversion factors for photons and other charge particles like electrons and positrons [55]. Figure 4.16, 4.17, 4.18 and 4.19 shows the variation of dose rate in units of pSv/s for different cooling periods for various slab materials. The maximum ambient dose rate was found to be 2.29×10^4 pSv/s

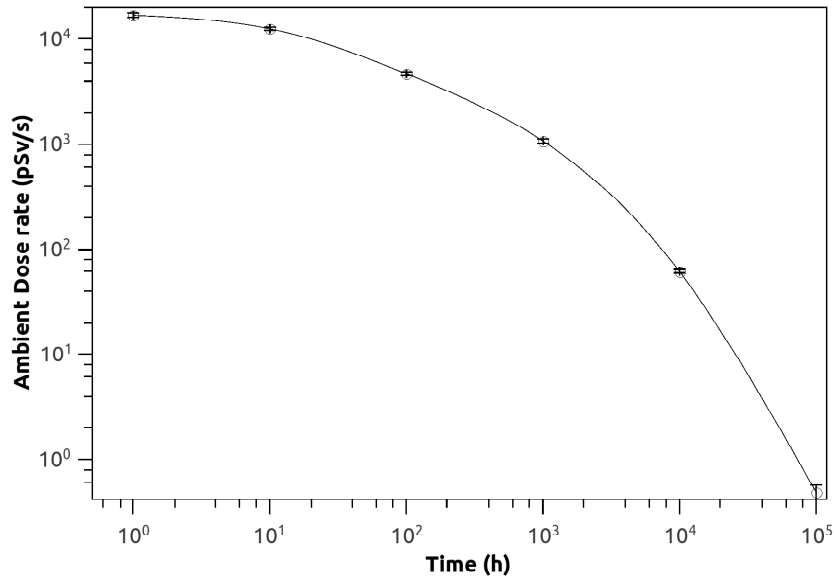


Figure 4.16: Variation of dose rate with different cooling times for Al slab material

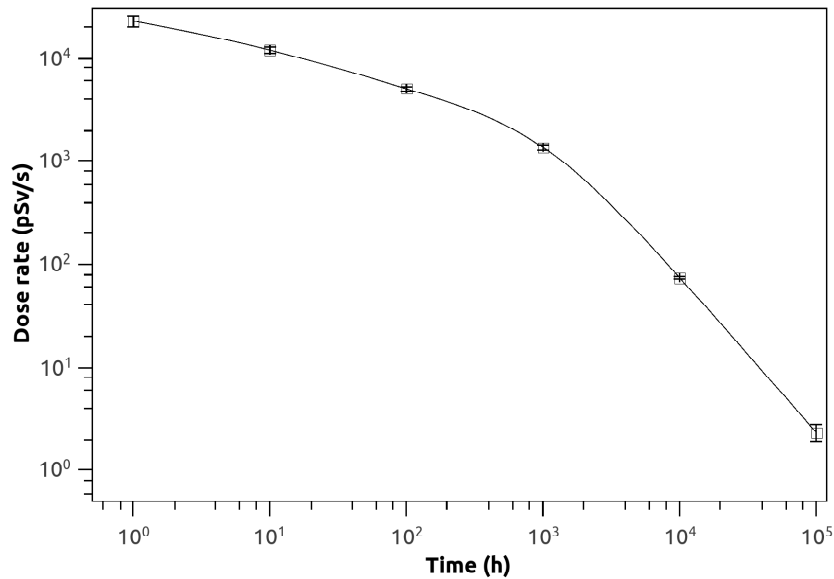


Figure 4.17: Variation of dose rate with different cooling times for Cu slab material

for copper, while the minimum ambient dose rate was found to be 1.12×10^4 pSv/s for concrete, immediately 1 hour after the shutdown of the beam. After a cooling period of 10^5 hours, the ambient dose rate falls off to 2.35 pSv/s for copper slabs, while for concrete, it falls off to 0.25 pSv/s. The minimum ambient dose rate was found for the material SS, 0.21 pSv/s, after the cooling period of 10^5 hours.

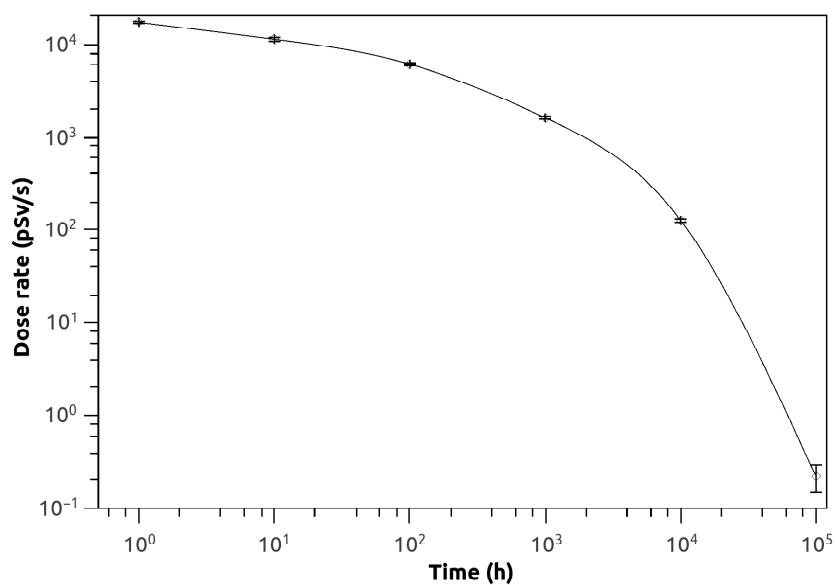


Figure 4.18: Variation of dose rate with different cooling times for SS slab material

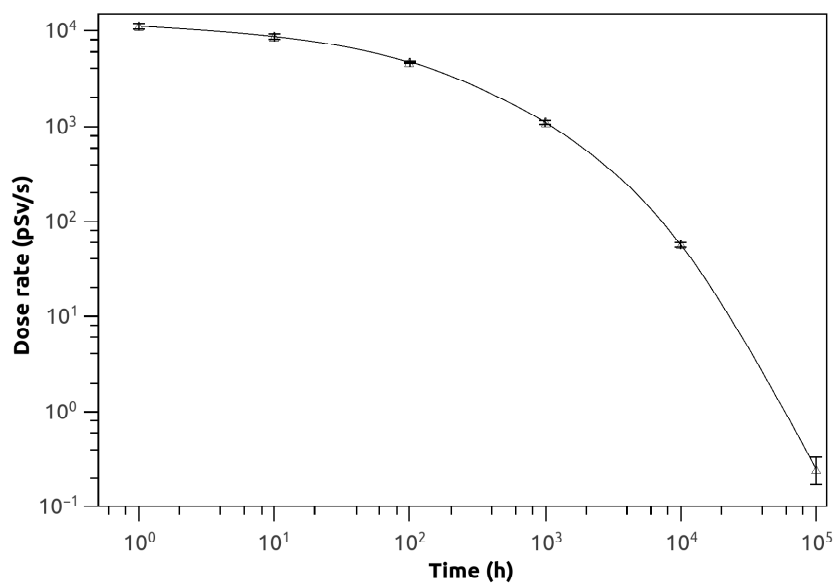


Figure 4.19: Variation of dose rate with different cooling times for Concrete slab material

4.3.2 Measurement of Residual Nuclei for SCC

Residual Nuclei measurements were carried out in the two slabs of various materials as well as for the primary target. The dimensions of the two cylindrical slabs have been mentioned earlier.

Residual Nuclei in SS target:

The interaction of 80 MeV proton with SS leads to the production of several residual nuclei and number of particles such as neutron, alpha, deuteron, triton, tritium, etc. The composition of SS (316L) is given in table 4.31. The density of SS is 8.0 g/cm³. Figure 4.20 shows the activity of ⁴⁹Cr after different cooling times. ⁴⁹Cr is a β emitter with a half life of 42.3 min. It is produced by various proton induced reaction with ^{nat}Fe, ^{nat}Cr, ^{nat}Ni and ^{nat}Mn. The reaction cross section at 80 MeV as calculated using TALYS [56] are 6.09555E+00 mb, 2.88421E+01 mb, 5.82118E-01 mb and 3.18745E+00 mb respectively.

Table 4.31: Composition of SS 316L used in FLUKA simulation

Element	Mass Fraction (%)
Cr	18.0
Mn	2.0
Ni	13.0
Fe	67.0

Figure 4.21 shows the activity of ⁶¹Co, ⁵⁷Ni, ⁵⁶Mn and ⁵⁵Co at various cooling times having T_{1/2} in hours. ⁶¹Co is a β emitter with a half life of 1.65 h. It is produced by neutron induced reactions. It is having a reaction cross section 4.09746E+01 mb at reaction threshold energy of 0.55 MeV. ⁵⁷Ni is a β emitter with a half life of 35.6 h. It is produced by proton induced reaction on ^{nat}Ni having reaction cross section of 5.98595E+01 mb at 80 MeV. ⁵⁶Mn is a β emitter with a half life of 2.58 h. It is produced by proton induced reaction with ^{nat}Fe and ^{nat}Ni having reaction cross section of 4.53628E-01 and 2.30900E-01 mb respectively.

Figure 4.22 shows the activity of ⁵⁹Fe, ⁵⁸Co, ⁵⁷Co, ⁵⁴Mn, ⁵²Mn, ⁵¹Cr, ⁴⁸V and

^{47}Sc at various cooling times having $T_{1/2}$ in days. ^{59}Fe is a beta emitter having half life of 44.5 days. It is produced by proton induced reaction with ^{nat}Ni having reaction cross section of 1.02771E-01 mb at 80 MeV. Typical reaction threshold for ^{64}Ni is 14.94 MeV. ^{58}Co decays through electron capture having a half life of 70.85 d. The reaction cross section is 32.76 mb. ^{57}Co decays by electron capture and is having a half life of 271.74 d. It is produced by proton reaction with ^{nat}Ni and ^{nat}Fe with reaction cross section of 9.18420E+01 mb and 2.24817E-01 mb respectively at 80 MeV. ^{54}Mn is a β emitter with a half life of 312.2 d. It is produced by proton reaction on ^{nat}Mn with reaction cross section of 1.22102E+02 mb. The threshold of the reaction is 8.15 MeV. ^{52}Mn is a β emitter with a half life of 5.591 d. ^{52}Mn is produced by proton induced reaction on ^{nat}Mn with a threshold at 23.15 MeV and reaction cross section of 5.86488E+01 mb at 80 MeV. ^{51}Cr decays by electron capture with $T_{1/2}$ of 27.7 d. It is a proton induced reaction end product on ^{nat}Cr with a reaction cross section of 1.33368E+02 mb. ^{48}V is a β emitter with $T_{1/2}$ of 15.97 d. ^{47}Sc is a β emitter with a half life of 3.35 d.

Figure 4.23 shows the activity of ^{60}Co and ^{55}Fe at different cooling times. ^{60}Co decays to ^{60}Ni through β decay, which further decays through γ radiation. It is having a half life of 5.26 years. It is produced through proton and neutron induced reaction on ^{nat}Ni . ^{55}Fe decays through electron capture with a half life of 2.744 years. It is produced through proton induced reaction with a total cross section of 1.34990E+02 mb at 80 MeV. The reaction threshold is 9.13 MeV for proton on ^{56}Fe .

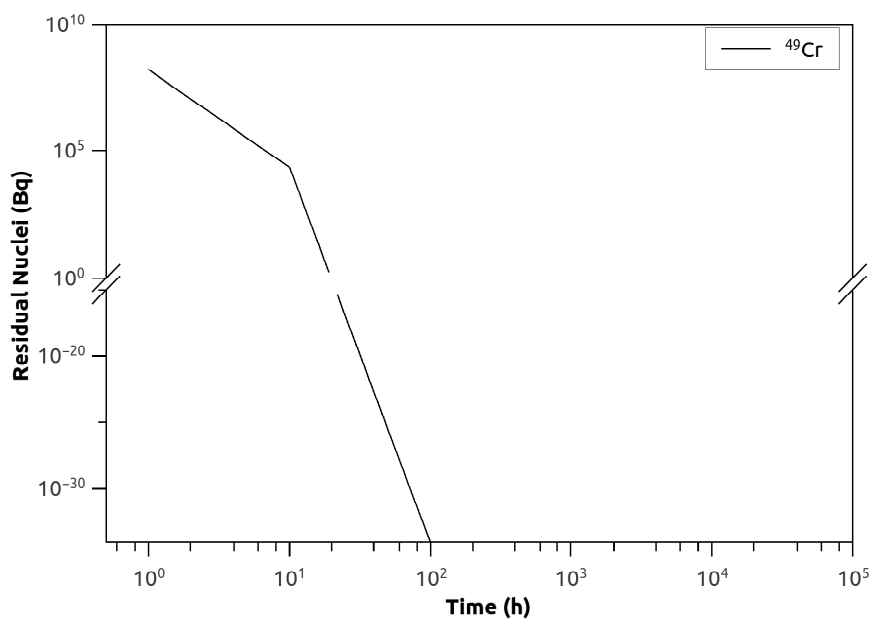


Figure 4.20: Variation of activity ($T_{1/2}$ in minutes) with different cooling times for SS primary target

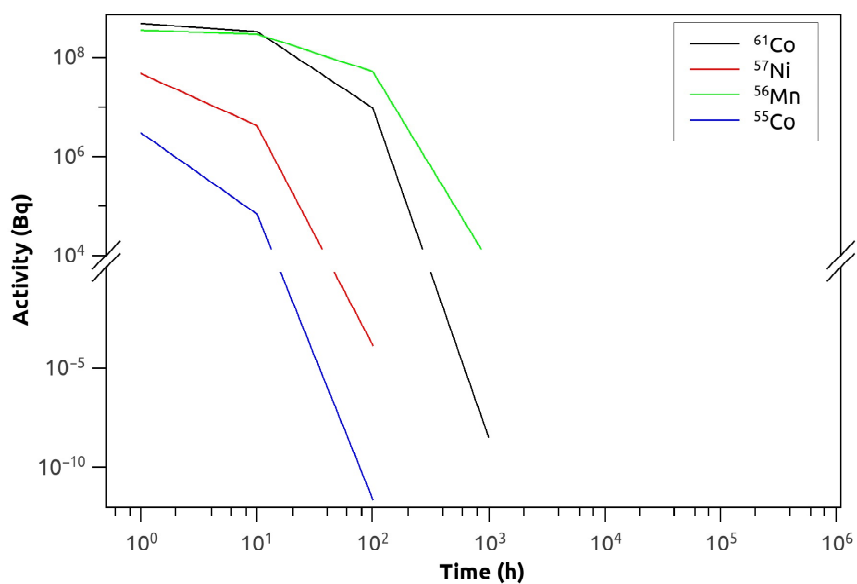


Figure 4.21: Variation of activity ($T_{1/2}$ in hours) with different cooling times for SS primary target

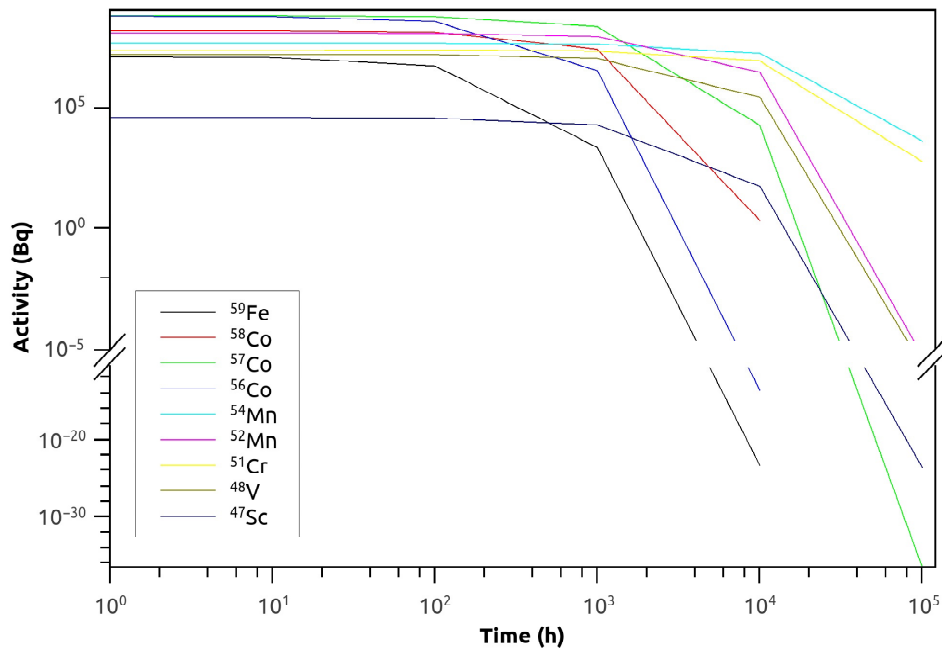


Figure 4.22: Variation of activity ($T_{1/2}$ in days) with different cooling times for SS primary target

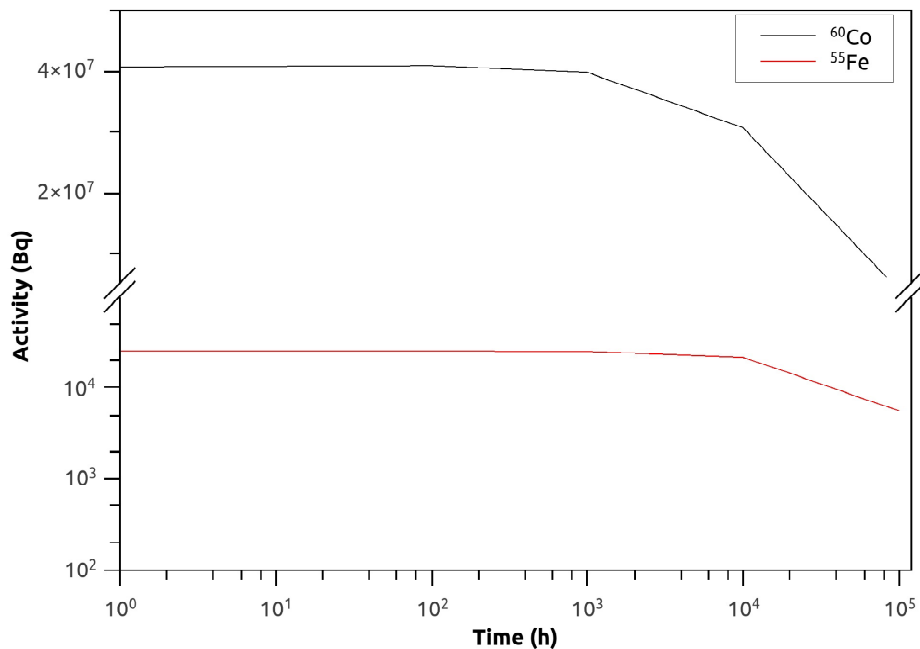


Figure 4.23: Variation of activity ($T_{1/2}$ in years) with different cooling times for SS primary target

Residual Nuclei in Cu (Slab 1):

Cu is naturally available with two isotopes namely, ^{63}Cu and ^{65}Cu with natural abundance of $\sim 69\%$ and $\sim 31\%$ respectively. The residual nuclei in the two slabs were generated due to the neutrons produced through the nuclear reaction of proton on the primary target. Figure 4.24 shows the activity of ^{66}Cu , ^{63}Zn , ^{62}Co , ^{62}Cu and ^{60}Cu having $T_{1/2}$ in minutes. ^{66}Cu is a β emitter with a half life of 51.2 m. It is produced through neutron induced reaction on ^{65}Cu with a reaction cross section of $1.83017\text{E}-01$ mb at 30 MeV and threshold energy is 7.065 MeV. ^{63}Zn decays through positron emission with a half life of 38.47 m. It is a product of proton induced reaction. ^{62}Co decays by β emission with a half life of 13.91 m. It is produced by ^{63}Cu having reaction cross section of $2.17811\text{E}+00$ mb and with ^{65}Cu of reaction cross section $3.84623\text{E}+00$ mb at 30 MeV. ^{62}Cu decays by positron emission with a half life of 9.67 m. The reaction cross section is $1.76302\text{E}-02$ mb with a threshold at 29.12 MeV on ^{65}Cu . ^{60}Cu decays through positron emission with a half life of 23.7 m. The variation of activity with different cooling time for ^{65}Ni , ^{64}Cu , ^{61}Co , ^{61}Cu and ^{56}Mn are shown in figure 4.25 having half life in hours. ^{65}Ni decays by β emission with a half life of 2.52 h. It is produced through neutron induced reaction on ^{65}Cu with a threshold at 1.38 MeV and having a reaction cross section of $1.47887\text{E}+01$ mb at 30 MeV. ^{64}Cu decays through both β^+ and β^- emission with a branching ratio of 61.5% and 38.5% with a half life of 12.7 h. Reaction cross section is $2.11152\text{E}-01$ mb for ^{63}Cu and $2.96076\text{E}+02$ mb for ^{65}Cu with a threshold at 10.06 MeV. ^{61}Co decays by β emission with a half life of 1.65 h. It is produced by neutrons on ^{63}Cu with a threshold at 9.69 MeV and a reaction cross section of $7.79846\text{E}+00$ mb at 30 MeV and also on ^{65}Cu with a threshold at 6.89 MeV and reaction cross section of $3.61421\text{E}+01$ mb at 30 MeV. ^{61}Cu decays by positron emission with a half life of 3.33 h. The reaction threshold for neutron on ^{63}Cu is 20.05 MeV and reaction cross section of $1.25959\text{E}+02$ mb at 30 MeV. ^{56}Mn decays by β emission with a half life of 2.58 h. The reaction threshold for neutron on ^{63}Cu is 5.53 MeV having a

reaction cross section of 3.61304E-01 mb at 30 MeV. Figure 4.26 shows the activity of ^{59}Fe , ^{58}Co , ^{57}Co , ^{56}Co and ^{54}Mn at different cooling periods. These isotopes are having their half lives in days. ^{59}Fe decays with β emission having maximum energy of 1.56 MeV with a half life of 44.49 d. Production through ^{63}Cu is having a threshold at 6.66 MeV and reaction cross section of 1.92632E+00 mb at 30 MeV. Again, production through ^{65}Cu is having a threshold at 16.15 MeV and reaction cross section of 1.36989E-03 mb at 30 MeV. ^{58}Co decays by positron emission with a half life of 70.86 d. ^{58}Co produced from ^{63}Cu is having a threshold of 16.49 MeV with reaction cross section of 3.83219E+01 mb at 30 MeV. ^{57}Co also decays through positron emission with a half life of 271.74 d. ^{56}Co is having a half life of 77.24 d. It decays through β^+ emission. ^{54}Mn is having a long half life of 312.12 d. Figure 4.27 shows the activity of various isotopes at different cooling periods with half lives in years. The isotopes shown in the figure are ^{63}Ni , ^{60}Fe , ^{59}Ni , ^{55}Fe and ^{53}Mn . ^{63}Ni decays by β emission with a half life of 101.2 y. Maximum energy of the β particles emitted by ^{63}Ni is 66.94 keV. Production through ^{63}Cu is having a reaction cross section of 1.96115E+01 mb at 30 MeV. With ^{65}Cu , the threshold is at 8.76 MeV and the reaction cross section is 1.23698E+02 mb at 30 MeV. ^{60}Fe decays through β emission with a half life of 2.62E+6 y. It is produced through neutron induced reaction on ^{65}Cu having threshold of 13.55 MeV and the reaction cross section is 3.64460E-02 mb at 30 MeV. ^{59}Ni decays by β^+ emission with a reaction threshold of 7.6E+4 y. End-point β energy is 50.5 keV. ^{55}Fe decays through positron emission with a half life of 2.744 y. ^{53}Mn decays through positron emission with a half life of 3.74E+6 y.

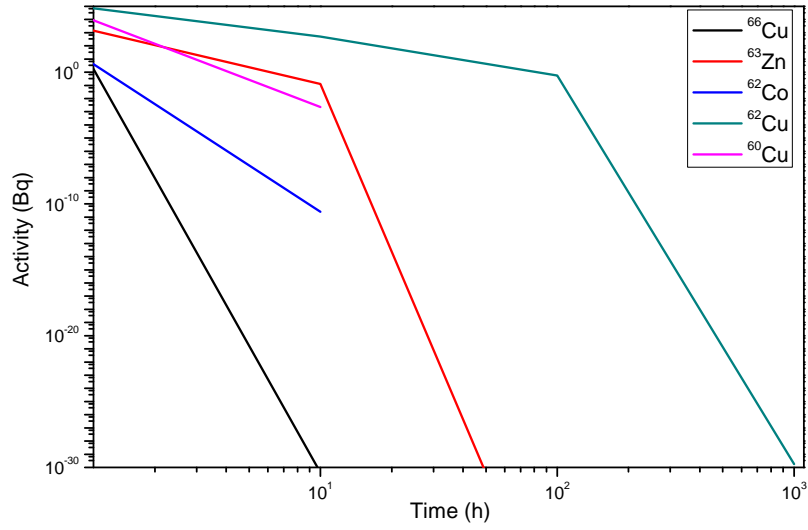


Figure 4.24: Variation of activity ($T_{1/2}$ in minutes) with different cooling times for Cu Slab1

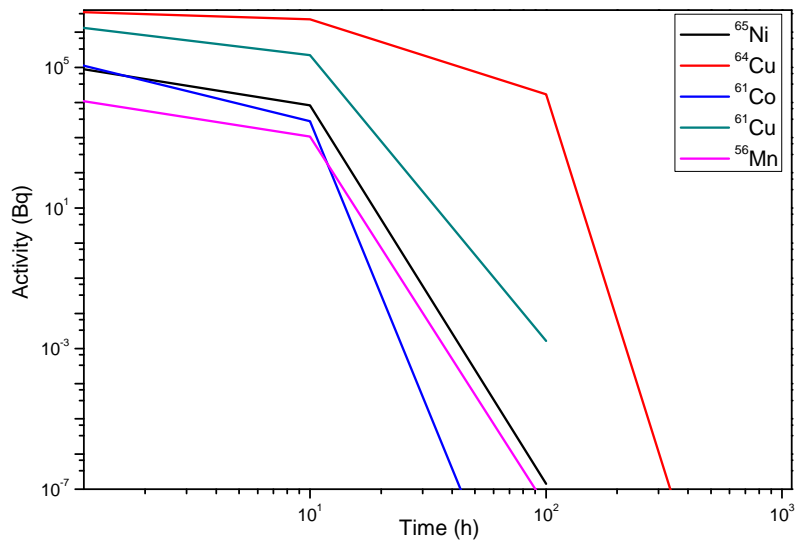


Figure 4.25: Variation of activity ($T_{1/2}$ in hours) with different cooling times for Cu Slab1

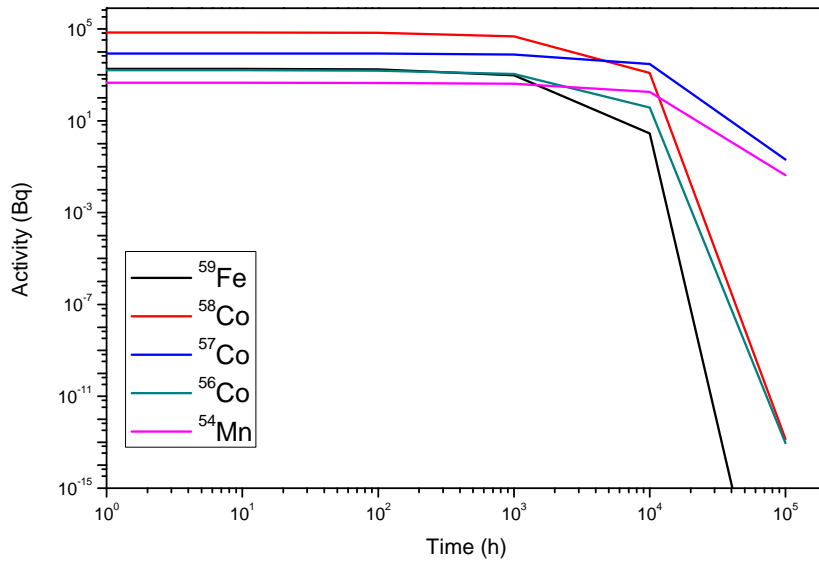


Figure 4.26: Variation of activity ($T_{1/2}$ in days) with different cooling times for Cu Slab1

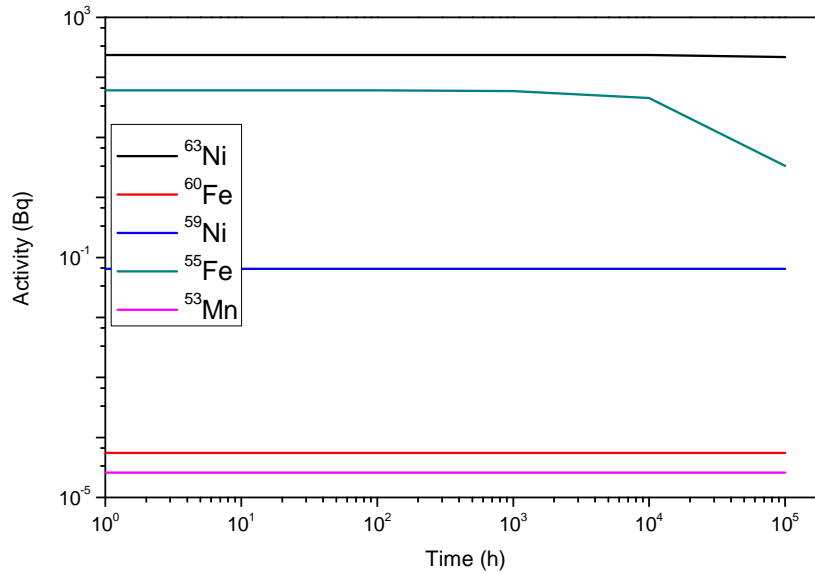


Figure 4.27: Variation of activity ($T_{1/2}$ in years) with different cooling times for Cu Slab1

Residual Nuclei in Concrete (Slab 1):

Concrete slabs with the dimensions as mentioned in figure 4.15 and the composition given earlier were used for the generation of the radio-nuclides from the neutrons coming from the primary target due to the proton bombardment. Figure 4.28 shows the radioisotopes having half lives in minutes. ^{38}K is a positron emitter with a maximum energy of 5.022 MeV. It is having a half life of 7.64 m. It is produced through n on Ca with a reaction threshold of 13.25 MeV and reaction cross section of $2.85418\text{E}+01$ mb at 30 MeV. ^{31}Si decays through beta emission having end point energy at 1.49 MeV. It is having a half life of 157.36 m. It is produced by interaction of n on Si. Reaction cross section is $1.65581\text{E}-01$ mb at 30 MeV. ^{29}Al is a β^- emitter with a half life of 6.56 m. It is produced through neutron induced reaction on ^{29}Si and ^{30}Si . ^{29}Si is having a threshold at 2.998 MeV with a cross section of $2.15260\text{E}+01$ mb at 30 MeV. ^{30}Si is having a threshold at 11.66 MeV with cross section of $1.42041\text{E}+02$ mb at 30 MeV. ^{18}F is a β^+ emitter with end point energy of 633.5 keV and half life of 109.77 m. It is produced in concrete by interaction of n on ^{24}Mg and ^{25}Mg . ^{24}Mg is having a threshold of 20.77 MeV and cross section of $3.77407\text{E}+00$ mb. ^{25}Mg is having a threshold of 21.85 MeV and cross section of $2.70309\text{E}-01$ mb. ^{13}N is a positron emitter with a half life of 9.965 m. End-point energy is 1.198 MeV. Production through ^{16}O is having a threshold of 26.61 MeV and cross section of $3.77421\text{E}-01$ mb. ^{11}C is a positron emitter with a end point energy of 960.4 keV and half life of 20.33 m. Total reaction cross section is $6.31180\text{E}+01$ mb for ^{nat}C at 30 MeV. Figure 4.29 shows the activity of ^{56}Mn , ^{42}K and ^{24}Na at different cooling periods with half lives in hours. ^{56}Mn decays to ^{56}Fe with the emission of β^- particles having maximum end point energy at 2.848 MeV and half life of 2.58 h. ^{42}K is a beta emitter with a half life of 12.36 h. Maximum end point energy of beta particles are 3.52 MeV. ^{42}K is produced through ^{42}Ca , ^{43}Ca and ^{44}Ca with n. Reaction threshold for ^{42}Ca is 2.809 MeV and cross section of $2.60560\text{E}+01$ mb. ^{43}Ca is having reaction threshold at 8.65 MeV with a cross section of $1.56604\text{E}+02$

mb. ^{44}Ca is having reaction threshold at 13.63 MeV and reaction cross section is $6.80195\text{E}+01$ mb at 30 MeV. ^{24}Na is a β emitter with a half life of 14.997 h. End point energy is 4.146 MeV. ^{24}Na is produced by neutron induced reaction on ^{24}Mg and ^{25}Mg with reaction threshold at 4.932 MeV and 10.236 MeV. Reaction cross sections are $1.34466\text{E}+01$ mb and $1.32531\text{E}+02$ mb respectively. Figure 4.30 shows the activity of ^{54}Mn , ^{37}Ar , ^{35}S , ^{32}P and ^7Be having half life in days at different cooling periods. The details of ^{54}Mn has been given earlier. ^{37}Ar is a positron emitter with a half life of 35.04 d. Reaction cross section for ^{40}Ca and ^{42}Ca are $2.39065\text{E}+01$ mb and $3.16365\text{E}+01$ mb respectively. ^{35}S is a beta emitter with a half life of 87.37 d. Maximum β energy is 167.33 keV. Production through ^{40}Ca with n is having a threshold energy at 15.31 MeV and cross section of $5.49068\text{E}-01$ mb at 30 MeV. It is also produced by neutron with ^{42}Ca having threshold at 6.63 MeV and cross section of $2.58353\text{E}+00$ mb. ^{32}P is a β emitter with end point energy of 1.71 MeV and $T_{1/2}$ of 14.268 d. It is produced through neutron induced reaction on ^{40}Ca with a threshold at 14.977 MeV and cross section of $8.13065\text{E}-02$ mb at 30 MeV. ^7Be is a pure β^+ emitter with a half life of 53.22 d. It is produced through ^{12}C with a threshold at 28.47 MeV and cross section of $4.24166\text{E}-03$ mb at 30 MeV.

Figure 4.31 shows the half life of ^{55}Fe , ^{53}Mn , ^{41}Ca , ^{40}K , ^{39}Ar , ^{26}Al , ^{22}Na , ^{14}C , ^{10}Be and ^3H at different cooling periods having $T_{1/2}$ in years. Details of ^{55}Fe and ^{53}Mn have been given earlier. ^{41}Ca is a positron emitter with a half life of $1.02\text{E}+5$ y. Production through ^{40}Ca , ^{42}Ca and ^{43}Ca are having cross sections of $1.75840\text{E}-01$ mb, $1.95775\text{E}+02$ mb and $1.41114\text{E}+02$ mb respectively. ^{40}K is β emitter with a branching ratio of 89.28%. It is having a half life of $1.248\text{E}+9$ y and end point β energy of 1.311 MeV. Cross sections for ^{40}Ca , ^{42}Ca and ^{43}Ca are $2.95353\text{E}+01$ mb, $1.68171\text{E}+02$ mb and $5.24422\text{E}+00$ mb respectively. ^{39}Ar is a pure β emitter with half life of 269 y and end point energy of 565.0 keV. Production through ^{40}Ca , ^{42}Ca and ^{43}Ca are having cross section of $2.14332\text{E}+01$ mb, $6.01040\text{E}+00$ mb and $4.79765\text{E}+01$ mb respectively. ^{26}Al is a β^+ emitter with a half life of $7.17\text{E}+5$ y. It

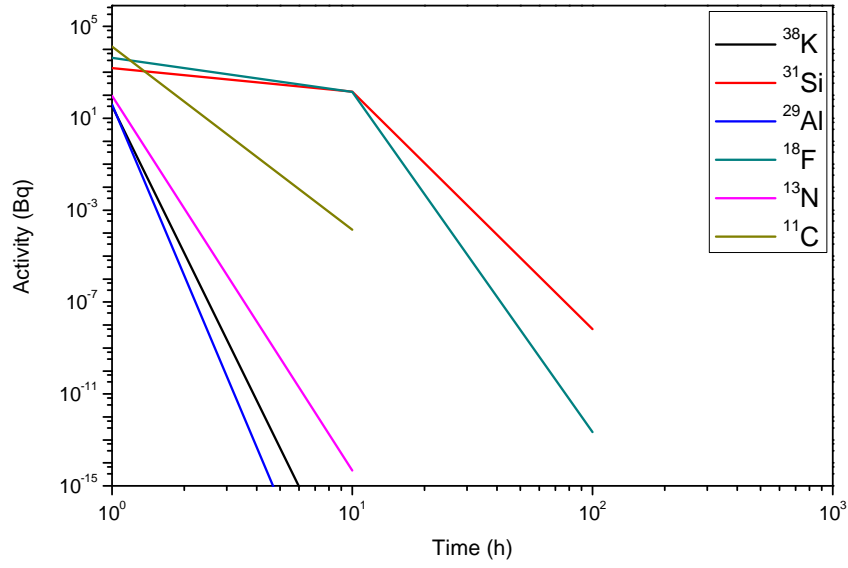


Figure 4.28: Variation of activity ($T_{1/2}$ in minutes) with different cooling times for Concrete Slab1

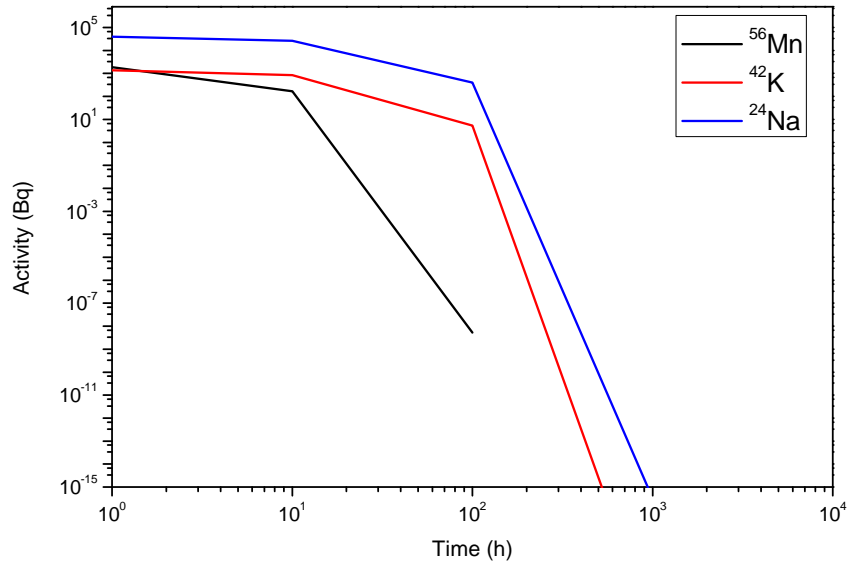


Figure 4.29: Variation of activity ($T_{1/2}$ in hours) with different cooling times for Concrete Slab1

is produced by interaction of neutron on ²⁸Si and ²⁹Si with a threshold at 16.825 MeV and 25.492 MeV. Cross sections are 1.73998E+01 mb and 4.18349E-01 mb respectively. ²²Na is a positron emitter with a half life of 2.603 y. Threshold energy

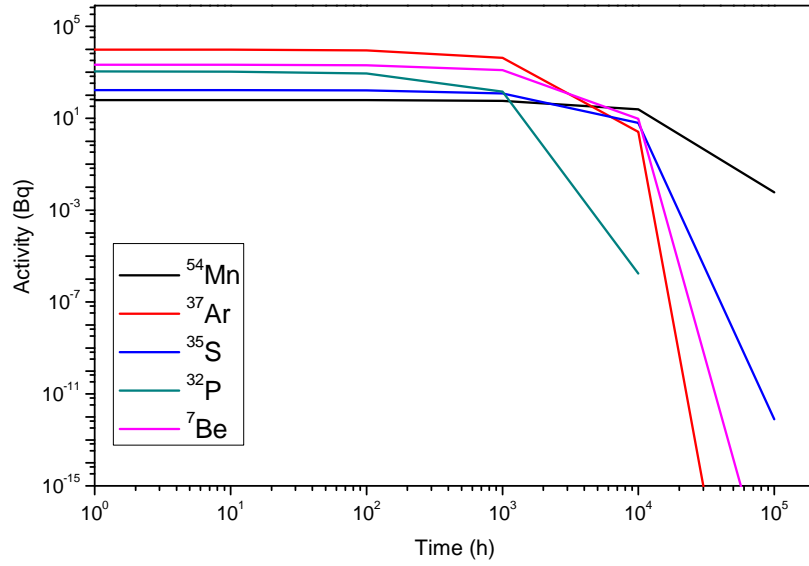


Figure 4.30: Variation of activity ($T_{1/2}$ in days) with different cooling times for Concrete Slab1

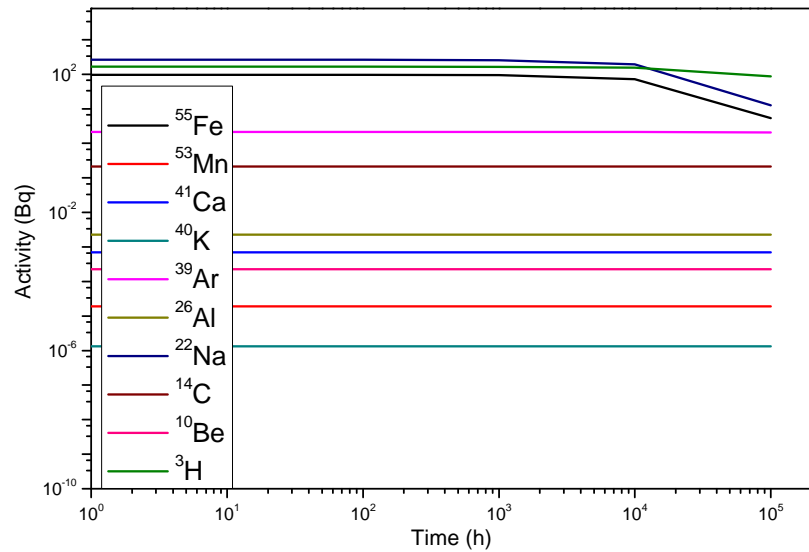


Figure 4.31: Variation of activity ($T_{1/2}$ in years) with different cooling times for Concrete Slab1

for ^{24}Mg and ^{25}Mg are 16.28 MeV and 23.88 MeV with cross section of $2.72916\text{E}+01$ mb and $1.68545\text{E}+00$ mb respectively. ^{14}C is a β emitter with a half life of 5700 y. End point energy is 156.47 keV. It is produced with the interaction of neutron

on ^{13}C having a cross section of $3.65845\text{E-}01$ mb at 30 MeV. ^{10}Be is a beta emitter with a half life of $1.387\text{E+}6$ y. End point β energy is 556.0 keV. Production through ^{12}C and ^{13}C is having a threshold energy at 21.10 MeV and 4.131 MeV respectively. Cross sections are $1.29987\text{E+}00$ mb and $3.06404\text{E+}00$ mb respectively. ^3H is a β emitter with a half life of 12.32 y and end point energy of 18.591 keV. The production of ^3H is with the interaction of neutron with various atoms of element present in Concrete.

Residual Nuclei in Aluminium (Slab 1):

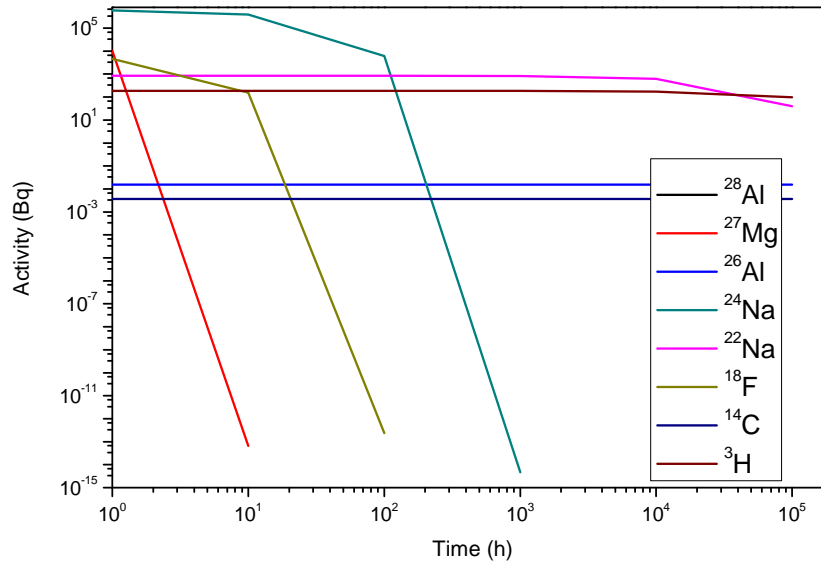


Figure 4.32: Variation of activity with different cooling times for Aluminium Slab1

Figure 4.32 shows the variation of activity of various isotopes produced by interaction of Al with neutron at different cooling periods. ^{28}Al is a β emitter with a half life of 2.24 m. End point β energy is 2.86 MeV. Cross section of production for neutron on ^{27}Al is $1.25524\text{E-}01$ mb at 30.0 MeV. ^{27}Mg is a β emitter with end point energy of 1.766 MeV and half life of 9.458 m. It is produced by the interaction of neutron on ^{27}Al with a threshold energy of 1.895 MeV and cross section of $7.04159\text{E+}00$ mb at 30 MeV. ^{26}Al is produced from ^{27}Al with a threshold of 13.54

MeV and cross section of $8.41950\text{E}+01$ mb. ^{24}Na produced from ^{27}Al is having a threshold of 3.249 MeV and cross section of $8.35635\text{E}+00$ mb. Production of ^{22}Na is having a threshold of 23.35 MeV and cross section of $1.26817\text{E}+00$ mb. ^{18}F , ^{14}C and ^3H is produced by the interaction of other particles generated due to the reaction of neutron with ^{27}Al . Among all the isotopes produced, the activity of ^{24}Na is the highest and ^{28}Al is the least.

Chapter 5

Shielding of Beam Dump

5.1 Introduction

Thin targets are required for Nuclear physics experiments for measuring excitation functions, pre-equilibrium emission processes, fission dynamics and time scales etc. The accelerated positive ion beam from the cyclotron passes through the target, which is desired. As a consequence, the rest of the beam requires to be dumped on some material, so that no interference from that event influences the experimental set up. The residual beam which is dumped on some material is called “beam dump”. Since the beam after falling on the dump under goes nuclear reactions, it is one of the major source of radiation which influences the experimental detectors. Moreover the unwanted radiation produced in the beam dump may increase the load on data acquisition system and cause significant radiation damage in detectors and electronics. The major objective of this study is the shielding of this beam dump. In this study, Monte Carlo code FLUKA has been utilized to design a suitable shield of the beam dump at K-130 cyclotron, VECC.

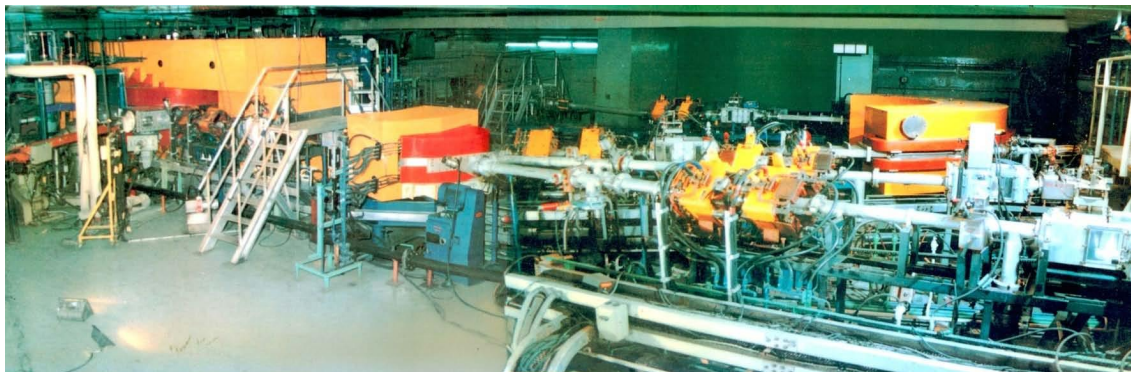


Figure 5.1: K-130 Cyclotron at VECC, Kolkata showing beam lines and main magnet



ECR-based Low Energy ion Beam Facility

Figure 5.2: ECR ion source of K-130 Cyclotron at VECC, Kolkata

5.1.1 General description of K-130 Cyclotron

K-130 cyclotron is one of the accelerator [18], which is operation at this centre since 1980. It has been delivering positive ion beams since then to many users. It is a sector focused isochronous cyclotron with three spiral sectors. The water cooled room temperature main magnet of diameter 224 cm, produces a maximum magnetic field of 21.5 kG in the pole gap. The cyclotron is capable of delivering protons from 6 to 60 MeV, deuterons from 12 to 65 MeV and alpha particles from 25 to 130 MeV using an internal Penning Ion Gauge (PIG) type ion source. The cyclotron can also accelerate heavy ions like nitrogen, oxygen, neon, argon with different charge states using an external Electron Cyclotron Resonance (ECR) ion source. External ECR ion source is shown in figure 5.2 The extracted beam current ranges from a few

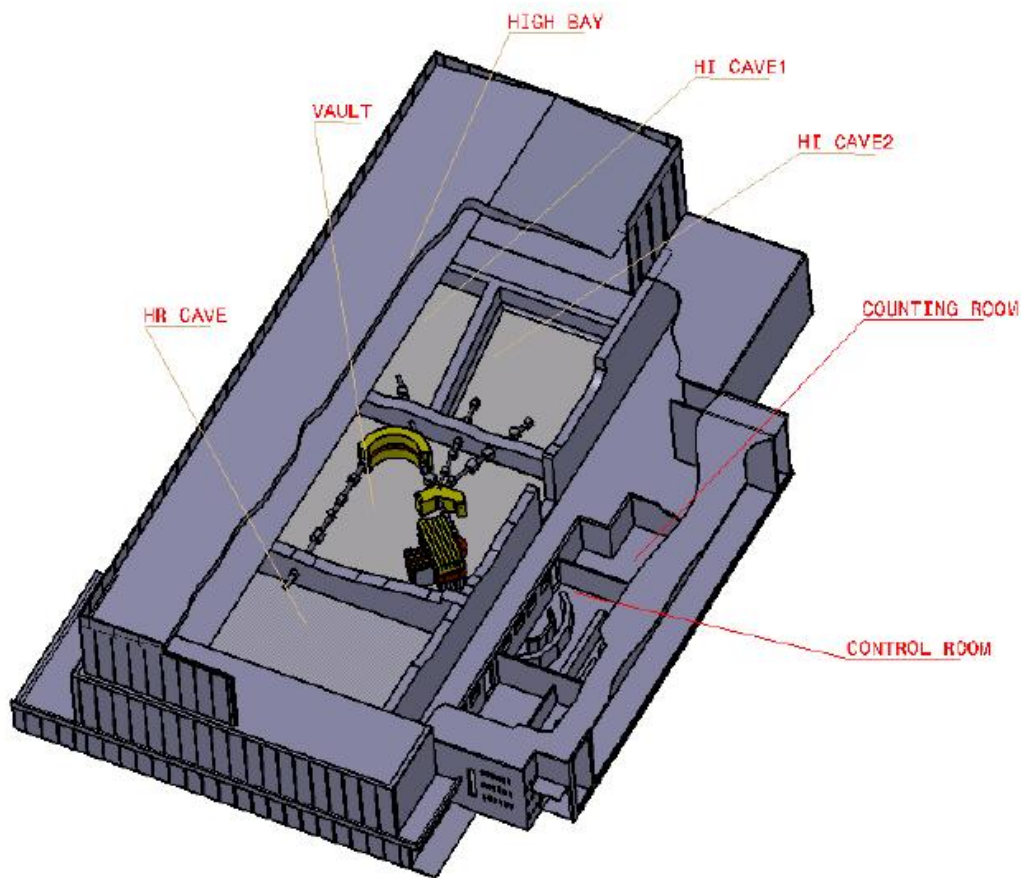


Figure 5.3: Layout of K-130 Cyclotron at VECC, Kolkata

pico-amperes to tens of micro-amperes. The layout of K-130 cyclotron at VECC is shown in figure 5.3.

5.2 Shielding Calculations of Beam Dump

The shielding calculations of the beam dump was carried out for the 3rd beam line of K-130 Cyclotron of VECC. The figure 5.4 shows the position of the beam dump along with the target chamber and the part of the beam line, which is used extensively for the experiments of Nuclear Physics and related studies. The target chamber of made up of SS304 with an outer diameter of 310.0 mm and a height of 140.0 mm. It is having a thickness of 10.0 mm. The beam line is made up of alu-

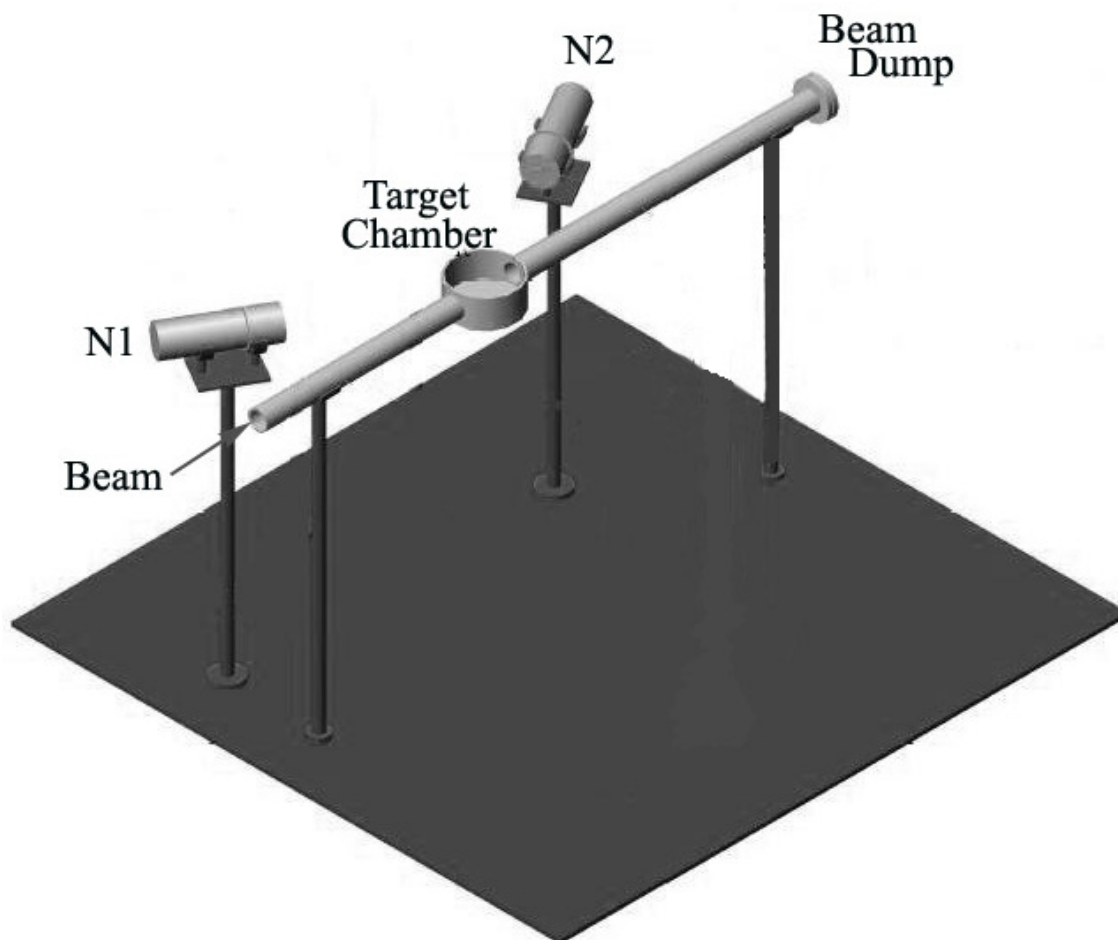


Figure 5.4: The 3rd beam line of K-130 Cyclotron with beam dump

minium having a thickness of 10.0 mm and a radius of 50.8 mm. The center of the target chamber and the beam dump is at a distance of 2840.0 mm. Beam dump is a graphite block of size 40 mm x 40 mm with a thickness of 15.0 mm. The beam line and the target chamber was considered inside a concrete shielded room having inner dimensions of 327.0 cm x 1490.0 cm and a height of 1064.0 cm, generally called “cave 2”. Concrete shielding of 150.0 cm was placed at each side of the wall. The shielding calculations were carried out for 50 MeV α -particles. The particles were made to interact with ^{181}Ta target having a thickness of 1.0 mg/cm². This study was carried out with Monte Carlo Code FLUKA (version 2011.2b.3). Neutron and Photon detectors used in this study was placed at a distance of 150 cm from the target at an angle of 150° and 15° as shown in figure 5.4 marked as N1 and N2. These two angles

were chosen to find the contribution of neutron and photon fluence at forward angle and backward angle. The goal of this study was to design a suitable shield of this beam dump, so that the neutron and photon fluence arising from the interaction of the beam particle is contributing minimum at the detector positions. The shielding calculations were carried out with High Density Polyethylene (HDPE), Lead and Iron. The material composition and density of Polyethylene used in the simulation geometry was $(C_2H_4)_n$ with a density of 1.0 g/cm^3 . Lead (Pb) was having a density of 11.35 g/cm^3 . Concrete shielding of the wall was having C (23.0%), O (40.0%), Si (12.0%), Ca (12.0%), H (10.0%) and Mg (2.0%) with a density of 2.35 g/cm^3 . Fe was taken with a density of 7.874 g/cm^3 . Advantages of using polyethylene is the large hydrogen content, ease of fabrication and its low weight, which can effectively slow down the high energy neutrons to thermal neutrons. Pb was considered for photon shielding because of its high atomic number (82). The variation of mass attenuation coefficient for Pb is shown in figure 5.5.

To evaluate the efficiency of different types of shielding designs for neutrons and photons arising from the beam dump, the neutron and photon fluence at the detector positions were compared with respect to a shield comprising of a hypothetical region, called “Black hole”. This region is also used outside the geometry of interest in any Monte Carlo code to stop the tracking of any particles reaching it. Therefore Black hole corroborates an ideal beam dump shielding condition.

Table 5.1 shows the neutron and photon fluence in units of $\text{no./GeV/cm}^2/\text{incident}$

Table 5.1: Neutron and Photon fluence at two detector positions

Type of Shield	Neutron Fluence			
	at 15°	Err %	at 150°	Err %
With No Shield	2.231E-05	2.90	7.892E-06	1.55
With Black Hole	2.019E-06	5.74	6.839E-07	13.04
Type of Shield	Photon Fluence			
	at 15°	Err %	at 150°	Err %
With No Shield	6.305E-05	2.27	1.090E-05	4.64
With Black Hole	3.193E-06	5.70	5.103E-07	7.10

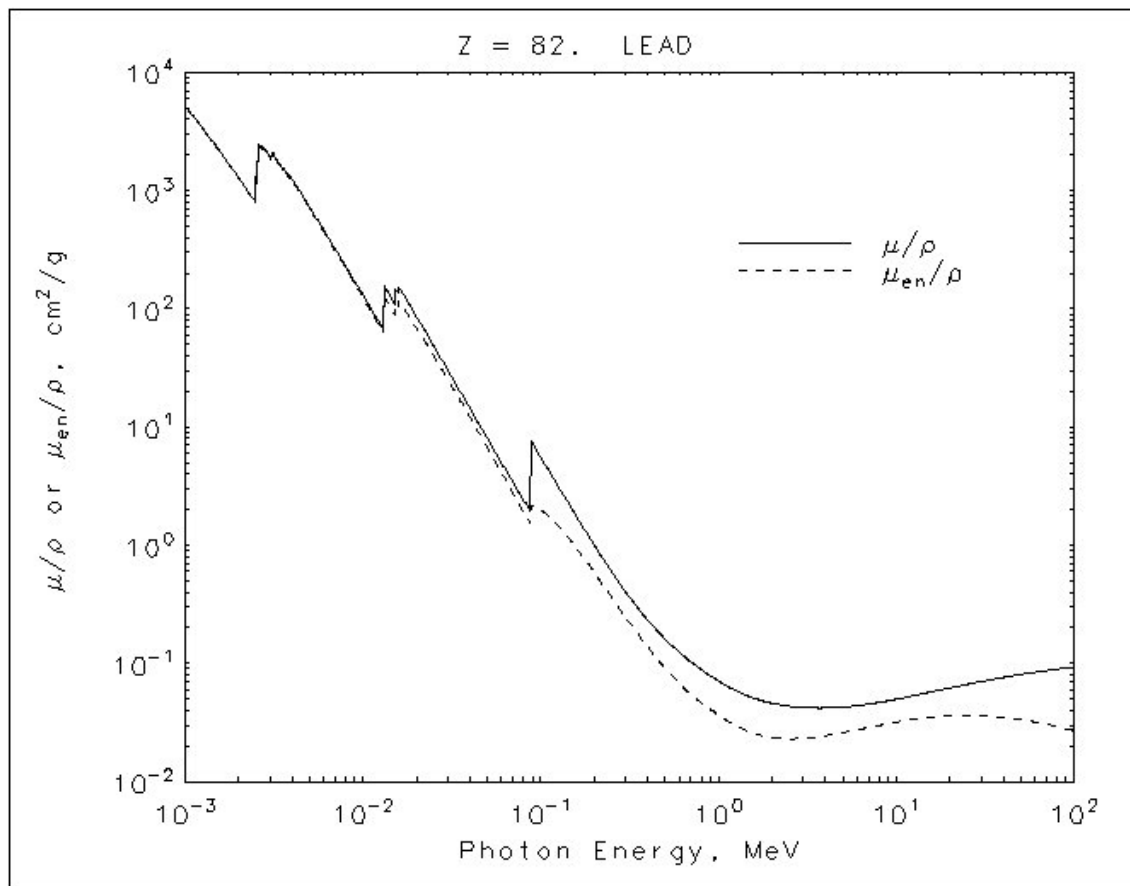


Figure 5.5: Variation of mass attenuation coefficient for Pb

particle at two detector positions, namely N1 and N2. In both the cases of “No Shield” and “Black hole”, there were contributions of neutrons and photons from the Ta^{181} target as well, which was also bombarded with 50 MeV α particles. Contribution to 15° detector is always more than the 150° detector due to more forward scattering of the particles, after undergoing nuclear reaction in the target. The ratio of the neutron fluence without shield to that of with black hole shield at 15° is 11.05. The same ratio for 150° detector is 11.54. The ratio of the photon fluence without shield to that with black hole shield at 15° detector position is 19.75. The same ratio at 150° detector position is 21.36.

Figure 5.6 shows different trial designs of the shielding for beam dump. Figure 5.6(a) shows the design made up of HDPE and Fe. Both HDPE and Fe were having cylindrical geometry with a radial thickness of 25.0 cm. The thickness of Fe was 10

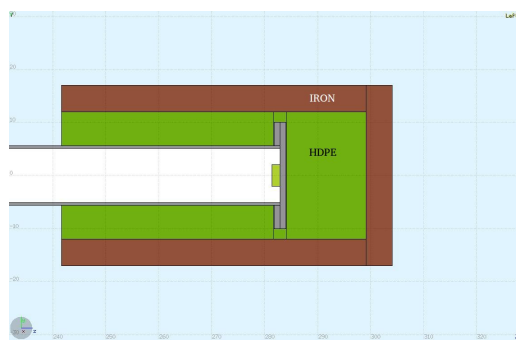
cm and that of HDPE was 40 cm. Next figure 5.6(b) shows the shield design, where additional shielding was put at the far end side of the beam dump. It comprised of additional HDPE thickness of 15.0 cm and Fe of 5.0 cm with the same radial thickness of 25.0 cm. In the third trial design as shown in figure 5.6(c), concentric cylinders of HDPE and Fe were used. Here the HDPE cylinder was having a radial thickness of only 6.42 cm. 5.0 cm thick Fe was used radially over HDPE. In figure 5.6(d), additional Fe thickness of 5.0 cm has been added in the front side of the shield design. Figure 5.6(e) shows the design where the Fe has been replaced with 5.0 cm thick Pb. Moreover, another 10.0 cm thick HDPE has been added on all sides. The final shield design has been shown in figure 5.7. It comprises of HDPE immediately outside side the beam line with beam dump. It is followed by Pb which is further shielded inside HDPE. Different thicknesses of Pb have been used at different sides. The whole shielding is enclosed in a cylindrical geometry of Fe having a thickness of 5.0 cm. Figure 5.8 shows the three dimensional geometry of the beam dump shield, with a cut out view, showing the inner shielding materials. Inside blue coloured material represents Pb and the outer most material is Fe. Rest of the materials are HDPE. Inside the beam line, the graphite beam dump is also seen in the figure.



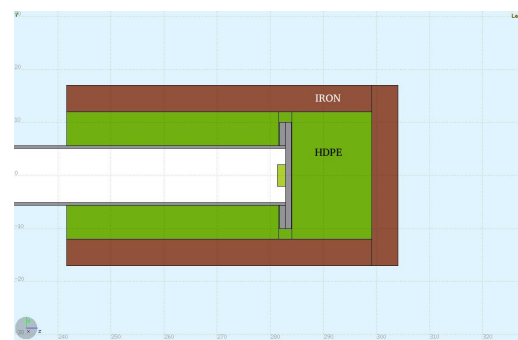
(a) First design of shield



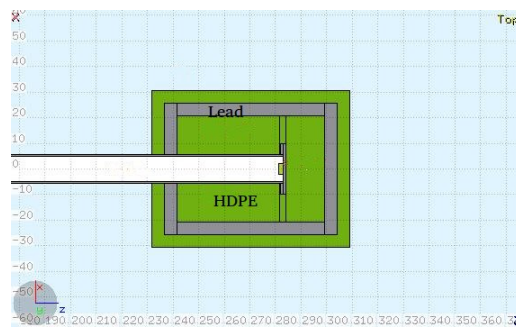
(b) Second design of shield



(c) Third design of shield



(d) Fourth design of shield



(e) Fifth design of shield

Figure 5.6: Different trial designs of Shielding of beam dump

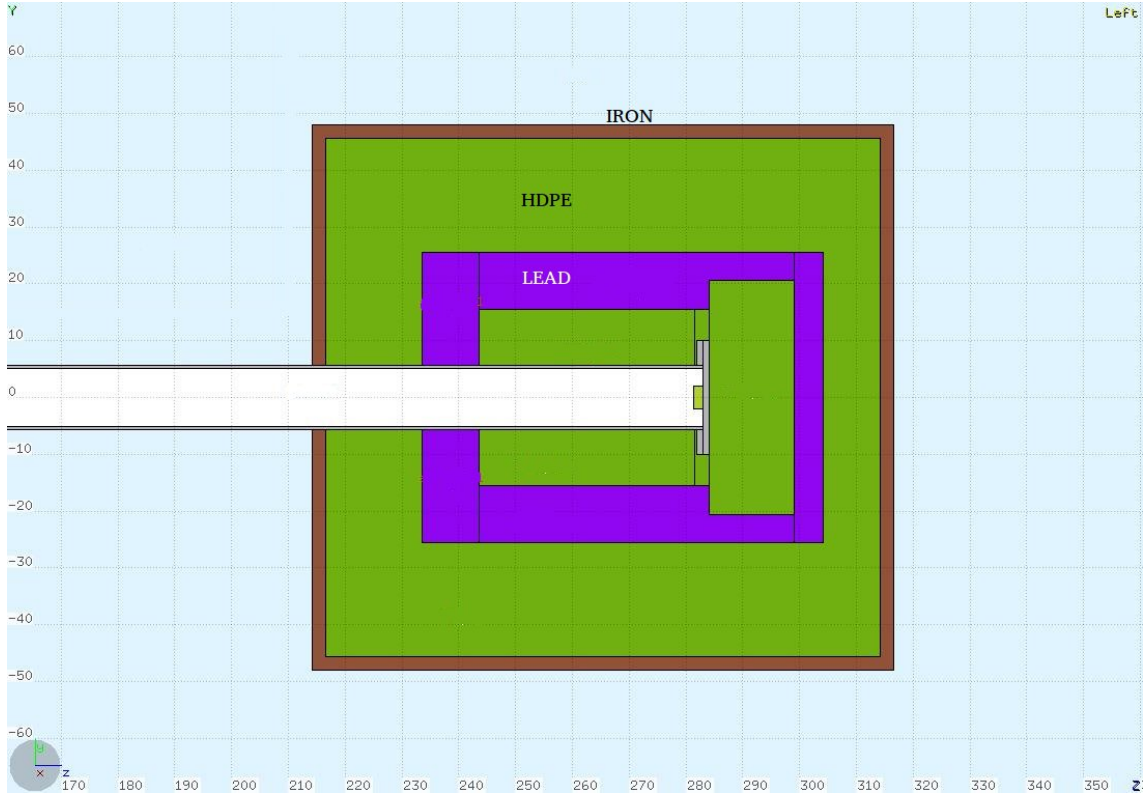


Figure 5.7: The final design of the shielding of beam dump for 3rd beam line of K-130 Cyclotron

Table 5.2: Neutron fluence at two detector positions with different designs of beam dump shielding

Design figure no	Neutron Fluence at detector positions			
	15 °	Error %	150 °	Error %
Figure 5.3 (a)	8.890E-06	13.144	4.222E-06	9.049
Figure 5.3 (b)	4.189E-06	8.925	1.889E-06	11.243
Figure 5.3 (c)	9.157E-06	3.939	3.136E-06	13.601
Figure 5.3 (d)	4.540E-06	13.387	1.720E-06	17.952
Figure 5.3 (e)	3.843E-06	22.763	1.453E-06	17.830
Figure 5.4	2.423E-06	4.707	1.003E-06	14.611

Table 5.2 shows the neutron fluence in units of neutrons/cm²/GeV/primary at two detector positions of 15° and 150°. Both the neutron fluence values are lowest for the final shield design. This is also shown as histogram plot in figure 5.9.

Table 5.3 shows the photon fluence in units of photons/cm²/GeV/primary at two detector positions of 15 ° and 150 °. The photon fluence at the detector positions are the lowest for the final design of the beam dump shield. This is also shown as

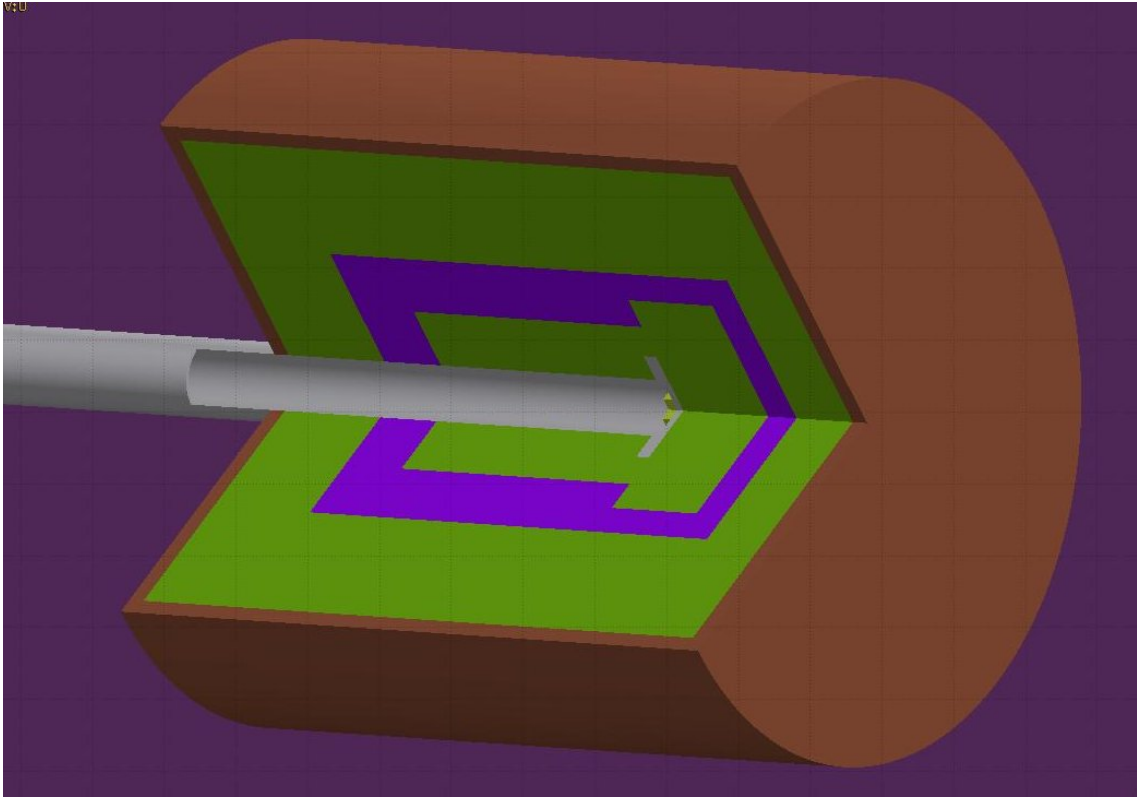


Figure 5.8: The 3D design of the shielding of beam dump

Table 5.3: Photon fluence at two detector positions with different designs of beam dump shielding

Design figure no	Photon fluence at detector positions			
	15 degree	Error %	150 degree	Error %
Figure 5.3 (a)	1.835E-05	2.767	4.371E-06	4.082
Figure 5.3 (b)	1.941E-05	1.042	4.849E-06	11.160
Figure 5.3 (c)	3.654E-05	3.062	7.678E-06	7.363
Figure 5.3 (d)	2.199E-05	3.769	4.214E-06	9.994
Figure 5.3 (e)	8.608E-06	4.381	1.464E-06	24.103
Figure 5.4	4.947E-06	7.801	6.459E-07	14.681

histogram plot in figure 5.10.

It can be further seen from table 5.1 and table 5.2 that the ratio of the neutron fluence with final shield design to that with black hole at 15° detector position is 1.20. The same ratio for 150° detector position is 1.47. From table 5.1 and table 5.3, it can be seen that the ratio of the photon fluence with final shield design to that with black hole at 15° detector position is 1.55. The same ratio at the detector position of 150° is only 1.26. So, the neutron fluence reduction with the final shield

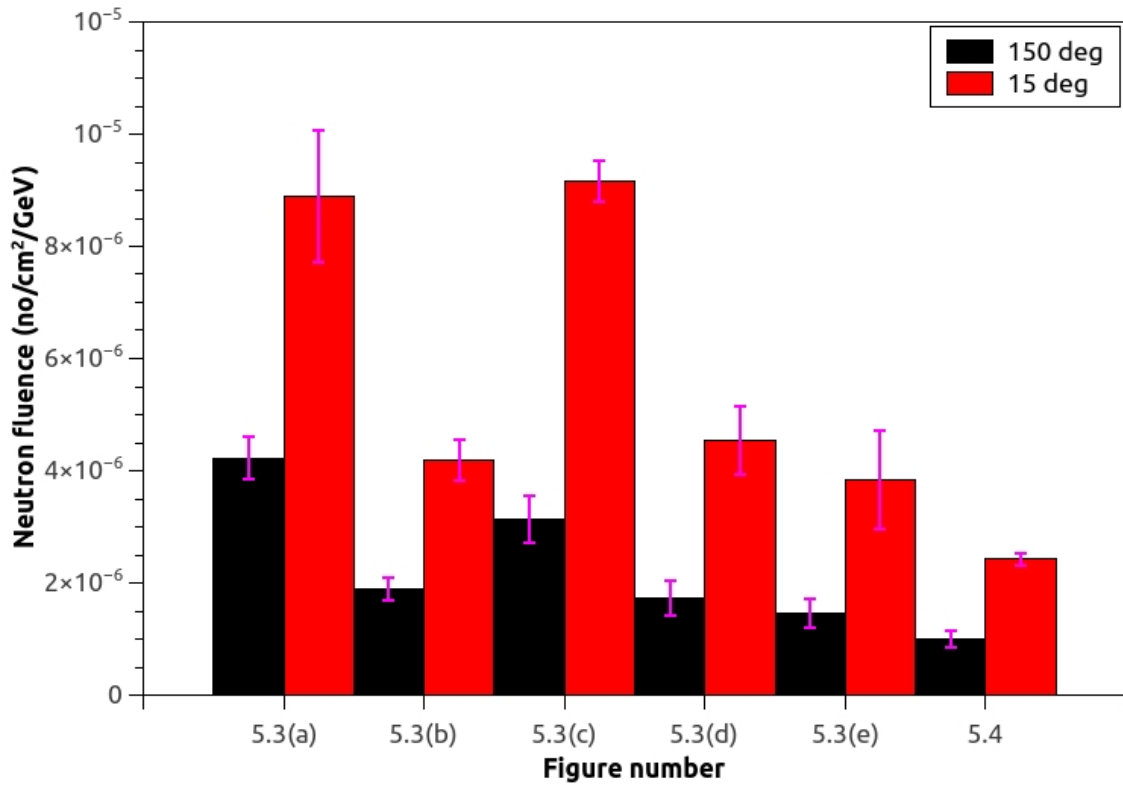


Figure 5.9: Neutron fluence histogram plot for different figures which have different shielding of beam dump

design at 15° detector position is 9.21 times and at 150° detector position is 7.85 times. The photon fluence reduction at 15° detector position is 12.74 times and at 150° detector position is 16.95 times.

Figure 5.11(a) and 5.12(a) shows the spatial distribution of the neutron and photon fluence around the geometry of interest, along with two detector positions N1 and N2 respectively, without any shielding around the beam dump. The colour code band in the right hand side shows the intensity at various positions, with black color showing the highest and the white as lowest. With the final design of the beam dump shield, the neutron and photon fluence spatial distributions are shown in figures 5.11(b) and 5.12(b). In both the cases, the neutron and photon fluence contribution from the Ta¹⁸¹ is also present. A significant reduction in both the neutron and photon fluence can be seen with the addition of final shield design around the beam dump.

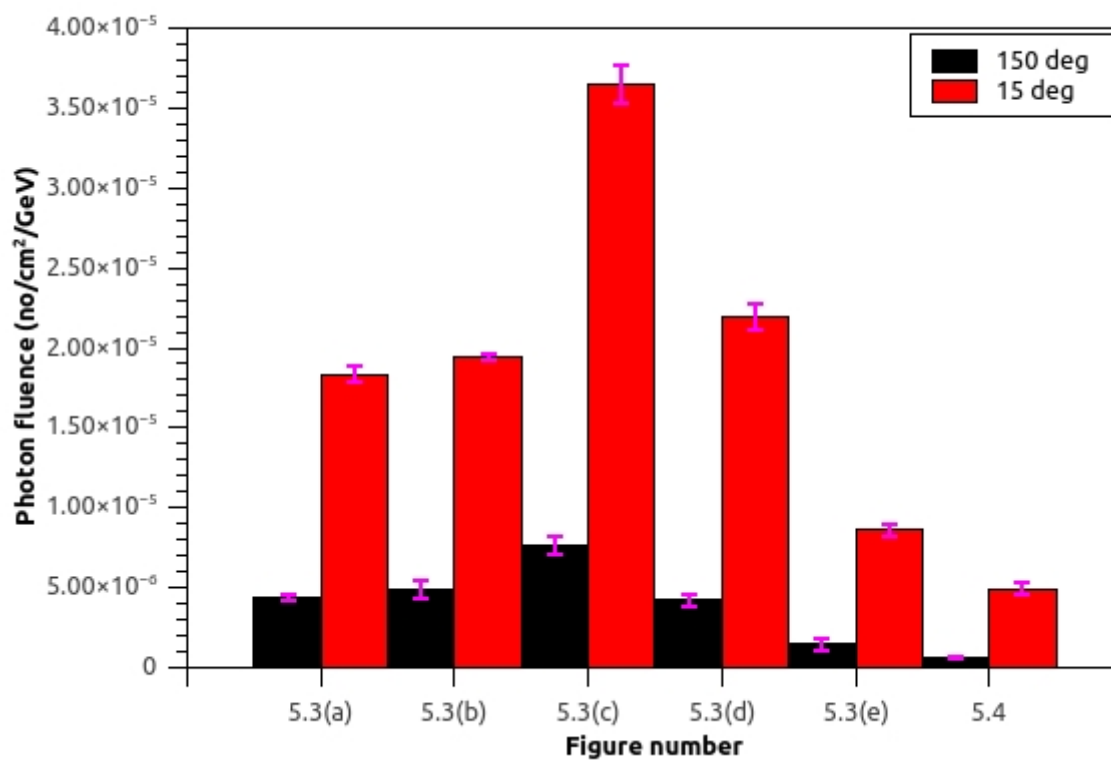


Figure 5.10: Photon fluence histogram plot for different figures which have different shielding of beam dump

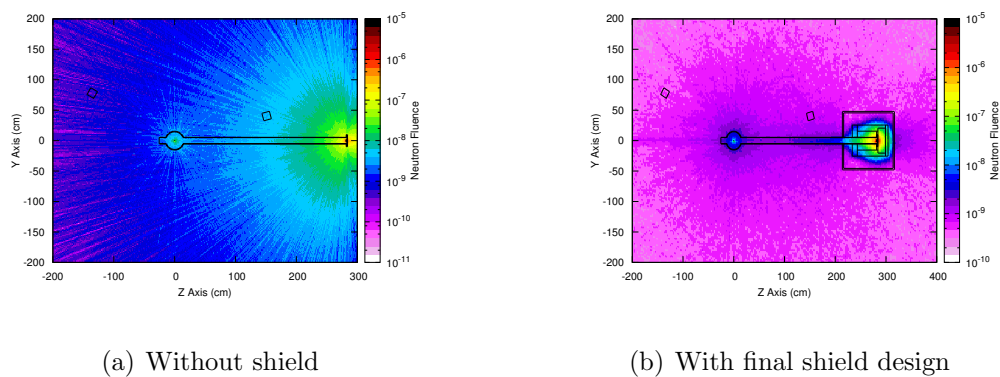


Figure 5.11: Spatial Distribution of neutron fluence without shield and with final design shield

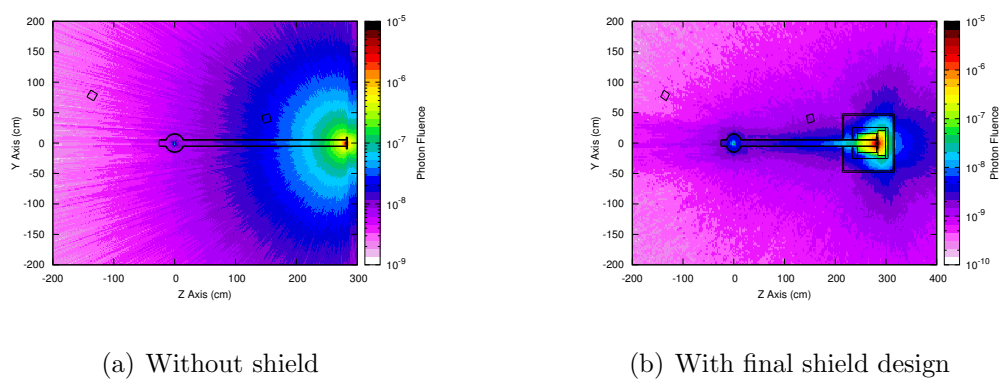


Figure 5.12: Spatial Distribution of photon fluence without shield and with final design shield

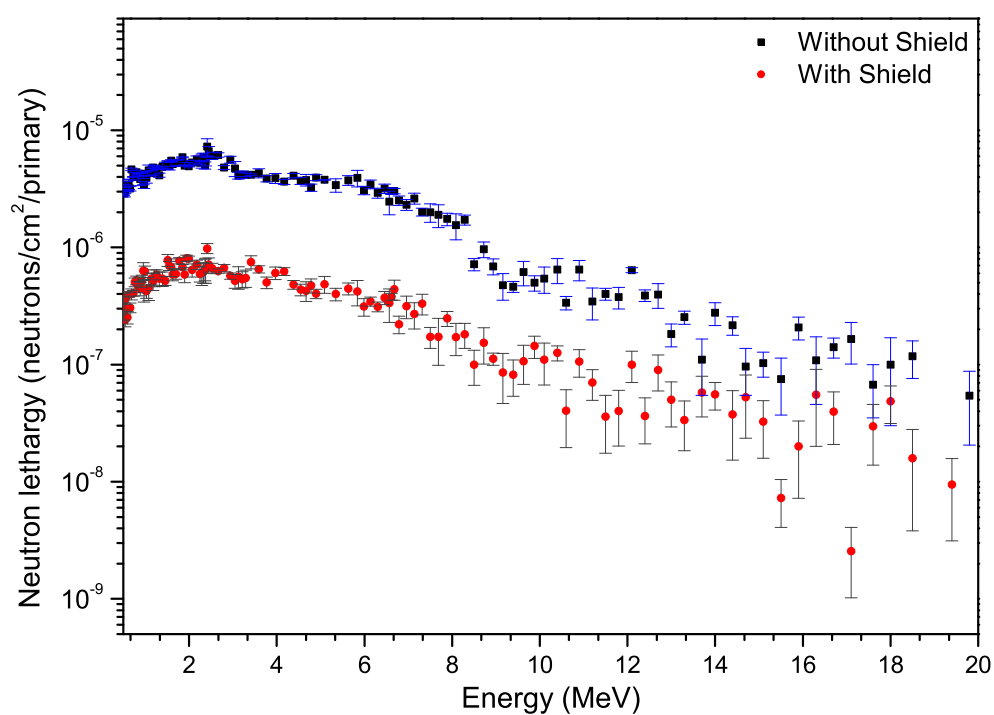


Figure 5.13: The spectral energy distribution of neutrons, without and with beam dump shield

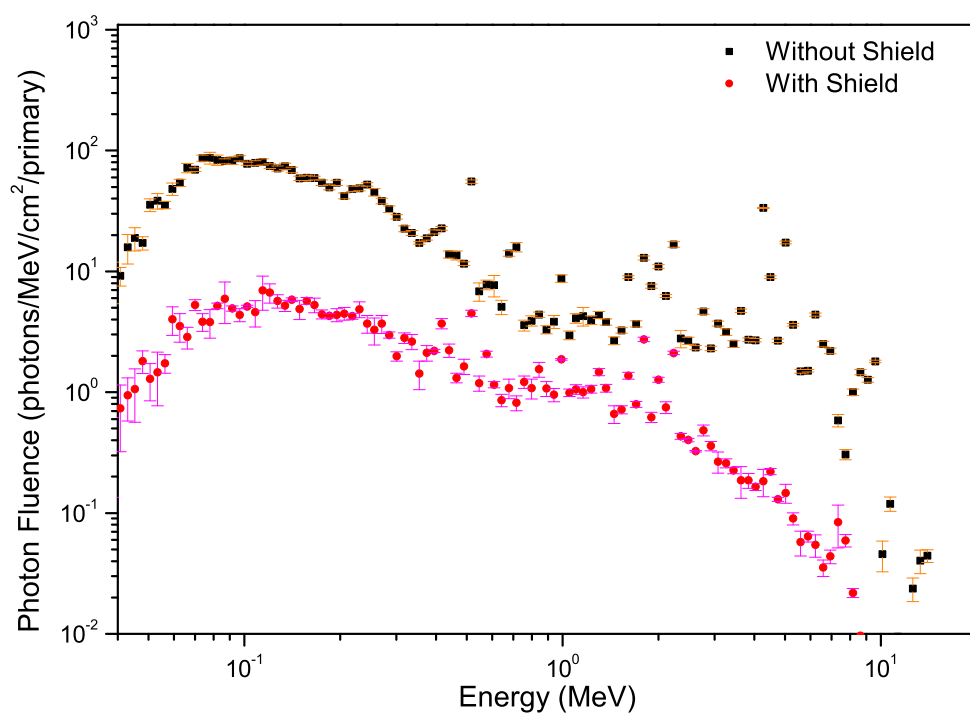


Figure 5.14: The spectral energy distribution of photons, without and with beam dump shield

The neutron and photon spectral energy distribution was also measured at N2, the detector at 15° position. This spectral distribution of neutrons and photons had contribution from Ta¹⁸¹ target bombarded with 50 MeV α particle as well as from the graphite beam dump, which produced neutrons and photons after various nuclear reactions. Figure 5.13 shows the semi-log plot of the neutrons without shield and with final shield design. The plot without shield shows a peak around 2.5 MeV, after which the contribution decreases. Figure 5.14 shows the log-log plot of the photons without and with final shield design of the beam dump. The photon spectrum shows a broad peak around 140 keV. Characteristic peaks from the prompt gamma rays can also be seen in the figure.

5.3 Experimental determination of Neutron and Photon spectra

5.3.1 Experimental determination of Neutron spectrum

Experimental determination of the neutron spectrum with different shielding configurations was carried out with Liquid Scintillator detector (BC501A) using Time of Flight (TOF) technique. The TOF technique [57] is a general technique for determining the kinetic energy of a travelling neutron, by measuring the time it takes to fly between two fixed points separated by a fixed distance. Liquid scintillator based detectors are generally used for this purpose because of its high light output, better detection efficiency and good gamma discrimination. Gamma discrimination is very well required for the neutron spectroscopy as in such cases, there is a huge gamma shower due to the nuclear interactions. BC-501A (manufactured by M/s Saint-Gobain) is one of the popular liquid scintillators used worldwide for neutron detection. This liquid scintillator is based on xylene or dimethylbenzene, C₆H₄(CH₃)₂. Some of the important properties of BC501A are described in the Ta-

ble 5.4. The neutron detection mechanism of BC501A scintillator detector is based on elastic scattering of neutron with proton, which strongly dominates over the other reaction channels in the energy range 0.1 MeV to 8 MeV region. At around 8 MeV, different inelastic channels gradually come up and they start playing significant roles in the detection mechanism. The neutron detector used as having a

Table 5.4: Properties of scintillator material BC501A

Scintillator properties	BC501A
Light output, % Anthracene	78
Wavelength of maximum emission, nm	425
Decay time of short component, ns	3.2
Ratio H:C atoms	1.212
Number of electrons per cc	2.87
Density, g/cc	0.874
Refractive index at 425 nm	1.530
Flash point T.O.C /degree C	24
Scintillator decay time	3.16 ns, 32.3 ns and 270 ns

dimension of 5" x 5". Cylindrical shaped detector cells were made up of 1.5 mm thick aluminium, which was filled with liquid scintillator BC501A. Internal walls of the cells were white painted for efficient light collection. Expansion chamber was made up of teflon capillary tube (inner diameter = 1.5 mm, outer diameter = 2.5 mm), which was rolled around the neutron cells, to take care of the thermal expansion of the liquid. Scintillator cells, sealed with 6mm thick pyrex glass, were viewed by 5 inch photo multiplier tube (PMT) (model: 9823B; Electron tube Ltd). The photo-multiplier tubes were provided with 1 mm thick μ - metal shield to protect them from magnetic field. The PMT and the voltage divider were covered with a cylindrical container, which held the PMT rigidly in position and also provided light tightness.

Since the mono energetic neutron sources are not readily available, the calibration of the liquid scintillator detector is usually done by standard γ -ray sources with known energies ^{137}Cs (E=662 keV), ^{22}Na (E = 511 keV, 1274.5 keV). As the pulse height response does not contain pronounced full energy peaks (except for energies

< 100 keV) the calibration procedure relies on the analysis of the Compton edge. Pulse shape discrimination was achieved by zero cross over (ZCO) technique. The difference between the constant fraction discriminator (CFD) and the ZCO timings was measured with a Time to Amplitude Converter (TAC) which is further connected to ADC. The block diagram of the neutron detector is shown in figure 5.15. Neutron spectrum measurements were carried out with different combination of dif-

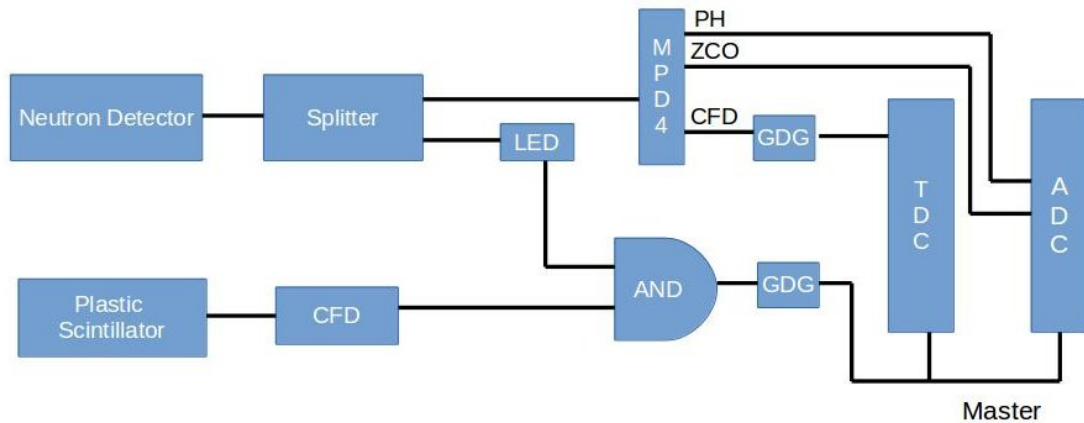


Figure 5.15: Block diagram of neutron detector used for measurement of neutron spectra from beam dump

ferent thicknesses of HDPE and Pb and without any shield. The neutron detector was setup at a distance of 1.08 m from the centre of the beam dump at 90° with respect to the beam direction. The experimental setup of the neutron detector and the HDPE shield can be seen in the figures 5.16 and 5.17. Figure 5.18 shows the experimental determined neutron spectrum with no shield, after 5 cm Pb shield and after 40 cm HDPE shield. The figure shows a peak at around 1 MeV, due to evaporation neutrons and decreases there after upto 20 MeV. It can be seen from the figure, there is little decrease in the neutron yield per unit energy bin with 5 cm Pb as compared to that of the neutron yield per unit energy bin with no shield as Pb is a poor shielding material for neutron. Moreover, these high energy neutrons interacts with Pb through (n, xn') multiplicity reaction. There is a considerable decrease in

the neutron fluence with 40 cm HDPE due to the elastic scattering of the neutrons with Hydrogen atoms in HDPE. Figure 5.19 compares the neutron spectrum with no shield to that with two combinations of composite shields comprising of HDPE and Pb. The first composite shield comprises of 10 cm HDPE + 5 cm Pb + 30 cm HDPE. The first layer of 10 cm HDPE was facing the beam dump and the last layer was facing the neutron detector, with Pb being sandwiched in between. The second composite shield comprised of 10 cm HDPE + 4 cm Pb + 10 cm HDPE. As can be seen from the figure, both these composite shield are successful in reducing the neutron yield per unit bin to a great extent. Being a semi-log plot of the data, much difference cannot be seen between the two composite shields. Figure 5.20 shows the plot of the neutron spectrum again with two different arrangements of composite shield comprising of Pb and HDPE. These were again compared with the neutron spectrum without any shield. The first combination of the composite shield comprised of 5 cm Pb followed by 40 cm HDPE, with the Pb shield facing the beam dump and the 40cm HDPE facing the neutron detector. There was a gap of few centimeters between the Pb shield and HDPE shield. Here again we find a considerable decrease in the neutron yield per unit energy bin with the composite shield to that with no shield. There is no difference in the neutron spectrum between the two shielding arrangements.

Figure 5.21 shows the comparison of the neutron spectrum generated experimentally with that generated using Monte Carlo code FLUKA, with no shield between the beam dump and the neutron detector. These figures show the maximum yield around 1 MeV and a decrease thereafter up to 20 MeV. Owing to the statistical fluctuations, this comparison of neutron spectrums were found to be acceptable for our study. Figure 5.14 shows the comparison of the experimental and FLUKA spectrum with 5 cm Pb shield between beam dump and the detector. Here also, we see little difference between the two spectrums. Moreover, in FLUKA simulation, pure Pb was considered, while experimental used Pb may not be in the purest form, which

may also attribute to the difference in the spectrum. Figure 5.23 shows the comparison of the neutron spectrums with 40 cm HDPE shield. The spectrum shows good match in the low energy range of neutrons, but beyond 5 MeV, there is a difference in the spectrum, which can be attributed to the statistical fluctuations of the data. Similar result of the neutron spectrum was found for figure 5.24, where the data matches in the low energy region of the neutron spectrum and then tend to differ at higher energies. In figure 5.24, the neutron spectrum from experiment and FLUKA were plotted with the shielding combination of 10 cm HDPE + 5 cm Pb + 30 cm HDPE, where the 10 cm HDPE was facing the beam dump and 30 cm HDPE was facing the neutron detector, with Pb sandwiched in between them. This shows that Monte Carlo code FLUKA can very well predict the experimental fluence spectrums.

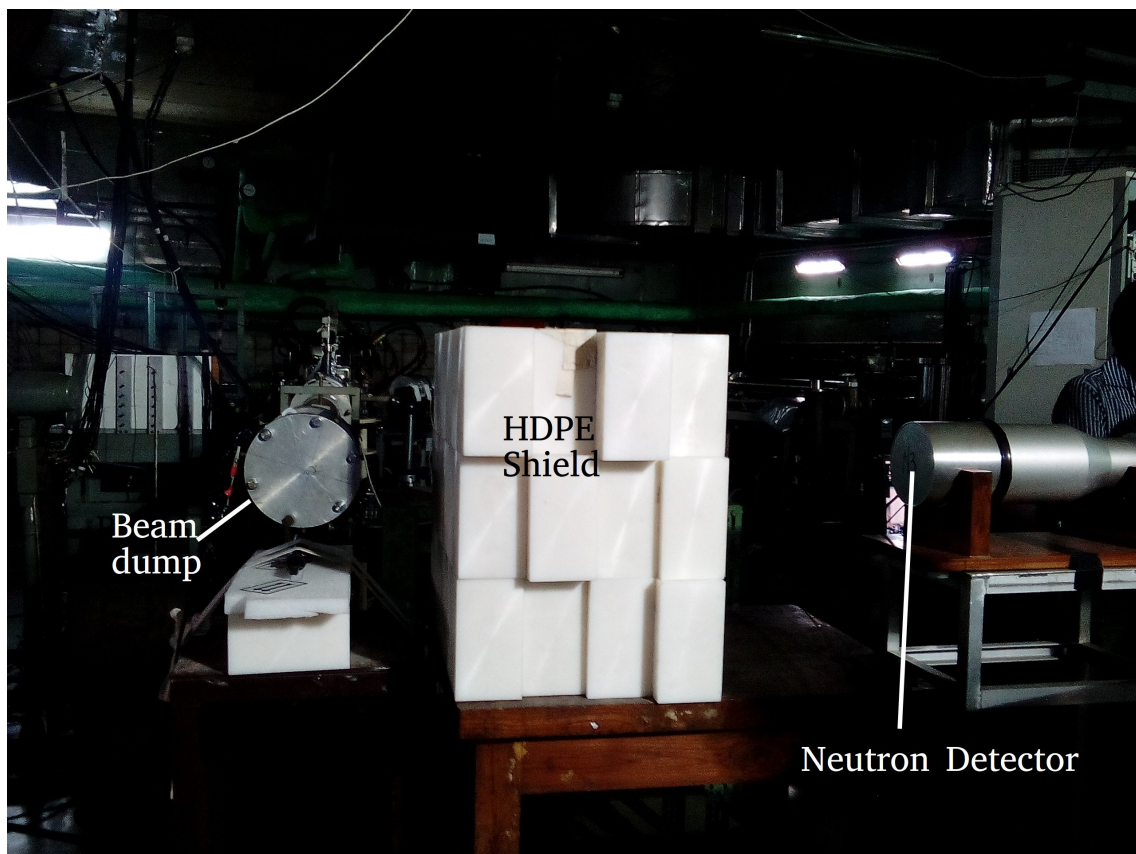


Figure 5.16: Experimental setup for the measurement of neutron spectrum. It shows the beam dump position, HDPE shield and the neutron detector

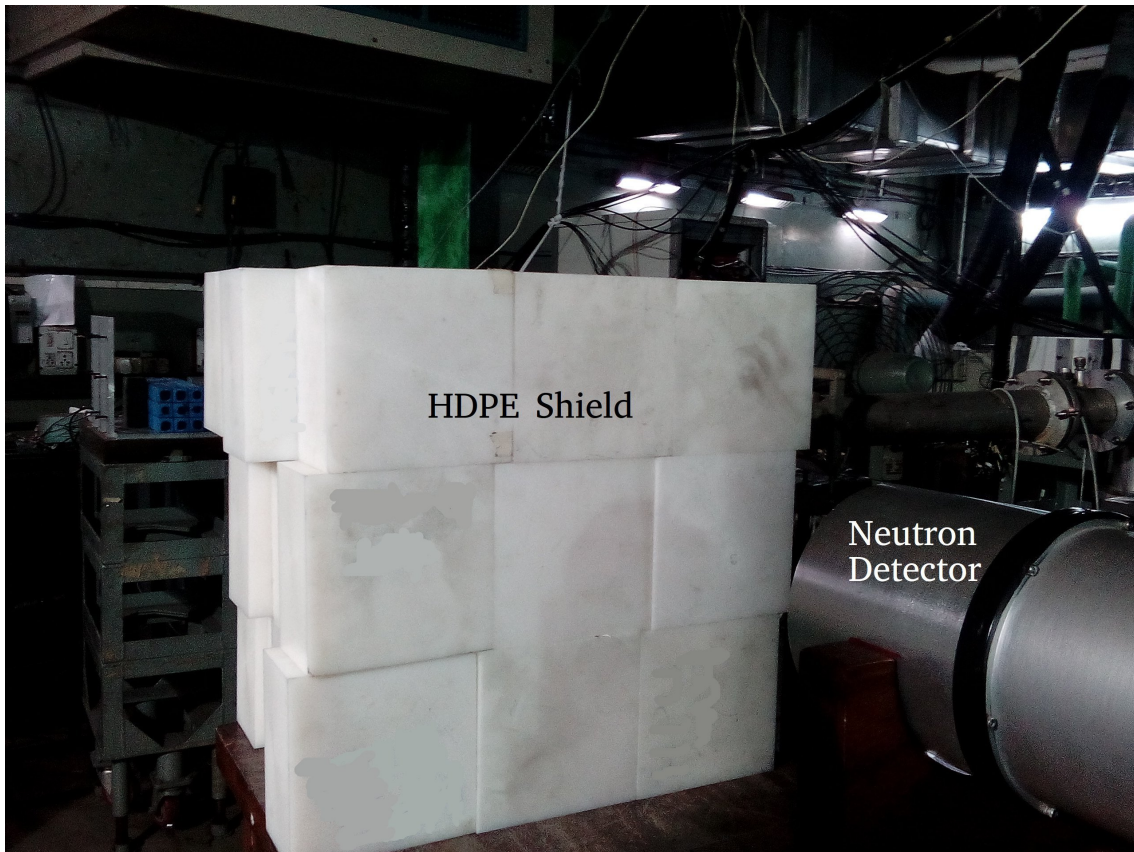


Figure 5.17: Experimental setup for the measurement of neutron spectrum from different viewing angle

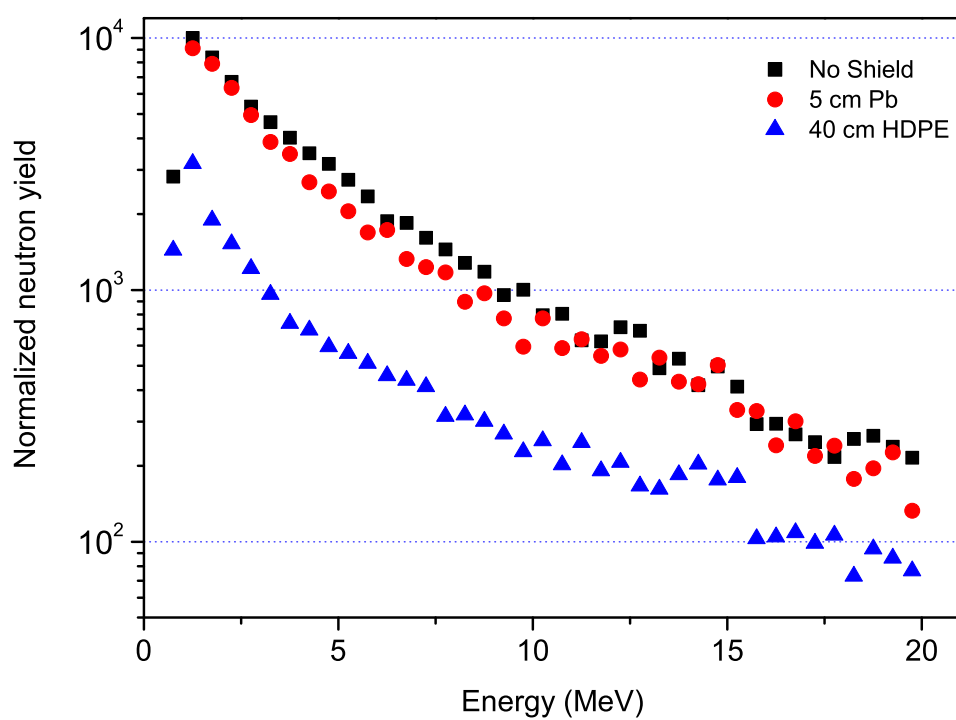


Figure 5.18: Experimental spectra of neutrons from beam dump without shield, after 5 cm Pb and after 40 HDPE

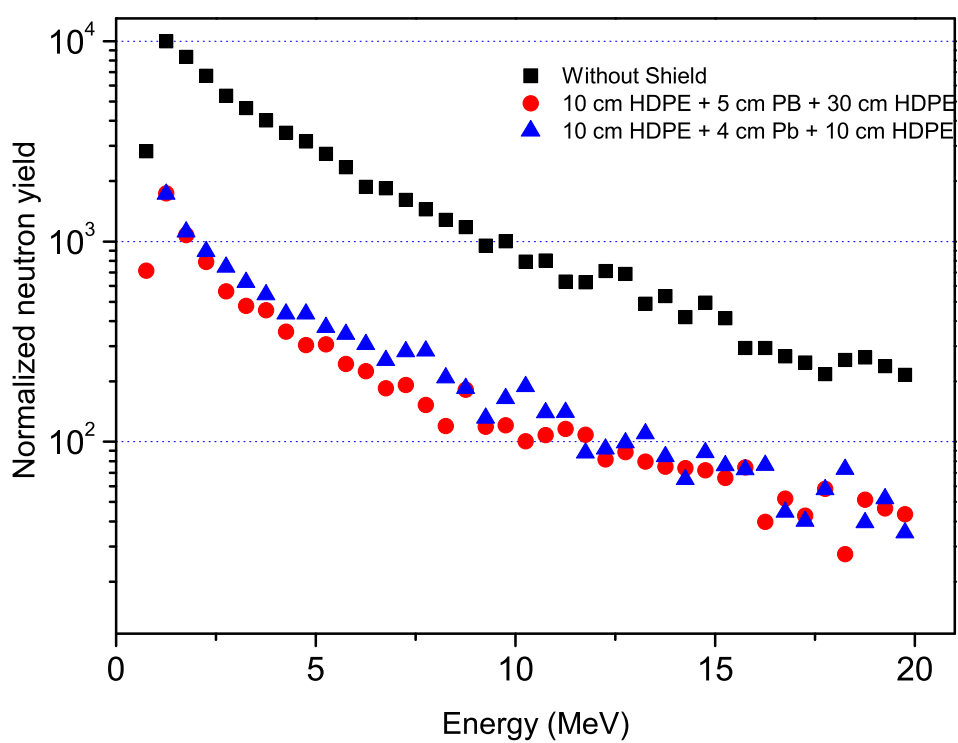


Figure 5.19: Experimental spectra of neutrons from beam dump without shield and after two combination of composite shields of Pb and HDPE (i) 10 cm HDPE + 5 cm Pb + 30 cm HDPE (ii) 10 cm HDPE + 4 cm Pb + 10 cm HDPE

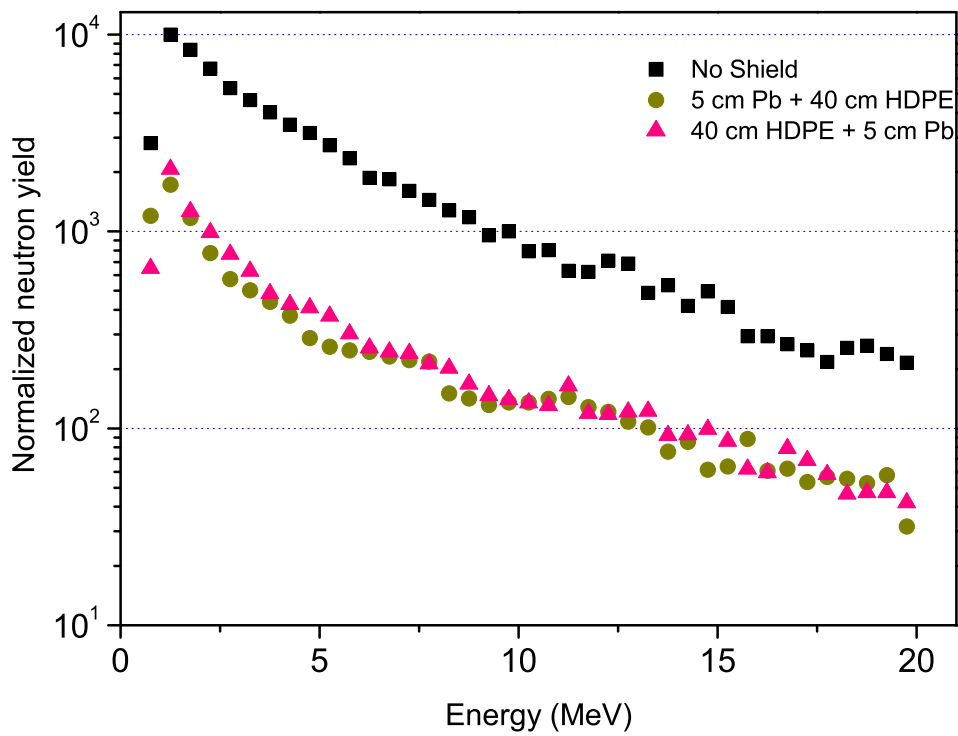


Figure 5.20: Experimental spectra of neutrons from beam dump without shield and after two combinations of composite shields of Pb and HDPE (i) 5 cm Pb + 40 cm HDPE with Pb near beam dump (ii) 40 cm HDPE + 5 cm Pb with HDPE near beam dump

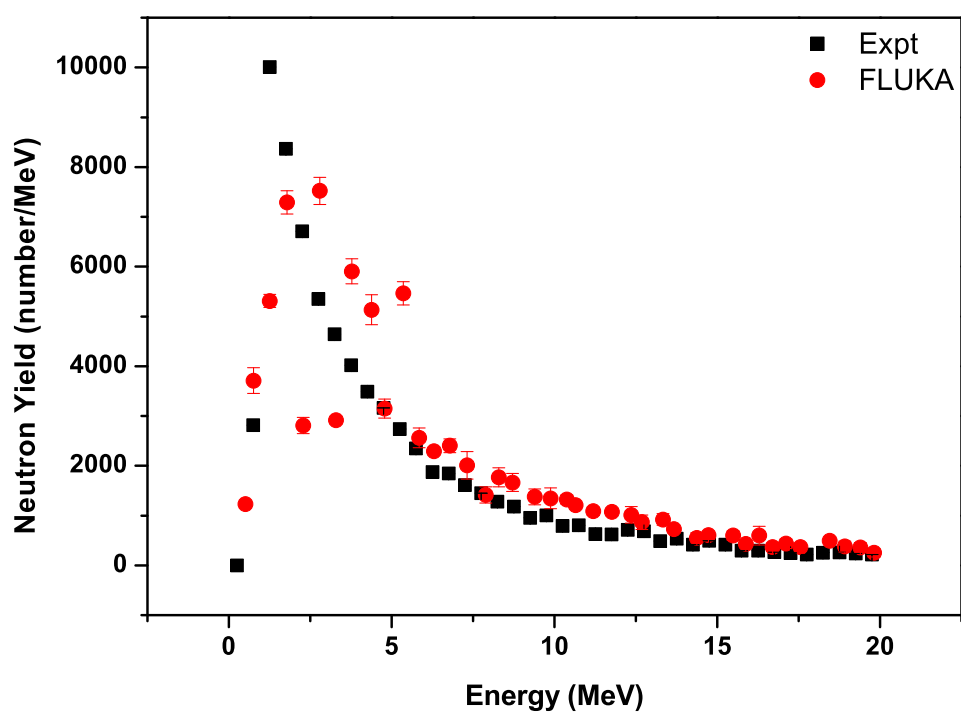


Figure 5.21: The experimental and FLUKA generated spectra of neutrons from beam dump without shield

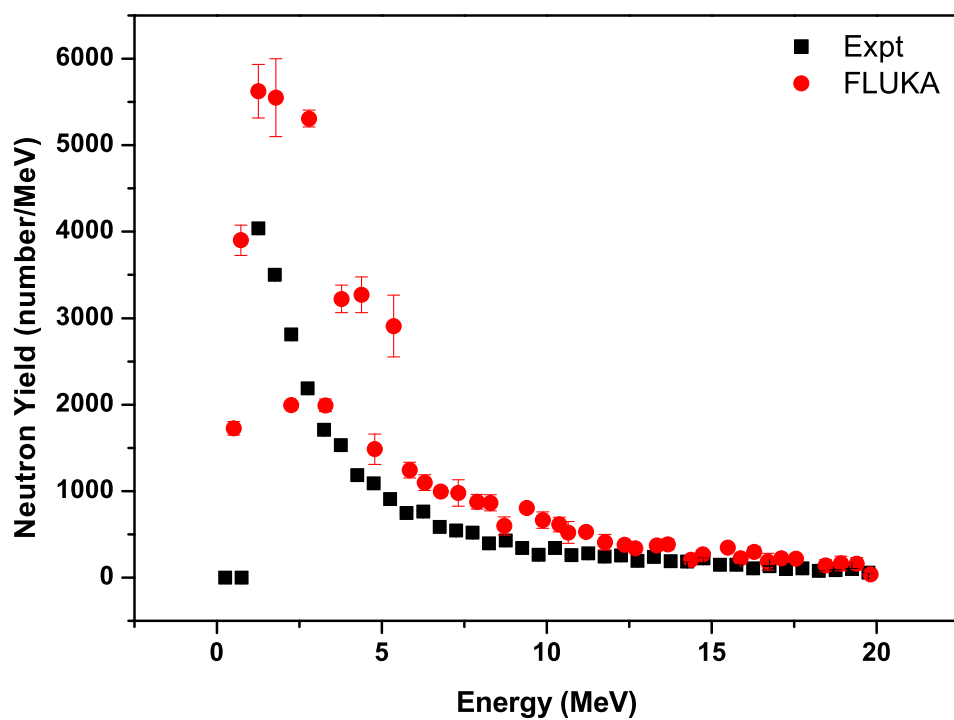


Figure 5.22: The experimental and FLUKA generated spectra of neutrons after Pb shielding of 5.0 cm

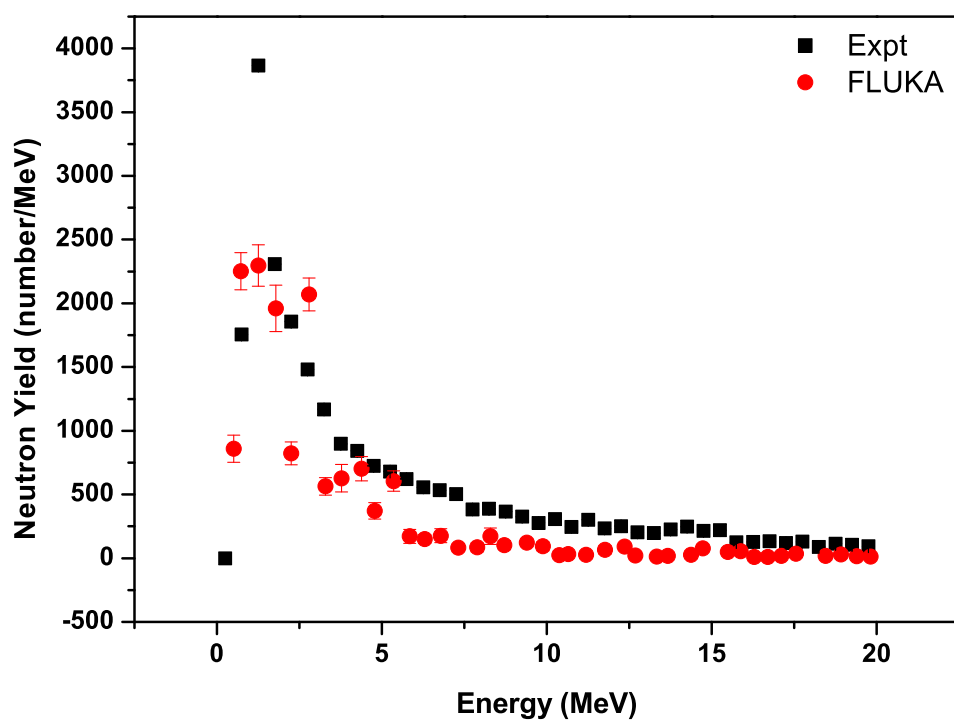


Figure 5.23: The experimental and FLUKA generated spectra of neutrons after 40 cm thick HDPE

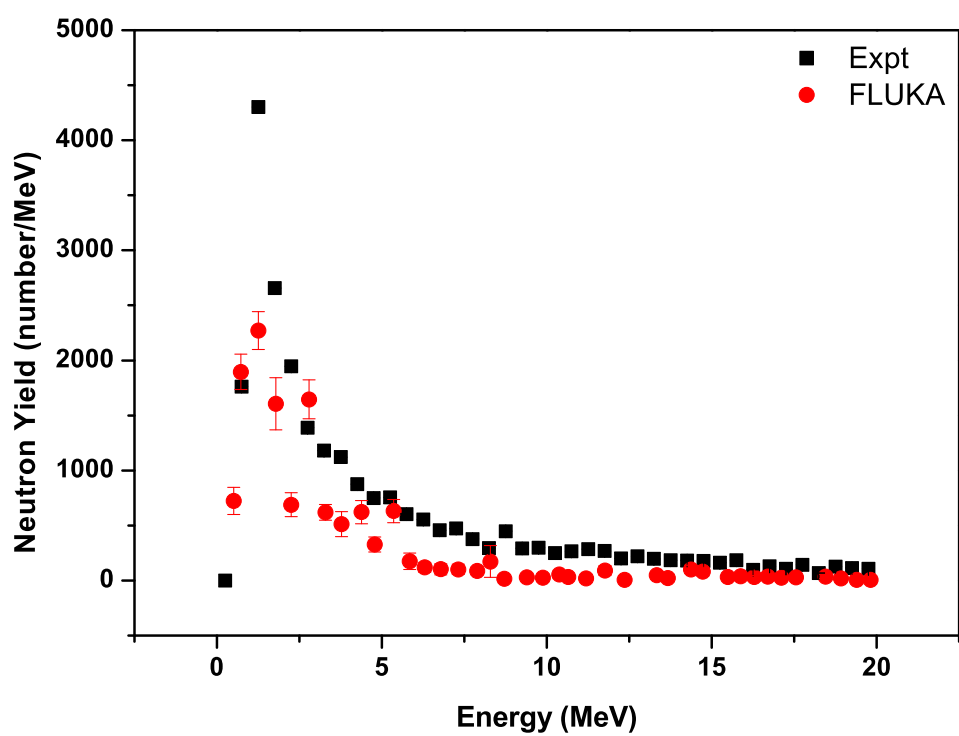


Figure 5.24: The experimental and FLUKA generated spectra of neutrons after composite shield of 10 cm HDPE and 5 cm Pb followed by 30 cm HDPE, where 10 cm HDPE is near the beam dump

5.3.2 Experimental determination of Photon spectrum

Experimental determination of the photon spectrum with different shielding configurations were carried out with BaF₂ detector using Time of Flight (TOF) technique [58]. Generally, NaI(Tl) and BaF₂ scintillators are used for γ -detection and spectroscopy. The energy resolution of BaF₂ is ideally a factor of two or three worse than that of its best NaI(Tl) counterpart, but they are comparable in terms of detection efficiency. The gain variation of BaF₂ is also significant with temperature. Still, BaF₂ is superior to NaI(Tl), especially in those applications where fast timing is essential, and the poorer energy resolution gets cancelled by the much better timing characteristics of BaF₂. Other major advantages of BaF₂ are, it is non-hygroscopic and has a very low neutron capture probability.

The BaF₂ detectors were 35 cm long, square faced (3.5 cm \times 3.5 cm), and were coupled with photonics XP2978 photo tubes having quartz window view. The detector system is highly granular which greatly reduces the possibility of any $\gamma\gamma$ and γ -neutron pile up events. the neutrons were rejected by time of flight (TOF) and pile-up events were rejected using pulse shape discrimination (PSD) in the detector. The energy calibration of the BaF₂ detector was done using laboratory standard γ -rays sources ²²Na (0.511 MeV, 1.274MeV), ¹³⁷Cs(0.662 MeV) and ²⁴¹Am-⁹Be (4.44 MeV). As carried out for neutron spectrum measurements, the photon spectrum measurements were carried out with different combination of different thicknesses of HDPE and Pb and without any shield. The photon detector was setup at a distance of 1.308 m from the centre of the beam dump at 90° with respect to the beam direction. Figure 5.25 shows the experimental arrangement for the measurement of the photon spectrum with different shielding configurations. Figure is shown with the Pb shield. It also shows the array of BaF₂ detector, out of which the central one was used for the measurement of the γ spectrum. Figure 5.26 shows the experimentally generated photon spectrum without any shield, with 5 cm Pb shield and with 40 cm HDPE. The figure shows a peak at 4.45 MeV from the first excited state of C¹².

This is arising out of the interaction of α with graphite beam dump. After this peak, there is a decreasing trend of the photon spectrum. As seen from the figure, there is not much reduction in the photon yield per unit energy bin due to HDPE shield as HDPE is a poor shield for photons due to its low effective atomic number. There is a significant reduction seen for 5 cm Pb shield. Pb is one of the best shielding materials for γ rays due to its high atomic number. Figure 5.27 shows the experimentally generated photon spectrum for no shield condition and two composite shields of Pb and HDPE. First composite shield comprises of 5 cm Pb followed by 40 cm HDPE and the second composite shield comprises of 4 cm Pb followed by 20 cm HDPE. The maximum reduction is seen for the first composite shield as compared to that of the second one.

Figure 5.28 compares the experimental photon spectrum with the FLUKA gener-



Figure 5.25: Experimental setup for the measurement of photon spectrum. It shows the lead shield and the BaF_2 detector along with the beam dump position

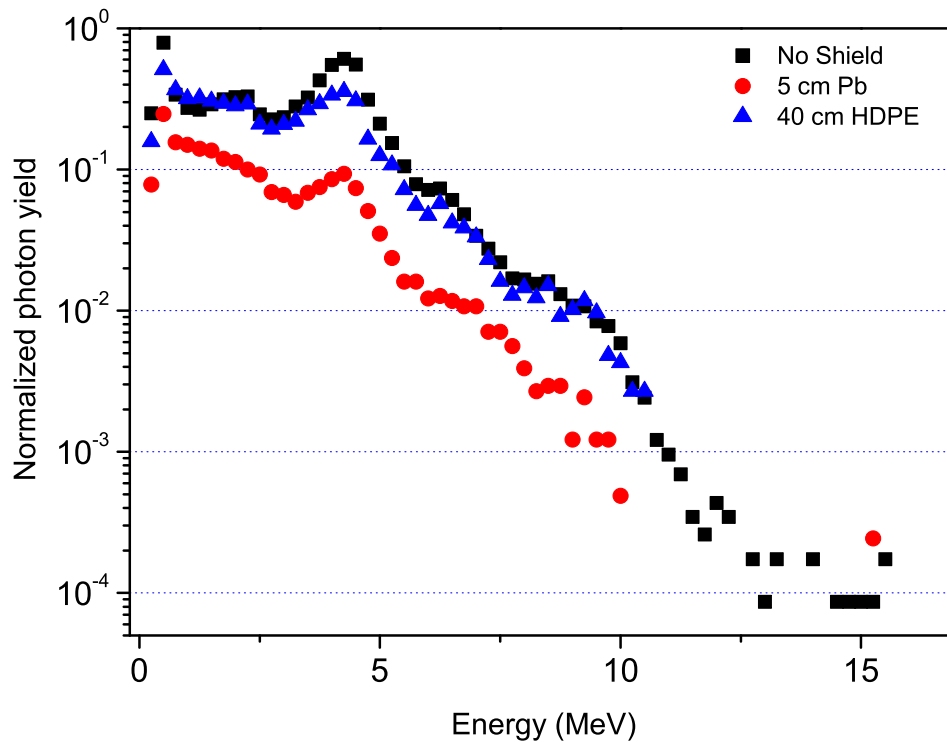


Figure 5.26: Experimental spectra of photons without shielding, after 5 cm Pb and 40 cm HDPE

ated spectrum with no shield condition. The figure shows a good agreement between the two spectrums. The peak at 4.45 MeV is also seen significantly in both the photon spectrums. Figure 5.29 compares the experimental and FLUKA generated spectrum with 5 cm Pb shield. Here also there is a good agreement between the two spectrums. The small difference in the spectrum can be attributed to the composition of Pb as considered in the FLUKA code with that used in the experiment. The comparison of the photon spectrums with 40 cm HDPE shield is shown in figure 5.30. Here a significant difference can be seen between the FLUKA generated spectrum with the experimental one. As already explained for the neutron spectrum, here also the difference can be due to the composition of HDPE.

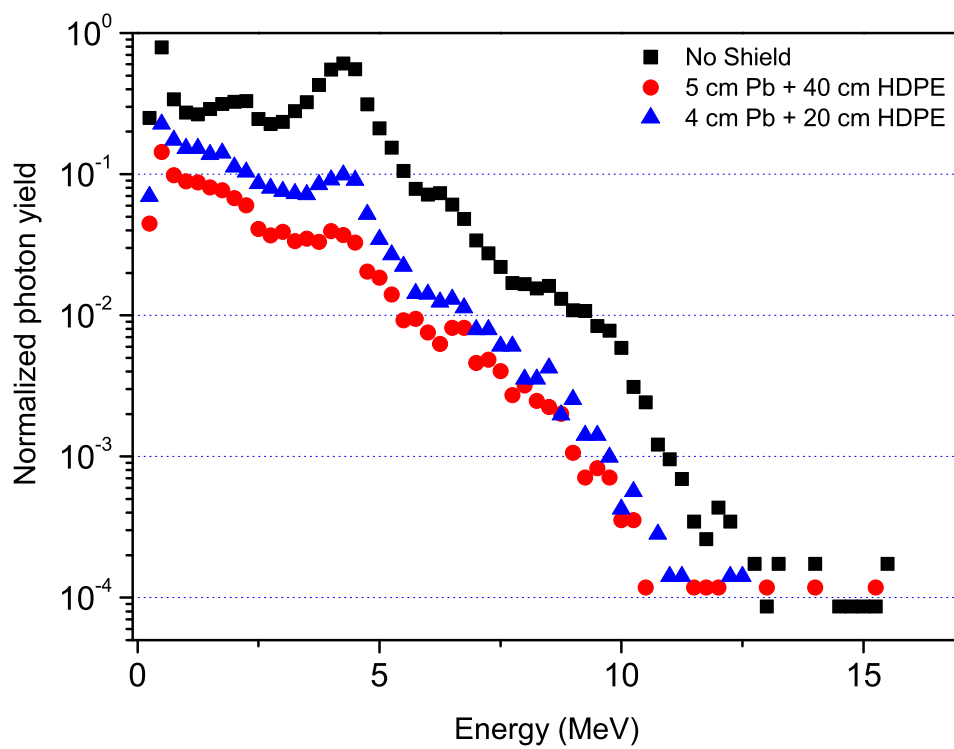


Figure 5.27: Experimental spectra of photons after composite shield of Pb and HDPE (i) 5 cm Pb + 40 cm HDPE (ii) 4 cm Pb + 20 cm HDPE

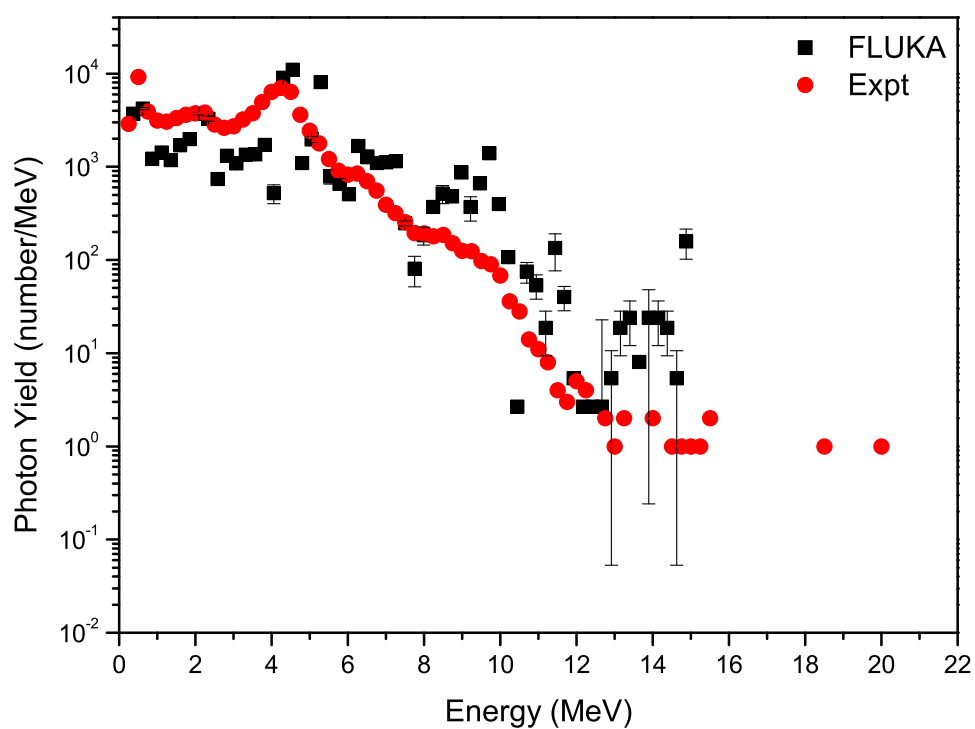


Figure 5.28: The experimental and FLUKA generated spectra of photons without shielding

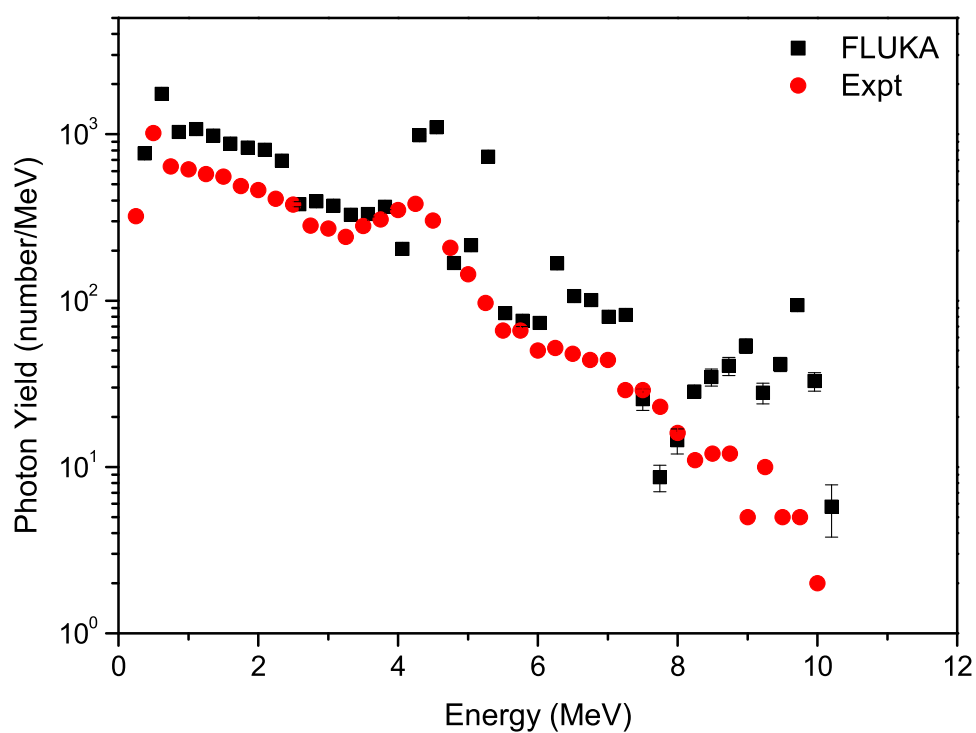


Figure 5.29: The experimental and FLUKA generated spectra of photons after 5 cm Pb shielding

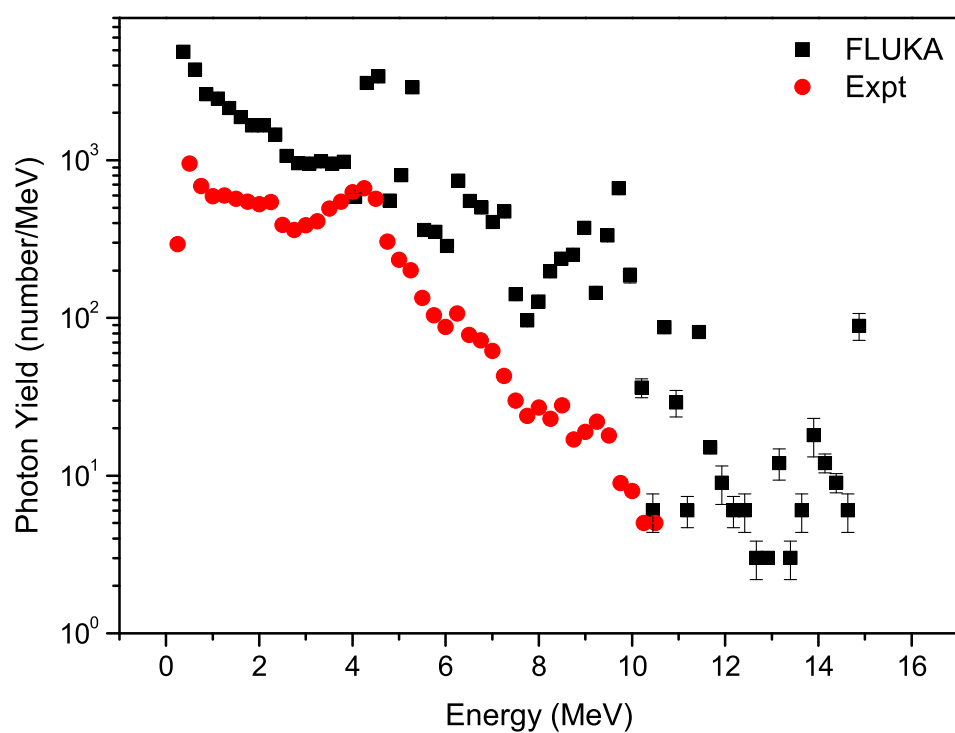


Figure 5.30: The experimental and FLUKA generated spectra of photons after 40 cm HDPE shielding

5.4 Residual nuclei estimation in the shield

Beam dump has been designed to stop most of the cyclotron beams after interacting with the target material, which generates showers of neutrons and photons. With the help of the shield for beam dump, this shower was stopped from contributing to the detectors placed around the target chamber. But, these neutrons will also in turn generate lot of radionuclides in the different materials of the shield. Estimation of these radionuclides and their activity is necessary, because, these radionuclides may contribute to the external dose to personnel, who are going either for regular maintenance of the cyclotron and also for experimental setup. Activity estimation for such cyclotron components are also required during their de-commissioning stages. Residual nuclei calculations have been carried out in different components of the beam dump shield using Monte Carlo code FLUKA. The calculations have been carried out for 1 nA beam current of α particles having an energy of 50.0 MeV. The irradiation profile comprised of beam “ON” condition for a period of six months and cooling periods of 0 hr, 1 hr, 6 hrs, 24 hrs and 1 month. The beam on period has been realized using “IRRPROFI” card of FLUKA. Different cooling periods has been fed in the code using the FLUKA card “DCYTIMES”. Activity calculations have been carried out in different regions of the beam dump shield as follows:

- Innermost region comprising of HDPE
- Pb just outside the innermost HDPE region
- HDPE region just outside Pb and inside the outermost Fe region
- Outermost Fe region.

Similarly, residual nuclei calculations in the above mentioned regions has also been carried out in FLUKA using “RESNUCLE” card of FLUKA.

5.4.1 Residual nuclei in Target

Residual nuclei calculations have been carried out in ^{181}Ta , which was irradiated with 50 MeV α for six months. The highest activity per unit volume per unit α particle was found for ^{11}C , which is a β^+ emitter with a half life of 20.364 minutes. Lowest activity was found for ^{10}Be , which is a β^- emitter with a half life of 1.51×10^6 years. Figure 5.31 shows the variation of activity (Bq/cm^3) per unit α particle with different cooling periods. The radio-isotopes produced in the Target by the interaction of α particles were identified and their variation with different cooling times are shown in table 5.5.

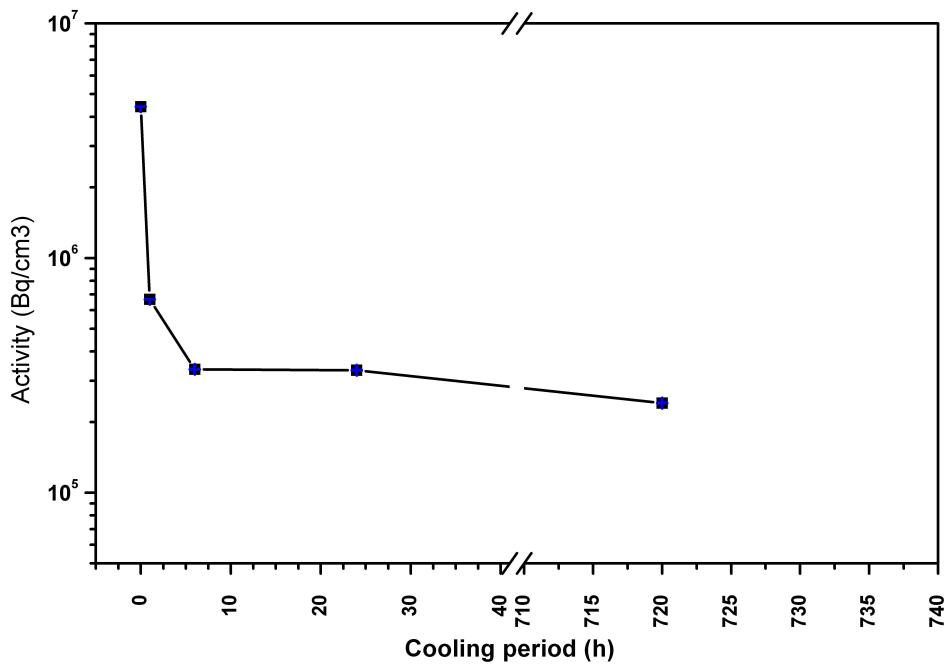


Figure 5.31: Variation of activity in ^{181}Ta target

Table 5.5: Variation of radio-isotopes with cooling time in Target

Isotopes	Activity (Bq/cc) per unit alpha particle					Half lives	Emitter
	Time= 0 h	Time= 1 h	Time= 6 h	Time= 24 h	Time= 720 h		
⁵⁹ Fe	2.90E+01	28.95	28.86	28.52	18.16	44.495 d	β^-
⁵⁷ Mn	5.965	1.22E-12				85.4 s	β^-
⁵⁶ Mn	3.88E+02	296.6	77.35	0.6124		2.5789 h	β^-
⁵⁵ Cr	4.66E-01	3.19E-06	4.77E-32			3.497 min	β^-
⁵⁵ Fe	274.7	274.7	274.7	274.5	269.1	2.744 Y	EC
⁵⁴ Mn	100	100	99.98	99.81	93.59	312.2 d	β^+
⁵³ Mn	9.42E-06	9.42E-06	9.42E-06	9.42E-06	9.42E-06	3.74E+06 Y	EC
⁵³ Fe	13.42	0.1232	3.01E-12			8.51 min	EC
⁵¹ Cr	23.81	23.79	23.66	23.22	11.24	27.70 d	EC

5.4.2 Residual nuclei in HDPE(Inside)

Residual nuclei in HDPE(Inside) were evaluated for the irradiation time of six months. This material is surrounding just outside the beam line pipe. These residual nuclei are generated by the neutrons, which in turn are generated from the beam dump, through the interaction of α particles. The highest activity was found for ¹²B, which is a β^- emitter with a half life of 20.20 ms. The lowest activity is for ¹⁴C, which is also a β^- emitter with a half life of 5700 years. Figure 5.32 shows the variation of activity at different cooling times, due to various radio-isotopes. Variation of radio-isotopes with different cooling times is shown in table 5.6.

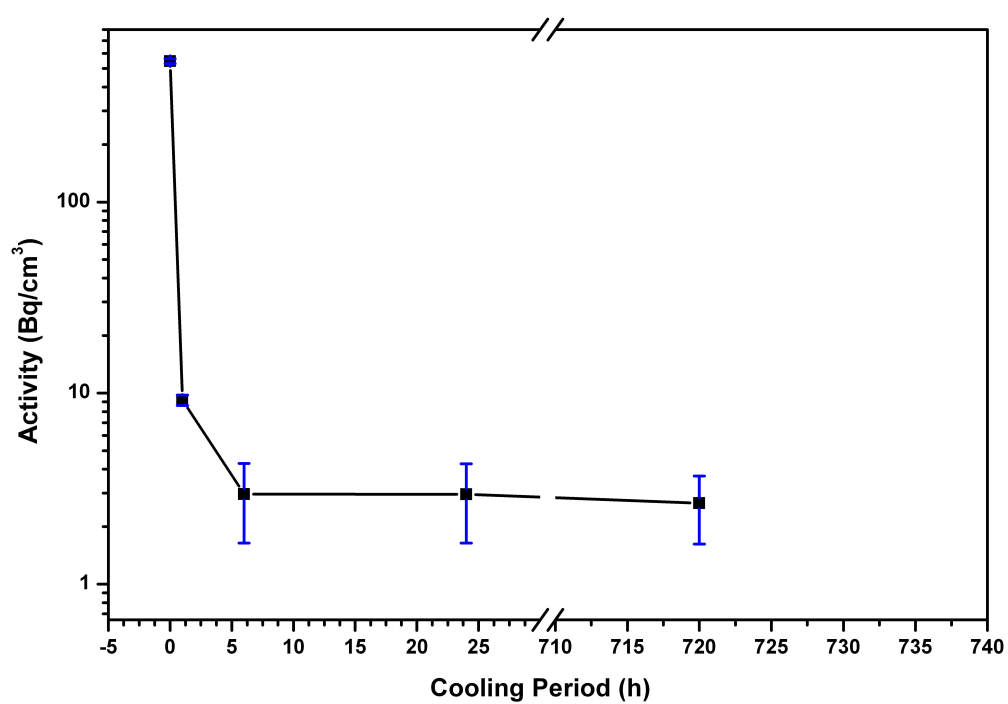


Figure 5.32: Variation of activity in HDPE(Inside)

Table 5.6: Variation of radio-isotopes with cooling time in HDPE(Inside)

Isotopes	Activity (Bq/cc) per unit alpha particle					Half lives	Emitter
	Time= 0 h	Time= 1 h	Time= 6 h	Time= 24 h	Time= 720 h		
¹⁴ C	7.33E-05	7.33E-05	7.33E-05	7.33E-05	7.33E-05	5700 Y	β^-
¹² B	49.35					20.20 ms	β^-
⁶ He	2.08					806.7 ms	β^-
³ H	2.85E-02	2.85E-02	2.85E-02	2.85E-002	2.84E-02	12.32 Y	β^-

5.4.3 Residual nuclei in Pb

Residual nuclei calculations have been carried out with the same conditions for Pb, surrounding the HDPE layer just outside the beam line. The highest activity was found for ²⁰⁹Pb, which is a β^- emitter with a half life of 3.234 h. Lowest activity was found for ²⁰²Pb, which decays by electron capture(EC). It is having a long half life of 5.25×10^4 years. The variation of activity is shown in figure 5.33. Table 5.7 shows the variation due to various radio-isotopes at different cooling times. These radio-isotopes have been produced due to the interaction of neutrons from the beam dump.

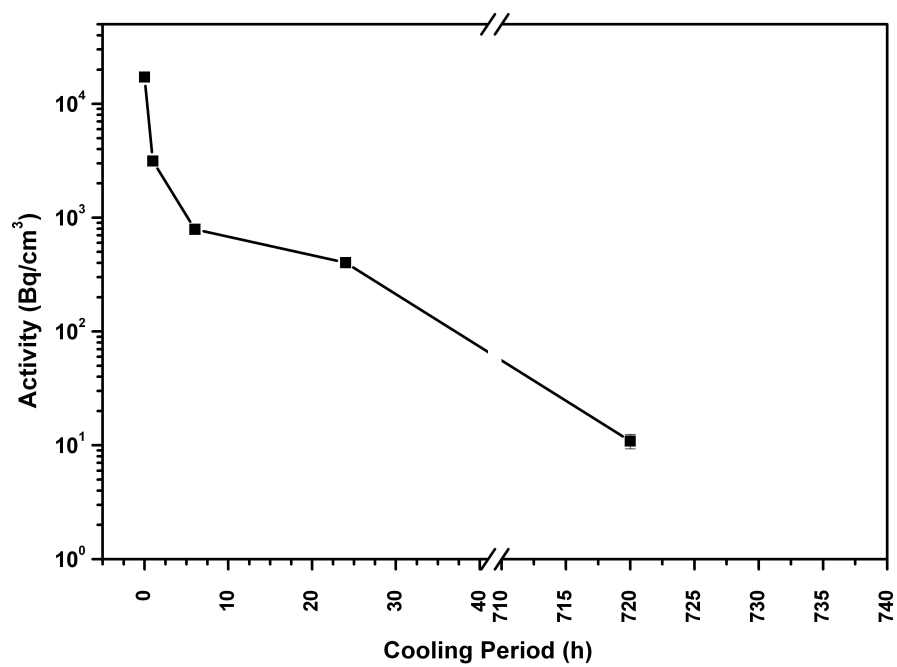


Figure 5.33: Variation of activity in Pb

Table 5.7: Variation of radio-isotopes with cooling time in Pb

Isotopes	Activity (Bq/cc) per unit alpha particle					Half lives	Emitter
	Time= 0 h	Time= 1 h	Time= 6 h	Time= 24 h	Time= 720 h		
²⁰⁹ Pb	5.15E+02	416.5	143.5	3.099		3.234 h	β^-
²⁰⁸ Tl	6.847	8.31E-06	2.18E-35			3.053 min	β^-
²⁰⁷ Tl	1.40E+01	2.29E-03	2.67E-22			4.77 min	β^-
²⁰⁶ Tl	1.29E+01	2.48E-03	1.01E-24			4.202 min	β^-
²⁰⁵ Hg	4.422	1.49E-03	6.38E-21			5.14 min	β^-
²⁰⁵ Pb	3.70E-04	3.70E-04	3.70E-04	3.70E-04	3.70E-04	1.73E+07 Y	EC
²⁰⁴ Tl	0.2111	0.2111	0.2111	0.211	0.208	3.783 Y	β^-
²⁰³ Hg	9.682	9.676	9.646	9.539	6.198	46.594 d	β^-
²⁰³ Pb	313.1	308.9	289	227.2	2.08E-02	51.92 h	EC
²⁰² Tl	0.5388	0.5387	0.5357	0.5152	9.97E-02	12.31 d	β^+
²⁰² Pb	7.03E-05	7.03E-05	7.03E-05	7.03E-05	7.03E-05	52.5E+03 Y	EC
²⁰¹ Tl	1.042	1.041	1.03	0.9247	1.27E-03	3.0421 d	EC
²⁰¹ Pb	1.036	0.9631	0.6643	0.1744	6.10E-24	9.33 h	EC
³ H	3.89E-02	3.89E-02	3.89E-02	3.89E-02	3.88E-02	12.32 Y	β^-

5.4.4 Residual nuclei calculation in HDPE(Outside)

Residual nuclei calculation has been carried out for HDPE, surrounding the Pb shield. As done earlier, the calculations have been carried out for a exposure period of six months, followed by different cooling periods. The maximum activity was found for ¹²B, which is a β^- emitter with a half life of only 20.20 ms. Lowest activity was found for ¹⁰Be, which is also a β^- emitter with a long half life of 1.51 x 10⁶ years. Variation of activity with different cooling periods is shown in figure 5.34. Table 5.8 shows the radioisotopes generated in HDPE(outside), and the variation of the same at different cooling periods.

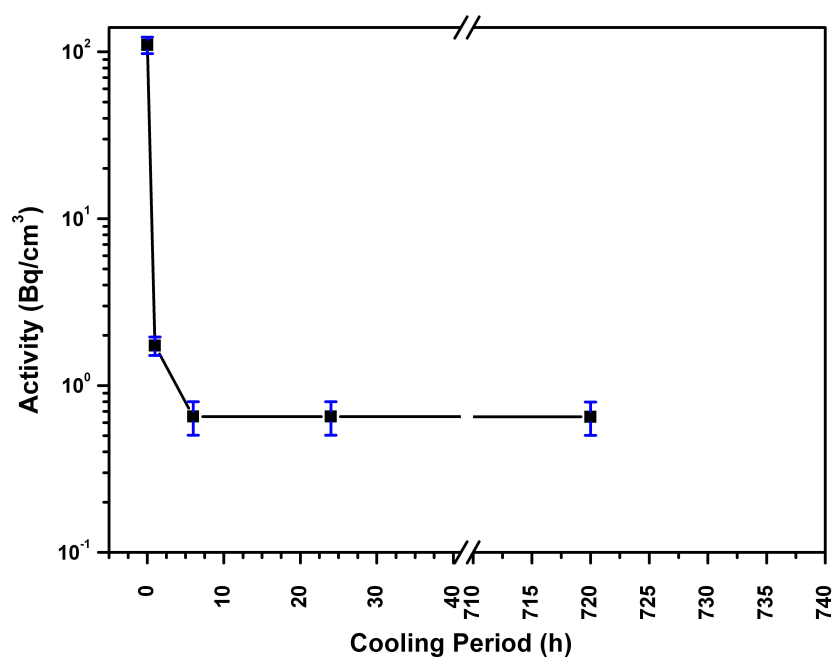


Figure 5.34: Variation of activity in HDPE(outside)

Table 5.8: Variation of radio-isotopes with cooling time in HDPE(outside)

Isotopes	Activity (Bq/cc) per unit alpha particle					Half lives	Emitter
	Time= 0 h	Time= 1 h	Time= 6 h	Time= 24 h	Time= 720 h		
¹⁴ C	1.18E-04	1.18E-04	1.18E-04	1.18E-04	1.18E-04	5700 Y	β^-
¹² B	100.9					20.20 ms	β^-
¹¹ C	8.33	1.084	4.04E-05	4.58E-21		20.364 min	β^+
¹⁰ Be	4.72E-07	4.72E-07	4.72E-07	4.72E-07	4.72E-07	1.51E+06 Y	β^-
³ H	0.6519	0.6519	0.6519	0.6518	0.6489	12.32 Y	β^-

5.4.5 Residual Nuclei in Fe

Calculations of residual nuclei have been carried out in Fe, which forms the outer most layer of the beam dump shield. It is surrounding the last layer of HDPE. The highest activity was recorded for ⁵⁶Mn, which is a β^- emitter with a half life of 2.5789 h. Lowest activity was recorded for ⁵³Mn, which decays through electron capture(EC). It has a half life of 3.74×10^6 years. Figure 5.35 shows the variation of activity with different cooling period. Table 5.9 shows the variation of radio-isotopes at different cooling periods.

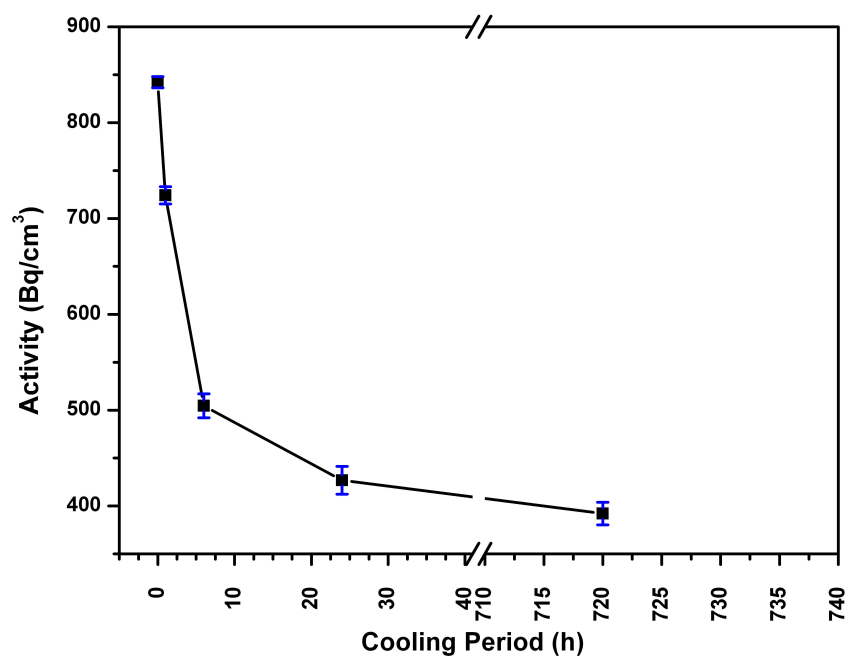


Figure 5.35: Variation of activity in Fe

Table 5.9: Variation of radio-isotopes with cooling time in Fe

Isotopes	Activity (Bq/cc) per unit alpha particle					Half lives	Emitter
	Time= 0 h	Time= 1 h	Time= 6 h	Time= 24 h	Time= 720 h		
⁵⁹ Fe	2.90E+01	28.95	28.86	28.52	18.16	44.495 d	β^-
⁵⁷ Mn	5.965	1.22E-12				85.4 s	β^-
⁵⁶ Mn	3.88E+02	296.6	77.35	0.6124		2.5789 h	β^-
⁵⁵ Cr	4.66E-01	3.19E-06	4.77E-32			3.497 min	β^-
⁵⁵ Fe	274.7	274.7	274.7	274.5	269.1	2.744 Y	EC
⁵⁴ Mn	100	100	99.98	99.81	93.59	312.2 d	β^+
⁵³ Mn	9.42E-06	9.42E-06	9.42E-06	9.42E-06	9.42E-06	3740000 Y	EC
⁵³ Fe	13.42	0.1232	3.01E-12			8.51 min	EC
⁵¹ Cr	23.81	23.79	23.66	23.22	11.24	27.70 d	EC

It was also observed from these calculations that the highest activity was generated in Pb, other than the beam dump itself. It was followed by Fe, HDPE (inside) and HDPE(outside).

Chapter 6

Summary and Conclusion

The aim of the present thesis is to carry out radiation dosimetry at different radiation facilities due to neutrons, photons, charged particles like betas. This thesis has emphasized the radiation dosimetry work in radiation facilities mainly in accelerator centres and space dosimetry. These are the most challenging fields with the development of new machines having higher particle energies, particle beam current for use in research and development and medical physics for the treatment and diagnosis such as cancer.

Emphasis of this work has also been given to the radiation personnel monitoring for the personnels working in these facilities. With new knowledge and experience, prescribed dose limits for the radiation workers are being brought down and handling and use of radiation becomes more safe not only for the radiation worker, but also for general public, our environment and future generation. Unlike earlier, dose for the individual organ like eye is matter of concern and whole body dose is not suffice for the reporting of dose for a radiation worker. Depending upon the type of work carried out in a particular facility, more than one personnel dosimeter can be used by the radiation worker, so that the dosimeter not only gives an idea of whole body dose, but also dose to other critical organ. This thesis has dealt only with the external personnel monitoring. So, the radiations of concern are neutrons, photons

and charged particles like betas.

The study of the response matrix for $\text{CaSO}_4\text{:Dy}$ based dosimeter has shown the feasibility for such dosimeter for neutron spectrometry available mainly in the environment of accelerators. Many studies in the literature have shown earlier the feasibility of neutron spectrometry using Bonner sphere with ^6Li based dosimeters, both in active and passive form. This is the first time, $\text{CaSO}_4\text{:Dy}$ based dosimeter, which is used in India for external personnel monitoring have been used for Bonner sphere spectrometry. It has successfully de-convoluted the neutron spectrum from ^{241}Am -Be source using the response matrix for the same. Such dosimeters can also be used for the thermal neutron personnel monitoring program in various radiation facilities. Spectrometry of neutrons is very important due to the change in the conversion factor for $H_p[10]$ with the energy of neutrons. In the study, the response matrix has been generated for neutron energy up to 20 MeV. For higher energy neutrons, modified Bonner sphere with Lead or Tungsten inserts are used and it has been shown in literature that the same can be used up to energy of 1 GeV. Separate response matrix will be required for the modified Bonner spheres.

Characterization of Lead Free Gulmarg Neutron Monitor (LFGNM) is important not only for the study of cosmic rays, but also for space/air crew dosimetry. In this study, the characterization of LFGNM was carried out, which comprised of 21 BF_3 detectors segregated in three channels, which operates continuously for recording the neutrons from cosmic rays. Optimization of the upper paraffin moderator was carried out from bare (0 cm) to 48 cm in steps of 2 cm. In this, the source used was Pu- α -Be neutron source, which was kept at a distance of 50 cm from the upper paraffin. The maximum response was found at a thickness of 6 cm. The energy response study was carried out in the energy range of 10^{-11} MeV to 10^4 MeV for neutrons. The maximum response was found at 2 MeV after which the response of the detector goes down. The output of the detector was again found to increase after 300 MeV. The Lead test of LFGNM was carried out with 2" and 4" Pb. The

response was found to increase with the increase in Pb thickness due to enhanced (n, xn') reaction. Angular response study of the neutron monitor was carried out in the energy range of 10^{-11} MeV to 10^4 MeV for 0° , 30° , 45° and 60° . The maximum response was found for 0° after which the response was found to decrease with the increase of angle of the source with respect to that of the detectors.

Residual nuclei calculations for accelerator facilities are important for radiological protection not only for the radiation workers, but also for the general public, as more and more accelerators are coming up in the public domain due to their use in diverse field. In this study, the residual nuclei calculations have been carried out for Medical Cyclotron facility and Super Conducting Cyclotron (K 500) of VECC, Kolkata. For Medical Cyclotron, residual nuclei calculations have been carried out for shielding materials such as concrete, soil and soil followed by concrete. Cyclotron operation time in this study was 7 days, 30 days and 300 days. Residual nuclei calculations have been carried out after the interaction of the primary beam (proton) is completely stopped in the target material (Ta) and various radiations such as neutrons and photons were tracked in different layers of concrete, soil and soil followed after concrete. For Super Conducting Cyclotron, residual nuclei calculations have been carried out not only for the shielding materials such as concrete, but also for different beam line components such as Al, SS (316L) and Cu. The primary beam (proton) was stopped completely in the SS target and the radiations produced from it were tracked in various materials for the calculation of residual nuclei in them. Ambient dose rates ($H_p[10]$) were also calculated for various cooling times of 1 hour to 10^5 hours. Variation of residual nuclei with cooling times for various materials were separated based on their half lives.

Study on the shielding calculation of the beam dump is essential for nuclear physics experiments and also for the radiation workers involved in the regular maintenance of the cyclotron. Primary beam after interaction with the beam dump produces huge shower of neutrons and photons. These neutrons and photons inter-

ferre with the detectors which are kept for recording them only from the target of interest, not from the beam dump. So, beam dump shielding is required, so that minimum number of neutron and photons from the beam dump can reach the detectors. In this study, the shielding was carried out with High density polyethylene (HDPE), Pb and Fe. Various designs were tried and the one with minimum contribution of neutrons and photons was chosen as the final design of the shield. Neutron and photon energy spectrum measurements were carried out with different shielding conditions at the detector positions. The shield for the beam dump can become one of the sources of radiation for the radiation workers involved in the maintenance of the cyclotron. So, residual nuclei calculations were carried out for the beam dump shield. The cyclotron operation time was taken as six months and the residual nuclei in various layers of the shield as well as in the thin target of Ta were carried out for different cooling periods of 0 h, 1 h, 6 h, 24 h and 30 days.

Future scope of work

- The study on the response matrix for $\text{CaSO}_4:\text{Dy}$ based dosimeter has been carried out up to the energy of 20 MeV using usual Bonner spheres of HDPE. This study can be extended to higher energies of neutron up to 1 GeV using Pb or W insert Bonner spheres.
- The study on the characterization of LFGNM has been carried out using Monte Carlo code FLUKA. The optimization of the upper paraffin moderator has been carried out experimentally and the values were found to be matching well with that obtained from simulation. Similarly, the energy response of the detector can be carried out for some points using dedicated neutron beam lines.
- The study of the residual nuclei calculations carried out for Medical Cyclotron and Super conducting Cyclotron of VECC using Monte Carlo simulation can

be verified experimentally once these Cyclotrons becomes operational.

Bibliography

- [1] United Nations. Scientific Committee on the Effects of Atomic Radiation. *Effects of Ionizing Radiation: Report to the General Assembly, with scientific annexes*. Vol. 1. United Nations Publications, 2008.
- [2] *Radiation and Risk—A Hard Look at the Data*. 2015. URL: http://inpp.ohiou.edu/~massey/pdf/4_Rad_risk.pdf.
- [3] *1990 Recommendations of the International Commission on Radiological Protection. ICRP Publication 60 Ann. ICRP 21 (1-3)*. ICRP, 1991.
- [4] Christian Wernli. “Individual monitoring at accelerator centres”. In: *Radiation protection dosimetry* 137.1-2 (2009), pp. 74–82.
- [5] Stefano Agosteo, Marco Silari, and Luisa Ulrici. “Instrument response in complex radiation fields”. In: *Radiation protection dosimetry* 137.1-2 (2009), pp. 51–73.
- [6] *Hand book on the use of TLD badge based on CaSO₄:Dy teflon discs for individual monitoring*. BARC/2002/E/025. BARC. 2002.
- [7] *AERB Safety Directive*. URL: http://aerb.gov.in/AERBPortal/pages/English/Constitution/directives_jsp.action.
- [8] M.P. Dhairyawan, P.K. Marathe, and O.P. Massand. “Use of CR-39 solid state nuclear track detector in neutron personnel monitoring”. In: *Radiation Measurements* 36.1–6 (2003). Proceedings of the 21st International Conference on Nuclear Tracks in Solids, pp. 435–438. ISSN: 1350-4487. DOI: <http://>

- [dx.doi.org/10.1016/S1350-4487\(03\)00166-5](https://doi.org/10.1016/S1350-4487(03)00166-5). URL: <http://www.sciencedirect.com/science/article/pii/S1350448703001665>.
- [9] BC Bhatt and MS Kulkarni. “Worldwide status of personnel monitoring using thermoluminescent (TL), optically stimulated luminescent (OSL) and radiophotoluminescent (RPL) dosimeters”. In: *International journal of Luminescence and Applications* 3.1 (2013), pp. 6–10.
- [10] A. Pradhan, J. Lee, and J. Kim. “On the scenario of passive dosimeters in personnel monitoring: Relevance to diagnostic radiology and fluoroscopy-based interventional cardiology”. In: *Journal of Medical Physics* 41.2 (2016), pp. 81–84. DOI: [10.4103/0971-6203.181634](https://doi.org/10.4103/0971-6203.181634).
- [11] *DIS-1 Dosimeter User’s guide*. 20966058. Version 1.04. URL: http://dosimetry.web.cern.ch/sites/dosimetry.web.cern.ch/files/download/DIS-1_UserManual.pdf.
- [12] Atomic Energy Regulatory Board. *Safety Guidelines on Accelerators*. 2005.
- [13] FD Brooks and H Klein. “Neutron spectrometry—historical review and present status”. In: *Nuclear Instruments and Methods in Physics Research Section A: Accelerators, Spectrometers, Detectors and Associated Equipment* 476.1 (2002), pp. 1–11.
- [14] H. Klein. “Photon spectrometry in mixed fields”. In: *Radiation Protection Dosimetry* 107.1-3 (2003), pp. 125–131.
- [15] *Cyclotron*. URL: <https://en.wikipedia.org/wiki/Cyclotron>.
- [16] G.N. Shah et al. “Lead-Free Gulmarg Neutron Monitor”. In: *Astroparticle Physics* 33.1 (2010), pp. 54–59. ISSN: 0927-6505. DOI: <http://dx.doi.org/10.1016/j.astropartphys.2009.11.003>.
- [17] GN Shah et al. “Neutron generation in lightning bolts”. In: (1985).

- [18] *K-130 Cyclotron Operation Manual*. Version 1.0. Variable Energy Cyclotron Centre, Kolkata, June 2012. 179 pp.
- [19] *Super conducting Cyclotron Operation Manual*. Variable Energy Cyclotron Centre, Kolkata, June 2008. 328 pp.
- [20] G Gualdrini. “Monte Carlo modeling for individual monitoring”. In: *Radiation protection dosimetry* 125.1-4 (2007), pp. 139–144.
- [21] I Kawrakow and D Rogers. “The EGSnrc code system: Monte Carlo simulation of electron and photon transport”. In: (2000).
- [22] Judith F Briesmeister. “MCNP-A General Monte Carlo Code N-Particle Transport Code Version 4C”. In: *LA-13709-M* (2000).
- [23] X MCNP. *Monte Carlo Team, MCNP—a general purpose Monte Carlo N-particle transport code, version 5*. Tech. rep. LA-UR-03-1987, Los Alamos National Laboratory, April 2003. The MCNP5 code can be obtained from the Radiation Safety Information Computational Center (RSICC), PO Box 2008, Oak Ridge, TN, 37831-6362, 5.
- [24] G. Battistoni et al. “The FLUKA code: Description and benchmarking”. In: *AIP Conference Proceeding 896. Proceedings of the Hadronic Shower Simulation Workshop 2006*. (Fermilab, Sept. 6–8, 2006). Ed. by M. Albrow and R. Raja. 2007, pp. 31–49.
- [25] A. Ferrari et al. “FLUKA: A multi-particle transport code (Program version 2005)”. In: CERN-2005-010, SLAC-R-773, INFN-TC-05-11 (2005).
- [26] Steve Chucas et al. “Preparing the Monte Carlo code MCBEND for the 21st Century”. In: *Proc. of the Eighth Int. Conf. on Radiation Shielding, Arlington, TX*. Vol. 1. 381. 1994, pp. 24–28.
- [27] Stephen M Seltzer. “An overview of ETRAN Monte Carlo methods”. In: *Monte Carlo Transport of Electrons and Photons*. Springer, 1988, pp. 153–181.

- [28] Francesc Salvat, José M Fernández-Varea, and Josep Sempau. “PENELOPE-2006: A code system for Monte Carlo simulation of electron and photon transport”. In: *Workshop Proceedings*. 2006.
- [29] JP Both and Y Peneliau. “The Monte-Carlo code TRIPOLI-4 and its first Benchmark interpretations”. In: (1996).
- [30] Sea Agostinelli et al. “Geant4—a simulation toolkit”. In: *Nuclear instruments and methods in physics research section A: Accelerators, Spectrometers, Detectors and Associated Equipment* 506.3 (2003), pp. 250–303.
- [31] Nicholas Metropolis and Stanislaw Ulam. “The monte carlo method”. In: *Journal of the American statistical association* 44.247 (1949), pp. 335–341.
- [32] A. Fassò, A. Ferrari, and P. R. Sala. “Radiation Transport Calculations and Simulations”. In: *Radiation Protection Dosimetry* (2009). DOI: [10.1093/rpd/ncp190](https://doi.org/10.1093/rpd/ncp190).
- [33] URL: https://en.wikipedia.org/wiki/Reverse_Monte_Carlo.
- [34] Vasilis Vlachoudis et al. “FLAIR: a powerful but user friendly graphical interface for FLUKA”. In: *Proc. Int. Conf. on Mathematics, Computational Methods & Reactor Physics (M&C 2009), Saratoga Springs, New York*. 2009.
- [35] H. R. Vega Carrillo et al. “Response matrix for a multisphere spectrometer using a ^6LiF thermoluminescent dosimeter”. In: *Radiation Protection Dosimetry* 81.2 (1999), pp. 133–140.
- [36] A. K. Bakshi et al. “Study on the response of indigenously developed $\text{CaSO}_4\text{:Dy}$ phosphor-based neutron dosimeter”. In: *Radiation Protection Dosimetry* 133.2 (2009), pp. 73–80. DOI: [10.1093/rpd/ncp019](https://doi.org/10.1093/rpd/ncp019).
- [37] Roberto Bedogni et al. “FRUIT: An operational tool for multisphere neutron spectrometry in workplaces”. In: *Nuclear Instruments and Methods in Physics Research A* 580 (2007), pp. 1301–1309. DOI: [10.1016/j.nima.2007.07.033](https://doi.org/10.1016/j.nima.2007.07.033).

- [38] R. M. Sternheimer. “Density effect for the ionization loss in various materials”. In: *Physical review* 103 (1956), pp. 511–515.
- [39] ISO 8529 Part-1. *Reference Neutron Radiations – Part 1: Characteristics and Methods of Production*. 2001.
- [40] Vladimir Mares and Hans Schraube. “Evaluation of the response matrix of a Bonner sphere spectrometer with LiI detector from thermal energy to 100 MeV”. In: *Nuclear Instruments and Methods in Physics Research A* 337 (1994), pp. 461–473.
- [41] K. A. Lowry and T. L. Johnson. *NRL Memorandum Report*. 1984.
- [42] M. Reginatto and P. Goldhagen. “MAXED, A Computer Code For Maximum Entropy Deconvolution of Multisphere Neutron Spectrometer Data”. In: *Health Physics* 77 (1999), pp. 579–583.
- [43] Manfred Matzke. *Unfolding of Pulse Height Spectra: The HEPRO program system*. N-19. PTB, 1994.
- [44] Bhaskar Mukherjee. “BONDI-97: A novel neutron energy spectrum unfolding tool using a genetic algorithm”. In: *Nuclear Instruments and Methods in Physics Research Section A* 432 (1999), pp. 305–312. DOI: [10.1016/S0168-9002\(99\)00535-5](https://doi.org/10.1016/S0168-9002(99)00535-5).
- [45] Bhaskar Mukherjee. “ANDI-03: a genetic algorithm tool for the analysis of activation detector data to unfold high-energy neutron spectra”. In: *Radiation Protection Dosimetry* 110 (2004), pp. 249–254. DOI: [10.1093/rpd/nch222](https://doi.org/10.1093/rpd/nch222).
- [46] M. Tomás et al. “MITOM: a new unfolding code based on a spectra model method applied to neutron spectrometry”. In: *Radiation Protection Dosimetry* 110 (2004), pp. 545–548. DOI: [10.1093/rpd/nch384](https://doi.org/10.1093/rpd/nch384).
- [47] H.P. William et al. *Numerical Recipes in Fortran*. Cambridge: Cambridge University Press, 1992.

- [48] *Quick Start Guide to FRUIT ver. 3.0*. 2010.
- [49] *Compendium of Neutron Spectra and Detector Responses for Radiation Protection Purposes. Supplement to Technical Reports Series No. 318*. Technical Report Series 403. IAEA, 2001.
- [50] John M. Clem and Lev I. Dorman. “Neutron monitor response functions”. In: *Cosmic Rays and Earth*. Springer, 2000, pp. 335–359.
- [51] J.W. Bieber et al. “Latitude survey observations of neutron monitor multiplicity”. In: *Journal of Geophysical Research: Space Physics (1978–2012)* 109.A12 (2004).
- [52] John R. Lamarsh and Anthony John Baratta. *Introduction to nuclear engineering*. Vol. 3. Prentice Hall Upper Saddle River, 2001.
- [53] R Nolte et al. “Quasi-monoenergetic neutron reference fields in the energy range from thermal to 200 MeV”. In: *Radiation protection dosimetry* 110.1-4 (2004), pp. 97–102.
- [54] *Nuclear Data Viewer*. URL: <https://t2.lanl.gov/nis/data/ndviewer.html>.
- [55] Stefan Roesler and Graham R Stevenson. “deq99.f-A FLUKA user-routine converting fluence into effective dose and ambient dose equivalent”. In: *CERN Technical Note CERNSC2006070RPTN* (2006).
- [56] Arjan J Koning, Stephane Hilaire, and Marieke C Duijvestijn. “TALYS-1.0”. In: *International Conference on Nuclear Data for Science and Technology*. EDP Sciences. 2007, pp. 211–214.
- [57] Kaushik Banerjee. “Study of nuclear dynamics using neutrons”. Homi Bhabha National Institute, 2013. Chap. Detector development. 167 pp. URL: <http://www.hbni.ac.in/phdthesis/phys/PHYS04200804001.pdf>.

- [58] Deepak Pandit. “Study of high energy photon from hot nuclear systems”. Homi Bhabha National Institute, 2011. Chap. High-energy γ -rays from spontaneous fission of ^{252}Cf . 104 pp.